

Expression, inhibition and *in silico* modelling of human neuronal nitric oxide synthase

A thesis submitted to Maynooth University in fulfilment of the requirements for the degree of

Doctor of Philosophy

by

Adam Curtin, B.Sc.



Department of Chemistry,

Maynooth University,

Maynooth, Co. Kildare, Ireland

October 2015

Research Supervisor: Dr. John Stephens

Head of Department: Dr. John Stephens

Contents

1	Introduction	1
1.1	Nitric Oxide Synthase enzymes: Structure and function	2
1.2	Biological role of NO	5
1.3	Disease states relating to nNOS.....	6
1.4	NOS binding sites and inhibitory compounds.....	7
1.4.1	BH ₄ binding site	7
1.4.2	Calmodulin binding site	9
1.4.3	NADPH binding site.....	11
1.4.4	Arginine binding site	12
1.4.4.1	Modified arginines	13
1.4.4.2	2-Aminopyridines.....	18
1.4.4.3	Other scaffolds.....	25
1.5	Current challenges in the field of NOS inhibition	28
1.6	Aims of the project.....	29
2	Computational Studies.....	30
2.1	Introduction	31
2.2	Structure based design overview.....	31
2.2.1	Building a homology model	32
2.2.2	Structural verification of model.....	34
2.2.3	Functional validation of model	37
2.2.4	Conformers of database	40
2.2.4.1	Omega.....	41
2.2.5	Tautomer and stereoisomer generation.....	42
2.3	Docking.....	44
2.3.1	Fast Rigid Exhaustive Docking (FRED)	44
2.3.2	Flexible docking.....	45

2.4	Homology modelling results	46
2.4.1	Sequence alignment.....	46
2.4.2	Structural validation.....	47
2.4.3	Docking protocol validation	51
2.4.4	nNOS homology model binding pocket analysis.....	53
2.4.5	Rotamers of Glu597 and Asp602 in human nNOS homology model.....	54
2.5	eNOS and iNOS crystal structures.....	56
2.5.1	Structural validation.....	56
2.5.2	Docking protocol validation with eNOS and iNOS crystal structures	57
2.5.3	Selectivity human nNOS homology model	59
2.6	Structure based drug design virtual screening	60
2.6.1	Docking results using human nNOS homology model.....	60
2.6.2	Comparison of top docking hits in eNOS, iNOS and nNOS	68
2.6.3	Structure based design conclusion	74
2.7	Ligand based drug design overview	75
2.7.1	Pharmacophore: Construction and validation.....	76
2.7.2	Pharmacophore screening	76
2.8	Ligand based drug design results.....	77
2.8.1	Pharmacophore one construction and validation	77
2.8.2	Pharmacophore one screen.....	80
2.8.3	Pharmacophore two construction and validation	85
2.8.4	Pharmacophore two screen.....	88
2.9	Human nNOS Crystal Structure.....	91
2.9.1	Comparing homology model and crystal structure binding sites	91
2.9.2	Screening results	94
2.10	Mixed arginine/diaminopyridine compounds	99
2.11	Conclusion.....	101

3	Synthesis of Computational Hit Compounds	103
3.1	Introduction	104
3.2	Classes of inhibitory compounds and their synthesis.....	104
3.2.1	Piperazine containing compounds.....	104
3.2.1.1	Synthesis of 41	104
3.2.1.2	Structural characterisation of 41	106
3.2.1.3	Synthesis of 37-40.....	122
3.2.1.4	Structural characterisation of 39	126
3.2.2	Urea containing compounds.....	133
3.2.2.1	Synthesis of 96 and 97	136
3.2.2.2	Structural characterisation of 97	137
3.2.2.3	Synthesis of compounds 94 and 95	148
3.2.2.4	Structural characterisation of compound 94 and compound 95.....	152
3.2.3	Modified arginine and thioether compounds.....	153
3.2.3.1	Attempted synthesis and characterisation of arginine/aminopyridine, compound 98	153
3.2.3.2	Attempted synthesis and characterisation of thioether, compound 88	159
3.3	Synthesis conclusion	162
4	NOS Expression, Assay Development and Compound Evaluation.....	164
4.1	Introduction	165
4.2	DNA sequencing and verification of insert	167
4.3	nNOS expression and purification	170
4.3.1	Establishing a jackpot clone	170
4.3.2	Initial large scale expression conditions	172
4.4	nNOS expression and cell growth conditions	175
4.4.1	IPTG induction.....	176
4.4.2	Growth Media	177
4.4.3	Growth temperature.....	179
4.4.4	Cell growth time course	180

4.4.5	nNOS expression and cell growth conditions conclusion	181
4.5	nNOS lysis and purification conditions	182
4.5.1	Lysis buffer screen.....	182
4.5.2	Ni-NTA purification screen.....	185
4.5.3	nNOS lysis buffer and purification conditions conclusion	188
4.6	nNOS co-expression with calmodulin	188
4.6.1	Co-expression with optimised conditions.....	189
4.7	nNOS protocol development conclusion	192
4.8	Human iNOS and human eNOS expression	194
4.8.1	Co-transformation of human eNOS and human iNOS with human calmodulin 194	
4.8.2	eNOS expression and purification.....	196
4.8.3	iNOS expression and purification.....	199
4.9	Human iNOS and human eNOS expression conclusion	201
4.10	Functional assay development	203
4.10.1	Assay Components.....	203
4.11	Standard curve construction.....	205
4.12	NOS assay development	206
4.13	Human nNOS Griess assay development.....	207
4.13.1	Positive and negative controls	208
4.13.2	Vehicle control	210
4.13.3	Dose response studies with human nNOS.....	212
4.13.4	nNOS lysate assay	213
4.14	eNOS and iNOS assay development	215
4.15	Assay development conclusion.....	218
4.16	Compound testing.....	219
4.16.1	Homology modelling flexible docking compounds.....	220

4.16.2	Pharmacophore one compounds.....	223
4.16.3	Pharmacophore two compounds	225
4.16.4	Crystal structure docking compounds	226
4.16.5	Literature and other compounds.....	227
4.16.6	Discussion on compound evaluation	229
4.17	Conclusion.....	231
5	Materials and Methods.....	233
5.1	Chemicals and reagents	234
5.2	Biological Materials and Methods	234
5.2.1	Vectors and host strains.....	234
5.2.2	DNA amplification and verification	239
5.2.2.1	Transformation of competent E. coli	239
5.2.2.2	Miniprep and subsequent analysis	239
5.2.2.3	Agarose gel analysis	240
5.2.2.4	Midiprep culture of plasmid	241
5.2.2.5	Preparation of glycerol stocks.....	241
5.2.2.6	Gene sequencing.....	241
5.2.3	Co-expression and isolation of NOS and calmodulin proteins.....	242
5.2.3.1	Competent cells, their transformation and expression screening.....	242
5.2.3.2	Large scale expression of NOS proteins and lysis of cells	243
5.2.3.3	Purification and storage of recombinant protein	245
5.2.4	Expression verification: One dimensional electrophoresis, Western blot and mass spectrometry.....	246
5.2.4.1	Pierce protein assay	246
5.2.4.2	SDS-PAGE Analysis	246
5.2.4.3	Coomassie staining	247
5.2.4.4	Western blot	247
5.2.4.5	Stripping and re-probing PVDF membranes	248
5.2.4.6	Mass spectrometry	248
5.2.5	Griess assay	250

5.2.5.1	Standard curve construction.....	250
5.2.5.2	Sample testing.....	251
5.3	Computational theory.....	252
5.3.1	Molecular mechanical calculations.....	252
5.3.2	Force fields.....	252
5.3.2.1	Bonded Functions	253
5.3.2.2	Non bonded functions	257
5.3.3	Protein minimizations	258
5.4	Other computational tools.....	259
5.4.1	Clustering	259
5.4.2	Pharmacokinetic predictions	259
5.5	Computational Methods.....	260
5.5.1	Structure based design	260
5.5.1.1	Homology model construction	260
5.5.2	Homology model structural verification	261
5.5.3	Homology model functional verification	261
5.5.4	Database preparation and docking.....	262
5.5.5	Flexible docking.....	263
5.5.6	Key residue rotamers	264
5.5.7	Crystal structures of iNOS and eNOS and their verification	264
5.5.8	Database preparation and docking of iNOS and eNOS.....	265
5.5.9	Published crystal structure docking	265
5.5.10	Pharmacophore construction	265
5.5.11	Pharmacophore validation.....	267
5.5.12	Screening commercial databases with pharmacophores	267
5.5.13	Pharmacophore evolution	267
5.6	Chemical Materials and Methods.....	269
5.6.1	Instrumentation	269

5.6.2	Synthesis of 1-(4-(5-chloro-2-methylphenyl)piperazin-1-yl)-3-(m-tolyloxy)propan-2-ol, compound 41 ⁸⁵	270
5.6.3	Synthesis of tert-butyl (6-aminopyridin-2-yl)carbamate	270
5.6.4	Synthesis of 4-(4,6-Dimethoxy-1,3,5-triazin-2-yl)-4-methyl-morpholinium chloride (DMTMM), Compound 101 ⁹²	271
5.6.5	Synthesis of triprotected aminoguanidinium, Compound 102.....	272
5.6.6	Synthesis of N-(3-chlorophenyl)-4-(naphthalen-1-ylmethyl)piperazine-1-carboxamide, Compound 37.....	273
5.6.7	Synthesis of 4-(naphthalen-1-ylmethyl)-N-phenylpiperazine-1-carboxamide, Compound 38.....	274
5.6.8	Synthesis of 4-(naphthalen-1-ylmethyl)-N-phenylpiperazine-1-carbothioamide, Compound 39	275
5.6.9	Synthesis of N-(3-chlorophenyl)-4-(naphthalen-1-ylmethyl)piperazine-1-carbothioamide, Compound 40	276
5.6.10	Synthesis of tert-butyl (2-aminoethyl)carbamate ¹⁷³	276
5.6.11	Synthesis of tert-butyl (2-(4-fluorobenzamido)ethyl)carbamate	277
5.6.12	Synthesis of N-(2-aminoethyl)-4-fluorobenzamide	278
5.6.13	Synthesis of 1-(isocyanatomethyl)-3-(trifluoromethyl)benzene, Compound 99	278
5.6.14	Synthesis of 4-fluoro-N-(2-(3-(3-(trifluoromethyl)benzyl)ureido)ethyl)benzamide, Compound 94	279
5.6.15	Synthesis of tert-butyl (2-benzamidoethyl)carbamate.....	280
5.6.16	Synthesis of N-(2-aminoethyl)benzamide.....	280
5.6.17	Synthesis of N-(2-(3-(3-(trifluoromethyl)benzyl)ureido)ethyl)benzamide, Compound 95.....	281
5.6.18	Synthesis of 4-fluoro-N-(2-(3-(3-(trifluoromethyl)phenyl)ureido)ethyl)benzamide, Compound 96.....	281
5.6.19	Synthesis of N-(2-(3-(3-(trifluoromethyl)phenyl)ureido)ethyl)benzamide, Compound 97.....	282

5.6.20	Synthesis of 2-(2-(phenylthio)ethyl)isoindoline-1,3-dione	283
5.6.21	Synthesis of (phenylthio)methanamine.....	284
6	Conclusion.....	285
6.1	Conclusion.....	286
6.2	Future work.....	289
7	Bibliography	290
8	Appendix	303
8.1	Amino acids.....	304
8.2	Rat nNOS aligned with human nNOS.....	306
8.3	Human nNOS construct aligned with published human nNOS sequence	307
8.4	Human eNOS construct aligned with published human eNOS sequence.....	310
8.5	Human iNOS construct aligned with published human iNOS sequence.....	311
8.6	Human calmodulin construct aligned with published human calmodulin sequence 313	
8.7	Oral presentations	314
8.8	Poster presentations.....	314
8.9	Publications.....	315

Declaration

I declare that the work presented in this thesis was carried out in accordance with the regulations of Maynooth University. The work is original, except where indicated by reference, and has not been submitted before, in whole or in part, to this or any other university for any other degree.

Signed: _____ Date: _____

Acknowledgments

Wow, I've been looking forward to writing this section for a while. Firstly I want to thank my supervisor John Stephens, my co-supervisor Fintan Kelleher and my unofficial supervisor Gemma Kinsella. I definitely would not have made it this far without their constant help and support, and willingness to answer the endless lists of questions I came up with.

I also have to thank my parents. They have always encouraged me when it came to academic pursuits. Doing a PhD would not have even crossed my mind without their support. Also thanks to Emma for the chats and banter, it really helped keep my head clear.

Once I realised what I had let myself in for with the PhD, it was my wonderful girlfriend Maire who kept me going. My parents may have got me to the start line, but Mar carried me across the finish. You will never know how grateful I am for that. I feel like this thesis is half hers as she has put up with so much complaining, late nights and weekends in work. More than anyone, she is responsible for getting me here.

I have met so many fantastic people during my time here in Maynooth. First thanks and acknowledgments have to go to Chig, Bar and Ross. We've known each other for nearly eight years, having done undergrad and PhDs together. I couldn't have asked for three better lads to go through the university process with. I'll always think back to that house in Moyglare with fond memories. From the mental neighbours to Nico and Murph wrestling beside the bins, it was great craic from start to finish.

Of course the others in the lab were, and are just as sound as the three lads. Old Andrew "two fires" Reddy, still alright despite being from Kildare (shudder). Justine "Special J", I'll leave the rad behind in the writing room, couldn't have you sitting at 10 K when you get to writing up. The grumpiest English man to ever live, Jack give me a shout if you're heading for a sneaky Boojum. Jessica, our Spanish import, thanks for making me look patient with the students. Thanks also to Mark and Muhib, didn't get to know you too well but best of luck with the research.

Outside of the synthesis lab then, I have to thank bad Michelle for arranging all the sessions, even if I did never show up. Mark Grace deserves a special mention for all the early morning shakes and chatting about work. Cheers man. Thanks to Ula and Alice for the sometimes off colour but always entertaining lunch time banter, I'll have to practice my

“normal” topics of conversation before I get a real job. Thanks to Finno and John Kealy for never letting me forget my brief Friday football career. I might see you out on the bike John.

Over on the “dark side” in the biology department I have to thank Siobhan, although I doubt she’ll be out of the dark room long enough to read this. Also thanks to Darren and Conor for helping me out massively with the expression and purification experiments. Best of luck in the future lads, you really deserve it. Since I’m talking about biology I want to express my gratitude to Prof. John Findlay for taking me into the lab and showing me the molecular biology ropes. I feel privileged to have learned from and worked with such an esteemed researcher. To Kate, Pam, Susan, Therese, Zita, Helen and Ash, thanks for all the help along the way, particularly for the chatting about the BioAT set up.

To the lads back home, Rourke, Chico, Whitey, Dawson, Sly, Ois and Lenny. I promise I’ll go get a real job now, and hopefully get out for a few pints more often. To Duigy, Shauna, Rinaldo and Shindler, thanks for the many, many, many games of beer pong and various trips away. Thanks also to Faylo and Bradshaw for helping me through some rough times before and during the PhD.

Of course I never would have made it this far without the support of the great academic staff in the department, all of whom lectured me at some point. So thanks to John Lowry, Trinny, Carmel, Maryanne, Sean, Malachy and Frances. Also thanks to Ken for all the orders, NMR fixes and general chat about swords and guns. I’d also like to mention Donna and Carol for organising all my modules and official registration details, I don’t know how you stayed on top of all the paperwork, but I am very grateful that you did. Finally for the Chemistry Department staff, I’d like to thank Ollie, Walter and Barbra for running various mass spec samples, and to Ria for making sure the whole place runs smoothly. Special thanks also to Noel who managed to resurrect many pieces of equipment and saved me a few quid during the PhD.

Dedication

To my parents, thanks for everything
and to Mar with all my love

Abstract

Nitric oxide (NO) is a free radical, gaseous molecule that is involved in a vast range of biological signalling processes including long term memory formation, neurogenesis, vasodilation and inflammation. The molecule is produced by a family of enzymes called nitric oxide synthases (NOS). There are three major isoforms of these NO producing enzymes, endothelial NOS (eNOS), inducible NOS (iNOS) and neuronal NOS (nNOS). eNOS is constitutively expressed in the circulatory system, while iNOS is inducibly expressed in response to cellular invasion by a pathogen. nNOS, which was the isoform targeted in this work, is constitutively expressed in the brain and central nervous system, where the NO it produces regulates many neurogenic pathways.

Over activation of nNOS leads to elevated levels of NO in the brain. This has been implicated in an array of serious physiological conditions including schizophrenia, Alzheimer's and Parkinson's disease. Modulation of nNOS over activation therefore represents a potential therapeutic avenue for treatment of a variety of debilitating and life threatening conditions.

The field of nNOS inhibition currently focuses almost exclusively on the arginine binding site of the rat nNOS isoform of the enzyme. The arginine binding site in rat nNOS does differ from that of human nNOS, and as such is not an ideal system with which to study human nNOS inhibition. Therefore, this work incorporated computational studies to model and examine the binding sites of human nNOS. These included construction and verification of a human nNOS homology model. This offered the best option for a detailed examination of the protein as no crystal structure of human nNOS was initially available. The model was used to screen for novel and selective human nNOS inhibitors. This structure based approach was complimented by the use of a ligand based design approach. To do this, a pharmacophore was constructed and used for high throughput screening for the identification of novel inhibitory compounds. The pharmacokinetic properties of the hit compounds were considered, as was their potential selectivity for human nNOS over human eNOS and human iNOS. Over 20 million compounds from the Maybridge and Zinc databases were screened with the various computational methods, and 72 were chosen for biological evaluation. This high throughput *in silico* screening approach has not been widely utilised in the search for human nNOS inhibitors, with only one such study reported. This publication did not attempt to biologically evaluate the potential nNOS inhibitors.

A functional assay was required to test the compounds identified from the *in silico* screens. This necessitated the recombinant expression of human nNOS, iNOS and eNOS proteins. The literature routinely reports rat nNOS, murine iNOS and bovine eNOS to test inhibitory compounds, so the establishment of an all human high throughput assay system represented a major step forward in the field. Bacterial cells were transformed with the DNA sequences for all three human NOS isoforms. The proteins were recombinantly expressed and purified from the resulting *E. coli* lysate. The procedure for human nNOS expression was optimised, and the co-expression of human nNOS with human calmodulin was achieved. Calmodulin is a vital co-factor for the production of NO from NOS and its co-expression with human nNOS has not previously been reported. The same approach was applied to eNOS and iNOS. The expressed human NOS proteins were then used to establish a functional, high throughput NOS assay using the Griess reaction.

Once established, the assay was used to screen the computationally derived hits for human nNOS inhibitory activity. Some hits could be purchased, but many had to be synthesised. The synthesised compounds were loosely classified into three classes, i) piperazine containing compounds, ii) urea containing compounds and iii) modified arginines and thioethers. The high throughput expression/assay system for human nNOS worked well, and although no novel inhibitory compounds were identified, it allowed for the testing of 72 *in silico* derived compounds. The assay system also allowed for determination of the IC₅₀ of the non-selective NOS inhibitor, L-NNA.

This work represents a valuable contribution to the field of nNOS inhibition as it is among the first projects to attempt large scale screening for human nNOS inhibitory compounds. The projects also succeed in the expression of all three human NOS proteins with human calmodulin, and a high throughput expression/assay system was established for human nNOS inhibition. Novel compounds were successfully synthesised, characterised and evaluated. This work provides a useful roadmap for the future development of human nNOS inhibitory compounds, as well as providing an established computational screening methodology and a high throughput functional human nNOS assays/expression system.

List of abbreviations

2,2,4,5,7-pentmethyldihydrobezofuran-5-sulfonyl group = Pbf

2-chloro-4,6-dimethoxy-1,3,5-triazine = CDMT

3PNF Homology Model = 3PNF-HM

3RQJ Homology Model = 3RQJ-HM

4-(4,6-Dimethoxy-1,3,5-triazin-2-yl)-4-methylmorpholinium chloride = DMTMM

Calcium binding region = CBR

Calmodulin = CaM

Central nervous system = CNS

Chemistry at HARvard Macromolecular mechanics = CHARMM

Colony forming units = cfu

Computer aided drug design = CADD

Correlation spectroscopy = COSY

Coupling constant = J

Cyclic guanosine 3',5'-monophosphate = cGMP

Dichloromethane = DCM

Dimethylformamide = DMF

Discrete optimised protein energies = DOPE

Distortionless enhancement by polarization transfer = DEPT

Dithiothreitol = DTT

Doublet of doublets = dd

Endothelial nitric oxide synthase = eNOS

Enhanced chemiluminescent = ECL

Escherichia coli = *E. coli*

Flavin adenine dinucleotide = FAD

Flavin mononucleotide = FMN

Formic acid = FA

Fourier transformation infrared = FTIR

Guanosine triphosphate = GTP

Guanylate cyclase = GC

Hertz = Hz

Heteronuclear multiple-bond correlation spectroscopy = HMBC

Heteronuclear single quantum correlation spectroscopy = HSQC

High resolution mass spectroscopy = HR-MS

Histidine tag = His-tag

Homology model = HM

Hydrogen bond = HB

Hydroxybenzotriazole = HOBT

Inducible nitric oxide synthase = iNOS

Infrared = IR

Isoelectric point = pI

Lysogeny broth = LB

Melting point = MP

Milli-Q = MQ

Multiplet = m

N,N-Dicyclohexylcarbodiimide = DCC

Neuronal nitric oxide synthase = nNOS

N-hydroxy-L-arginine = L-NOHA

Nickel Nitriloacetic acid = Ni-NTA

Nicotinamide adenine dinucleotide phosphate = NADPH

Nitric oxide = NO

Nitric oxide synthase = NOS

N-methylmorpholine = NMM

Nuclear magnetic resonance = NMR

N^ω-Nitro-L-arginine = L-NNA

Optical density = OD

Petroleum ether = Pet ether

Pharmacokinetic = PK

Phosphate buffered saline = PBS

Phosphate buffered saline with 1% triton = PBST

Piecewise Linear Potential = PLP

Polyvinylidene fluoride = PVDF

Porphyrin = Por

Probability density function = PDF

Protein databank = PDB

Protein kinase G = PKG

Quartet = q

Reactive nitrogen species = RNS

Reactive oxygen species = ROS

Receiver operator characteristic = ROC

Retention factor = R_f

Room temperature = RT

Room temperature = rt

Root mean square deviation = RMSD

Singlet = s

Sodium dodecyl sulphate = SDS

Sodium dodecyl sulphate polyacrylamide gel electrophoresis = SDS-PAGE

Super optimal broth with catabolite repression = SOC

t-butyloxycarbonyl = Boc

Terrific broth = TB

Tetrahydrobiopterin = BH₄

Tetrahydrofuran = THF

Tetramethylethylenediamine = TEMED

Thin layer chromatography = TLC

Time of flight = TOF

Trifluoroacetic acid = TFA

Ultraviolet = UV

Wavelength (nm) = λ

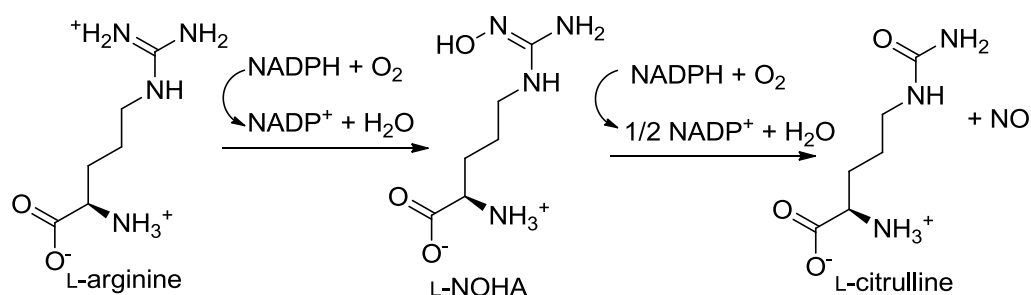
The journey of 1,000 miles begins with a single step

Lao Tzu

1 Introduction

1.1 Nitric Oxide Synthase enzymes: Structure and function

Nitric oxide synthases (NOS) are a family of enzymes that produce the key signalling molecule nitric oxide (NO) from L-arginine and molecular oxygen via an N-hydroxy-L-arginine (L-NOHA) intermediate (**Scheme 1.1**).¹



Scheme 1.1 Production of NO from L-arginine and molecular oxygen.

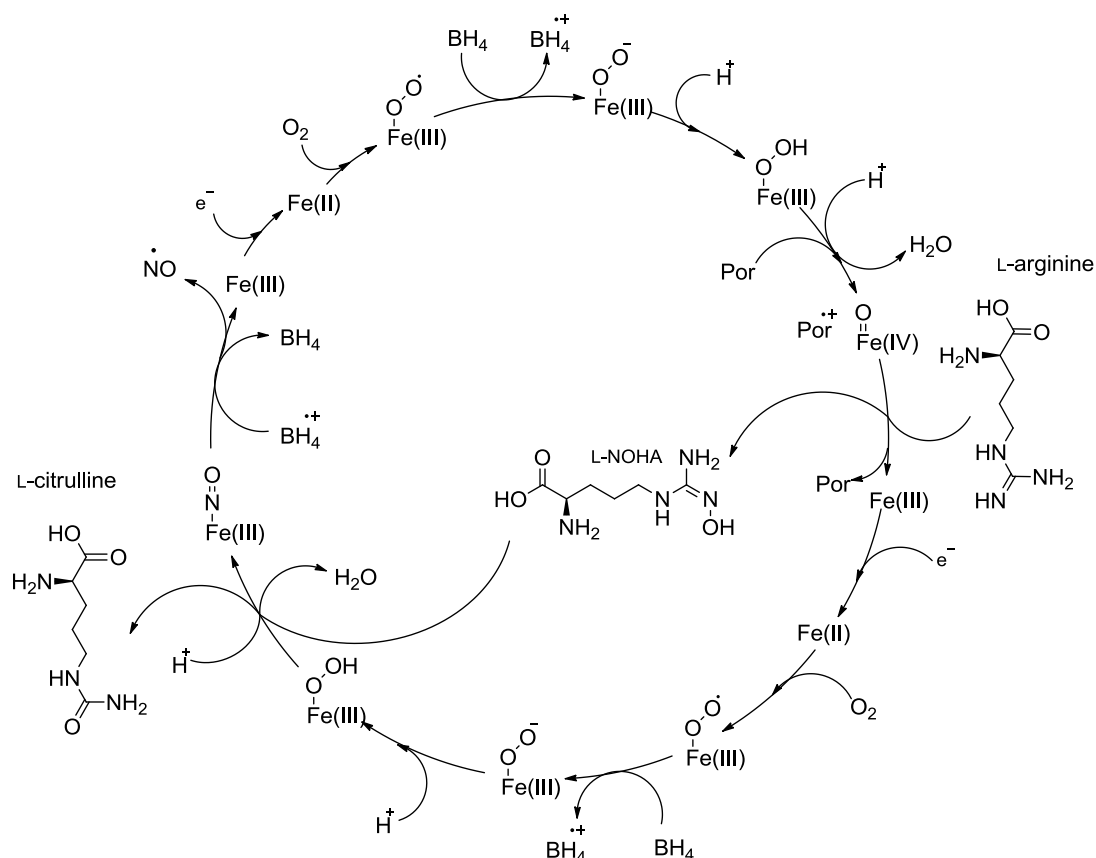
There are three mammalian isoforms of the NOS enzyme, endothelial NOS (eNOS), neuronal NOS (nNOS), and inducible NOS (iNOS).² Endothelial NOS produces NO for use in the vascular system where it regulates vasodilation and vascular pressure.³ eNOS has also been observed in the lungs and trachea where it modulates ciliary motility and smooth muscle relaxation.³ nNOS is localized primarily in the brain and central nervous system (CNS). The NO produced by this isoform is used for neurogenesis and regulation of the cholinergic, dopaminergic and glutaminergic signalling pathways, among others.⁴ iNOS produces NO in response to infection of host cells by bacteria or other pathogens. This NO has been observed to have both pro and anti-inflammatory effects and also some tumour suppression activity.⁵

All three isoforms exist as homodimeric enzymes, with each monomer consisting of an N-terminus oxygenase domain and a C-terminus reductase domain.² These domains are connected by a calmodulin binding region (CBR). The oxygenase domain contains a non-catalytic zinc, tetrahydrobiopterin (BH_4) and the catalytic active site, which binds L-arginine and a heme moiety. The reductase domain employs nicotinamide adenine dinucleotide phosphate (NADPH), flavin adenine dinucleotide (FAD) and flavin mononucleotide (FMN) to shuttle electrons from the reductase domain to the iron at the centre of the heme co-

factor in the catalytic active site.¹ In the active site, L-arginine then becomes oxidised to L-citrulline and NO is produced.⁶ The zinc ion in the oxygenase domain, while not directly participating in the catalytic cycle, provides a co-ordination site for four symmetry related cysteine residues, two from each monomer. This tetrahedral coordination sphere is an integral part of the dimer interface of NOS enzymes.⁷⁻⁹

Activation of eNOS and nNOS is dependent on calmodulin (CaM) binding.¹⁰ This binding event is controlled by calcium levels where an increase in cellular calcium concentration facilitates formation of the NOS/CaM complex. Without CaM the enzymes are far less efficient at electron transfer and activity notably decreases.¹¹ This system offers a regulatory mechanism for the constitutively expressed eNOS and nNOS. In contrast, CaM is bound to iNOS even at very low cellular calcium concentrations. This isoform is inducibly expressed and is therefore regulated at the transcriptional level, rather than by calcium binding events.¹²

The mechanism of NO production is conserved across all three isoforms, with the heme iron in the arginine binding site playing a central role in the catalytic cycle. Although some of the specifics of this pathway have yet to be elucidated, a proposed cycle is provided in **Scheme 1.2** adapted from the literature.¹²⁻¹⁴ The exact nature of the oxidative species is still unclear.¹³



Scheme 1.2. Proposed NOS catalytic cycle, (Por=porphyrin).¹⁵

The proposed cycle begins with the heme iron in the resting (III) oxidation state. An electron, transferred from the reductase domain, reduces the heme iron to the (II) oxidation state. Molecular oxygen binds to the iron and subsequent electron transfer from tetrahydrobiopterin (BH₄) and protonation generates an iron peroxy complex. Protonation, electron transfer (from the porphyrin ring) and loss of water generates the iron (IV) complex with a doubly bound oxygen atom.^{10,13} The iron (IV) complex then reacts with L-arginine to form the intermediate L-NOHA and iron (III) is regenerated. A similar sequence of steps is then repeated, starting with the transfer of an electron from the reductase domain, reducing the heme iron to the (II) oxidation state. Once the iron (III) peroxy species is generated it reacts with L-NOHA to produce L-citrulline and an iron (III) nitrosyl species. In the final steps, the NO radical is formed and released along with the regeneration of iron (III) to restart the cycle.

1.2 Biological role of NO

As briefly alluded to above, NO is involved in a range of biological signalling processes. To exert these effects NO stimulates guanylate cyclase (GC), an enzyme which catalyses the production of cyclic guanosine 3',5'-monophosphate (cGMP) from guanosine triphosphate (GTP) (**Figure 1.1**).

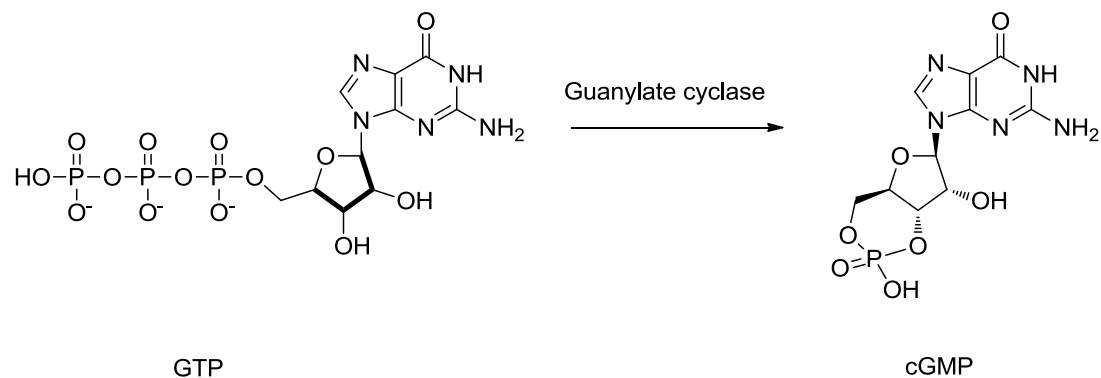


Figure 1.1. Production of cGMP from GTP, catalysed by guanylate cyclase.

cGMP then binds to allosteric sites on protein kinase G (PKG). The binding of cGMP to PKG results in a 3-10 fold increase in the phosphotransferase activity of PKG.¹⁶ PKG then phosphorylates a huge range of sites on a myriad of proteins, resulting in a diverse range of biological effects.¹⁷⁻²⁰ These effects include neuronal signal transduction, vasodilation, increased pain perception and calcium release events.¹⁶ The effects of NO production on physiological function are clearly wide ranging and of vital importance. The malfunction of the NOS enzymes will therefore have serious and potentially fatal implications. This is of particular importance for nNOS owing to its key role in neurological signalling.

1.3 Disease states relating to nNOS

Malfunction of nNOS has been linked to a range of disease states. Over activation of nNOS leads to elevated levels of NO in the brain and CNS. This has been associated with chronic neurological conditions including Alzheimer's, Parkinson's and Huntington's diseases.²¹⁻²⁴ Post mortem brain tissue of schizophrenia sufferers was also reported to have double the levels of NO metabolites when compared to the tissue of patients not affected by the condition.²⁵

Over active nNOS can also lead to an increase in the levels of damaging oxidative species in the brain. This may be compounded by the uncoupling of the electron transport chain of nNOS as shown in **Scheme 1.2**. This uncoupling can occur in the absence of BH₄, resulting in the production of reactive oxygen species (ROS) such as superoxide O₂⁻. This superoxide can further react to generate reactive nitrogen species (RNS), such as peroxynitrite (ONOO-).^{6,14,26} Both of these species can inflict oxidative stress on cells, resulting in translation errors and protein aggregation.²⁷

Due to the number of disease states that NO is implicated in, over active nNOS represents an attractive therapeutic target. Partial inhibition of the protein may reduce the levels of NO, ROS and RNS in the brain and go some way to addressing the debilitating conditions outlined above. However, targeting of nNOS is not without its challenges. The protein is localised mainly in the brain, and so any potential inhibitor must have the ability to cross the blood brain barrier (BBB). Also, as the NO produced by nNOS is involved in a vast array of normal biological functions, any inhibitory effects must be partial and transient.

The third issue which must be confronted for nNOS inhibition is that the iNOS and eNOS isoforms have similar binding sites and mechanisms of action to that of nNOS. Any inhibitory molecule must therefore selectively target nNOS, while leaving iNOS and eNOS unaffected. The current literature for nNOS inhibition has explored both the selectivity and efficacy of a number of compound classes, which have been targeted at four key sites in the NOS enzymes. These four binding sites, and the compounds used to inhibit them, will be outlined in the following sections.

1.4 NOS binding sites and inhibitory compounds

To date several families of small molecule inhibitors have been developed to partially inhibit overactive nNOS. These inhibitors have been targeted at four potential therapeutic target sites. These sites are:

1. The tetrahydrobiopterin (BH₄) binding site, located in the oxygenase domain.
2. The CaM binding site, which sits between the oxygenase and reductase domains.
3. The NADPH binding site, which is located in the reductase domain.
4. The catalytic active site, which is located in the oxygenase domain and binds arginine for production of NO.

Of these four sites, the arginine binding site is by far the most studied, and is the most popular target for nNOS inhibition. The other three sites, and the compounds used to inhibit them will be briefly discussed, followed by a more detailed discussion of the arginine binding site, which was the target of this work. The nNOS isoform will be the focus of the discussion and, where appropriate, some comments will be made on the selectivity profile of the literature compounds.

1.4.1 BH₄ binding site

Tetrahydrobiopterin, BH₄ (**Figure 1.2**) is a pterin ring containing prosthetic group which is crucial for NOS function. It participates in electron transfer during NO production, and also plays a role in NOS dimer formation and stabilisation, which is necessary for enzyme activation.²⁸

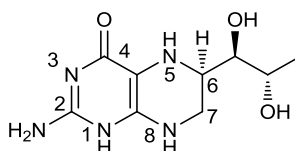


Figure 1.2. Tetrahydrobiopterin with numbered positions.

An image of BH₄ in the rat nNOS binding site is shown in **Figure 1.3**.²⁹ The strongest interaction between the binding site and BH₄ was identified as a π stacking interaction with the primary amine substituted ring and the side chain of Trp678 (see Appendix, **Table 8.1**, for all amino acid one and three letter codes and **Figure 8.1** for side chain structures). An extensive network of hydrogen bond (HB) interactions was also identified.²⁹ N-3 of BH₄ forms a direct HB with the carboxylate of the heme moiety and a solvent mediated interaction also exists between the same propionate group and the C-4 carbonyl. This carbonyl group also directly HBs with Arg596. The primary amine at C-2 interacts with the heme propionate and HBs with Trp678. The N-8 hydrogen interacts with Val677, and the BH₄ dihydroxypropyl chain extends into the pocket formed by side chains of Trp(B)306, Met336 and Trp(B)676. The dihydroxypropyl chain also interacts with Ser334 and Phe(B)691 carbonyl oxygens and with His(B)692 via structural water.²⁹

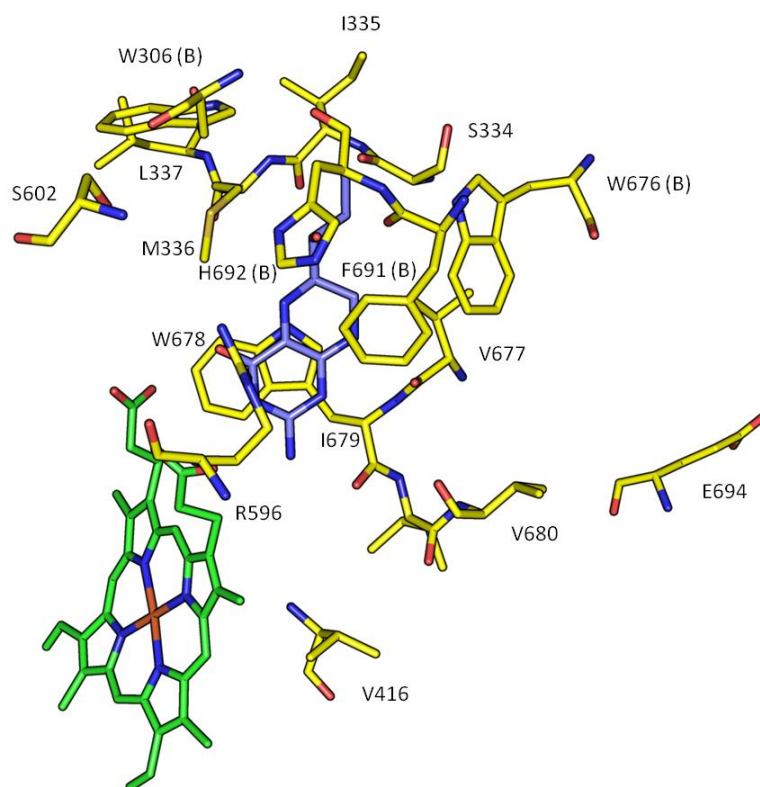


Figure 1.3. Rat nNOS BH₄ binding site with BH₄ bound (PDB: 4D2Y).²⁹ BH₄ is shown in blue, heme in green and key residues in yellow. Waters removed for clarity. All images generated with pymol.³⁰

A small number of inhibitors have been designed to target this site in an attempt to decrease over activation of nNOS.²⁹ The most successful of these to date is a modified BH₄ compound, **1**, shown in **Figure 1.4**. This had an IC₅₀ of 3.68 μM against human nNOS, with a 58.20 and 8.62 fold selectivity over human eNOS and human iNOS respectively.²⁹

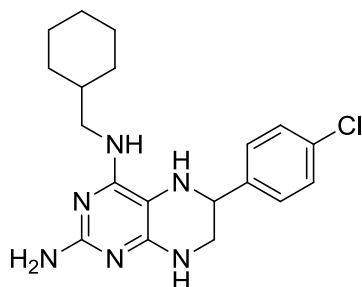


Figure 1.4. Human nNOS inhibitory compound which targets BH₄ binding site.²⁹ (**1**)

While this compound was not crystallised in the human nNOS BH₄ binding site, the key interactions between it and the binding site were computationally predicted. The predicted interactions were similar to those observed for the natural substrate in the binding site as described above. The primary amine group HBs to the heme carboxylate and also to the Trp678 residue. The hydrogen on N-8 interacts with Val677. The C-4 carbonyl of BH₄ is replaced by a C-4 NH in **1**, which breaks the HB interaction with Arg596. The large p-chlorophenyl group is accommodated by a pocket formed by TrpB306, Met336 TrpB676 and Glu694. This pocket plays a key role in the selectivity of **1** for nNOS over eNOS and iNOS. Replacement of Met336 with a valine (as in eNOS) resulted in lower binding affinity for **1**.³¹

1.4.2 Calmodulin binding site

The second potential site for nNOS inhibition is the calmodulin binding site of the enzyme. CaM binding to NOS enzymes is an integral part of their function. The CBR of the enzymes is a ~25 amino acid sequence located between the oxygenase and reductase domain.³² CaM binding allows a 70 Å conformational change to occur in the NOS proteins, as determined by nuclear magnetic resonance (NMR) spectroscopy and hydrogen deuterium exchange mass spectrometry.^{33,34} This conformational change facilitates the transfer of an

electron from the final reductase partner, FMN, to the heme moiety in the oxygenase domain of another NOS monomer as illustrated in the schematic (**Figure 1.5**).¹¹

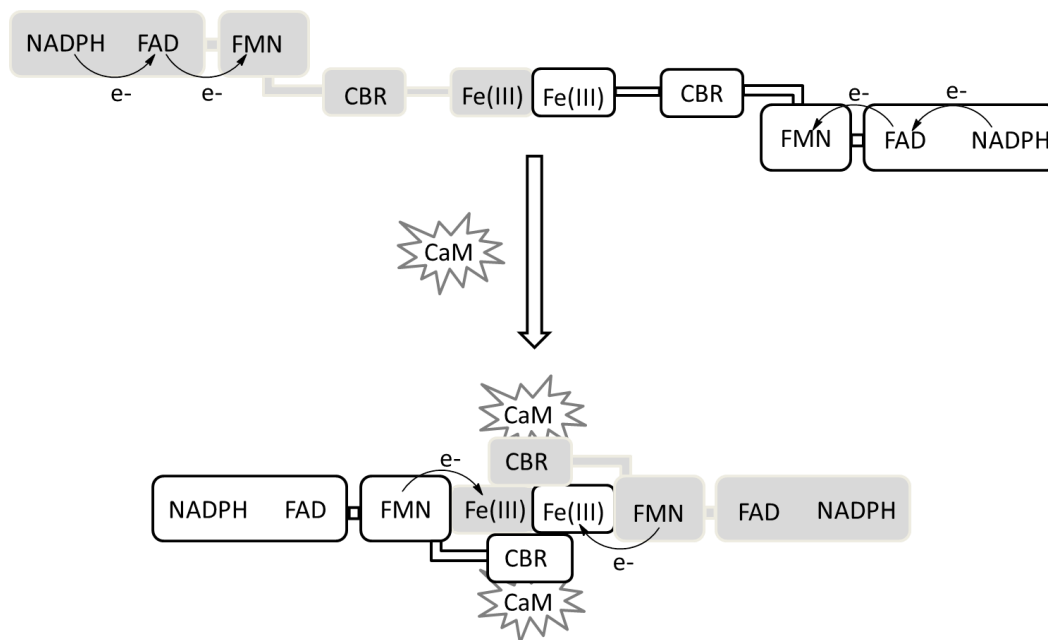


Figure 1.5. CaM mediated hinge of NOS proteins. The NOS protein is shown in its dimeric form, with one monomer in grey and the other in white.¹⁵

Some compounds have been developed which bind to the CBR site of nNOS and inhibit CaM interaction with the NOS enzyme. This prevents the “hinge” mechanism as shown above and reduces NO production. These compounds include monobutyltin trichloride and the breast cancer treatment tamoxifen, **2** (**Figure 1.6**), which was shown to reduce nNOS activity by 10-30%.³²

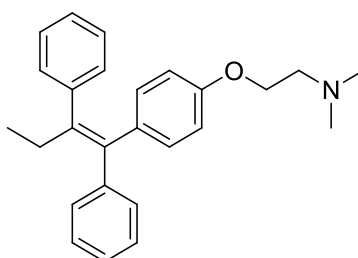


Figure 1.6. Tamoxifen, **2**, which was used for nNOS calmodulin inhibition studies.³²

The CBR of nNOS has not been as extensively studied as other sites such as the arginine binding site for nNOS inhibition. One of the key challenges associated with targeting the CBR region of nNOS is generating significant isoform selectivity. CaM binds to all three NOS isoforms using a 1-5-8-14 binding pattern. This binding motif is common for proteins that interact with calmodulin.^{35,36} The CBR of the three human isoforms, and the residues which are used to interact with CaM, are shown in **Table 1.1**. The 1-5-8-14 residue motif is conserved precisely in human nNOS and eNOS, while there are two residue changes in the iNOS motif. The iNOS sequence contains more hydrophobic residues than either of the constitutive isoforms, which may explain the higher affinity of iNOS for CaM.³⁷

Table 1.1. CBR of three human NOS isoforms, 1-5-8-14 residues highlighted in bold

Isoform (residues)	Alignment
Human iNOS (412-431)	REI PLKVLVKAVL FACMLMR
Human eNOS (493-512)	RK KTFKEV ANAVKISASLMG
Human nNOS (732-751)	RAIG FKKLA EAVKFSKLMG

Another potential challenge with targeting the CBR region of nNOS is that the design of compounds to disrupt protein-protein interactions is often difficult no matter what the target.³⁸ This is due to the fact that the binding sites for protein-protein interactions are often solvent exposed and are not amenable to formation of strong interactions with potential inhibitors.

1.4.3 NADPH binding site

NOS catalysis is driven by the reduction of NADPH, which binds to the reductase domain of NOS enzymes. The NADPH binding site therefore offers a potential intervention point at which the NOS catalytic cycle could be halted, thus inhibiting enzyme activity. The compounds which have been explored for this purpose have involved the coupling of an NADPH mimicking moiety with a chromophore, such as **3** shown in **Figure 1.7**.³⁹

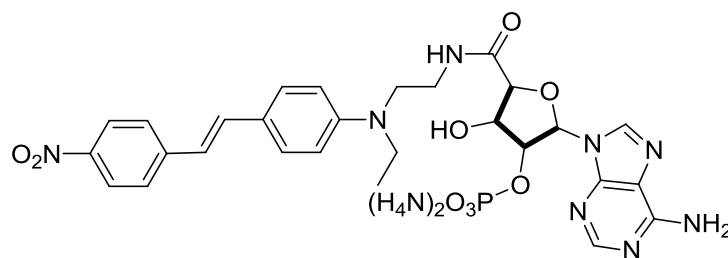


Figure 1.7. 3 which was designed to target the NADPH binding site of the NOS proteins. The right portion of the molecule was designed to bind the NADPH site, while the left portion acts to capture electrons.³⁹

3 was designed to trap electrons and block the electron flow in the NOS electron transport chain. The predicted interactions between **3** and the NADPH binding site of the NOS enzymes all involved conserved arginine residues (Arg1400, Arg1314, Arg1284 and Arg1010).³⁹ **3** was reported to bind to nNOS, however this approach to nNOS inhibition struggled to generate selective inhibitors. There is also the possibility that **3** will interact with the NADPH binding site of other enzymes not related to NOS. This may result in serious off target effects. As such, **3** is one of only four compounds that have been designed to target the NADPH binding site of nNOS.^{39,40}

1.4.4 Arginine binding site

The vast majority of nNOS inhibition studies are focused on the arginine binding site of the enzyme.^{27,41,42} This site facilitates the binding of L-arginine, the natural substrate for nNOS. Blocking of the site with a small molecule inhibitor has the potential to address the over activation of nNOS enzymes, and to aid in the treatment of the conditions discussed in section 1.3. The inhibitory compounds that have been explored for this purpose can be divided into two main categories. The first category is modified arginine compounds. These compounds attempt to mimic the binding of the natural substrate in the nNOS catalytic active site, and act as competitive inhibitors of L-arginine. The second class of inhibitors are 2-aminopyridine containing compounds. These also act as competitive inhibitors of the L-arginine binding site, but have demonstrated some unexpected binding poses.

1.4.4.1 Modified arginines

One of the earliest compounds developed for nNOS inhibition was N ω -nitro-L-arginine (L-NNA), **4**.⁴³ This compound has a very similar structure to arginine, differing only in the inclusion of a nitro group on the end of the guanidinium side chain (**Figure 1.8**).

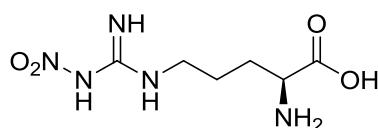


Figure 1.8. L-NNA, **4**, one of the earliest arginine mimics studied for nNOS inhibition.⁴³

This compound was crystallised in the rat nNOS binding site (PDB 1K2R: reported in PDB only, not in the literature) to examine the key interactions between inhibitor and active site. An image of L-NNA in the rat nNOS binding site is shown in **Figure 1.9**.

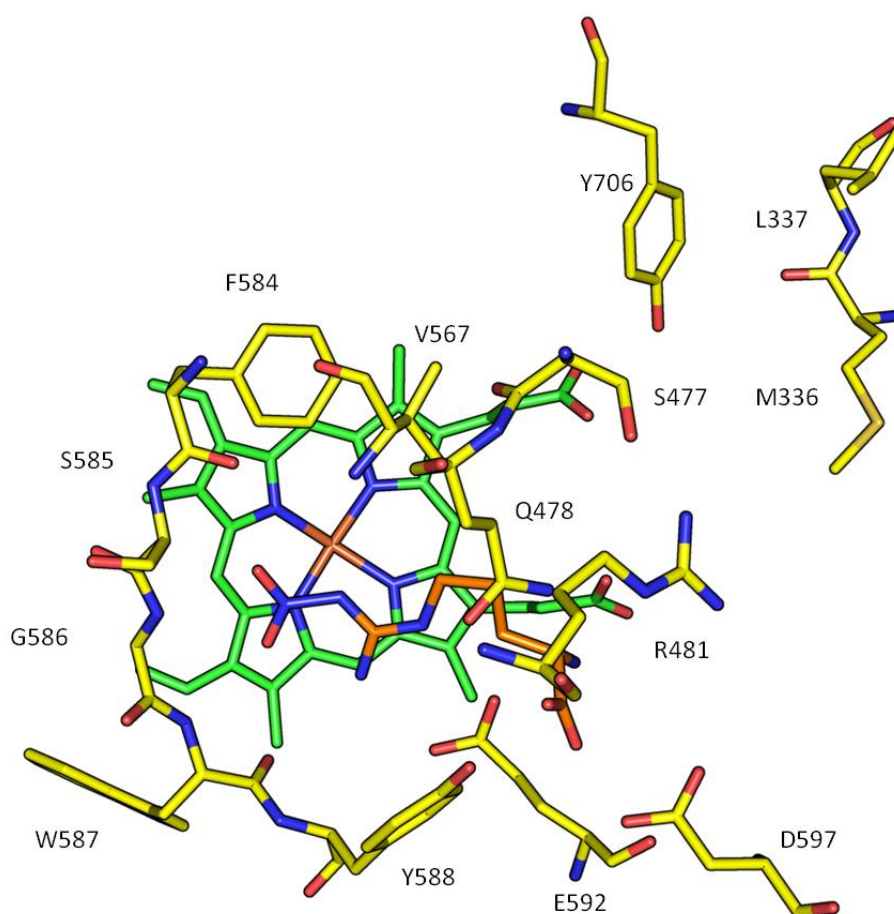


Figure 1.9. Rat nNOS arginine binding site with L-NNA (orange) bound (PDB: 1K2R). Heme is shown in green, residues in yellow. Hydrogens, waters and BH₄ have been omitted for clarity.

Glu592 was observed to form several HB interactions with the nitro guanidino group of the L-NNA inhibitor. Asp597 was also involved in binding via water mediated electrostatic interactions with the primary α amino group of the inhibitor. The C terminus carboxamide of L-NNA formed HBs with Gln478, Arg481 and Ser477 while the side chain amino group interacts via a water molecule with the heme propionate.⁴⁴

While L-NNA was seen to be an effective rat nNOS inhibitor, with an IC₅₀ of 6 μ M, it was also found to target bovine eNOS, making it a non-selective inhibitor.⁴⁵ Attempts were made to improve its selectivity by synthesising a range of analogues such as those shown in **Figure 1.10**, **5**, **6** and **7**. These were observed to have K_i values of 0.13 μ M, 0.12 μ M and 0.07 μ M for rat nNOS, and 200 μ M, 300 μ M and 130 μ M for bovine eNOS.⁴⁴

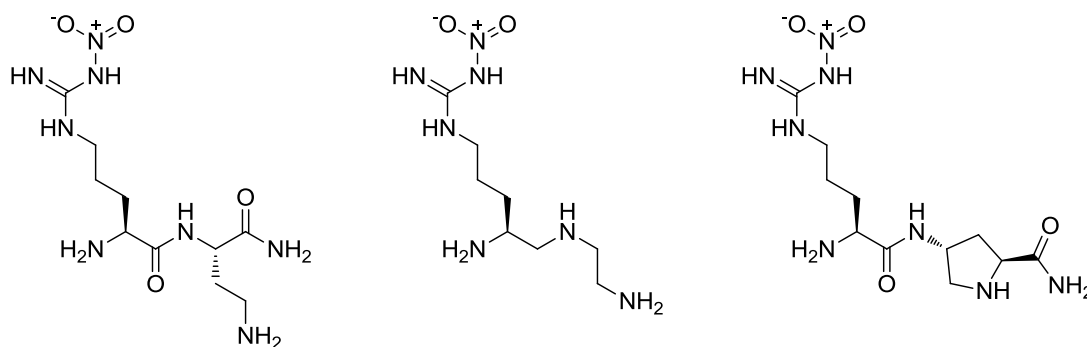


Figure 1.10. Modified L-NNA analogues, **5**, **6** and **7**, designed to study and improve inhibitor selectivity for nNOS over eNOS.⁴⁴

7 was crystallised in the bovine eNOS and rat nNOS binding site in an attempt to elucidate the reasons for its nearly 2000 fold selectivity for nNOS over eNOS. In the rat nNOS site the guanidine group made a bifurcated HB with Glu592. The nitro group made an additional HB with the protein backbone, strengthening the interaction of the inhibitors with the binding site. In bovine eNOS the inhibitors made the same interactions with the equivalent glutamic acid, Glu363. In eNOS, either the guanidine to Glu bond, or the nitro to backbone HB was stretched slightly (~ 3.2 Å), which partly explains the selectivity of the compounds.⁴⁴ The most important difference between eNOS and nNOS however was thought to be the replacement of Asp597 in nNOS with Asn368 in eNOS. It was hypothesised that the presence of the negatively charged residue in nNOS encouraged the inhibitors to adopt a curled configuration. This allowed the α amino group on the inhibitors to be stabilised by both Asp597 and Glu592 in nNOS. In eNOS, this dual stabilisation was not possible as the aspartic acid was replaced by an asparagine.⁴⁴ The extended binding conformation of **7** in bovine eNOS and its curled binding conformation in rat nNOS are shown in **Figure 1.11**. Notice the proximity of the primary amine of the inhibitor to E592 in rat nNOS (2.8 Å), while the equivalent primary amine is further removed from E363 in bovine eNOS (5 Å).⁴⁴

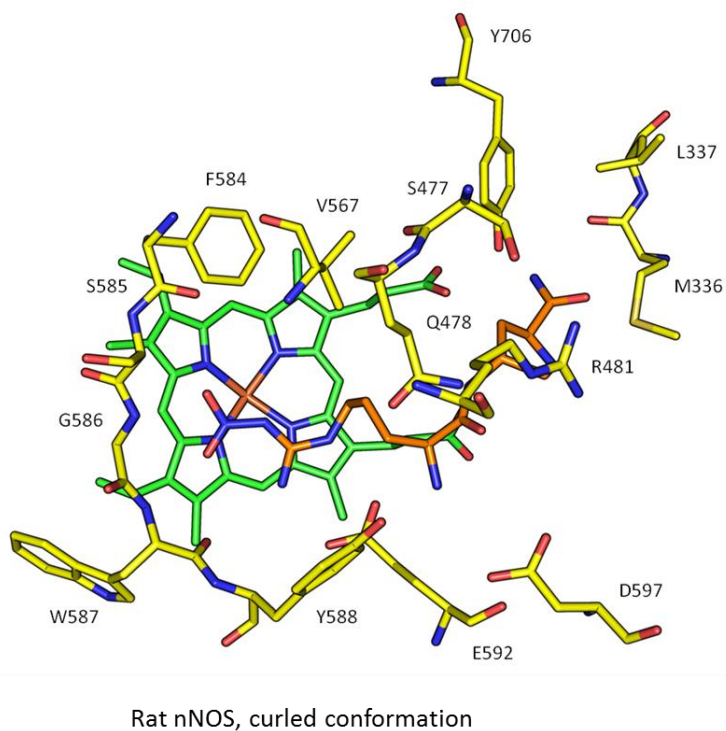
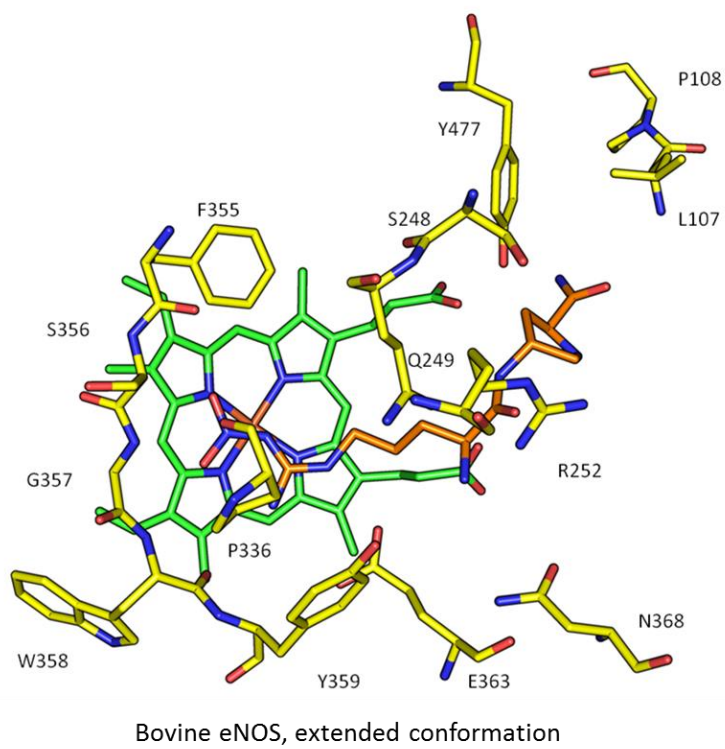


Figure 1.11. Bovine eNOS with **7** bound in extended conformation (PDB: 1P6N) vs rat nNOS with **7** bound in curled conformation (PDB:1P6J).⁴⁴

Further analysis of the precise binding modes of the arginine inhibitors using molecular docking has been reported. A selection of nNOS inhibitory arginine mimics, including **5**, **6** and **7**, were flexibly docked into the arginine binding site of rat nNOS, human iNOS and bovine eNOS.⁴⁶ This resulted in the identification of four “sub-pockets” within the rat nNOS arginine binding sites that could potentially be used to guide the design of inhibitors. The four pockets were termed S, M, C1 and C2.⁴⁶ The S pocket is found above the heme ring and is comprised of residues Phe584, Val567 and Pro565. The M pocket is located between the substrate catalytic site and the substrate access channel. This pocket includes the residues Asp597, Ser477, Ser568, Gln478, Arg481, Asn569 and Arg603. The C1 and C2 pockets are a little removed from the substrate binding cavity and constitute the substrate access channel. The C1 pocket contains Met336, L337, Glu307, Asn601 and Ser602 while the C2 pocket contains Pro708, Asp709, Pro710 and Gln500 (**Figure 1.12**).

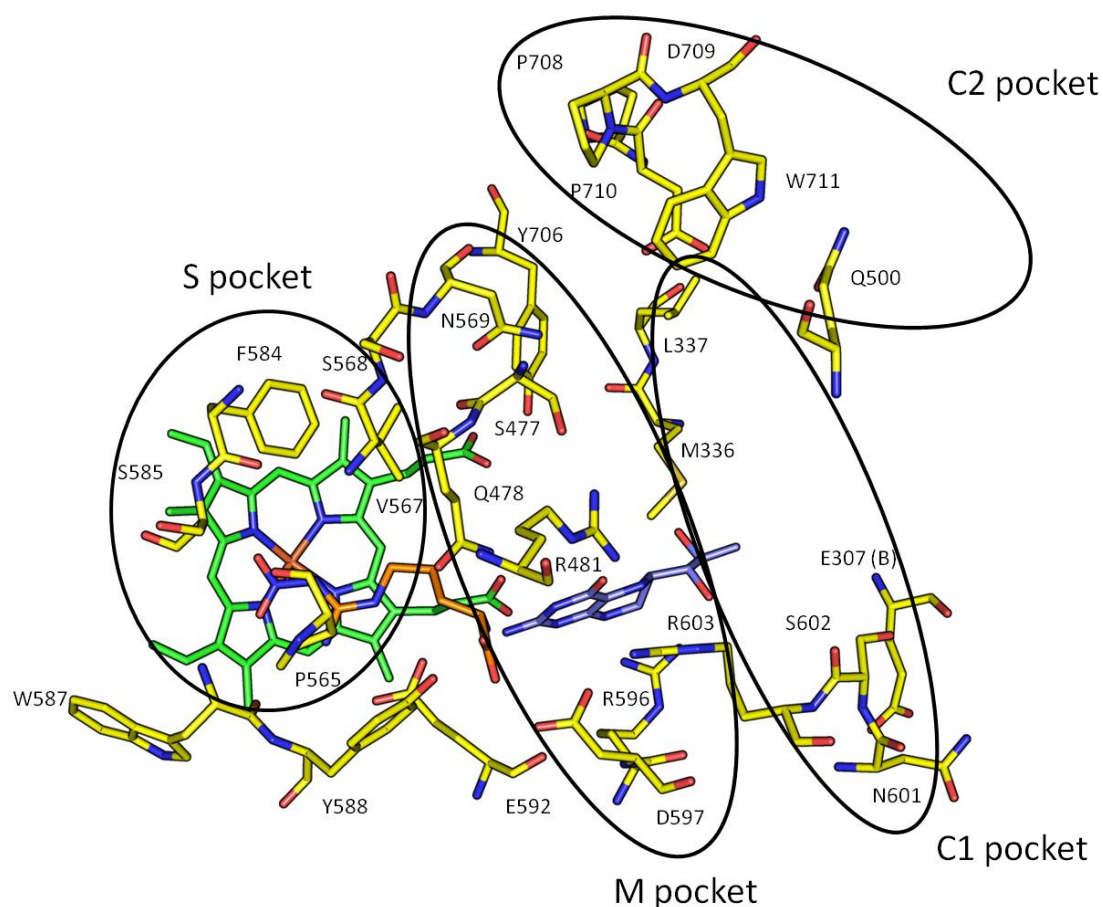


Figure 1.12. Sub pockets of the rat nNOS arginine active site with L-NNA bound.⁴⁶ (PDB:1K2R)

The S pocket (with the exception of the Asn370Ser difference in iNOS) is identical in the three NOS isoforms used in this study, (rat nNOS, bovine eNOS and human iNOS). As such, it is difficult to explain the selectivity exhibited by some L-arginine analogues when only considering binding in the S pocket.

The M pocket is defined by residues Ser477 and Ser568 in rat nNOS or Ala262 and Ala353 in human iNOS, which are postulated to be responsible for selectivity between the two isoforms. Alternatively, introduction of a positively charged functional group on inhibitory ligands would be unfavourable for eNOS binding in the M pocket. The nNOS M pocket is a more negative environment than the eNOS M pocket, with rat nNOS residue Asp597 being replaced by Asn368 in the bovine eNOS M pocket. This highlighted the significance of the M pocket in the design of isoform selective ligands.

The C1 pocket differs among the NOS isoforms (rat nNOS, bovine eNOS and human iNOS) at five residues. Two selective regions were found, the first at residues Met336 and Leu337 of rat nNOS and another at residues Glu307, Asn601 and Ser602 of rat nNOS. A histidine residue, His342 in human nNOS, (equivalent to Met336 in rat nNOS), could potentially be used to guide selective ligand design in this pocket.

There are four residues in the C2 pocket that differ across the NOS isoforms (rat nNOS, bovine eNOS and human iNOS). The most important residues determined for selectivity are at the rat nNOS Asp709/human iNOS Glu494 positions. The authors postulated that inhibitors with a positively charged functional group positioned near the Asp709 of rat nNOS should be selective towards nNOS.⁴⁶

1.4.4.2 2-Aminopyridines

The other main class of nNOS inhibitor is 2-aminopyridine containing compounds. Compounds such as **8** had been observed to have non-specific NOS inhibitory properties.⁴⁷

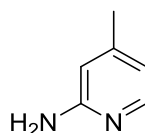


Figure 1.13. Substituted 2-aminopyridine, **8**, that was observed to have non-specific NOS inhibitory activity.⁴⁷

8 had an IC_{50} of 0.075 μ M for nNOS, 0.072 μ M for eNOS and 0.17 μ M for iNOS. The species isoforms used for testing were not described in the publication.

In an attempt to improve the selectivity and efficacy of the 2-aminopyridines, Ji *et al.* made use of a *de novo* design approach that focused on the “minimal pharmacophoric element” that was required for inhibition in each NOS isoform.⁴⁸ This study made use of the “sub pockets” of the rat nNOS arginine binding site as described in **Figure 1.12**. It was proposed, for nNOS selective inhibition, that compounds should have an amidino group positioned close to the Glu592, and a nitrogen atom should be near Asp597. This should allow selectivity over eNOS, which has a Asn in place of the Asp as previously discussed.⁴⁸ It was also suggested that placing nitrogen atoms on potential inhibitors close to the heme propionate groups should facilitate formation of charge-charge interactions and HBs. The S pocket, meanwhile, was thought to facilitate hydrophobic and/or steric interactions.

Based on this analysis and fragment docking studies, **9** in **Figure 1.14** was developed.⁴⁸ This exhibited low nano-molar rat nNOS inhibitory potency, and a 1,000 fold rat nNOS selectivity over bovine eNOS.⁴⁸

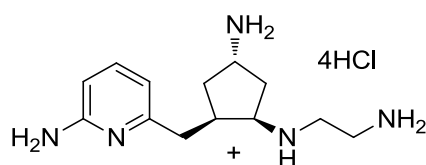


Figure 1.14. 2-aminopyridine containing compound developed from fragment screening, **9**. This was screened as a mixture of enantiomers.⁴⁸

To improve the efficacy and selectivity of **9**, further computational refinement was carried out by Ji *et al.*⁴⁹ This resulted in the development of **10**, shown in **Figure 1.15**. This had a K_i

of 0.014 μM for rat nNOS inhibition and a 2,000 fold selectivity over bovine eNOS and 290 fold over murine iNOS. The 2-aminopyridine **10** was initially tested as a mixture of diastereomers.⁴⁹ The four stereoisomers were subsequently resolved.⁵⁰

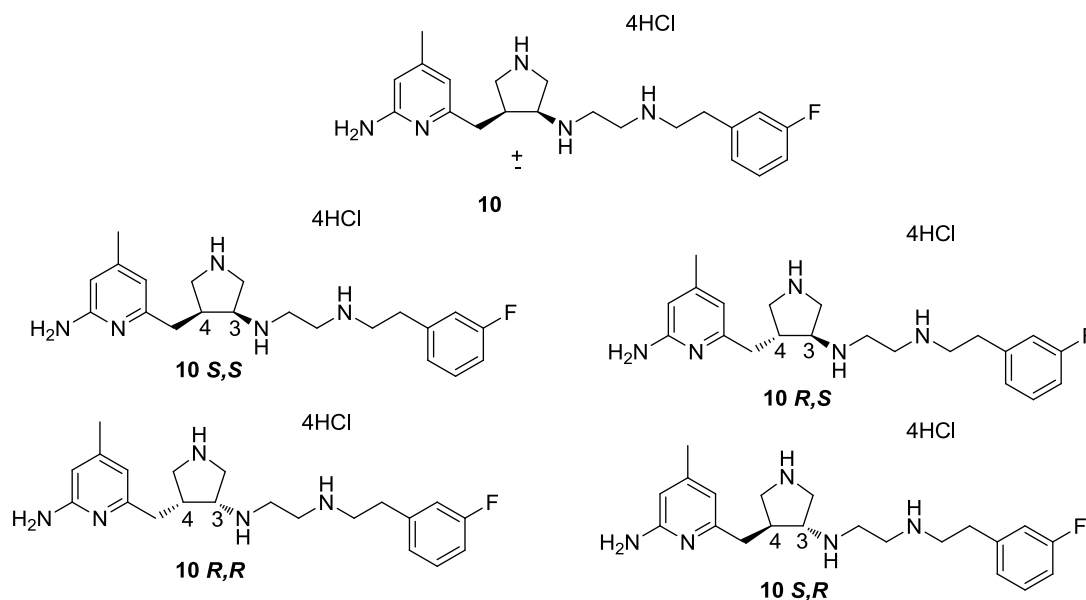


Figure 1.15. Unresolved aminopyridine **10** and the subsequently resolved stereoisomers.^{49,50} The 3*S*,4*S* (**10 S,S**) and the 3*R*, 4*R* (**10 R,R**) stereoisomers had K_i values of 52.2 nM and 5.3 nM respectively for rat nNOS.

Crystallographic studies revealed that compound **10 S,S** interacted with the rat nNOS arginine binding site via HBs between the conserved Glu592 and the 2-aminopyridine on the inhibitor. Water mediated HBs formed with Asp597 and the 2-aminopyridine formed a pi-pi interaction with the heme. The flourophenyl arm was located in the hydrophobic pocket formed by Met336 and Leu337 (**Figure 1.12**). This is referred to as the “normal” binding mode of nNOS inhibitors by the authors, with the 2-aminopyridine interacting with Glu592. Interestingly, the *R* configured inhibitor (**10 R,R**), adopted a different and novel binding mode with rat nNOS. This “flipped” binding mode saw the flourophenyl group orientated above the heme moiety. This then formed a π stacking interaction with the porphoryin ring. The 2-aminopyridine motif extended away from the heme moiety and induced a conformational shift in Tyr706. The aminopyridine then formed a bifurcated salt

bridge with the heme propionate A, as well as a π stacking interaction with the Tyr706. HB interactions were also observed between the pyrrolidine ring and the heme propionate B.

The *R,R* stereoisomer possesses remarkable selectivity, with the rat nNOS K_i value being 3,800 and 700 times lower than K_i value for bovine eNOS and murine iNOS respectively. In rat nNOS, the 4 methyl group is accommodated by a hydrophobic pocket comprised of Met336, Leu337 and Trp306. This pocket is not available in iNOS, hence the selectivity over this isoform. The eNOS selectivity is more difficult to explain as the crystal structure studies suggest that the binding mode for **10** *R,R* in eNOS and nNOS is the same.⁵⁰ Some selectivity differences between the two isoforms can be explained by residue differences between the eNOS and nNOS arginine binding pockets, with Asp597 in nNOS becoming Asn in eNOS and Met336 in nNOS becoming Val in eNOS. However mutation studies indicated that these residue differences were not the only contributory factors for selectivity.⁵⁰ Mutation studies also indicated that the flexible Tyr706 contributes significantly to binding in nNOS, while contributing very little to binding in eNOS. Therefore, targeting the Tyr706 site with these new flipped binding mode compounds offers the potential of highly selective and efficacious nNOS inhibitors.

Compounds such as **10** *S,S* and **10** *R,R* have great potential as nNOS inhibitors. However, their development was hampered by their somewhat poor “drug-like” properties as both **10** *S,S* and **10** *R,R* have a large number of rotatable bonds and contain several ionisable groups. Attempts have been made to improve the drug-like features of these compounds and to make them more pharmacokinetically and pharmacodynamically favourable, while retaining the nNOS selective “flipped” binding modes as described above.⁵¹ These studies resulted in compounds such as **11** and **12**, shown in **Figure 1.16**.

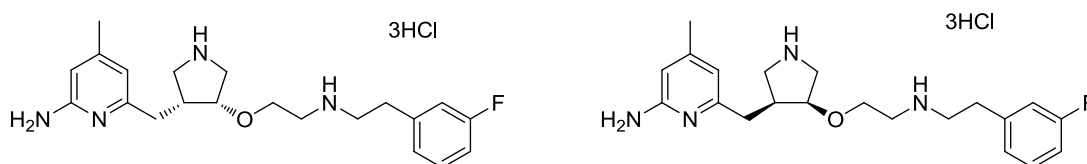


Figure 1.16. Modified 2-aminopyridines designed to improve the pharmacokinetic profile of the 2-aminopyridine family of nNOS inhibitors, **11** and **12**.⁵¹

11 has a K_i of 7 nM for rat nNOS, 2,667 fold selectivity over bovine eNOS and 806 fold selectivity over murine iNOS.⁵¹ This is the most efficacious rat nNOS inhibitor reported to date. **11** was shown to adopt the flipped mode of binding (**Figure 1.17**), as previously described, where the 2-aminopyridine interacts with Tyr706 to improve the binding affinity for nNOS.⁵² As before, inverting both stereocenters (**12**) resulted in a switching of binding mode to the “normal” mode (**Figure 1.18**), with the aminopyridine positioned to interact with the heme ring. This indicates the crucial role stereochemical considerations must play in nNOS inhibitor design. **12** has a K_i of 220 nM for rat nNOS, 270 fold selectivity over bovine eNOS and 60 fold selectivity over murine iNOS.⁵³

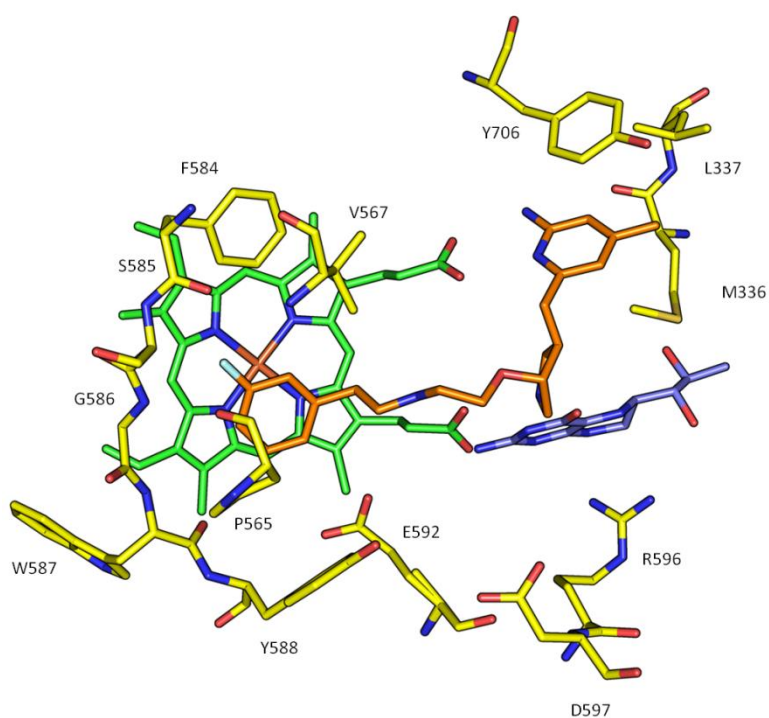


Figure 1.17. The flipped binding mode of **11** (PDB:3NLM).⁵² Note how Y706 is orientated to interact with the 2 aminopyridine ring.

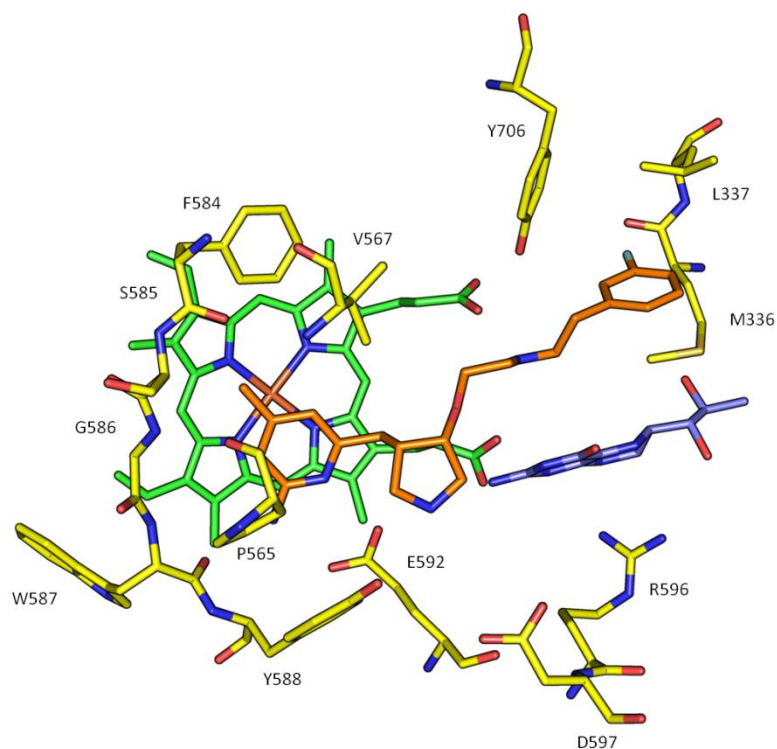


Figure 1.18. The normal binding mode of **12** (PDB:3NLK).⁵² Note how the Y706 does not position itself to interact with the fluorenyl ring.

Compounds with two 2-aminopyridine rings joined together by a linker have also been developed for nNOS inhibition.⁵⁴ An example of such an inhibitor, **13**, is shown in **Figure 1.19**. This compound has a K_i of 25 nM for rat nNOS and a 107 fold and 58 fold selectivity over bovine eNOS and murine iNOS respectively.⁵⁴

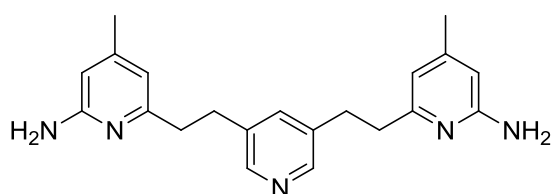


Figure 1.19. Two 2-aminopyridine rings joined by a central linker which demonstrated moderate selectivity for nNOS (**13**).⁵⁴

One of the most interesting features of **13** was its binding mode as determined by crystallization of **13** with rat nNOS (**Figure 1.20**).⁵⁵ It was observed, as expected, that **13** used one of the 2-aminopyridine moieties to form a network of HBs with Glu592 and

Trp587. The second 2-aminopyridine moiety formed HB interactions with one of the heme propionates as well as a pi-pi interaction with Tyr706. Unexpectedly, a second molecule of **13** bound to the BH₄ binding site by using the central pyridine nitrogen to interact with the zinc atom present in the BH₄ site. This resulted in the displacement of the BH₄ and a rearrangement of several residues, in particular Arg596, which moved to interact with Glu592 and Asp600 of the substrate binding site. This movement opened a second zinc binding site in nNOS. The binding of a second zinc atom resulted in a tightening of the dimer interface in nNOS. This opening of a second zinc binding site was not observed in eNOS, potentially due to the tighter dimer interface of this enzyme. This may explain the selectivity of **13** for nNOS over eNOS.

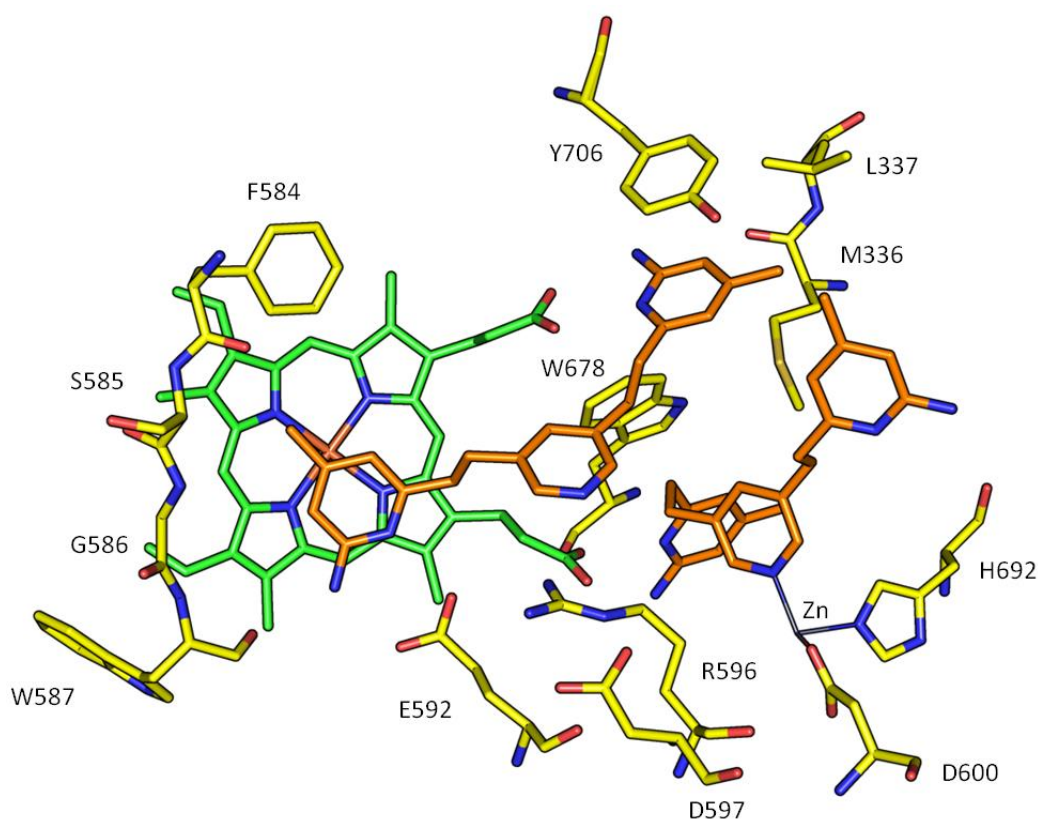


Figure 1.20. **13** interacting with both the arginine and BH₄ binding sites of rat nNOS (PDB 3N5W).⁵⁵

1.4.4.3 Other scaffolds

Some studies have examined alternate scaffolds to the two discussed above. These studies have been limited to thiophene and imidazole containing classes. The thiophene based scaffolds, such as **14** shown in **Figure 1.21**, bind to the rat nNOS arginine pocket by forming HBs with Glu592 and the heme propionate.⁵⁶ The chlorophenyl ring of **14** is accommodated by the hydrophobic pocket consisting of Leu337 and Met336, and the interaction is further stabilised by π stacking with the Tyr706 side chain. **14** has IC₅₀ values of 0.035 μ M, 3.5 μ M and 5 μ M against rat nNOS, human eNOS and murine iNOS respectively.⁵⁶

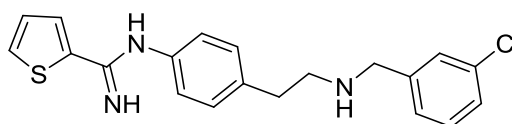


Figure 1.21. A thiophene based inhibitor with an IC₅₀ of 0.035 μ M for rat nNOS, **14**.⁵⁶

Modification of one of the secondary amines to an alcohol substituted piperidine ring resulted in **15**, **Figure 1.22**. This was observed to have superior inhibitory properties against rat nNOS, with an IC₅₀ of 17 nM and a 1664 fold selectivity for rat nNOS over bovine eNOS.⁷⁴

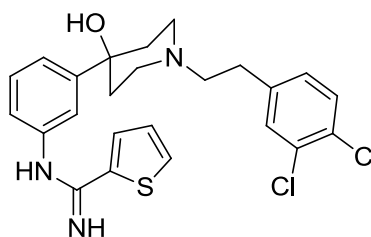


Figure 1.22. Modified thiophene based inhibitor with an IC₅₀ of 17 nM against rat nNOS, **15**.⁷⁴

The imidazole based scaffolds adopt a different binding mode within the nNOS arginine active site. These compounds co-ordinate to the Fe at the centre of the heme moiety in the

active site via one of the imidazole nitrogens. Imidazole itself is a weak inhibitor of nNOS, with an IC_{50} of 290.6 μM .⁵⁷ Various substituents have been added to imidazole in an attempt to improve its efficacy as a nNOS inhibitor. These substituents include phenyl rings (**16**) and various amino acids (**17**), **Figure 1.23**.^{54,55,58,59}

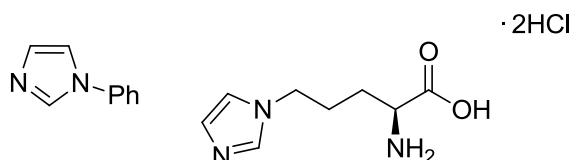


Figure 1.23. Phenyl and amino acid substituted imidazoles, **16** and **17**, with nNOS IC_{50} values of 25 μM and 19 μM respectively.^{58,59}

Recently, the field has begun to examine the applicability of the imidazole containing inhibitors for inhibition of human nNOS. The most efficacious compound developed was **18**, shown in **Figure 1.24**. This had an K_i of 0.125 μM against human nNOS, with a 202 fold selectivity over bovine eNOS and a 33 fold selectivity over murine iNOS.⁶⁰ The nitrogen of the pyridine ring of **18** was reported to make a HB with His342 in the human nNOS binding site and was also seen to have a favourable PK profile in a CYP3A4 inhibition assay.

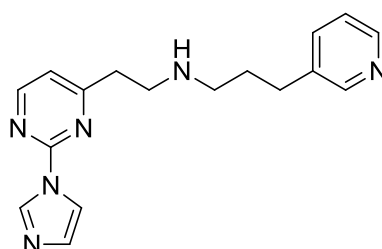


Figure 1.24. **18** that was seen to be active against human nNOS.⁶⁰

The potential of the Fe co-ordinating binding modes observed for imidazole containing compounds was further explored through the development of thioester modified arginines, such as **19**, **Figure 1.25**.⁶¹ This compound co-ordinates with the Fe using the sulphur atom, and also forms the HB interactions with Glu592 that has been previously observed for the

modified arginine inhibitor class of compounds. The terminal ethyl group of **19** fits into the hydrophobic pocket created by Pro565, Val567 and Phe584 in rat nNOS. The Fe-S distance is 2.5-2.6 Å (**Figure 1.26**).

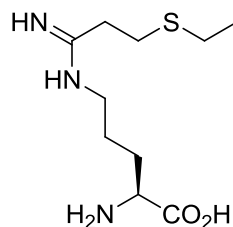


Figure 1.25 AN Fe co-ordinating compound, **19**, that also forms some of the "classic" modified arginine scaffold interactions with the rat nNOS binding site.⁶¹

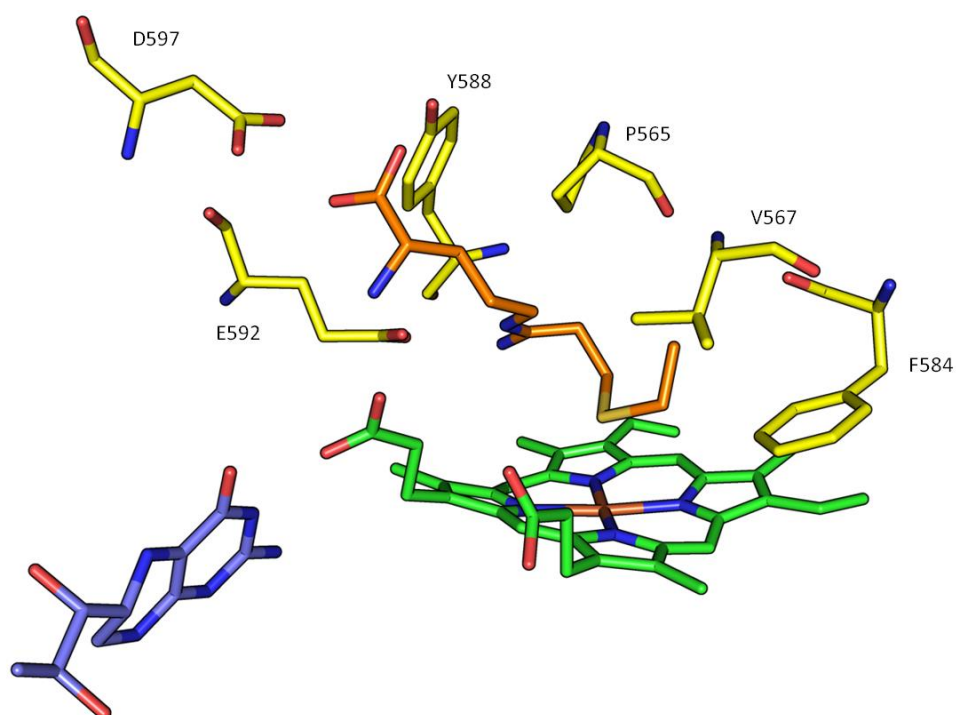


Figure 1.26. **19** co-crystallised with rat nNOS (PDB: 3JT4). The Fe-S distance was 2.6 Å.⁶¹

1.5 Current challenges in the field of NOS inhibition

While the above compounds demonstrate that there has been some success in the field of nNOS inhibition, there remain several significant challenges in this area of research. The first issue that needs to be addressed is the lack of a uniform assay system based on the human isoform of nNOS. Almost all of the compounds described above were tested for their nNOS inhibitor activity against the rat isoform of the enzyme. This does not represent an ideal system when attempting to address and study the over activation of human nNOS. Furthermore, the specificity tests for inhibitory compounds are conducted using mixed species isoforms, most commonly rat nNOS, bovine eNOS and murine iNOS. This again does not provide a reliable and accurate system for determination of the selectivity of compounds for human nNOS over human eNOS and iNOS. The comparison of inhibitory compounds across publications is made all the more difficult due to the use of a variety of assay system for testing nNOS activity, these include radiolabelled arginine assays, whole cell assays, Griess assays and hemeoglobin conversion assays.

The second weakness in the field is the over reliance on the modified arginine and 2-aminopyridine based scaffolds for nNOS inhibition. While these scaffolds have provided some promising compounds, selectivity and efficacy issues remain. Movement of the field towards a more diverse scaffold set has the potential to improve the activity of nNOS inhibitory compounds. The currently reported inhibitory compounds also suffer from poor “drug-like” characteristics. While some efforts have been made to address this issue, particularly with the chiral 2-aminopyridine, there remains scope for development in this area.

The third issue for human nNOS inhibition is the lack of application of modern *in silico* screening tools. Some computational studies have been conducted; however these have focused on the precise binding modes of already known active compounds, and not on the search for novel inhibitory scaffolds. The power and potential of large scale *in silico* screens for identifying potential inhibitors could make a significant contribution to the field of human nNOS inhibition.

1.6 Aims of the project

The overall aim of this project is to design a novel, selective and druggable human nNOS inhibitor. To achieve this, the challenges in the field as outlined above will need to be addressed in turn. The first of these challenges to be tackled will be the lack of computational screens to identify human nNOS inhibitors. No human nNOS crystal structure was initially available at the beginning of this work; hence the construction of a human homology model will be attempted. This will then be screened with large compound databases with the aim of identifying a novel inhibitory scaffold for human nNOS. Ligand based drug design will also be employed through use of pharmacophore construction and screening. A particular emphasis will be placed on the pharmacokinetic properties of any potential human nNOS inhibitors.

Work will also be conducted on advancing the contemporary assay systems for nNOS inhibition from the current standard of rat nNOS, bovine eNOS and murine iNOS. The project aims to move to an all human NOS assay system. This would make any successful inhibitory more “druggable”, and would represent a major advancement in the field. This will be done through the use of recombinant expression of the three human NOS proteins using a bacterial host, and purification using affinity chromatography. These isolated proteins will then be used to establish a functional assay system for testing of the *in silico* derived novel nNOS inhibitory scaffolds. Co-expression with human calmodulin will also be attempted. This approach has yet to be reported for human nNOS, and should yield maximally functional NOS proteins. It is hoped that the assay system will be high throughput, cost effective and transferable to allow other research groups to study human nNOS inhibition.

The project will also focus on synthetic organic chemistry, and its use to access some of the compounds that will result from the *in silico* screen. While some of the screened compounds will be commercially available, many will have to be synthesised. The use of synthetic techniques to access novel scaffolds from the screens will therefore be of critical importance. These techniques should also allow the synthesis of a variety of scaffolds which will advance the field of human nNOS inhibition beyond the two favoured families of compounds which are reported in the literature.

2 Computational Studies

2.1 Introduction

The field of nNOS inhibition is currently focused on the modification and testing of two ligand scaffolds and predominantly uses rat nNOS for inhibitor testing. These scaffolds are based on the natural NOS substrate, L-arginine, and on substituted 2-aminopyridines (see chapter one, section 1.4.4). This project departs from these much explored ligand families, as well as from the use of rat nNOS for inhibitor testing, and instead seeks to identify novel ligand scaffolds using the human nNOS enzyme. To achieve this, a high throughput screening approach will be employed using both structure based and ligand based design techniques.

This type of approach has been attempted only once before in the field of nNOS inhibition. This publication is recent, and does not attempt to biologically evaluate the effectiveness of the proposed inhibitors.⁶² This project will employ a more extensive *in silico* examination of the human nNOS binding site, and also aims to biologically evaluate the hit compounds.

Other groups in the field have regularly utilised *in silico* techniques for visualisation and representation of known rat nNOS inhibitors in their binding sites.^{27,63-65} These compounds were not derived from high throughput screening. The work presented in the following chapter therefore represents a novel and innovative method of screening for human nNOS inhibitors that has not yet been exploited.

2.2 Structure based design overview

The structure based design methodologies used during this project are outlined in **Figure 2.1**.

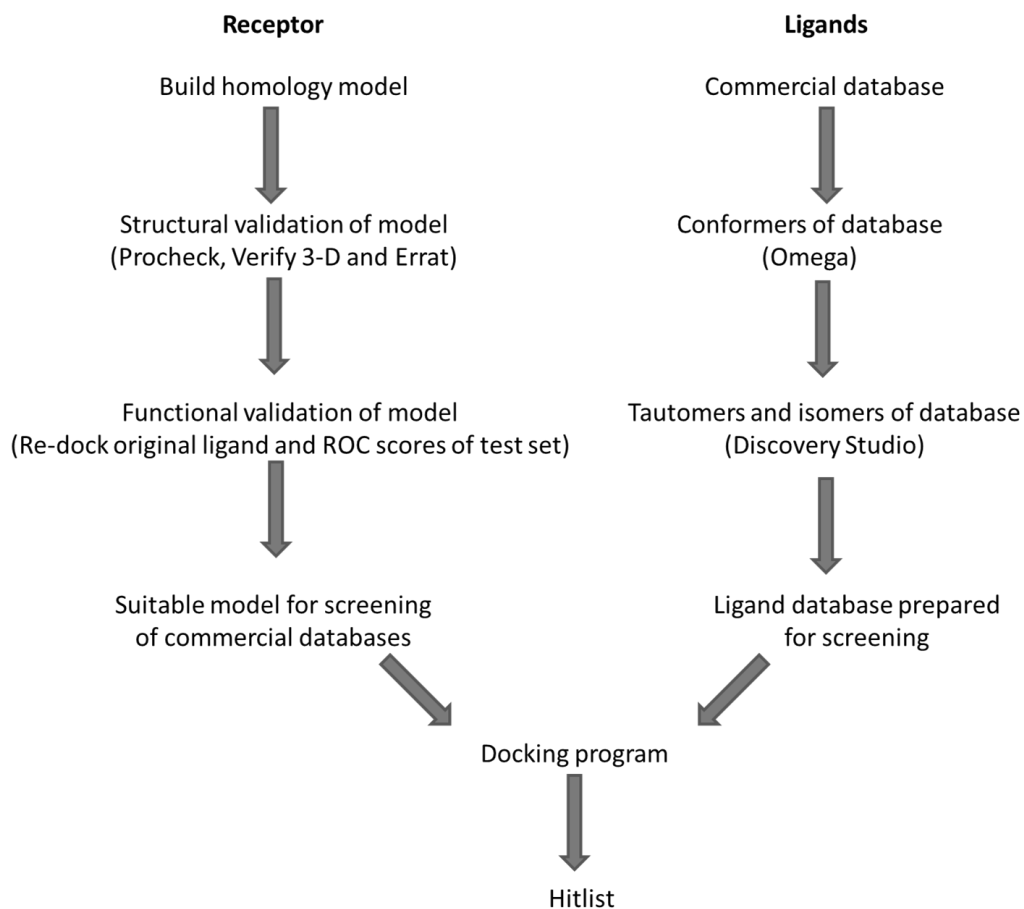


Figure 2.1. Structure based drug design overview.

The workings of each of these steps will be outlined briefly in the following sections.

2.2.1 Building a homology model

Sequencing technology has become increasingly sophisticated over the past decade and as a result protein amino acid sequences are readily accessible. However, publication of crystal structures to match these sequences has not been as rapid. On the 22nd of October 2015 Uniprot, a repository for protein amino acid sequences, had 5,278,3601 entries, while the PDB had only 113,130 entries, demonstrating the gulf between sequence and crystallization data.

Crystallization of proteins is often difficult and time consuming and so 3-D structures of many fully sequenced proteins are not yet available. In cases where the sequence of a protein is known, but its 3-D structure is not, a homology model is necessary for carrying out structure based design.

Homology modelling is based on two major observations:

- i) The structure of a protein is determined by its amino acid sequence. Knowing the sequence of the protein should therefore make it possible to predict its structure.¹⁴⁷
- ii) Proteins with similar amino acid structures should adopt similar structures. Therefore, if two proteins have similar amino acid sequences then they will have similar structures.¹⁴⁷

The 3-D structure to be developed is known as the target structure, which has a corresponding (known) target sequence. The other partner in the homology modelling protocol is the template, which has known sequence and structure. The target sequence can be used to search databases of potential template sequences to identify homologous templates. The level of sequence homology between template and target is directly proportional to the level of structural homology. In this way, an unknown protein structure can be developed from a known protein sequence. There are several general methods for homology model construction, such as rigid body assembly and satisfaction of spatial restraints. All of these methods make use of the same generic steps for model generation, which will now be briefly outlined.

Step one is to search for structures related to the target sequence. This is best achieved using a sequence alignment searching tool that is linked to the PDB. This search will return the known protein structures which bear some degree of sequence similarity to the target. These structures form the list of potential templates. Step two is to select which template is most suitable for model construction. Of key importance is the sequence similarity between target and template. The higher this similarity the more accurate the target structure will be. If the target and the template have a similarity of 40% or higher the model which results should be accurate. Lower similarity scores between the two sequences may result in a poor model.¹⁴⁸ A template structure with high resolution is also desirable. Additionally, it is useful if the template structure has all known co-factors co-crystallized with it, particularly if they are known to influence ligand protein interactions.¹⁴⁸

Some modelling programs allow input of several templates. This can be of particular benefit in cases of low target-template sequence homology.

Once the template has been selected the next step is to build the model. Biovia's Discovery Studio program uses the Modeller algorithm for homology model construction.¹⁴⁹ Modeller constructs models using a process called "satisfaction of spatial restraints". This approach uses distance geometry or optimization techniques to satisfy a set of spatial restraints in the target structure. In Modeller these restraints are derived from two sources. Firstly, restraints for the target are derived from restraints observed in the template. For example, if it is observed that the residues at position 100-110 in the template and target sequences are the same, the dihedral side chain and main chain angles and N, O distances can be taken directly from the template structure. In areas where the template and target sequence differ, the geometry and bonding angles of the residues are calculated using the CHARMM force field by calculating a series of probability density functions (pdfs) for each residue. For example, a glutamic acid is unlikely to have its side chain orientated towards another acidic residue due to the charge repulsions involved. This type of side chain arrangement therefore receives a low probability score. By moving the side chains away from each other the charge repulsion may be reduced, but the side chain bond angle may then become more unfavourable. Several variations are trialled and each is assigned a probability based on the score generated using CHARMM. The final model is then constructed by combinations of the pdfs into a discrete optimised protein energy (DOPE) score for each model.¹⁵⁰ The model which is most probable will score best, while models with improbable geometries will score poorly.

Once the model is built the final step is to check for potential model errors. It is often beneficial to generate more than one model, particularly if the sequence alignment required manual adjustment. Once generated the homology models must be structurally and functionally validated.

2.2.2 Structural verification of model

Errat is a system that analyses the non-bonded interaction energies between carbon, nitrogen and oxygen atoms within a protein structure.⁷² The calculated energies are

compared to a set of reference non-bonded interaction energies. A sample output is shown below (**Figure 2.2**).

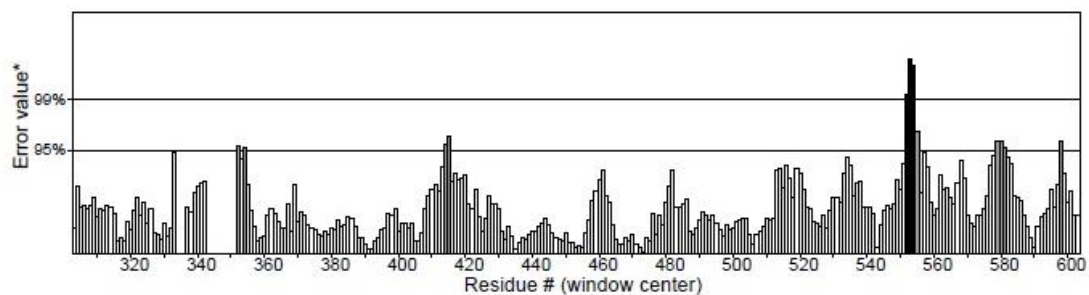


Figure 2.2. Sample Error plot.

It is expected that 95% of residues of a robust protein structure should be below the 95% error limit.⁷² Areas of the protein which are mis folded will move outside this error limit as the heavy atoms are either too close together (causing steric clashes) or too far apart (causing unusually long bond lengths).

Procheck analyses the backbone angles of all crystal structure and generates a Ramachandran plot.⁶⁸ The plot is split into a most favoured region (red), an additionally allowed region (brown), a generously allowed region (yellow) and a disallowed region (white) (**Figure 2.3**).

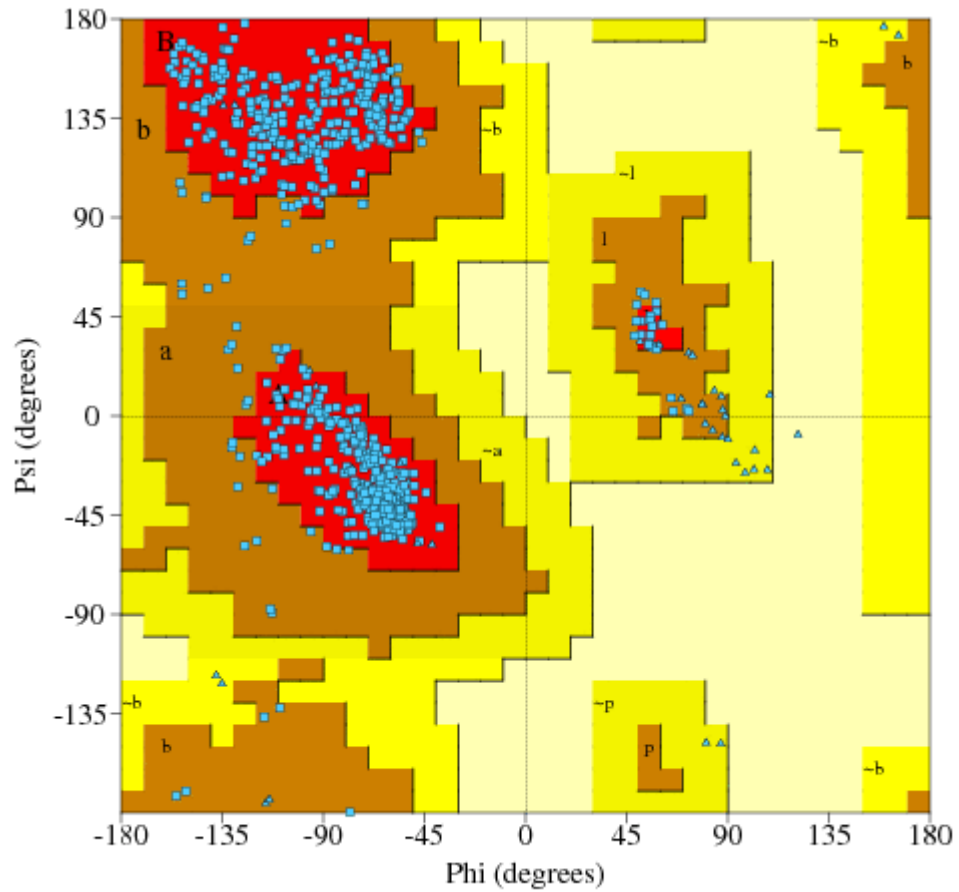


Figure 2.3. Sample Ramachandran plot.

The phi (ϕ) axis represents the peptide bond angle and psi (ψ) represents the carbon-carbon bond angle in the backbone.

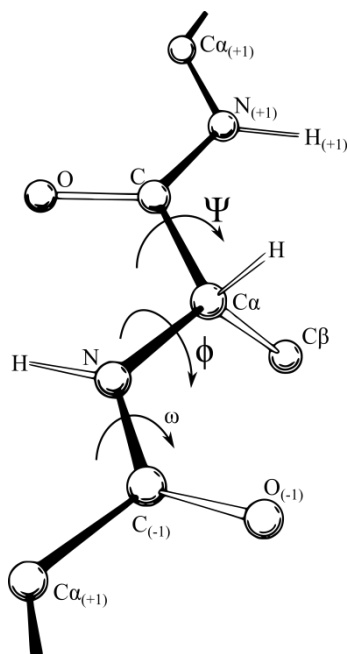


Figure 2.4. Phi and psi angles in a protein backbone.¹⁴³ ϕ represents the N-C α angle, while ψ represents the C-C α angle.

It is expected for a good quality structure that 90% of the residues will fall into the allowed regions of the Ramachandran plot. However, two residues can appear in the disallowed regions of the plot, these are glycine and proline. These residues are exceptional due to the nature of their side chains which affects the backbone angles they can adopt. These appear as triangles on the graph, while all other residues appear as squares.

Verify 3-D examines how closely the 3-D coordinates of the crystal structure model match the 3-D profile as calculated from the protein's amino acid sequence. The 3-D profile of a residue is calculated based on how deeply buried the residue is, the fraction of polar atoms in the side chain and the local secondary structure. If the 3-D profile and the 3-D structure of the model match closely (>80% matching), the structure passes the test.⁷¹

2.2.3 Functional validation of model

The three tools above are useful for structural validation of the protein models. Functional tests of the docking protocol using the structure must also be carried out. The simplest of

these tests is to examine how well binding poses of co-crystallized inhibitors can be reproduced by the docking program. The inhibitor is removed from the protein binding site and a conformer ensemble of the inhibitor is docked into the binding site. The original, crystallised pose is compared to the re-docked pose using root mean square derivatives, RMSDs.

Equation 1. RMSD equation.¹³³

$$RMSD = \sqrt{\frac{\sum_{i=1}^{N_{atoms}} d_i^2}{N_{atoms}}}$$

Where N_{atoms} is the number of atoms over which the RMSD is measured and d_i is the distance between the coordinates of atom i in the two structures (original and re-docked) when they are overlaid. An RMSD score of less than 2 Å is widely accepted as distinguishing between success and failure in reproducing known binding poses.⁷⁵

The second functional test is to measure how well a small test set can be docked into the binding site of the protein. This is done using a relatively small collection of ligands (~1000) called a test set. Some of the ligands in the test set are experimentally validated binders of the target site of the crystal structure (actives), while some of the ligands are deliberately chosen as they are known not to bind to the target site (decoys). The decoys may have similar physico-chemical properties to the actives in order to ensure a robust test of the model and the docking procedure.

The most common ratio of decoys to actives is 33:1.¹³⁹ Actives are chosen based on a low IC_{50} value against the target of interest. The value for a “low” IC_{50} is target dependent. The decoys can be molecules randomly taken from a commercial database such as Maybridge or Zinc, or they can be compounds specifically chosen as they are known not to act against the target of interest. The ChEMBL website (<https://www.ebi.ac.uk/chembl/>) is a useful source for the building of these test sets. Targets can be searched, for example nNOS, and the inhibitory compounds are then sorted based on IC_{50} values. The most active can then be chosen and suitable decoys are also readily accessible.

Once the test set has been constructed its conformers are generated (section 2.2.4.1) and docked into the crystal structure. Docking scores are returned and are analysed using Receiver Operator Characteristics (ROCS). This scores how well the docking program can pick the active compounds out of the test set, while discarding the decoys.¹⁴⁴ Active compounds should score better than the decoy compounds if the model is accurate. Two sample ROC graphs are shown in **Figure 2.5**. (For docking scoring functions see Section 2.3.1)

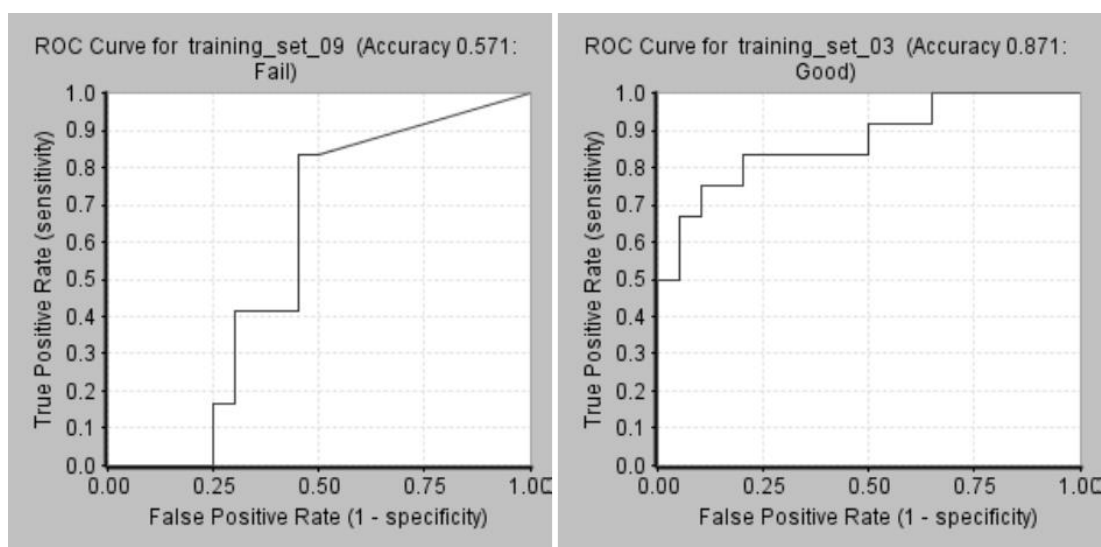


Figure 2.5. Sample ROCS tables.

ROC curves plot the true positive rate (sensitivity, y-axis) against the false positive rate (1-specificity, x-axis).¹⁴⁵ ROC scores run between zero and one based on the area under the ROC curve. The closer the ROC score is to one, the more accurate the docking protocol is at distinguishing between actives and decoys.¹⁴⁶ If molecules are randomly assigned as actives or decoys a ROC score of 0.5 is returned. Such a protocol is not useful for identifying active compounds. The left panel in **Figure 2.5** represents this scenario. The right panel in **Figure 2.5** represents a more accurate docking protocol, scoring 0.871 and is classed as a good model

2.2.4 Conformers of database

A single molecule can have many binding poses for one target site. It is therefore necessary to analyse as many of these binding poses as is computationally practical to determine the likely bioactive conformation. To achieve this, several conformations of the target molecule are generated. This can be done in either a systematic or a stochastic manner. Systematic conformer generation involves generating all possible conformers of a given molecule. This is usually not possible due to a phenomenon called the combinatorial explosion. As the number of rotatable bonds in a molecule increases the possible number of conformers increases exponentially.¹³³ If large numbers of compounds are being docked into one target site this becomes a considerable computational task.

Stochastic conformer generation is widely used to avoid the combinatorial explosion. This essentially involves random generation of conformers and minimization of the resulting structures. The process is outlined in **Figure 2.6**.

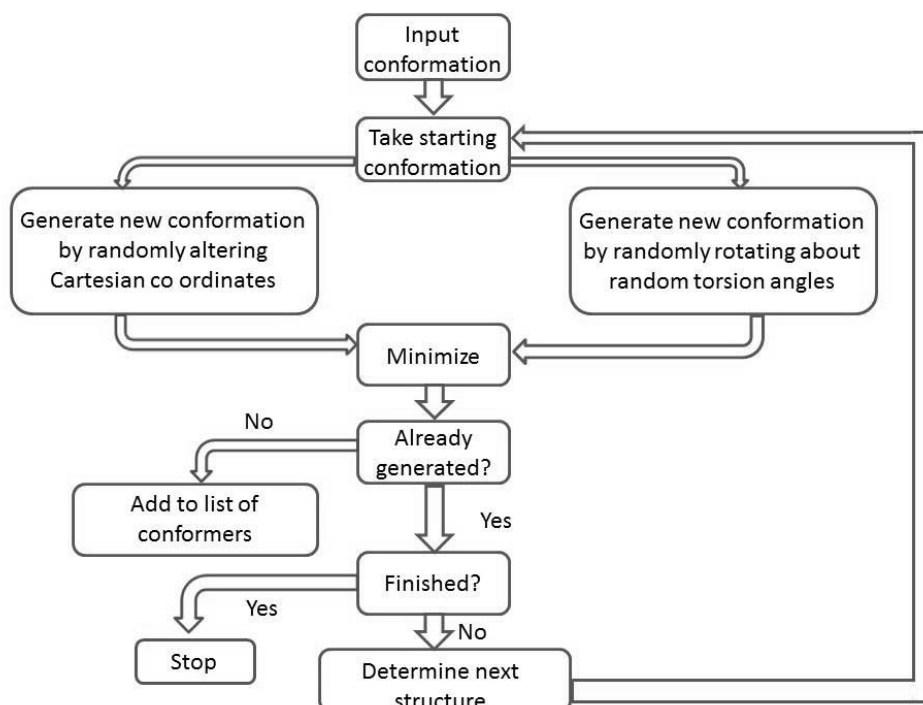


Figure 2.6. Flowchart for stochastic conformer generation.

Openeye's Omega is a popular stochastic conformer generation program.¹³⁹ Omega uses a variation of stochastic conformer generation that avoids the energy minimization step. The energy minimization can often lead to highly compact structures that do not accurately reflect the structure of species in solution. Owing to its importance for this work Omega will be discussed in more detail in the Section 2.2.4.1.

2.2.4.1 Omega

Rigid docking programmes (eg FRED, discussed in section 2.3) hold both the ligand and protein in a fixed conformation throughout the docking process. However, a degree of flexibility can be conferred on the ligands by docking a conformer ensemble of each molecule.⁷⁴ The collections of conformers can be generated using the Openeye program, Omega. This program takes an input molecule and constructs conformers of it using five steps. The first two steps are pre-programmed while the remaining three are molecule specific and are completed at run time. Omega makes use of the Merck Molecular Force Field (MMFF94).¹⁴⁰ This is a computationally derived molecular mechanics and dynamics force field. It describes and tries to predict what forces will act on atoms when they are combined and how these forces will affect the geometry of the molecule.¹⁴⁰

The first step in Omega is compilation of a fragment database. A large commercial database of molecules (e.g. Zinc) is fragmented into continuous rings and small linear linkers.¹⁴¹ One or more 3-D conformations for each fragment are then constructed by embedding each atom of each fragment in a random position in space and ensuring that these atoms are still connected in a logical way. Electrostatic and Van der Waals forces are removed from each fragment. This process is repeatedly applied and the lowest energy conformers that are unique in root mean square deviation (RMSD) space are retained.¹³⁹ This ensures duplicated fragments are avoided.

The second pre-programmed step is generation of a torsion sampling dictionary. Torsion is the twisting of an object due to applied force. In this case, the objects which are being twisted are atomic bonds and the forces acting on these bonds include kinetic energy and steric interactions. A list of torsions for bonds in small molecules is constructed using samples derived from the protein data bank, PDB, and energy scans of torsions against the

MMFF94. This list defines at what angles torsions should be sampled for particular bonds. Common torsions must obey very strict rules which are unique for that torsion. More unusual torsions are subject to more generic rules and repeated sampling. This torsion sampling directory is applied to the target molecule in step four of the Omega process.¹³⁹

The third step is the first of the molecule specific operations, the 3-D structure generation. The input molecule is fragmented and the possible structures of each fragment are taken from the fragment database, which was described in step one. If there is no entry in the database corresponding to one of the generated molecular fragments, the algorithm from step one is applied. The parent molecule conformers are then assembled by overlapping the fragments in accordance with geometric and chemical rules.¹³⁹

Step four is torsion driving. All the rotatable bonds of all the conformers are compared to the torsion library from step two and the correct torsion angles are applied. Several torsions are applied to each HB to build up a large data base. Torsions which result in severe atom clashes or duplication are removed.¹³⁹

Finally, the data set generated from the first four steps is sampled. The conformer with the lowest overall energy is taken as the first molecule in the output sample set. Higher energy conformers are then added to this sample set until the user defined sample size is obtained. At no stage in this process is a minimization of the conformers conducted.

2.2.5 Tautomer and stereoisomer generation

Different conformations of molecules are possible due to the flexibility of bonds which allows them to rotate. There are other ways in which one molecule can adopt a variety of forms, most notably tautomers and stereoisomers.

Tautomerism most often occurs by movement of a hydrogen from one atom to another, and rearrangement of double bonds along its path of travel eg keto-enol tautomerism (**Figure 2.7**).

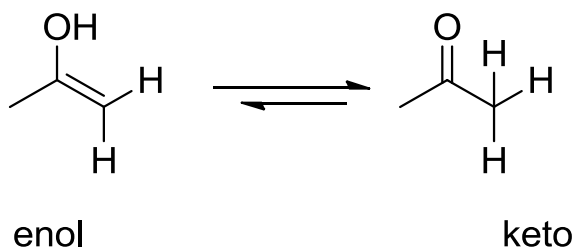


Figure 2.7. Keto/enol tautomerism.

Tautomers can be generated by a variety of methods *in silico*. The software used in this work was Biovia's Discovery Studio which deals with tautomers by generation of the canonical, or most favourable, tautomer. Another tautomer generation method is enumerating all possible tautomers, although this can contribute to the combinatorial explosion phenomenon as previously described.

Canonical tautomer generation involves first constructing a list of all possible tautomers of the query molecule. There are a variety of set rules which can be applied for this process depending on the exact structure of the query molecule.¹⁴² Once all the tautomers have been enumerated the canonical, or most likely, tautomer is decided based on another set of scoring rules. Each tautomer is scored based on what types of structures it contains. Examining the keto/enol example, the keto form is the chemically more favoured form; therefore that tautomeric form would be given a higher score than the enol form, which is less favoured.¹⁴² This process is repeated for all tautomerisable portions of the molecule until the overall most favoured tautomer is decided on.

A final consideration for molecular structure is the stereoisomeric forms which the molecules can adopt. Biovia's software enumerates all possible stereoisomers up to a user set cut off. This addresses both chiral centres to generate the *R* and *S* enantiomers at each stereocentre and also double bond geometry to generate the *E* and *Z* forms of the molecules. Stereoisomer generation is followed by a coordinate "clean up" to ensure that no atom overlaps or clashes occurred during the isomer generation.

Following generation of stereoisomers, tautomers and conformers the ligands are ready for docking into the active site of the protein of interest.

2.3 Docking

2.3.1 Fast Rigid Exhaustive Docking (FRED)

Openeye's Fast Rigid Exhaustive Docking (FRED) fits a conformer library a target site of the user's choice.^{74,151} For this project the databases were sets of conformers generated by Omega. FRED scores how well each ligand fits into the target based on ligand size and shape. Those that fit best are given the most negative scores. FRED does this in two steps. The first step is the exhaustive search function. This analyses and docks all possible rotations and translations of each ligand being docked into the binding site. Any conformations which do not fit within the defined binding site are discarded and the remaining ligands are given a preliminary score.

The second step is optimization. The ligands which were not discarded in the first step are moved around the binding site in very small movements to determine the exact best position for the small molecule in the binding site. The poses are then scored again and the number of poses defined by the user are retained and saved, the rest are discarded.¹⁵² In this way, the best orientations of ligands in the binding site are deduced.

FRED Version 2.2.5 applies seven force field based scoring functions to rank ligand and binding site interactions. These are Chemgauss2, Chemgauss3, Chemscore, Consensus, PLP_docked, Screenscore and Shapegauss.⁷⁴

As implied by the name, Shapegauss represents all the atoms in the system as smooth Gaussian functions, and relies solely on the shape of the ligand to assess its binding affinity.¹⁵³ The scoring function measures to what degree various Gaussian functions in the system overlap. If there is a large degree of overlap between atoms of the binding site and atoms of the ligand a high score is awarded.¹⁵¹ Chemgauss2 and Chemgauss3 operate on the same Gaussian principles but also take into account the position of HBing and aromatic groups.¹⁵³

Piecewise Linear Potential (PLP) incorporates HBing interactions as well as steric interactions due to carbon, nitrogen, sulphur, fluorine, oxygen and iodine atoms.⁷⁶ Screenscore takes several different parameters into account when scoring a binding pose;

these include steric interactions, HBs, metal atom interactions, aromatic interactions and penalties for clashes and the number of rotatable ligand bonds.¹⁵³

The consensus function attempts to collate the binding information from all of the scoring functions into one ranked list. For each scoring function a list of the binding poses of each molecule is created ordered by rank. Each pose is then assigned a consensus structure score equal to the sum of that pose's rank in each list. The best scoring pose is retained, while all others are discarded.¹⁵⁴

Chemscore was developed based on work previously conducted by Böhm.¹⁵⁵ It scores poses using four different terms, namely HBing interactions, lipophilic interactions, ligand-metal interactions and a final term that considers contributions from rotatable bonds which are frozen because of contact with the receptor.¹⁵⁶

Certain scoring functions may perform better depending on the exact nature of the protein and ligand partners whose interactions are being examined.¹⁵⁷ Prediction of which scoring function will perform best is difficult and as a result it is necessary to test all scoring functions with the test set. The performance of each scoring function with the test set is scored using ROCS and the best performing one can then be used for database screening.

The FRED docking protocol was updated during the course of this project and was employed in some of the later docking studies. FRED 3.0.0 outputs only one docking function, Chemgauss4. This has improved HB detection relative to previous chemgauss scoring functions and also accounts for HB network effects.¹⁵⁸ Similar to older iterations of the chemgauss functions, chemgauss4 scores a range of interactions including sterics, HB donors and acceptors, co-ordinating groups, metals, lone pairs, polar hydrogens and chelator co-ordinating groups.¹⁵⁹

2.3.2 Flexible docking

FRED docking is powerful as it can be used to examine a large number of potential binding poses in extensive databases. Large numbers of molecules can be handled as the binding site into which they are docked is held in a fixed orientation, with no movement of residue side chains permitted. To more closely mimic *in vivo* conditions and improve the accuracy

of the docking protocol a degree of flexibility can be conferred on these side chains using FlexDock in Discovery Studio.¹⁶⁰

The flexible docking begins by selection of the side chains which will be allowed to move. This is usually defined as all residues within either 4 Å or 8 Å of the ligand that was co-crystallized in the protein binding site. A selection of rotameric states are generated for the residue side chains using ChiFlex, and the energy of these rotamers is calculated using CHARMM.¹⁶¹ The ligand database is then docked into the active site and the side chains are further refined to generate the most favourable ligand-receptor interactions. The resulting compound list is ranked based on how well the ligands interacted with the flexible binding site following side chain refinement.¹⁶⁰

2.4 Homology modelling results

2.4.1 Sequence alignment

As a human nNOS crystal structure was not initially available, a human nNOS homology model (HM) was developed for the screening of commercial ligand databases. Rat nNOS, with a 93.84% sequence identity to human nNOS, was chosen as the template for homology model construction. Full sequence alignments are provided in Appendix 8.1, all alignments were performed with Clustal Omega.⁶⁶ The key binding site residues of the arginine binding site, shown in **Table 2.1**, are largely conserved between the rat and the human sequences, with a single residue difference occurring where Leu337 in rat nNOS is replaced with His342 in the human isoform. These key residues were within 8 Å of the arginine binding site in the rat nNOS crystal structure. The residues have been widely reported to form interactions with nNOS inhibitory compounds, see chapter one, section 1.4.4.

The hydrophobic pocket containing the Leu337 residue (Met336, Leu337, Tyr706) has been noted to play a crucial role in rat nNOS inhibitor binding.⁵³ In human nNOS, Leu337 is replaced with a His342. Leucine has a t-butyl side chain, while histidine has an imidazole ring containing side chain. The histidine side chain is more amenable to HB formation due to the nitrogen in the imidazole ring. It may also form π stacking aromatic interactions, and

charge-charge interactions. Leucine may repel potential inhibitors from the pocket due to its steric bulk. Due to the differences in interaction types between these two residues, the leucine to histidine change could greatly impact inhibitor binding in the human isoform. It has also been observed that a variety of nNOS inhibitors have different IC₅₀ values for rat nNOS versus human nNOS. This suggests that the inhibitors interact differently with rat and human binding pockets.^{45,53} Construction of a human nNOS homology model may therefore be useful in the identification of a novel class of selective human nNOS inhibitors.

Table 2.1. Alignment of key binding site residues of human nNOS and rat nNOS.

Human nNOS	Rat nNOS
M341	M336
H342	L337
S482	S477
Q483	Q478
R486	R481
V572	V567
F589	F584
S590	S585
G591	G586
W592	W587
Y593	Y588
E597	E592
D602	D597
Y711	Y706

2.4.2 Structural validation

Two human nNOS homology models were developed based on the *holo* rat nNOS template structures. The protein databank (PDB) codes of these template structures were 3PNF (1.94 Å) and 3RQJ (1.84 Å).^{65,67} The models based on these templates were constructed as per chapter five, section 5.5.1.1. The human nNOS homology models will be referred to as 3PNF-HM and 3RQJ-HM. Crystal structure waters were explicitly included in the models. There were 398 water molecules in the 3PNF template and 388 waters in the 3RQJ

template. There were 16 waters within 8 Å of the 3PNF binding site and 10 waters within 8 Å of the 3RQJ binding site. The position of the remaining water molecules were largely conserved between the templates. In both the 3PNF and 3RQJ templates, a water mediated HB formed between the ligands and Asp597.^{65,67}

The generated homology models were first analysed with Procheck.⁶⁸ This was carried out with and without water molecules from the template present, and with and without minimizations applied to the models. The minimization method employed was steepest descent followed by conjugate gradient using the Chemistry at HARvard Macromolecular mechanics (CHARMm) force field.⁶⁹ The original templates were also analysed via Procheck and the results are summarized in **Table 2.2** and **Table 2.3**.

Table 2.2. 3RQJ homology model variations Procheck scores.

	3RQJ	3RQJ-HM	3RQJ-HM with water	3RQJ-HM minimized	3RQJ-HM minimized with water
Number of residues	814	836	836	836	836
Most favoured	92.4%	70.2%	70.2%	82.9%	83.2%
Allowed	7.3%	26.7%	25.2%	16.3%	16.0%
Generously Allowed	0.3%	2.6%	4.1%	0.8%	0.5%
Disallowed	0%	0.5%	0.5%	0%	0.3%

Table 2.3. 3PNF homology model variations Procheck scores.

	3PNF	3PNF-HM	3PNF-HM with water	3PNF-HM minimized	3PNF-HM minimized with water
Number of residues	819	836	836	836	836
Most favoured	92.3%	94.4%	93.6%	87.5%	87%
Allowed	7.7%	5.2%	5.8%	11.8%	12.5%
Generously Allowed	0%	0.3%	0.5%	0.5%	0.4%
Disallowed	0%	0.1%	0%	0.1%	0.1%

The most favoured, allowed, generously allowed and disallowed classifiers were originally determined by examination of the dihedral angles in a set of 463 protein crystal structures.⁷⁰ The most favoured region is defined as areas of the Ramachandran plot which contained over 100 residues per pixel when the backbone angles of this test set were analysed. The allowed region is defined as areas of the Ramachandran plot which contained over eight residues per pixel following test set examination. The generously allowed region is the area of the graph which extends out by two pixels around the allowed region. All space outside these regions is defined as disallowed.⁷⁰

A protein model is deemed stereochemically satisfactory when a high percentage of residues (over 90%) are in the most favoured regions.⁶⁸ This was observed for the non-minimized 3PNF-HM structures. The minimized 3PNF-HM structures had a greater percentage of their residues in the allowed region when compared to the non-minimized structures. This indicated that the protein minimization procedure may have resulted in the adoption of less favourable backbone bond angles. Also of note was the fact that the 3PNF-HM models performed slightly better without the water molecules present, although the difference between the solvated and non-solvated models was small. It may be beneficial to include the water molecules in spite of their detrimental effect on the backbone bond angles, as they may mediate HB interactions between the binding site and potential inhibitors during docking studies.

The 3RQJ-HM performed more poorly in this test than the 3PNF-HM. None of the various 3RQJ-HM structures scored greater than 90% of residues in the most favoured regions. Interestingly, the minimized versions of 3RQJ-HM scored better than the non-minimized versions. This was the opposite than what was observed for the 3PNF-HM. Similar to 3PNF-HM, the inclusion or exclusion of waters in the 3RQJ-HM had very little impact on the model quality from a structural perspective in the Procheck test.

The quality of the overall 3-D structure of the models was probed using Verify-3D, a tool which compares the 3-D structure of a protein with the expected 3-D structure based on the protein's sequence.⁷¹ The non-bonded interaction energies between the heavy atoms of the protein backbone were also analysed using Errat (**Table 2.4** and **Table 2.5**).⁷²

Table 2.4. Verify 3-D and Errat scores of 3RQJ models.

Structure	Verify 3-D Score	Errat Score
3RQJ	88.89%	93.199%
3RQJ-HM	88.20%	74.211%
3RQJ-HM with water	88.20%	74.211%
3RQJ-HM minimized	90.02%	88.417%
3RQJ-HM minimized with water	91.66%	83.835%

Table 2.5. Verify 3-D and Errat scores of 3PNF models.

Structure	Verify 3-D Score	Errat Score
3PNF	90.5%	94.598%
3PNF-HM	88.41%	72.588%
3PNF-HM with water	89.13%	73.083%
3PNF-HM minimized	90.44%	90.509%
3PNF-HM minimized with water	91.64%	86.910%

All versions of both models scored greater than 80% in the Verify 3-D test, which indicates that the 3-D structures of the models were robust.⁷¹ “Good” protein models should ideally score greater than 80% in the Errat test. This examines non-covalent interactions between N, C and O atoms.⁷² All of the non-minimized versions of the models failed this test, indicating that in the non-minimized versions, the distances between the heavy chain atoms were incorrect. Application of the minimization procedure rectified these errors, resulting in a much higher Errat percentage score. This suggests that the interatomic distances are more correct in the minimized protein models. Detailed examination of the Errat plots of the non-minimized models identified that some of the binding site residues displayed high energies, suggesting that these model may be unsuitable for docking applications. Based on these results, the non-minimized versions of the homology models were omitted from further testing.

From the structural validation tests it appeared that the 3PNF-HM (minimized) performed slightly better than the 3RQJ-HM (minimized), in both the solvated and non-solvated forms.

This was particularly evident in the Procheck test. However, as the differences in scores between the models were not large for the other structural validation tests, both 3PNF-HM and 3RQJ-HM minimized models were taken forward for further testing.

2.4.3 Docking protocol validation

The first test of the docking protocol was re-docking of the template co-crystallized ligand into the homology model binding site, and comparison of the re-docked pose with the original binding pose using root mean square deviations (RMSD) of the heavy chain atoms. The 3RQJ and 3PNF template ligands, **20** and **21**, are shown in **Figure 2.8**.^{65,73}

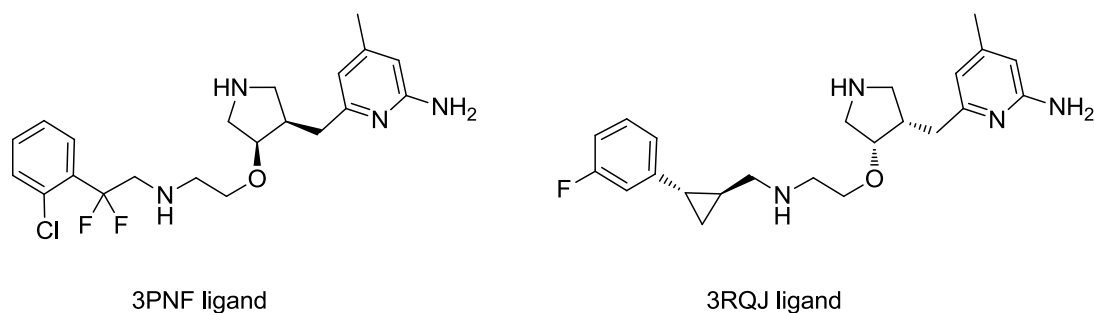


Figure 2.8. Co-crystallised ligands of 3PNF and 3RQJ, **20** and **21**.^{65,73}

All docking functions for Fast Rigid Exhaustive Docking (FRED) 2.2.5 (Chemgauss 2, Chemgauss 3, Chemscore, Consensus, Plp_docked, Screenscore and Shapegauss) were analysed and the best scoring function for each model was noted (**Table 2.6**).⁷⁴

Table 2.6. Comparison of re-docked versus crystalized binding poses using RMSD.

Model	RMSD Score	Best FRED docking function
3PNF HM with water minimized	1.356 Å	All equal
3PNF HM no water minimized	0.678 Å	All equal
3RQJ HM with water minimized	1.79 Å	PLP_docked
3RQJ HM no water minimized	0.82 Å	All equal

An RMSD of less than 2 Å indicates that the protocol is capable of accurately docking ligands into the protein binding site.⁷⁵ As can be seen in **Table 2.6**, the docking protocol reproduced the binding pose of the co-crystallized ligand satisfactorily in all models. All scoring functions performed equally well in all models, except for the 3RQJ-HM with water model. PLP_docked performed best here. PLP_docked places particular emphasis on the steric interactions of heavy atoms of the ligand with the protein binding site.⁷⁶ The better performance of this function may suggest that steric interactions play a larger role in the binding of the 3RQJ ligand when compared to the 3PNF ligand.

The docking protocol was further tested through the use of a test set (see chapter five section 5.5.3). Only one experimentally validated human nNOS inhibitor was available at the time of model construction, therefore the test set was made up of rat nNOS inhibitors.⁴⁵ The accuracy of the docking protocol with the test set was analysed using receiver operator characteristic (ROC) curves. The scores are presented in **Table 2.7**.

Table 2.7. Performance of the docking protocol with the models using a test set.

Model	ROC Scores	Best FRED docking function
3PNF HM with water minimized	0.79	Chemscore
3PNF HM no water minimized	0.69	Chemscore
3RQJ HM with water minimized	0.76	All equal
3RQJ HM no water minimized	0.71	All equal

Discovery Studio, which was used to generate the ROC scores in this project, groups the scores based on their performance. A score of 0.5-0.6 is a failure, 0.6-0.7 is poor, 0.7-0.8 is fair, 0.8-0.9 is good and above 0.9 is excellent. Although the ROC scores are similar for the 3PNF-HM and 3RQJ-HM, it was observed that 3PNF-HM performed slightly better than 3RQJ-HM. The models with explicit waters present also performed better. This, coupled with the previous structural validation results and the re-docking of the co-crystallized ligand results, led to the conclusion that the minimized version of 3PNF-HM with waters was the most structurally and functionally robust model. The inclusion of waters in the models may also allow for identification of compounds which form solvent mediated HBs with the nNOS binding site. The 3PNF-HM with water model was therefore used for all commercial database screening.

2.4.4 nNOS homology model binding pocket analysis

An overlay of the template 3PNF and the 3PNF-HM is shown in **Figure 2.9**.

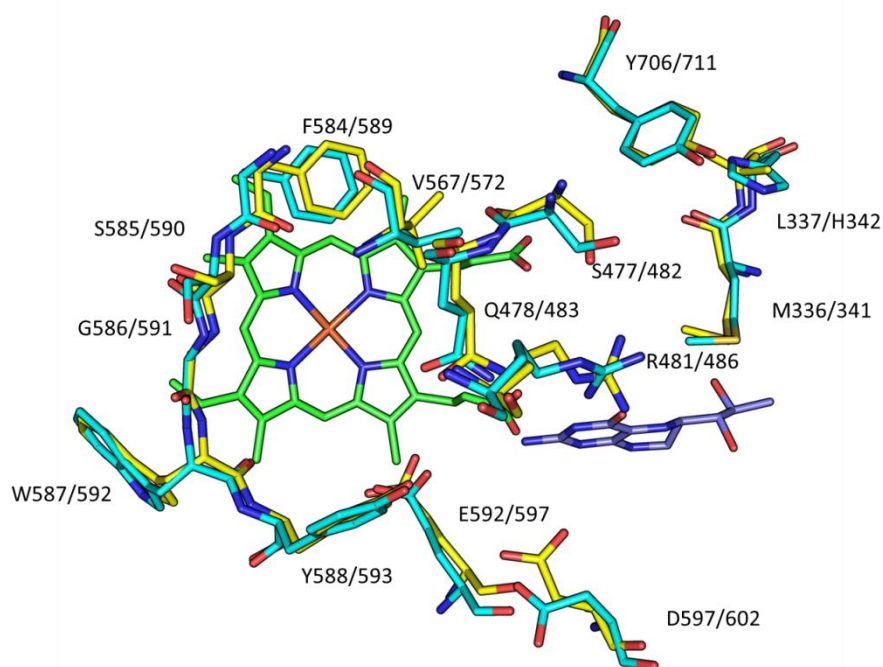


Figure 2.9. 3PNF rat template (yellow backbone) overlaid with 3PNF-HM (cyan backbone). BH₄ shown in blue, heme shown in green. Numbering of residues is template/homology model. Waters omitted for clarity.

As predicted by the sequence alignment the binding site of the rat and human isoforms was similar, with the only residue difference being Leu337 in the rat isoform becoming Hid342 in the human model. There was also a difference in rotameric states of the Asp597/602 (rat/HM). In the homology model the side chain of Asp602 is not orientated towards the substrate binding site. This may weaken the interactions of potential inhibitors by preventing the formation of H_Bing interactions with the Asp602 residue.

2.4.5 Rotamers of Glu597 and Asp602 in human nNOS homology model

The effect of the differing rotameric states of GLU597/602 (template/HM) was investigated by enumerating the three rotamers of this residue in the 3PNF-HM minimized with water and re-docking the test set. The ROC scores generated are shown in **Table 2.8**.

Table 2.8. Rotamers of D597.

Rotamer number	ROC score, 3PNF minimised with water
1 (original)	0.79
2	0.76
3	0.73

No improvement in the ROC scores were observed, therefore the original rotameric state of Asp602 was retained in the homology model.

In a further attempt to improve the ROCS score of the 3PNF-HM key binding site interactions of nNOS inhibitors, as reported in the literature, were examined in detail. It was found that Glu592 in the rat nNOS structure (Glu597 in the 3PNF-HM) mediates crucial HB interactions with both the natural substrate (L-arginine) and with a large range of inhibitors.^{48,64,77,78} It has also been noted that this residue can adopt a variety of rotameric states depending on the binding mode of nNOS inhibitors.⁵² Glu597 in the 3PNF-HM has seven possible rotameric states. These states were enumerated in turn and the nNOS test set was docked into the binding site to see if the ROC scores could be improved. The results are summarised in **Table 2.9**.

Table 2.9. Analysis of rotamers of Glu597.

Rotamer Number	ROC score, 3PNF minimized with water
1 (original)	0.79
2	0.55
3	0.54
4	0.54
5	0.73
6	0.77
7	0.63

Again, no improvement was observed on testing of alternate rotameric states for the Glu597 residue. Indeed, many of the rotamers resulted in significantly worse ROC scores. The original rotamer of E597 was therefore retained for docking applications.

2.5 eNOS and iNOS crystal structures

Crystal structures of human eNOS and iNOS were used to assess how isoform specific the docking protocol and resulting hit lists were. Two *holo* structures were studied for eNOS and iNOS. The iNOS structures had PDB codes of 3E7G (2.2 Å resolution) and 4NOS (2.25 Å resolution).^{79,80} The eNOS structures used were 1M9M (1.96 Å resolution) and 3NOS (2.40 Å resolution).^{80,81} As the energy minimized 3PNF-HM with co-crystallised waters was to be used for nNOS docking, all validations of iNOS and eNOS crystal structures were carried out on the minimized versions of the proteins with explicit waters present.

2.5.1 Structural validation

The robustness of the eNOS and iNOS crystal structures were assessed in the same manner as the nNOS homology models (Procheck in **Table 2.10** and Verify 3-D, Errat **Table 2.11**).

Table 2.10. Procheck results of eNOS and iNOS crystal structures.

	1M9M	3NOS	3E7G	4NOS
Number of residues	830	854	848	854
Most favoured	91.6%	88.9%	91.0%	89.4%
Allowed	8.4%	10.8%	9%	10.6%
Generously Allowed	0%	0.3%	0%	0%
Disallowed	0%	0%	0%	0%

Table 2.11. Verify 3-D and Errat scores of eNOS and iNOS structures.

Structure	Verify 3-D Score	Errat Score
1M9M	91.50%	89.770
3NOS	90%	90.051
3E7G	88.12%	94.011
4NOS	92.87%	90.073

The eNOS 1M9M structure passed the Procheck stereochemistry test, with 91.6% of residues in the most favoured regions. The 3NOS structure fell below the 90% limit for residues in the most favoured regions, although it was a marginal failure with 88.9% in the most favoured region. 1M9M performed better in the Verify 3-D test than the 3NOS structure, with scores of 91.5% and 90% respectively. This trend was reversed in the Errat test, with 3NOS outperforming 1M9M. However, as previously observed in the Procheck tests, the differences between the two eNOS crystal structures in the validation tests was minimal, indicating that both 1M9M and 3NOS would be suitable for docking applications.

For iNOS, 3E7G passed the Procheck test (91% in the most favoured region), while 4NOS scored 89.4%, slightly below the desired 90% for residues in the most favoured regions. 3E7G also scored better in the Errat test, while 4NOS did better in the Verify 3-D test. Similar to the eNOS structures, these validation tests revealed that there was very little difference between the two iNOS structures. As such, no one crystal structure was chosen for docking studies at this stage and further validation tests were required.

2.5.2 Docking protocol validation with eNOS and iNOS crystal structures

The initial test of the docking protocol with the iNOS and eNOS structures involved reproducing the binding poses of the co-crystallised ligands for each structure using FRED docking. The structures of the co-crystallised ligands, **22-25**, are shown in **Figure 2.10**. The re-docked binding poses were compared with the original binding poses using RMSD scores (**Table 2.12**).

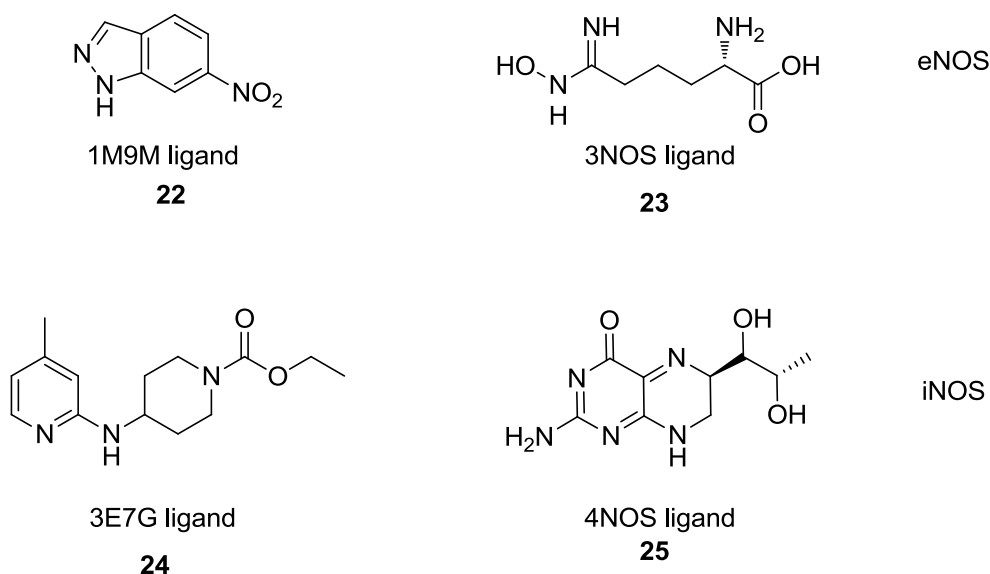


Figure 2.10. eNOS and iNOS co-crystallised ligands, **22-25**.⁷⁹⁻⁸¹

Table 2.12. RMSD scores on reproduction of original binding pose for eNOS and iNOS crystal structures.

Structure	RMSD	Best FRED docking function
1M9M	4.66 Å	All equal
3NOS	0.80 Å	All equal
3E7G	1.17 Å	All equal
4NOS	1.16 Å	All equal

The docking pose was successfully reproduced in all models, except for 1M9M. The RMSD score for the re-docked ligand in this case was outside of the acceptable 2 Å limit. Closer inspection of the re-docked binding pose revealed that the 1M9M ligand had been flipped in the binding site relative to its original position. The ligand was a small heterocycle (**Figure 2.10**) which could be orientated into the binding site in a variety of poses. The docking protocol was not effective at identifying which of these orientations was correct for binding in the 1M9M structure. Although the failure with the 1M9M structure was most likely due to the nature of the ligand rather than the crystal structure, it was decided to omit 1M9M from further testing.

Similar to the nNOS procedure, the FRED docking protocol was tested with eNOS and iNOS test sets, developed as per chapter five, section 5.5.8. These were docked into the crystal structures and ROC scores generated (**Table 2.13**). Explicit waters were included for all structures.

Table 2.13. eNOS and iNOS test set ROC scores.

PDB Code	Isoform	ROCS best function	Function score
3NOS	eNOS	ChemGauss3	0.75
4NOS	iNOS	Chemscore	0.56
3E7G	iNOS	Chemscore	0.70

The 3NOS structure performed relatively well in the test, achieving a ROC score of 0.75 using the ChemGauss3 docking function. This structure was therefore used for eNOS docking applications. For iNOS, 3E7G was seen to score better in the test set screen, scoring 0.70, compared to 4NOS with a score of 0.56. As a result, 3E7G was deemed to be the iNOS structure of choice for docking.

2.5.3 Selectivity human nNOS homology model

One of the aims of this work was to develop a selective human nNOS inhibitor. Attempts to build this selectivity into the screening process were made from an early stage. The test sets for eNOS and iNOS were docked into the 3PNF-HM to assess whether or not the human nNOS homology model and FRED docking protocol were selective for nNOS inhibitors over eNOS and iNOS inhibitors. This would also identify which, if any, of the FRED scoring functions were more effective at identifying nNOS inhibitors. The ROC score of the 3PNF-HM with the nNOS haystack is also provided for reference (Table 2.14).

Table 2.14. 3PNF-HM docked with the iNOS and eNOS test set.

Scoring function	3PNF-HM with iNOS test set	3PNF-HM with eNOS test set	3PNF-HM with nNOS test set
Chemgaus2	0.54	0.79	0.68
Chemgaus3	0.55	0.55	0.57
Chemscore	0.53	0.51	0.79
Consensus	0.77	0.70	0.52
PLP	0.65	0.64	0.59
Screenscore	0.56	0.69	0.54
Shapegauss	0.89	0.82	0.73

The best performing scoring function for 3PNF-HM with the nNOS test set was Chemscore, which achieved a ROC score of 0.79. This function also performed poorly with the iNOS and eNOS test sets, scoring 0.53 and 0.51 respectively. This indicated the Chemscore was capable of identifying nNOS inhibitors, while being ineffective at identifying iNOS and eNOS inhibitors. As a result, the screening of commercial datasets using Chemscore and the 3PNF-HM should select nNOS inhibitors and discard eNOS and iNOS inhibitors.

2.6 Structure based drug design virtual screening

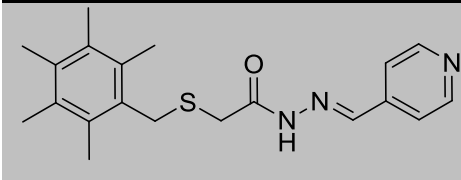
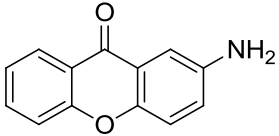
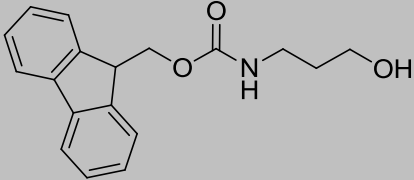
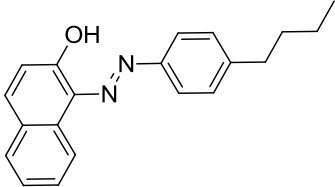
2.6.1 Docking results using human nNOS homology model

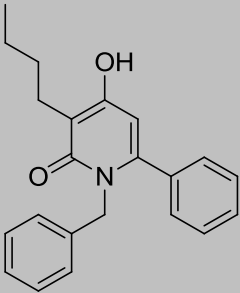
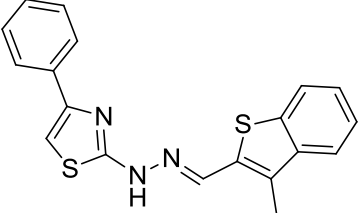
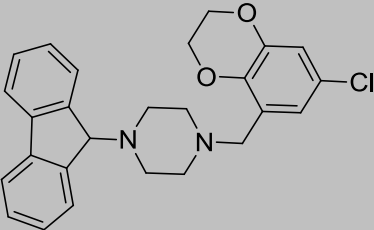
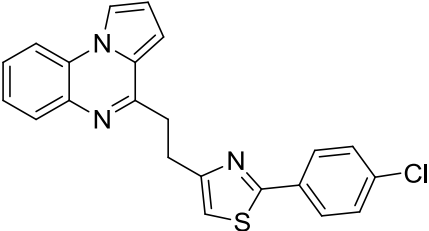
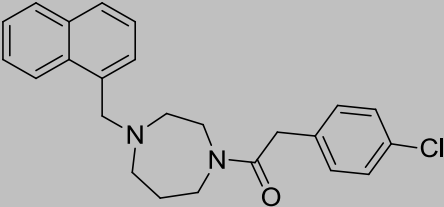
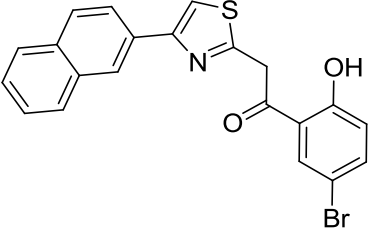
With the homology model and docking protocol verified, the screening of Maybridge (screening library, 53,000 compounds, <http://www.maybridge.com/>) and Zinc (drug-like available now subset, 10.6 million compounds, <http://zinc.docking.org/>) commercial databases was conducted as per chapter five, section 5.5. The commercial datasets were pre-filtered with a Pipeline Pilot BBB filter. This was carried out in an effort to ensure BBB permeability for the hit compounds generated by the screening trials. Following FRED docking of the pre-filtered Maybridge and Zinc databases, flexible docking of the top 100 compounds from each database was carried out as per chapter 5, section 5.5.4. The resulting hit lists were analysed and a number of compounds were selected for biological evaluation. The selection process was mainly based on the rank of the compound in the docking list. The ADMET properties (calculated by Biovia's Discovery Studio) and the potential of the compounds to be structurally modified in subsequent SAR studies were also taken into consideration.

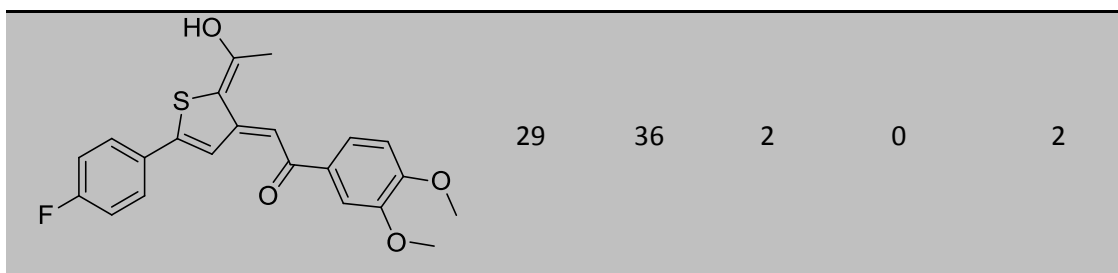
The compounds chosen were also as diverse as possible to ensure maximum possible coverage of chemical space. The structures and rank numbers of the hit compounds chosen for biological evaluation are presented in **Table 2.15** and **Table 2.16**. The blood brain barrier (BBB) levels of the chosen structures from the Maybridge screen (**Table 2.15**) were seen to be very favourable, with all structures apart from one having a BBB level of two or less. A BBB level of zero indicates that the compound is extremely BBB permeable, one is a compound with high BBB permeability and two is a medium level of BBB permeability, (see

chapter five, section 5.4.2). The bloodstream absorption levels were also promising, with all compounds apart from one scoring either zero or one. A score of zero indicates that the compound would be well absorbed into the bloodstream, while a score of one indicates moderate levels of absorption, (See chapter five, section 5.4.2). Finally, the predicted aqueous solubility of the chosen compounds varied quite widely. The lower the aqueous solubility value, the less aqueous soluble the compound. An ideal value for this attribute is four. At this level of aqueous solubility the compound is predicted to be sufficiently soluble for drug administration and distribution. A higher value may result in rapid elimination of the drug candidate from the body before the active ingredient has an opportunity to pass into the bloodstream from the intestine and interact with the desired physiological target.

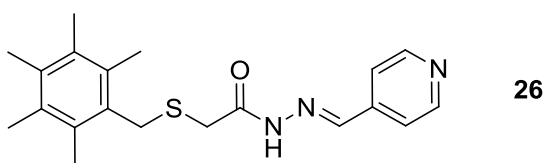
Table 2.15. Biologically evaluated compounds derived from 3PNF-HM flexibly docked with Maybridge dataset.

Compound Structure	Rank	Compound No.	BBB level	Bloodstream absorption level	Aqueous Solubility level
	1	26	1	0	2
	4	27	2	0	3
	5	28	2	0	3
	7	29	4	2	1

	9	30	1	0	2
	10	31	0	1	1
	12	32	0	0	1
	16	33	0	1	1
	17	34	1	0	2
	19	35	1	0	1



An image of **26**, which ranked highest in the Maybridge screen, bound into the 3PNF-HM is shown in **Figure 2.11**. Interactions between the ligand and the binding site include H-bonding to Glu597, hydrophobic interactions with Met341, His342, Pro570, Tyr683 and Tyr711. There is also a predicted π stacking interaction with the heme moiety. The two main inhibitor classes for rat nNOS inhibition have been reported to form interactions with several of these residues including Glu592 (Glu597 in human nNOS), Met336 (Met341 in human nNOS), Leu337 (His342 in human nNOS), Pro565 (Pro570 in human nNOS), Tyr711 (Tyr706 in human nNOS).⁴⁹ Of particular interest was the predicted interaction with the His342 residue in the human nNOS binding site. In rat nNOS the His342 becomes a leucine residue. Interaction with the His342 residue could therefore help to facilitate the design of a new scaffold for human nNOS inhibition.



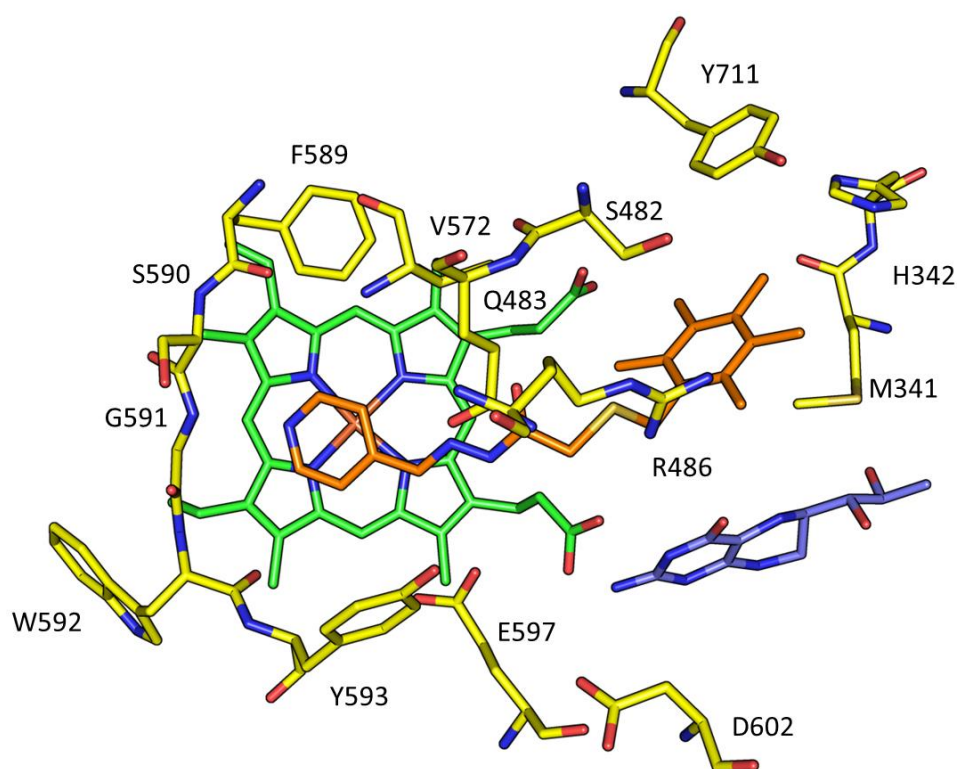


Figure 2.11. 3PNF homology model with **26** bound. Structure of **26** is also shown separately. Residues in yellow, heme in green, BH₄ in blue, ligand in orange. Waters omitted for clarity.

One of the high ranking compounds of interest from the Maybridge screen with 3PNF-HM (**Table 2.15**) was not available for purchase, **34**. A number of versions of this structure were therefore synthesised. The synthesised compounds were chosen based on similarity to **34** and are shown in **Figure 2.12**.

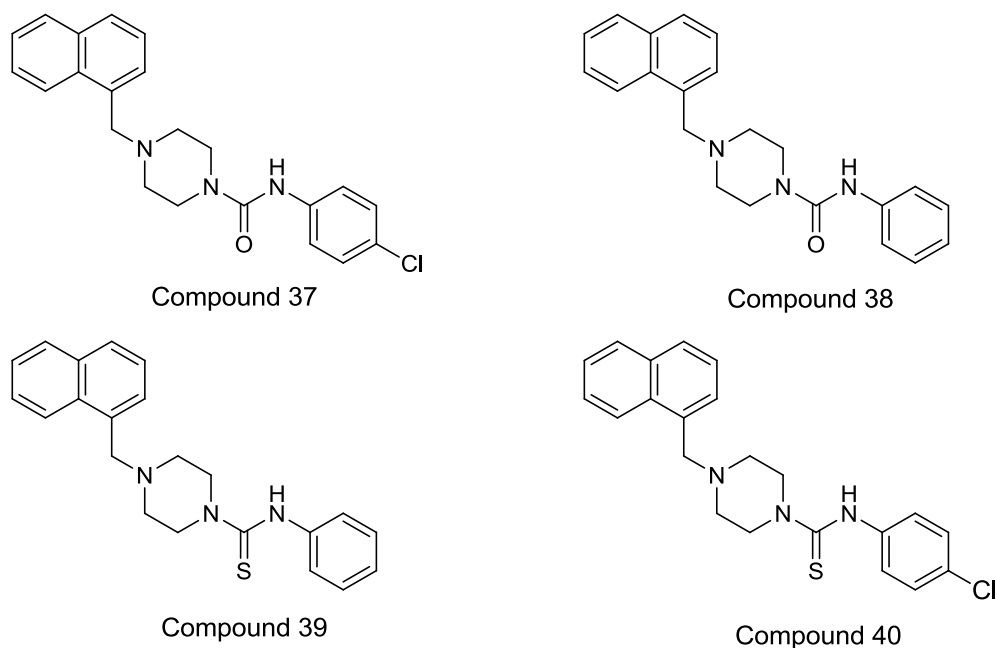
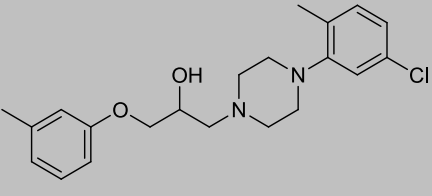
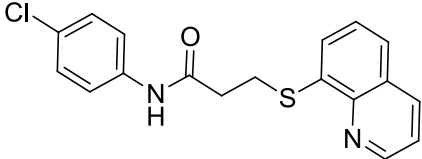
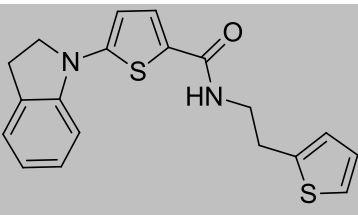
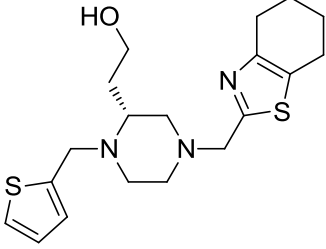
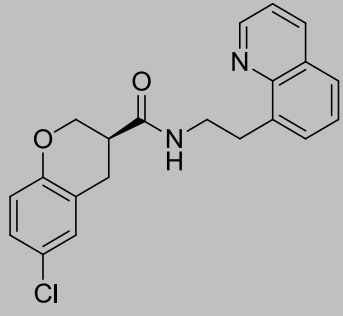
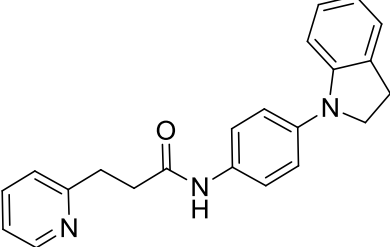


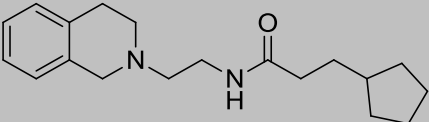
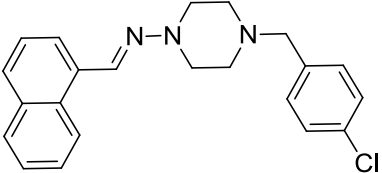
Figure 2.12. Compounds synthesised based on **34**. (**37-40**)

The core was modified to a six membered piperazine ring, rather than the more unusual seven membered dinitrogen ring seen in **34**. This piperazine ring was more synthetically accessible than the seven membered ring. A secondary amine was added adjacent to the carbonyl group. It was envisaged that this could act as a potential HB donor and interact with the acidic residues in the nNOS pocket (Glu597, Asp602). The inclusion of the amine also allowed for bond formation via well synthetic methodologies. The chlorine moiety from the screening hit was retained, and a version of the compound without the chlorine was synthesised to explore the effects of the substituent on activity. Finally, two derivatives were synthesised where the carbonyl oxygen was substituted for the less electronegative sulphur to examine the electronic effects at this position. It was thought that replacement of the oxygen for the sulphur would increase the pKa of the hydrogen on the neighbouring nitrogen, strengthening any potential H-bond interactions between it and the binding site.

The proposed structures were flexibly docked into the nNOS homology model binding site, and scored 14.9356, 14.7354, 14.0519 and 13.8756 respectively with cDOCKER, (**37-40**). While these scores were lower than the score of the parent compound (**34**, 17.3910), they were still relatively high and indicated that **37-40** may form interactions with the human nNOS binding site.

Table 2.16. Biologically evaluated compounds derived from 3PNF-HM flexibly docked with Zinc dataset.

Compound Structure	Rank	Compound No.	BBB level	Bloodstream Absorption level	Aqueous Solubility level
	1	41	0	0	2
	3	42	1	0	2
	9	43	0	0	2
	13	44	1	0	3
	14	45	1	0	2
	18	46	1	0	2

	19	47	1	0	2
	21	48	1	0	2

Similar to the Maybridge screen, the BBB and bloodstream absorption levels for the Zinc compounds were again seen to be favourable, while the aqueous solubility levels were all either two or three. This was as expected as the Zinc dataset had been pre-selected to screen only drug like candidates and the BBB like filter had also been applied. Many of the high ranking compounds had broadly similar features, with an aromatic ring at each end of the molecules, joined by a linker which contained a HB donor. This would allow interaction with the heme propionate and the Tyr711 residue, while the HB donor could potentially interact with one or more of the HB acceptors in the 3PNF-HM binding site, such as Glu597 and Asp602.

The top ranked compound from the Zinc screen (**41**) bound to the 3PNF-HM is shown in **Figure 2.13**. Interactions between the ligand and the binding site include π stacking interaction with the heme porphoryin, hydrophobic interactions with Val687 and Pro685 (not shown), and two solvent mediated HBs to Asp717 and Arg723. These interaction types have not been previously observed for nNOS inhibition. Interestingly, the disubstituted aromatic ring of the hit compound did not form a π stacking interaction with Tyr711. Literature precedent suggests that aromatic rings which are situated close to Tyr706 (rat nNOS) can form π stacking interactions with the side chain of this residue. The expected HB with Glu597 or Asp602 was also not predicted. Compounds from the Zinc screen were purchased and **41** was synthesised for biological evaluation.

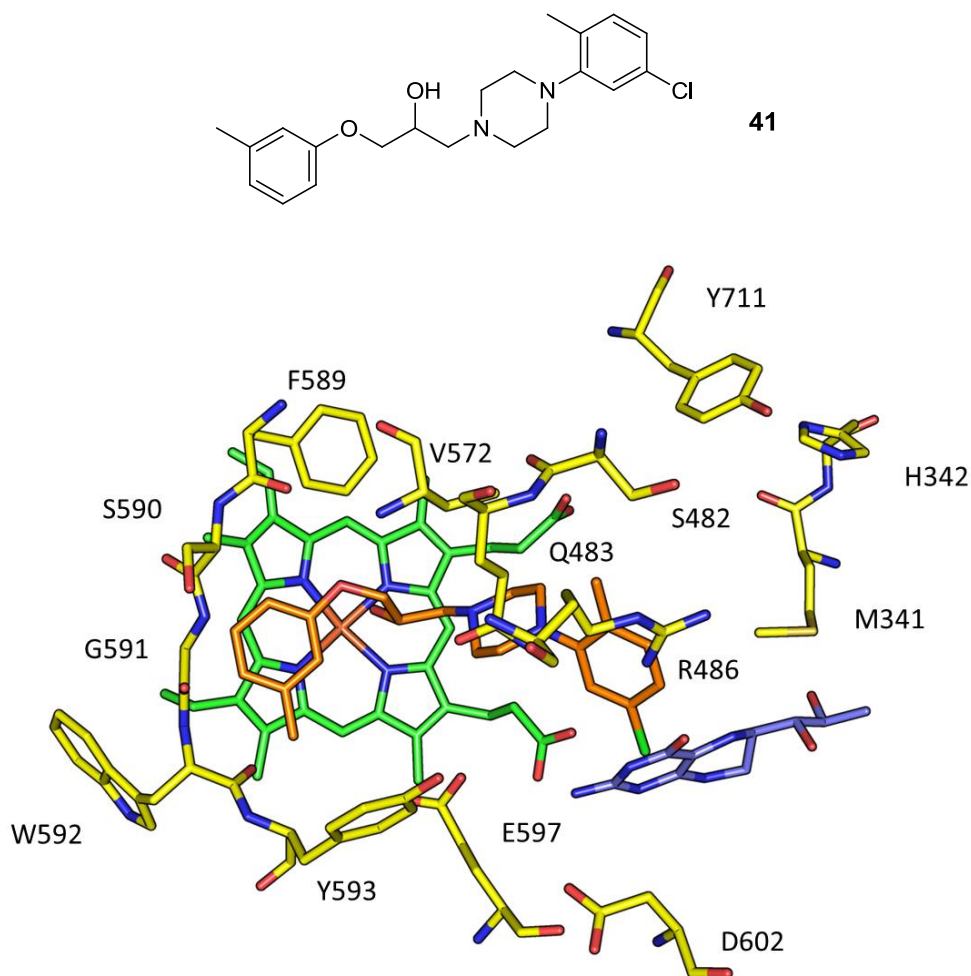
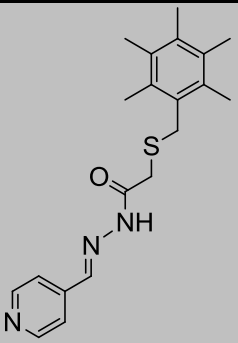
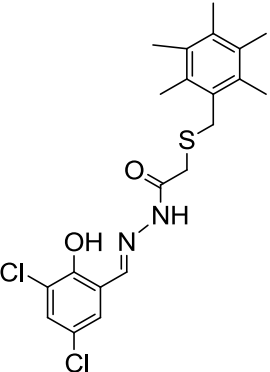
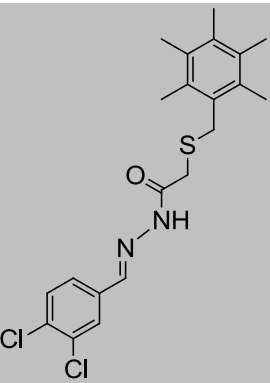
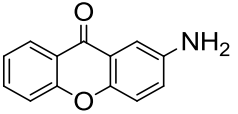
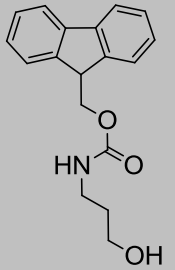


Figure 2.13. 3PNF-HM binding site with **41** bound. **41** is also shown separately. Binding site residues in yellow, heme in green, BH₄ in blue and ligand in orange. Waters omitted for clarity.

2.6.2 Comparison of top docking hits in eNOS, iNOS and nNOS

Zinc and Maybridge were also docked into the human iNOS and human eNOS crystal structures as validated in section 2.5.2. The top ten hits from the nNOS screens of Zinc and Maybridge are shown in **Table 2.17** and **Table 2.18**, along with the rankings of each hit compound in the eNOS and iNOS docking screens (see chapter five, section 5.5.7 for iNOS and eNOS docking procedure). An alignment of the key binding site residues in the three human isoforms is provided in **Table 2.19**.

Table 2.17. Top ten Maybridge hits from nNOS HM, and their ranks when docked with human eNOS and human iNOS.

Structure	nNOS HM rank	Human eNOS rank	Human iNOS rank
	1	2	1
	2	1	Outside top 100
	3	3	Outside top 100
	4	4	Outside top 100
	5	5	5

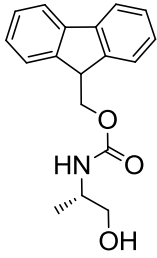
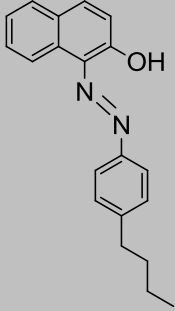
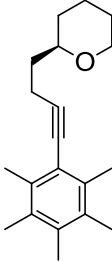
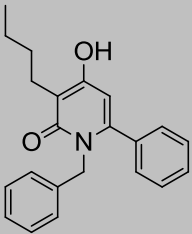
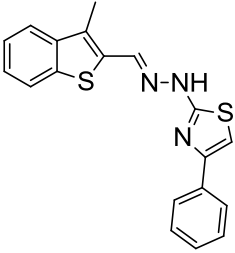
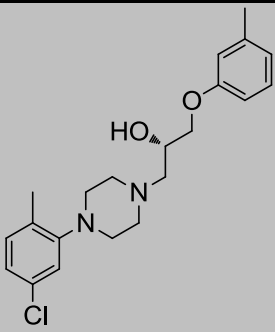
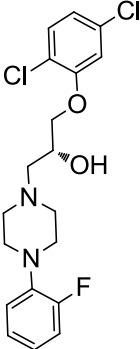
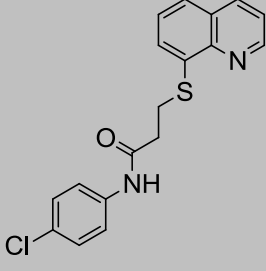
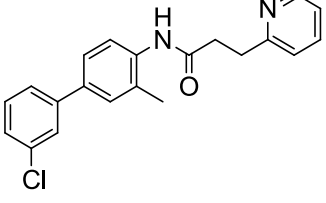
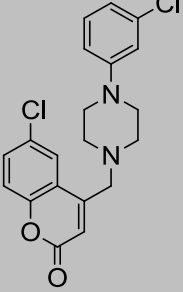
	6	7	4
	7	6	Outside top 100
	8	9	15
	9	19	7
	10	8	Outside top 100

Table 2.18. Top ten Zinc hits from nNOS HM, and their ranks when docked with human eNOS and human iNOS.

Structure	nNOS HM rank	Human eNOS rank	Human iNOS rank
	1	4	2
	2	3	10
	3	6	Outside top 100
	4	1	35
	5	10	7

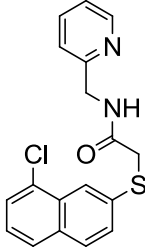
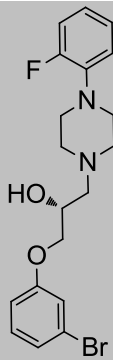
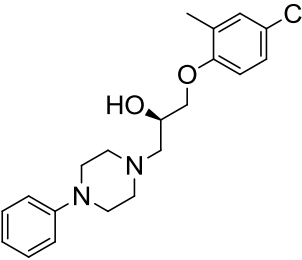
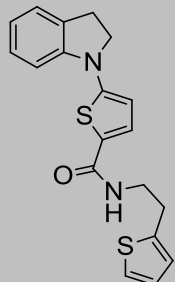
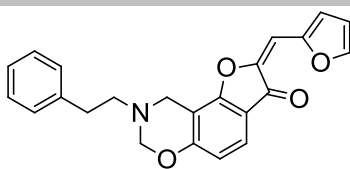
	6	12	78
	7	11	Outside top 100
	8	5	3
	9	18	Outside top 100
	10	15	14

Table 2.19. Comparison of key binding site residues in human iNOS, eNOS and nNOS.

iNOS	eNOS	nNOS
M120	V104	M341
T121	F105	H342
A262	S246	S482
Q263	Q247	Q483
R266	R250	R486
V352	V336	V572
F369	F353	F589
N370	S354	S590
G371	G355	G591
W372	W356	W592
Y373	Y357	Y593
E377	E361	E597
D382	N366	D602
Y491	Y475	Y711

iNOS, eNOS and nNOS had many of same compounds in their respective top ten hit lists. This was despite the fact that the validation steps with Chemscore suggested that the scoring function was capable of identifying selective human nNOS inhibitors. It was not surprising that many of the potential hit compounds were the same for the three isoforms. As can be seen in **Table 2.19** many of the key residues are identical between the NOS human isoforms, making selectivity for one isoform difficult to predict and achieve. A protein sequence alignment of the three isoforms, conducted with Clustal Omega, revealed a 52.6% identity and a 70.9% similarity between the isoforms. It was also observed that the docking protocol was more selective for nNOS over iNOS, than nNOS over eNOS. This suggests that preventing off target effects in eNOS may be more difficult than preventing off target effects in iNOS.

This has been borne out in the literature, as all reported nNOS inhibitors exhibit some degree of inhibitory activity towards the other two isoforms, (chapter one, section 1.4). It was decided to continue with biological evaluation of the chosen nNOS hits. If a successful hit compound was identified, selectivity for nNOS could then be explored via SAR modification. This would potentially be targeted towards the Asp602 residue in nNOS,

which is replaced by an Asn366 in eNOS. The pK_a of the aspartic acid side chain is 3.9, while the asparagine side chain is not deprotonated at physiologically relevant pH levels.⁸² Therefore, selective targeting of human nNOS over human eNOS may be achieved by targeting a HB donor towards the Asp602 residue. The deprotonated carboxylic acid group of aspartic acid will be capable of forming HB interactions with the HB donor, while the protonated asparagine side chain in eNOS will not be capable of forming these types of interactions.

Selectivity for nNOS over iNOS could potentially be achieved by targeting of the His342 residue in nNOS, which is replaced by Thr121 in iNOS. The pK_a of the imidazole ring in the histidine side chain is ~ 6.0 , while threonine's side chain remains protonated at physiologically relevant pH levels.⁸² The deprotonated imidazole ring of histidine could therefore act as a HB acceptor with a potential inhibitor, while the protonated threonine of eNOS would not act in this way.

2.6.3 Structure based design conclusion

The structure based design approach described above represented a worthwhile study as such a high throughput screening approach with a human nNOS homology model has not yet been reported. Also, it was expected that the model that was developed should be accurate owing to the sequence similarity between target and template. It was therefore hoped that the compounds identified would act as novel human nNOS inhibitors. The compounds identified also had favourable PK properties and were predicted to form a variety of interactions with the human nNOS binding site. The compounds, as outlined in **Table 2.15** and **Table 2.16**, were purchased or synthesised for biological evaluation. This structure based design approach was complimented by a ligand based design approach. The use of two separate computational methods sought to maximize the chances of identifying efficacious and selective human nNOS inhibitors. The ligand based design experiments that were conducted will be outlined in the next section.

2.7 Ligand based drug design overview

While comparative modelling focuses on the predicted binding site of the protein target of interest, ligand based drug design (LBDD) examines known inhibitors of the target. These known inhibitors can be used to predict the types of features that may result in enzyme inhibition. A pharmacophore is developed where the important features of the active ligands are orientated relative to each other. The pharmacophore is then used to screen commercial databases to find compounds whose features match the features of the pharmacophore. The general approach used in this project is outlined in Figure 2.14. Notice that many of the procedural steps for model validation are the same as those used for the structure based drug design. The preparation of the commercial database is also identical to the methods already described for the structure based drug design.

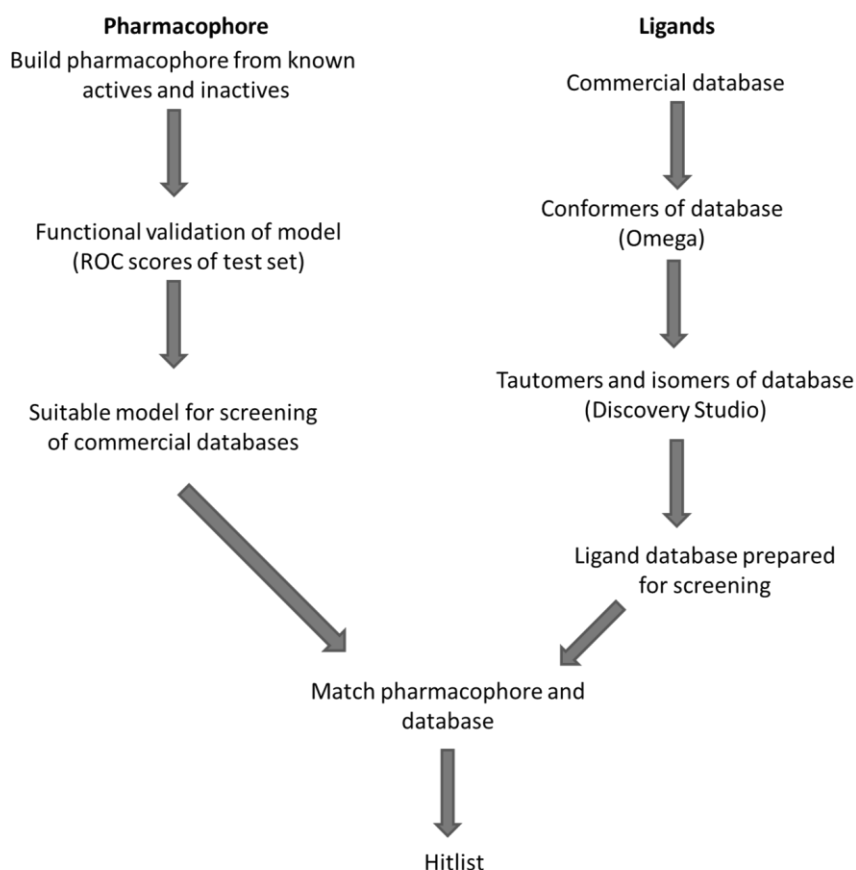


Figure 2.14. Ligand based drug design overview.

2.7.1 Pharmacophore: Construction and validation

A pharmacophore is defined as a set of features that is common to a series of active molecules.¹³³ These features are also referred to as pharmacophoric groups and include structures such as HB donors and acceptors, positively and negatively charged groups and hydrophobic groups.

All pharmacophores were constructed using CATALYST software.¹⁶³ This generates and validates pharmacophoric models and screens databases in one convenient protocol. 2-D pharmacophores are generated using HipHop.¹⁶³ A 2-D pharmacophore is used when the bioactive conformation of the ligands is unknown.

The input file for pharmacophore generation using HipHop contains a set of active compounds which have a high affinity for the target, and a set of inactive compounds which have a low affinity for the target. The cut offs for high and low affinity are target dependent. The most active compound is assigned a principle number of two, the rest of the actives are assigned a principle number of one and the inactives are assigned as zero. A range of options can then be altered for the pharmacophore generation, including how many features of the active compounds may be omitted from the pharmacophore (max omit), whether or not the feature placement is flexible and the number of excluded volumes to include. The excluded volumes are regions of space into which placement of a pharmacophoric feature would be unfavourable. These are generated using the inactive compounds.^{164,165} Often a combination of these options can be trialled to generate a number of pharmacophores that are then validated to determine the best performing conditions.

Validation of pharmacophoric models is conducted in a similar fashion to validation of docking protocols, i.e. through the use of a validation set and scoring with ROCS curves. It is important to omit the compounds used for pharmacophore generation from this validation set.

2.7.2 Pharmacophore screening

With a pharmacophore model generated and validated it can then be used to screen large molecule databases. This involves “matching” of the pharmacophoric features to the

ligands in the database. As the bioactive conformation of the ligands is unknown, a conformer ensemble of the ligand database is used. The ligands are then ranked using FitValue, with larger values indicating a better fitting ligand.¹⁶⁶

2.8 Ligand based drug design results

2.8.1 Pharmacophore one construction and validation

Initial attempts to develop a nNOS pharmacophore used large numbers of active and inactive compounds from the ChEMBL database (<https://www.ebi.ac.uk/chembl/>). All compounds with an IC₅₀ of 10 μM or less for nNOS were designated as nNOS actives (550 compounds), while all compound with an IC₅₀ of 30 μM or more for nNOS were designated as inactives (300 compounds). These were clustered as per the chapter five, section 5.5.10 and the pharmacophore generated. It should be noted that a search of the ChEMBL database using human nNOS as the target returns over 800 compounds. However, examination of the publications from which these compounds are derived reveals that no testing on human nNOS was conducted in the vast majority of cases.

Generation of a pharmacophore from this set failed. This was attributed to the fact that many of the most active nNOS inhibitors in the ChEMBL database are small nitrogen heterocycles, which do not have enough features to generate a useable pharmacophoric model. A pharmacophore usually has 3-6 features, depending on the structures of the compounds used to construct the model.

This led to the use of individually chosen active and inactive compounds for development of the next pharmacophoric model. The active compounds were chosen based on structural diversity, and avoidance of the potentially overly simple small nitrogen heterocycles. Compounds developed from the structure based design which had proven inactive in nNOS inhibition assays were also included in the inactive compound list for the training set. The exact compounds used for pharmacophore generation are outlined in chapter 5, section 5.5.10.

A variety of conditions were trialled for the development of this model, with ten models generated for each set of conditions. The pharmacophores were tested using the nNOS test set developed during the homology model construction. The test set was carefully checked to ensure it did not contain any compounds that had been used in the training set as this would potentially skew the validation results. The best scoring pharmacophores from each set of conditions is show in **Table 2.20** (conditions outlined in chapter five, section 2.7.1).

Table 2.20. Pharmacophore generation conditions and ROC scores of the best model from each.

Pharmacophore	Excluded Volumes	Rigid or Flexible	Max Omit Feature	ROCS score
A	0	Rigid	0	0.731
B	0	Rigid	1	0.774
C	50	Rigid	0	0.765
D	50	Flexible	1	0.780
E	0	Flexible	0	0.787
F	50	Flexible	0	0.805

The six parameter sets all resulted in good to very good ROC scores, ranging from 0.731 to 0.805. The best performing pharmacophore, pharmacophore F, gave a strong ROC score of 0.805. The generation parameters for this model allowed for excluded volumes, flexible ligand mapping and had a max omit value of zero. The presence of excluded volumes in the model was welcome, as the generation set contained several experimentally validated inactive human nNOS inhibitors from the structure based design studies. As very few compounds have been tested with isolated human nNOS, the inclusion of known inactive compounds in the pharmacophore model represented an important step forward in the field. Pharmacophore F is shown in **Figure 2.15**.

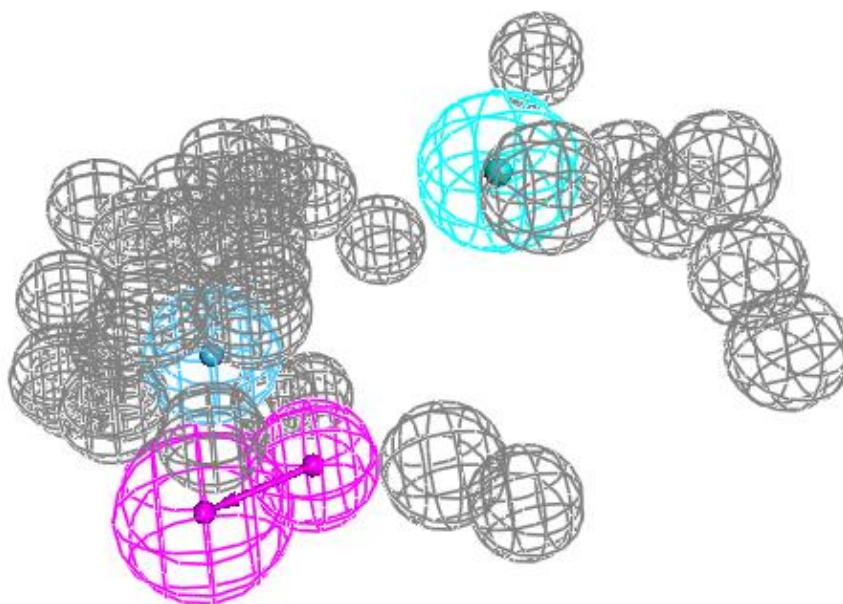
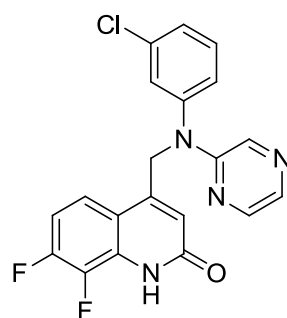


Figure 2.15. Image of pharmacophore F. HB donor in pink, hydrophobic aromatic in blue, hydrophobic non-aromatic in cyan, excluded volumes in grey.

The pharmacophore had three feature types, a HB donor (pink) a hydrophobic aromatic (blue) and a hydrophobic non aromatic (cyan). The excluded volumes are shown in grey and are derived from the inactive compounds in the training set. These suggested features mirrored the features of the human nNOS binding site quite closely.⁸³ The HB donor is pointing towards the bottom of the pocket, where the key glutamic acid residue (Glu597) is available to form H-bond interactions. The hydrophobic aromatic feature sat above the space which is occupied by the heme moiety in the binding site. The residues surrounding the heme in the binding site of human nNOS are Ser588, Tyr585 and the three hydrophobic residues Gly587, Trp586, Phe589. The excluded volumes around the hydrophobic aromatic feature represented these five residues. Finally, the hydrophobic non-aromatic feature sits close to where the His342, Met341 and Tyr711 hydrophobic pocket is located in the human nNOS binding site. To illustrate this comparison, an image of the most active compound used for pharmacophore generation (ChEMBL1944717, **49**, IC_{50} of 12 μ M for human nNOS in whole cell assay) is shown aligned to the pharmacophore and docked into the homology model binding site in **Figure 2.16**.⁸⁴



ChEMBL1944717
Compound 49

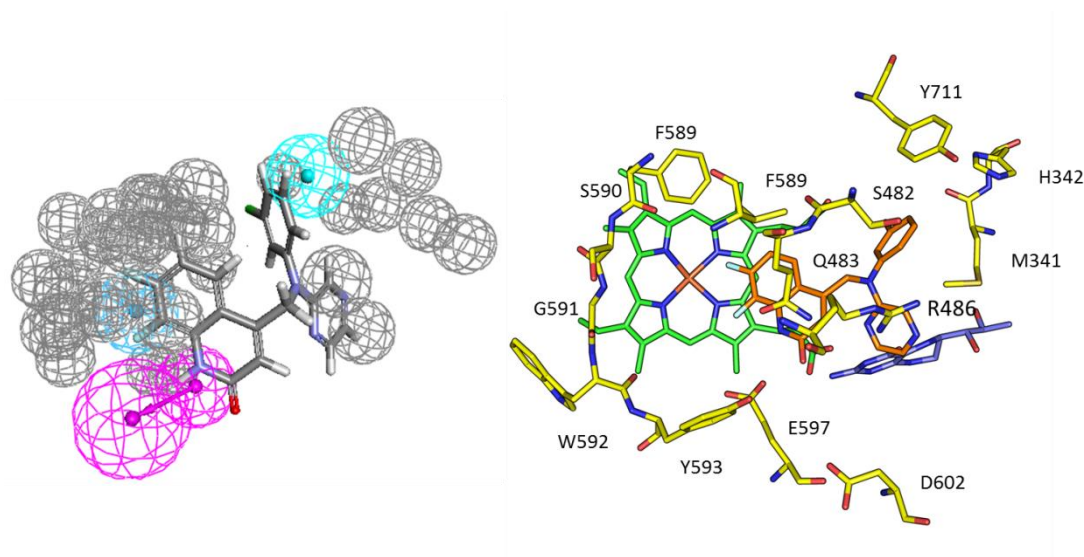
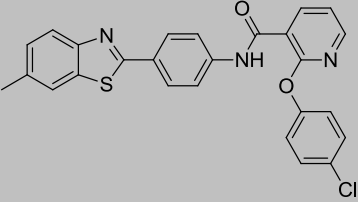
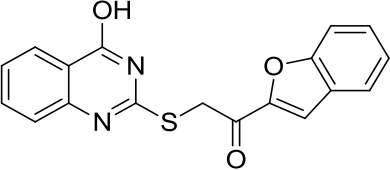
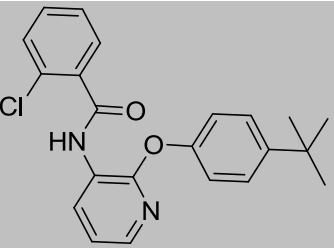
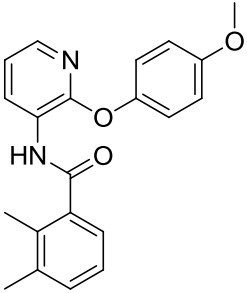
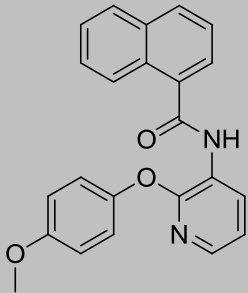
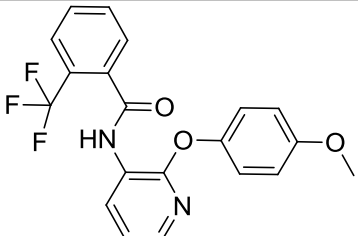


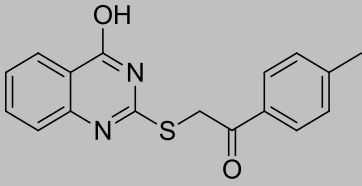
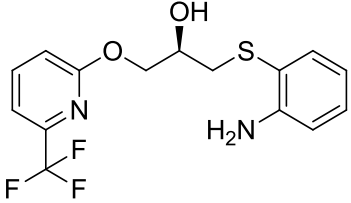
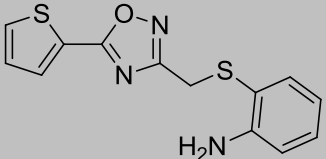
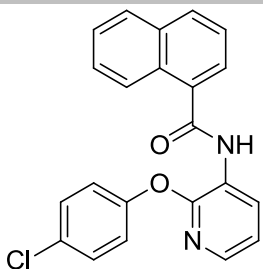
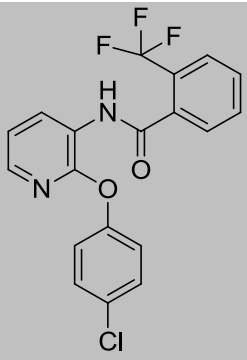
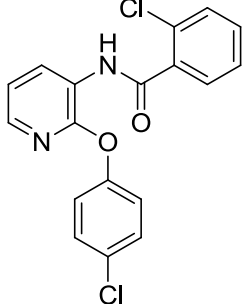
Figure 2.16. Pharmacophore F and 3PNF-HM with compound 49 orientated in similar poses. For pharmacophore HB donor in pink, hydrophobic aromatic in blue, hydrophobic non-aromatic in cyan, excluded volumes in grey. For 3PNF-HM residues in yellow, heme in green, BH₄ in blue and ligand in orange. Waters omitted for clarity.

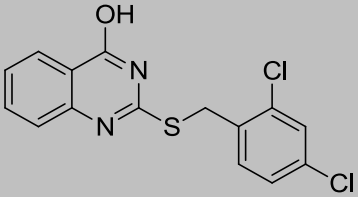
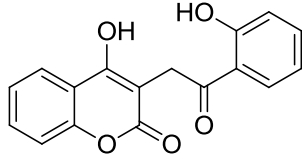
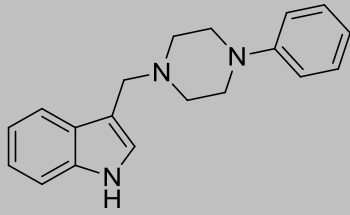
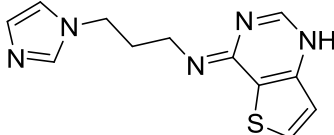
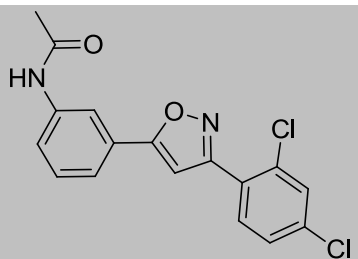
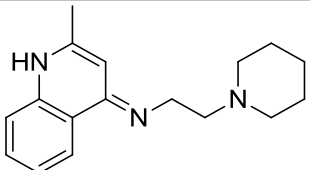
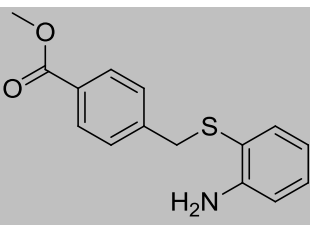
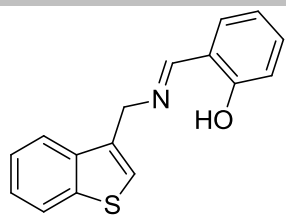
2.8.2 Pharmacophore one screen

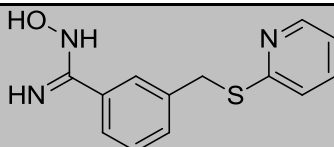
The list of compounds chosen for biological evaluation from a screen of commercial datasets (Zinc and Maybridge) using pharmacophore F is shown in **Table 2.21**. The overall rank of the compounds in the screening list is also shown.

Table 2.21. Pharmacophore round one screening.

Compound Structure	Rank	Compound No.	BBB level	Bloodstream Absorption level	Aqueous Solubility level
	1	50	4	2	1
	2	51	1	0	1
	4	52	0	0	1
	5	53	1	0	2
	6	54	1	0	2
	7	55	1	0	2

	8	56	1	0	2
	9	57	2	0	2
	10	58	2	0	3
	11	59	1	0	1
	12	60	1	0	1
	13	61	1	0	2

	14	62	0	0	1
	15	63	3	0	3
	16	64	1	0	2
	17	65	3	0	4
	18	66	1	0	2
	19	67	0	0	2
	20	68	2	0	3
	21	69	1	0	2

	42	70	3	0	3
---	----	----	---	---	---

The PK properties of the hits were again largely favourable, although there a larger number of non BBB permeable compounds ranked highly in the hit list. Despite their less favourable BBB properties, the compounds shown in **Table 2.21** were advanced for biological evaluation. If one of the compounds proved to have nNOS inhibitory activity, it could be chemically modified to improve its PK profile.

The highest ranked compound (**50**) from this screen aligned to pharmacophore F, is shown in **Figure 2.17**.

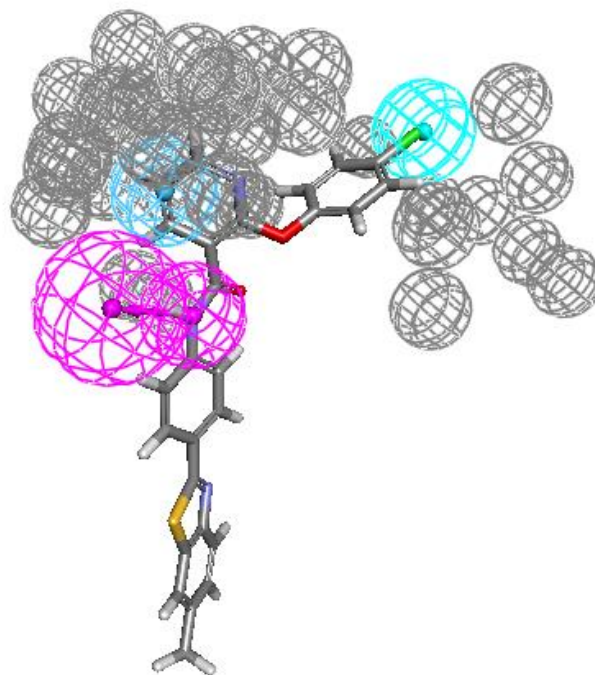
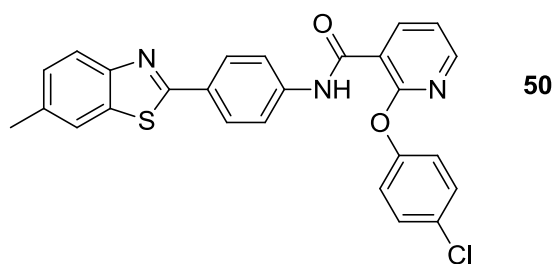


Figure 2.17. Pharmacophore F with **50** aligned. **50** is also shown separately. HB donor in pink, hydrophobic aromatic in blue, hydrophobic non-aromatic in cyan, excluded volumes in grey.

The secondary amine of **50** sits in the HB donor site, while the disubstituted pyridine ring occupies the hydrophobic aromatic feature. The chlorine from the disubstituted benzene extends into the non-aromatic hydrophobic region. The molecule also avoids all excluded volumes. The thiazole ring containing portion of the molecule extends below the HB donor pocket. This may potentially clash with residues in this region which were not modelled by the pharmacophore. This could impact the compound's binding ability and effectiveness. Surprisingly, compounds with a similar core to **23**, which matched the pharmacophoric elements but lacked the apparently superfluous thiazole "tail", did not rank in the top 500 compounds of this screen.

2.8.3 Pharmacophore two construction and validation

Following biological evaluation of the compounds shown in **Table 2.21** (Section 4.16) a second iteration of the pharmacophore was developed to refine the model. The performance of the compounds from the previous pharmacophore in an nNOS inhibition assay (chapter four section 4.16) was taken into account for generation of the second pharmacophore. The generation of the second pharmacophore also included the best reported human nNOS inhibitor, **Figure 2.18**.⁴⁵ This inhibitor was omitted from the generation of the first pharmacophore as it was not indexed in the ChEMBL database. Failure of the first pharmacophore to identify a novel human nNOS inhibitor prompted a more thorough search of the literature for active human nNOS inhibitors, which resulted in the identification of the compound shown **Figure 2.18**. Ten pharmacophores were generated in this second iteration, using the previously identified optimum parameters (50 excluded volumes, flexible fitting, max omit zero). The ROC scores for the ten pharmacophores are shown **Table 2.22**. These ROC scores were generated using the same test set as was used in the first pharmacophore iteration (section 2.8.1).

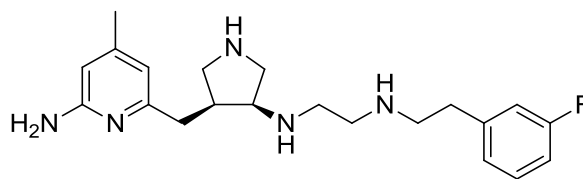


Figure 2.18. Human nNOS inhibitor used as active for generation set.⁴⁵

Table 2.22. ROC scores of the second generation of pharmacophores (50 Excluded volumes, flexible fitting, max omit zero).

Pharmacophore	ROC score
G	0.672
H	0.607
I	0.506
J	0.712
K	0.546
L	0.651
M	0.540
N	0.557
O	0.632
P	0.515

The best scoring pharmacophore was pharmacophore J, **Figure 2.19**. The ROC scores were less impressive for this round of pharmacophore generation, suggesting that the second pharmacophore was less accurate at identifying nNOS inhibitors. The inclusion of the extra excluded volumes in pharmacophore J compared to pharmacophore F may have made it more difficult of the compounds of the test set to align with the pharmacophoric features of pharmacophore J, thus resulting is lower ROC scores for this iteration.

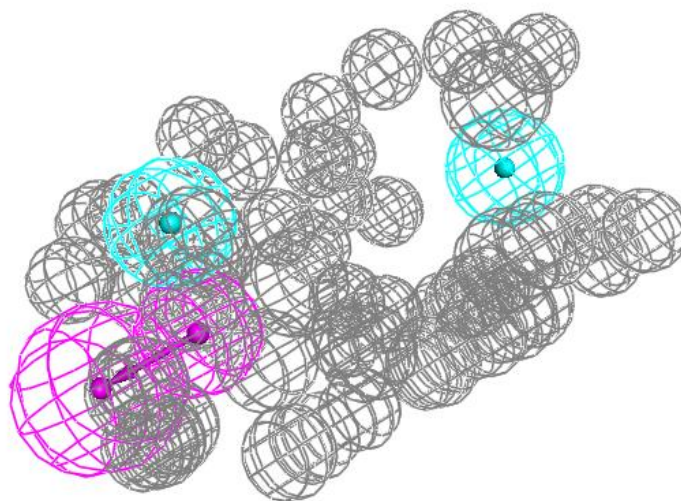


Figure 2.19. Image of pharmacophore J. HB donor in pink, hydrophobic non-aromatic in cyan, excluded volumes in grey.

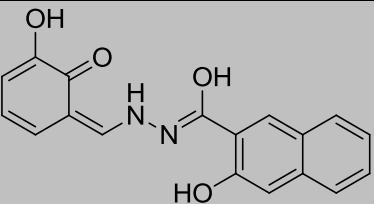
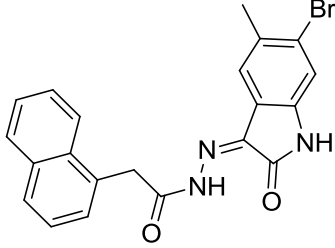
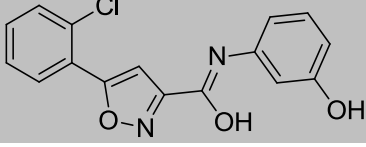
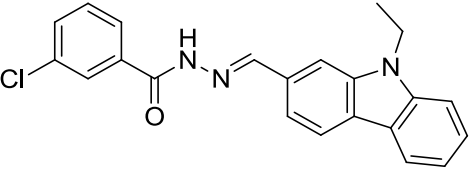
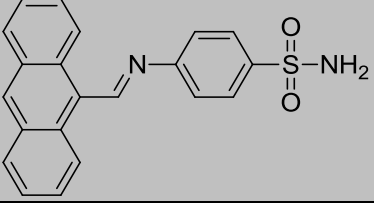
The HB donor feature and its direction were retained in pharmacophore J. This would allow compounds that matched pharmacophore J to form HB interactions with the key Glu597 residue in the human nNOS binding pocket. A hydrophobic non-aromatic feature sat close to the HB donor feature. Similar to pharmacophore F, this suggested that the residues surrounding the heme moiety in the binding site were hydrophobic in nature. However, the change of the feature from an aromatic hydrophobic (pharmacophore F) to a non-aromatic hydrophobic (pharmacophore J) was unexpected. It was initially thought that this feature represented the aromatic heme moiety in the nNOS binding site, and compounds which formed aromatic π stacking interactions with this moiety would fit pharmacophore F well. This π stacking interaction was deemed less important in pharmacophore J.

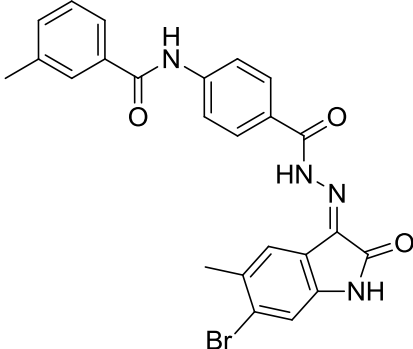
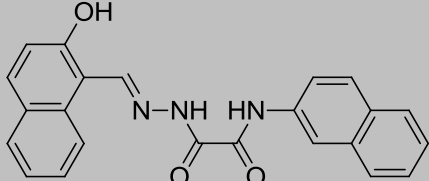
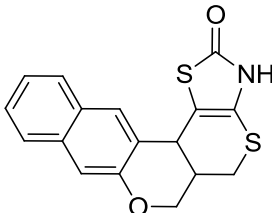
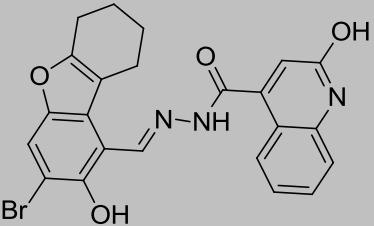
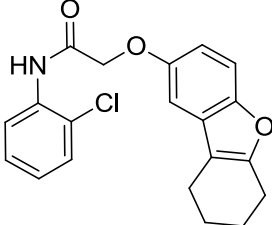
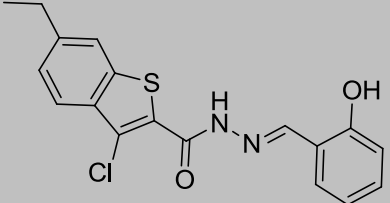
The final non-aromatic hydrophobic feature in pharmacophore J matched the remaining non-aromatic hydrophobic feature in pharmacophore F. There were a larger number of excluded volumes in pharmacophore J due to the increased number of inactives in the training set. This provided a more complete view of the binding pocket.

2.8.4 Pharmacophore two screen

Screening of Maybridge and Zinc was conducted with pharmacophore two, and the compounds chosen for biological evaluation are shown in **Table 2.23**.

Table 2.23. Pharmacophore 2 screened list.

Compound Structure	Rank	Compound No.	BBB level	Bloodstream Absorption level	Aqueous Solubility level
	1	71	1	0	1
	2	72	4	1	1
	4	73	1	2	2
	5	74	1	0	2
	6	75	2	0	1

	9	76	4	2	2
	11	77	4	0	2
	13	78	1	0	1
	18	79	4	2	1
	22	80	1	0	1
	40	81	1	0	1

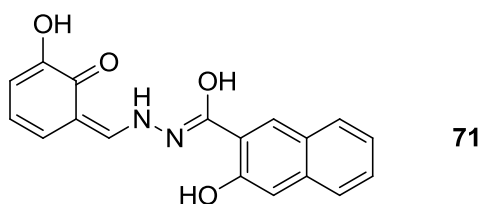
The features of pharmacophore J suggested that non aromatic moieties would be favoured close to a HB donor. Taking **71** as an example, the disubstituted phenol ring is non aromatic as represented in **Table 2.23**. However, it is unlikely that **71** exists solely as this tautomer. The most likely structure would reform the aromaticity of the ring, while breaking the carbonyl double bond. This would then potentially form a second HB donor feature on the

ring with the protonation of the oxygen. As the ligand databases are screened through the pharmacophore as localised structures, this potential delocalisation and reformation of the aromatic character of the ring was not taken into account by the algorithm.

The naphthyl ring at the other end of **71** is obviously aromatic, and therefore does not match with the other non-aromatic hydrophobic feature of pharmacophore J. It is questionable, therefore, if there is a large difference between aromatic and non-aromatic hydrophobic features in the pharmacophore generation and screening procedure. The other molecules in the hit list all follow this type of trend, with large degrees of aromatic character being retained across the list.

The BBB values of the hit compounds from this screen were markedly increased relative to previous screens. Several compounds with a BBB of three or four ranked highly in the list. While this did present a potential PK issue, it was decided to continue with testing of these compounds as the initial goal of the project was to identify a human nNOS inhibitor. The BBB permeability issues could then potentially be addressed through structural modifications. These may include removal of ionisable groups and decreasing the molecular weight of the compound to below 300 Da. The absorption levels were seen to be favourable for the top ranked compounds, while the aqueous solubility levels were less favourable.

The highest ranking compound from this screen, **71**, is shown overlaid with pharmacophore J in **Figure 2.20**. The alcohol group occupies the HB donor feature, while the ring it is attached to occupies the non-aromatic hydrophobic pocket nearby. The di substituted naphthyl group occupies the remaining non aromatic hydrophobic feature.



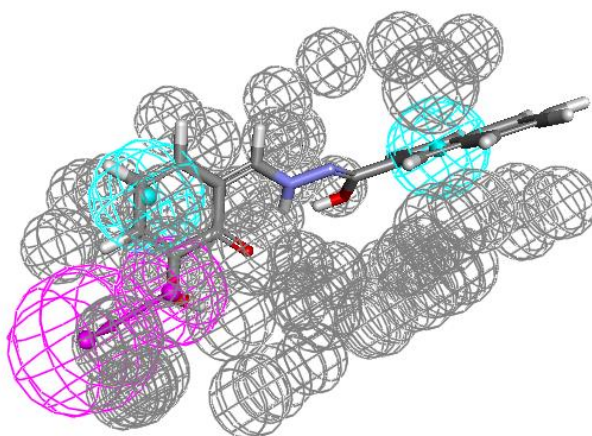


Figure 2.20. Pharmacophore J with **71** aligned, along with **71** shown separately.

2.9 Human nNOS Crystal Structure

2.9.1 Comparing homology model and crystal structure binding sites

The first crystal structure of human nNOS only became available in 2015, PDB code 4DN1.⁸³ This was expedient as it allowed for screening of commercial databases using the actual structure of the human protein. It also allowed for comparison of the homology model with the crystal structure to assess the accuracy of the modelling experiments. An image of the human nNOS binding site taken from the crystal structure is provided in **Figure 2.21**. An overlay of the 3PNF-HM with the 4DN1 crystal structure is shown in **Figure 2.22**.

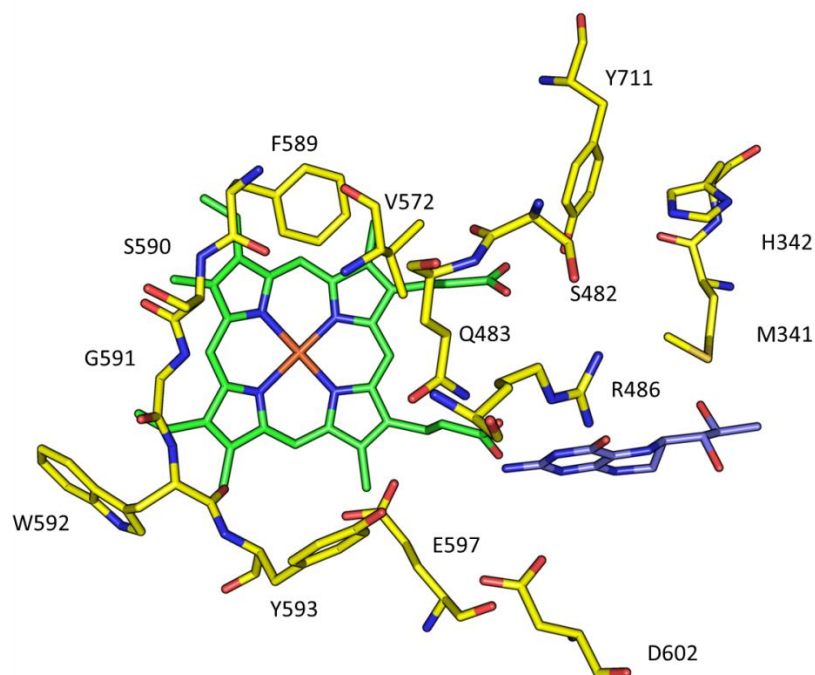


Figure 2.21. 4DN1 human nNOS crystal structure binding site. The residues are shown in yellow, heme in green and BH₄ in blue. Waters omitted for clarity.⁸³

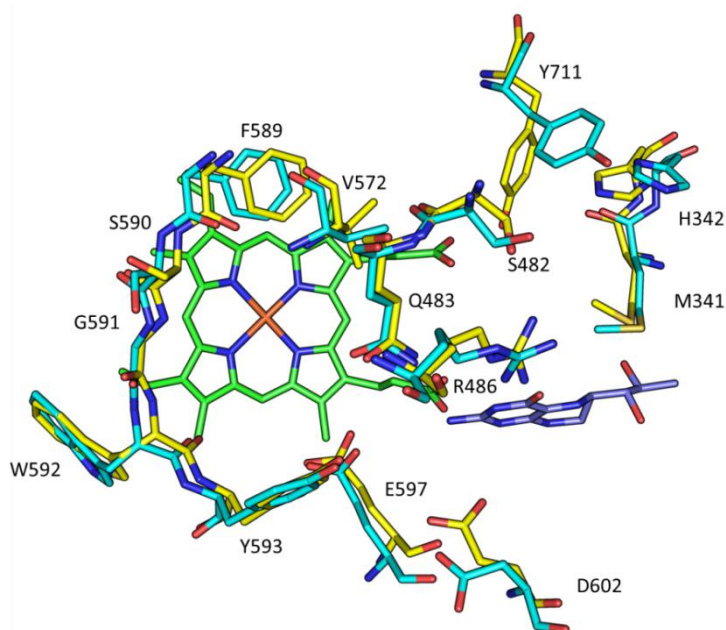


Figure 2.22. Overlay of 3PNF Homology model (cyan) with 4DN1 crystal structure (yellow). The heme moiety is in green and BH₄ is in blue. Waters omitted for clarity.⁸³

It was observed that the crystal structure and homology model binding site residues were identical, and their side chains adopt similar orientations. Two of the residues exhibited alternate rotamer states in the crystal structure than was predicted by the homology model. Asp602 has been reported to form HB interactions with nNOS inhibitors in the rat binding site.^{48,49,63} Due to the similarity of the rat and human pockets it is reasonable to assume that Asp602 is capable of forming HBs with inhibitors in the human isoform also. In the homology model the side chain of this residue was pointed away from the pocket cavity, which is centred over the heme moiety, while in the crystal structure the side chain was pointed into the cavity, available to form HB interactions. The difference between the heavy chain atoms of Asp602 in the crystal structure, and the heavy chain atoms of D602 in the homology model was measured using RMSD (Å). An RMSD value of 2 Å or lower indicates that the two structures being compared are largely similar.⁷⁵ The difference between Asp602 in the homology model and D602 in the crystal structure was found to be 2.06 Å, very slightly above the 2 Å cut off point which indicates similarity. This difference in rotameric states of the side chains may impact on the types of inhibitors which dock successfully into the human nNOS crystal structure binding site.

The second rotameric difference between the crystal structure and the homology model was at Tyr711. In the homology model the aromatic ring of the residue was seen to adopt a conformation that would facilitate π stacking with an inhibitor in the binding site. Examination of the 3PNF rat nNOS template structure revealed that its ligand (**Figure 2.8**) adopted a “flipped” binding pose, placing its aminopyridine moiety close to Tyr706. This induced rotation of Tyr706 and this rotameric state was conserved in the homology model.⁶⁵ In the crystal structure the ring is pushed behind Ser482, perhaps eliminating this potential interaction. The difference in the position the heavy chain atoms for Tyr711 in the crystal structure and the homology model were again assessed using RMSD. A value of 4.28 Å was obtained, indicating that the position of the Tyr711 side chain was considerably different in the homology model when compared to the crystal structure. This may cause different compounds to interact with the crystal structure binding site than those that were previously seen to interact with the homology model binding site.

Overall, the homology model and the crystal structure were in good agreement, with the only real differences being the rotameric states of the residues as outlined above. This was encouraging as it suggests that the nNOS homology modelling procedure had been accurate, and had produced a reliable representation of the human nNOS binding site.

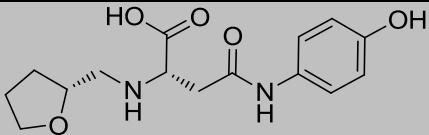
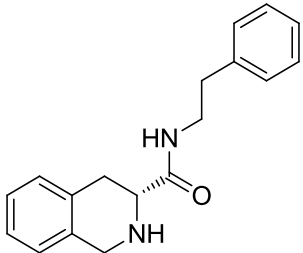
2.9.2 Screening results

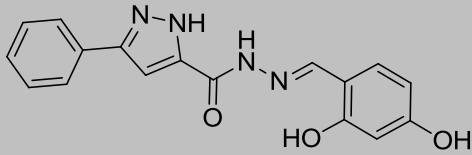
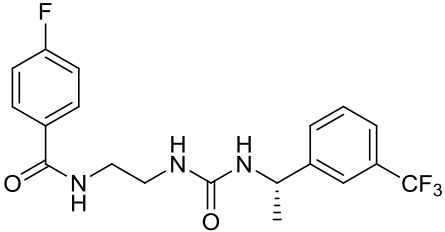
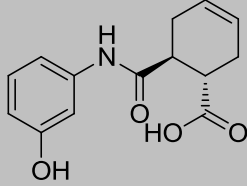
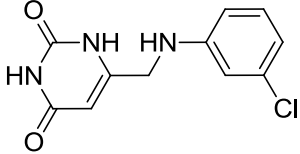
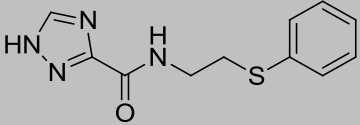
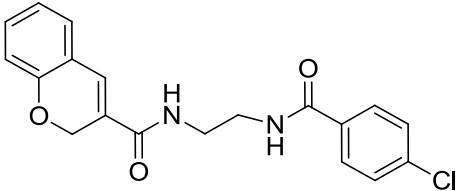
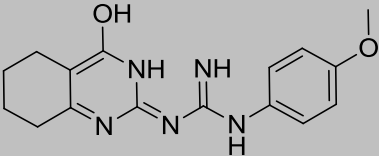
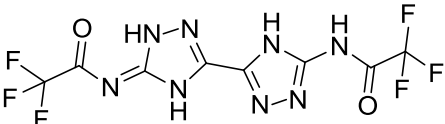
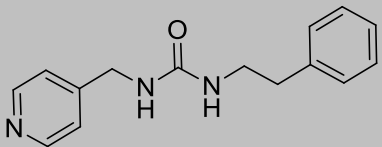
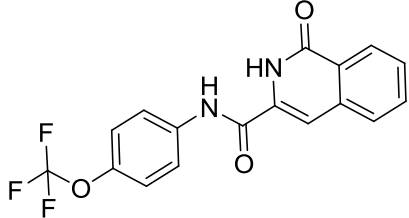
The FRED docking protocol had been updated to 3.0.0 during the course of this work. This used only one docking scoring function, Chemgauss4, as opposed to the seven functions used by FRED 2.2.5, (for a more in depth discussion of FRED 3.0.0 and FRED 2.2.5 see chapter five, section 2.3.1). The nNOS test set was docked through the nNOS crystal structure using the new Chemgauss4 architecture. This achieved a ROC score of 0.76. As a comparison, the test set was re-docked through the 3PNF-HM using Chemgauss4 and achieved a ROC score of 0.81. This was interesting as the homology model performed better than the crystal structure with the test set, perhaps due to the differences in rotameric states as described above. The homology model also performed better with the Chemgauss4 scoring function than with the previous FRED scoring function, suggesting that Chemgauss4 may be more accurate at docking molecules into the human nNOS binding site.

The commercial databases (Zinc and Maybridge) were screened with the human nNOS crystal structure, 4DN1, using this new Chemgauss4 scoring functions in the hopes of identifying a potential hit compound. The crystal structure was screened as an energy minimized structure with co-crystallized waters included.

The compounds chosen for biological evaluation from this screen, and their rank in the docking list, are shown in **Table 2.24**.

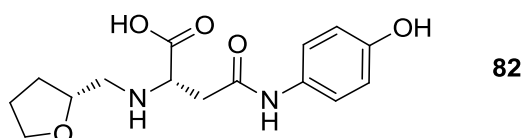
Table 2.24. Top hits from human nNOS crystal structure screening.

Compound Structure	Rank	Compound No.	BBB level	Bloodstream Absorption level	Aqueous Solubility level
	1	82	4	3	5
	5	83	2	0	3

	7	84	4	0	3
	11	85	2	0	2
	12	86	3	0	4
	26	87	3	0	3
	34	88	3	0	3
	36	89	2	0	3
	54	90	3	0	2
	82	91	4	1	2
	91	92	2	0	3
	106	93	2	0	2

Interestingly, the compounds which scored best for the crystal structure docking generally had a higher BBB level than was observed for the high ranking compounds from the homology model docking. The lowest BBB score for these compounds was two, which indicates a medium level of BBB permeability. Three compounds scored three (which is low level of BBB permeability), while three more, including the highest ranking compound, scored four. The compounds which scored four were seen to have multiple ionisable groups such as amines and alcohols which are not ideal for BBB permeability. The top ranking compound also had a poor aqueous solubility score and an unfavorable absorption profile. Nevertheless, biological evaluation was conducted with these compounds. If a positive hit was identified from this screen, structural modifications could be performed at a later date to improve the pharmacokinetic profile of the compounds.

An image of the top ranking hit from this screen, **82**, in the 4DN1 binding site is shown in **Figure 2.23**.



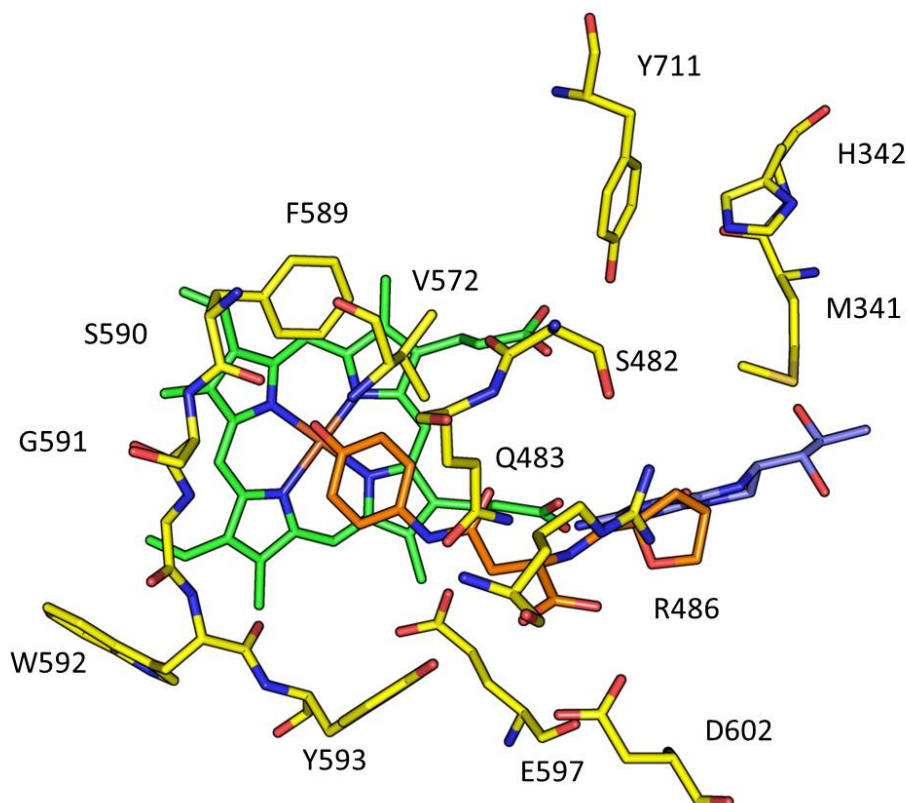


Figure 2.23. 4DN1 crystal structure binding site with **82**. **82** is also shown separately. Residues in yellow, heme in green, BH4 in blue, ligand in orange. Waters omitted for clarity.

It was predicted that **82** would form two HBs with Arg486, two with Arg608, Tyr567, (not shown) Tyr593, Glu597 and with the heme propionate. There is also a predicted electrostatic interaction with Glu597 and Asp602, a π stacking interaction with the heme ring and hydrophobic interactions with Pro570 (not shown) and Val572. This appears promising as the compound forms an array of interactions with the binding site which have been previously observed in the literature, including interacting with the key Glu597 residue (See chapter one, section 1.4.4).

Similar to the homology model docking, not all of the compounds of interest were commercially available. Therefore, a number of compounds based on compound 85 were synthesised for biological evaluation. The compounds were chosen based on synthetic accessibility and availability of starting materials and are shown in **Figure 2.24**.

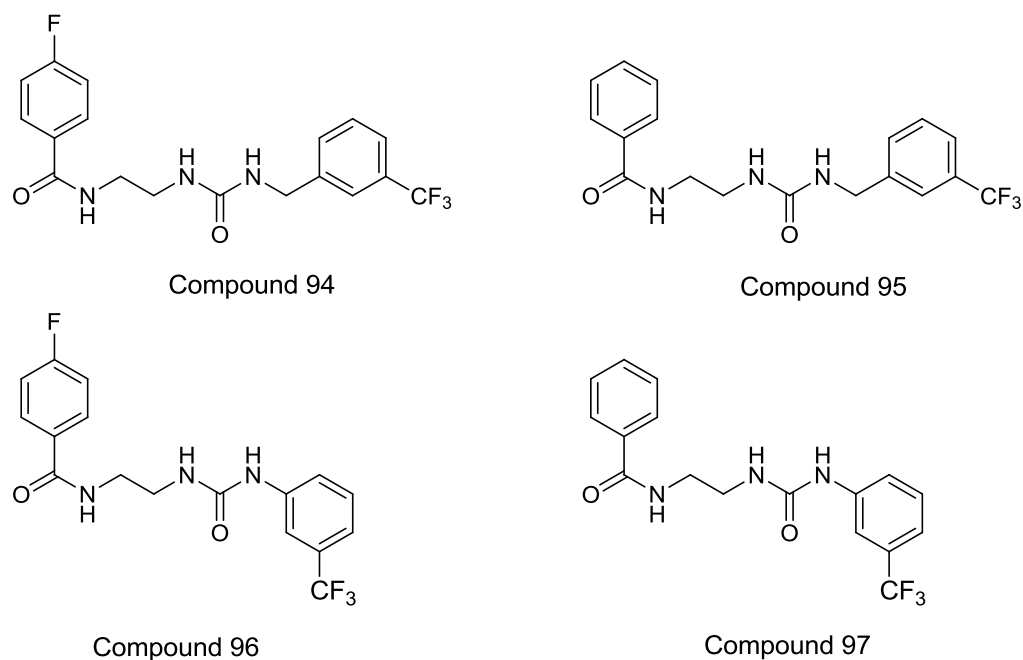


Figure 2.24. Synthetic targets based on compound 85, compounds 94-97.

For ease of synthesis, the chiral centre was removed from the molecules. It was envisaged that if nNOS inhibitory activity was observed with this family of compounds, the chiral centre would be re-introduced to determine its effect on activity. It was hoped that the inclusion of HB donors close to both aromatic rings would allow the compounds to bind into the active site in a variety of poses. The HB donor beside either ring could form interactions with Glu597 or Asp602, while the adjacent aromatic ring would pi stack with the nNOS heme moiety. The other aromatic ring could then stretch to interact with Tyr711, facilitating the formation of a HB between the donor and the heme propionate groups, as is often observed for the aminopyridine class of inhibitors (See chapter one, section 1.4).

These proposed structures were re docked into the 4DN1 binding site, and received Chemgauss4 scores of 15.6342, 15.0324, 14.8652 and 14.6398 respectively (94-97). These were lower scores than was observed for the parent compound (85, 15.705), however they were still sufficiently high to make their synthesis and testing a worthwhile exercise.

2.10 Mixed arginine/diaminopyridine compounds

As outlined in chapter one, section 1.4.4, the two main classes of inhibitors for nNOS at this time are modified arginines and substituted aminopyridines. It was hypothesised that combining of both arginines and aminopyridine motifs into a single structure may generate a novel human nNOS inhibitor. Modified arginines, such as L-NNA, attempt to mimic the interactions of the natural substrate, L-arginine with the nNOS binding site. These include HB interactions with Trp592 and Glu597 and as well as water mediated HB interactions with the heme propionate.⁸³ The guanidinium group of L-arginine is also capable of forming π stacking interactions with aromatic systems such as the heme porphoryin ring.

The substituted diaminopyridine group is capable of interacting with the nNOS binding site in two ways. The first being through π stacking with the heme ring, and formation of HBs with the Glu597 and Asp602 residues located below the ring. The second interaction that these motifs can form is with the Tyr711 residue via π stacking and with the heme propionate via HBing.⁵⁵ Compounds with two substituted aminopyridine moieties can form both of these interaction types at once.⁵⁴

As of yet, no “mixed” modified arginine and diaminopyridine structures have been attempted for synthesis or biological evaluation. It was envisaged that a mixed compound could be capable of forming the arginine type interactions, as well as the aminopyridine type interactions with the human nNOS binding site, perhaps resulting in a potent nNOS inhibitor. The synthesis of one such structure, **98**, was attempted and is shown in **Figure 2.25**. The compound was docked into the 4DN1 binding site to verify the predicted binding pose. This is shown in **Figure 2.26**.

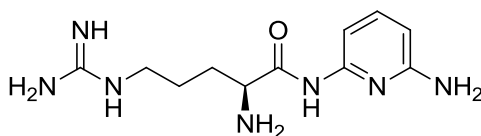


Figure 2.25. Mixed arginine/diaminopyridine, **98**.

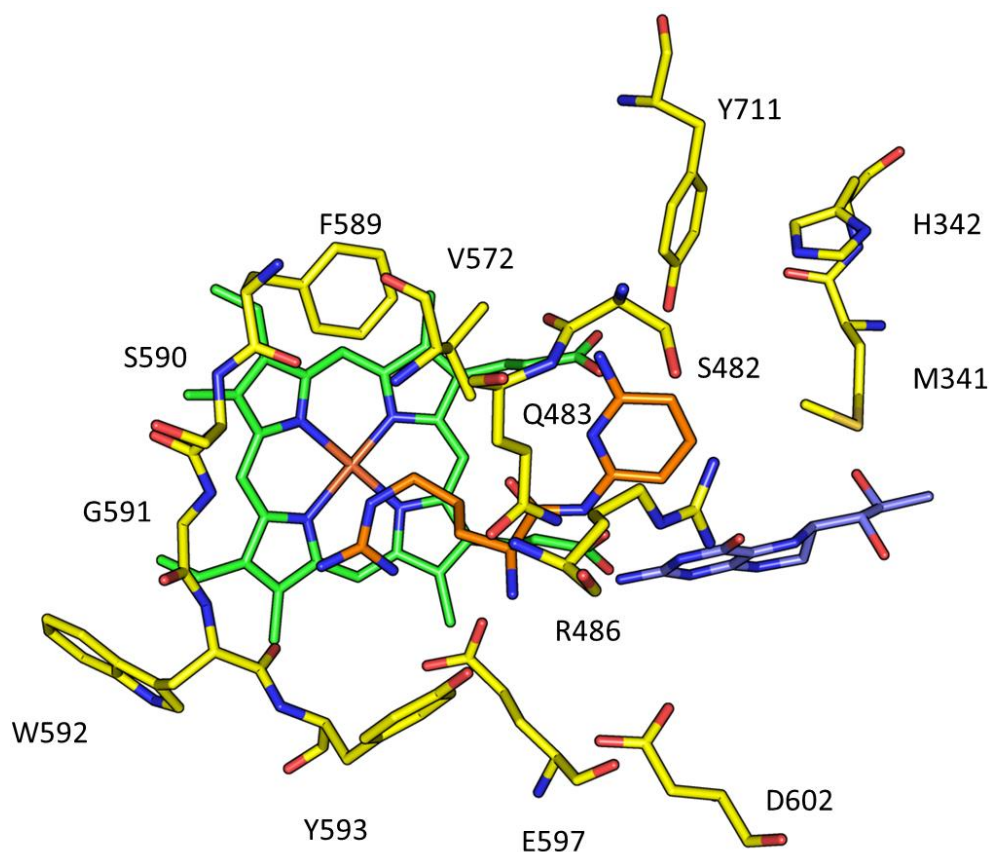


Figure 2.26. Predicted binding mode of **98** in the human nNOS crystal structure. Binding site residues in yellow, heme in green, BH₄ in blue and ligand in orange.

The guanidinium group of **98** was positioned close to the heme moiety, mimicking the binding of the L-arginine substrate. HB interactions were observed between the guanidinium nitrogens and the Glu597, Trp592 and Ser482. The aminopyridine moved towards the Tyr711 and formed HB interactions with the heme propionate as expected. Although, in this prediction, the Tyr711 is not orientated to form a π stacking interaction with the aminopyridine, it is possible that this residue would rotate to facilitate this type of interaction. This has been previously observed in aminopyridine based inhibitors, (see chapter, one section 1.4).⁵² It was hoped, therefore, that **94** would be capable of binding to the human nNOS binding site, and would elicit an inhibitory response.

2.11 Conclusion

Following the general theme of this work, these computational studies have focused on the human isoforms of the NOS enzymes by development of a human nNOS homology model based on a rat nNOS template. A key residue difference of Leu337 (rat) versus His342 (human) was incorporated into the model. Also noted was a difference in rotameric state of Asp602 in the homology model. The model performed well with structural validation testing, and achieved an acceptable ROC score of 0.79 when analysed with a test set containing nNOS inhibitors and decoy compounds. The binding pose of the template's co-crystallized ligand was also successfully reproduced with the model. The data suggests that a robust human nNOS homology model was developed. Docking was conducted with the Maybridge and Zinc commercial databases, which generated a list of compounds for biological evaluation in the nNOS inhibition assay.

A pharmacophore was also developed for nNOS. This was generated utilising compounds from the ChEMBL database, as well as from experimentally tested compounds from the homology model screen. The first pharmacophore scored well when tested with a validation set, achieving a ROC score of 0.805. Commercial datasets were screened against this model and a hit list generated. Some of the best ranking compounds were biologically evaluated.

The pharmacophoric model was then refined, using experimental data from biological evaluations, to generate a second model. This was again validated and commercial datasets screened to yield a third hit list for biological screening.

The first human nNOS crystal structure was reported in 2015.⁸³ The arginine binding site of the homology model was compared to the crystallized binding site and the two were found to be in close agreement. However, different rotameric states were observed in the Tyr711 and Asp602 residues, which may have affected the interactions of potential inhibitors. The crystal structure was validated and screened to give a 4th list of compounds for biological testing.

A *de novo* scaffold was also designed based on the literature precedent of modified arginines and aminopyridines as nNOS inhibitors. This was seen to dock well into the crystal structure binding pocket, forming the expected interactions such as a HB with E597.

A number of potential nNOS inhibitors had been identified using an array of computational methods. This approach to nNOS inhibitor design is not utilised in the literature, with the current trends for nNOS inhibition favouring modification of two major known scaffolds (modified arginines and modified aminopyridines). With these potential nNOS inhibitors identified, the next step in the process was to synthesize the promising inhibitor candidates. The results of this work are presented in the following chapter.

3 Synthesis of Computational Hit Compounds

3.1 Introduction

Several of the potential human nNOS inhibitors identified through the computational studies needed to be synthesised, while others could be purchased directly. The synthetic approaches employed will be discussed in this chapter.

3.2 Classes of inhibitory compounds and their synthesis

3.2.1 Piperazine containing compounds

3.2.1.1 Synthesis of 41

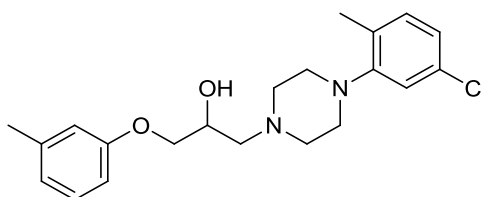
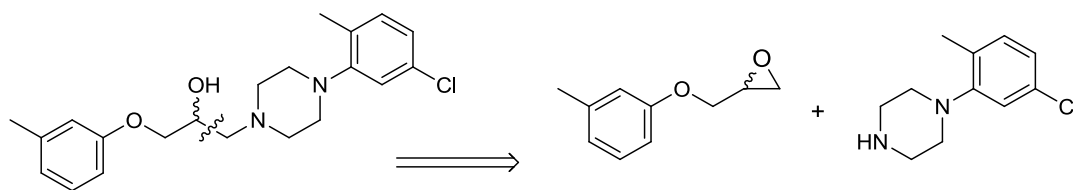


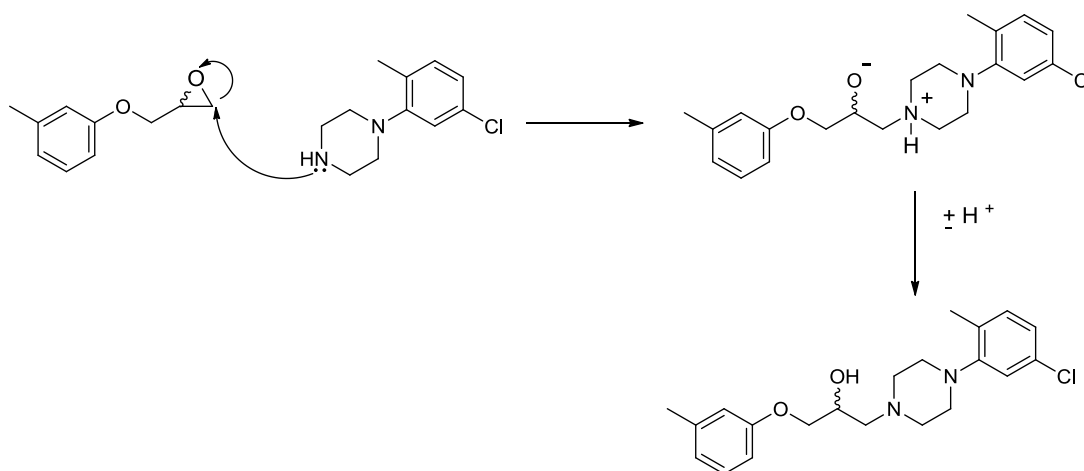
Figure 3.1. Structure of **41**.

The compound (**Figure 3.1**) was identified from initial screens of the nNOS homology model with the Zinc database, (chapter two, section 2.6.1). Both enantiomers were ranked top of the hit list in this screen, but neither were commercially available. The synthesis of the racemic product was conducted based on the retrosynthetic plan illustrated in **Scheme 3.1**. It was envisaged that the target compound could be synthesised in a single step from the commercially available epoxide and aryl piperazine **Scheme 3.2**. This strategy would exploit nucleophilic attack by the aryl piperazine and epoxide ring opening to give **41**.



Scheme 3.1. Retrosynthetic plan for **41**.

The procedure for the forward reaction was based on a previous literature report, which utilised a similar epoxide and piperazine system.⁸⁵ The two reagents were reacted neat in a 1:1 ratio with no base added. A mechanism for the forward reaction is shown in **Scheme 3.2**.



Scheme 3.2. Forward reaction for **41**.

The protonated piperazine attacks the epoxide at the less sterically hindered site, opening the ring to generate the intermediate. Subsequent protonation of the anionic oxygen, and deprotonation of the cationic piperazine nitrogen generated the product as shown. The product, purified by column chromatography, was obtained in 56% yield. Using NMR, mass spectrometry and IR spectroscopy **41** was characterised.

3.2.1.2 Structural characterisation of 41

The structure of **41** with numbered protons and carbons is provided in **Figure 3.2**.

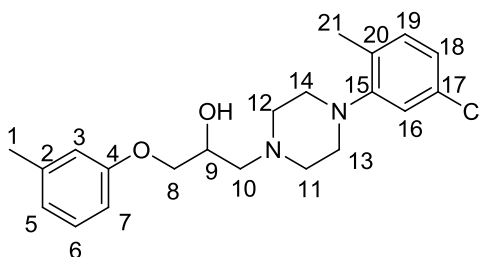


Figure 3.2. **41** with numbered protons and carbons.

The full ^1H NMR spectrum of AC001 is shown in **Figure 3.3** and an expansion of the aromatic region signals is shown in **Figure 3.4**. There are four clear aromatic signals, a triplet at 7.18 ppm (1H), an unsymmetrical doublet at 7.09 ppm (1H), a multiplet from 6.99-6.95 ppm (2H) and another multiplet from 6.80-6.74 ppm (3H).

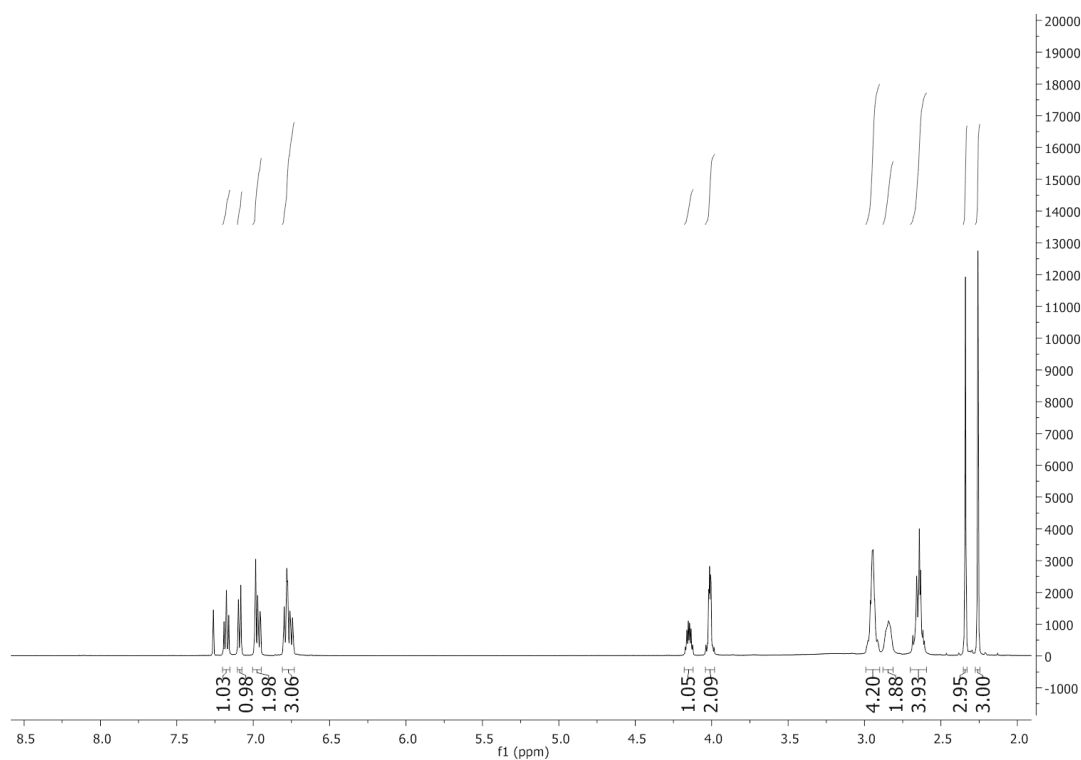


Figure 3.3. Full ^1H spectrum of AC001.

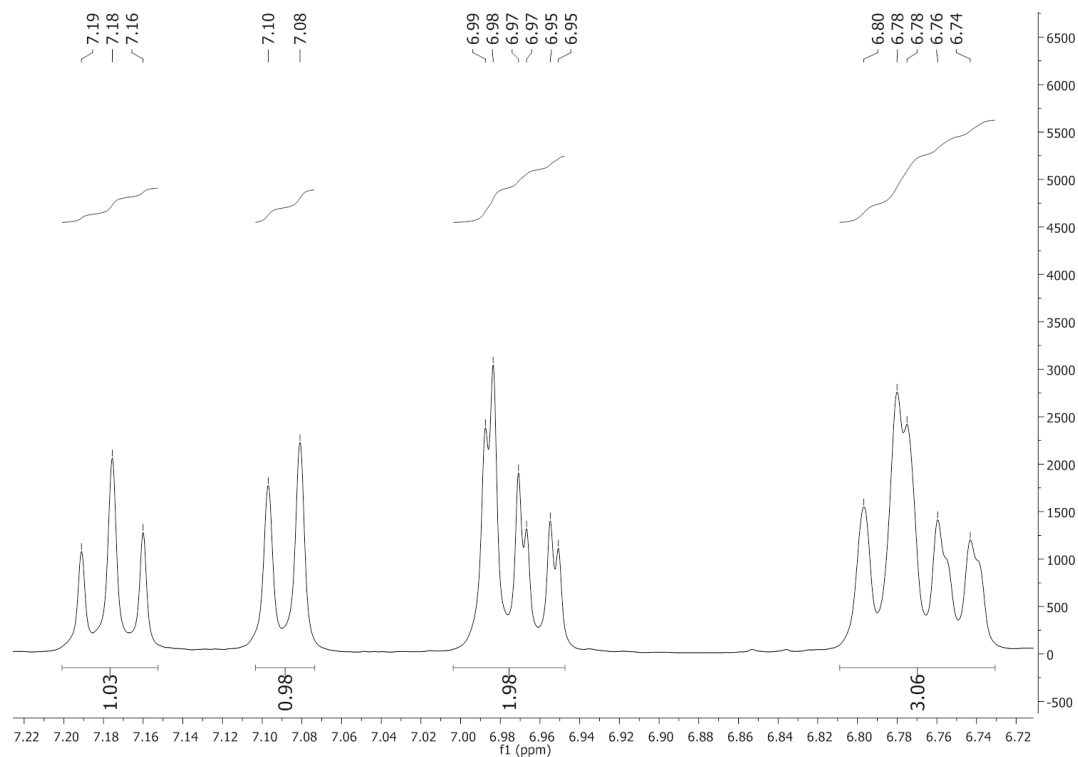


Figure 3.4. Aromatic proton signals of AC001.

The four aromatic signals can be considered as two separate spin systems, as evidenced by the COSY spectrum (**Figure 3.5**). One spin system is made up of H3, H5, H6 and H7 while the other is comprised of H16, H18 and H19.

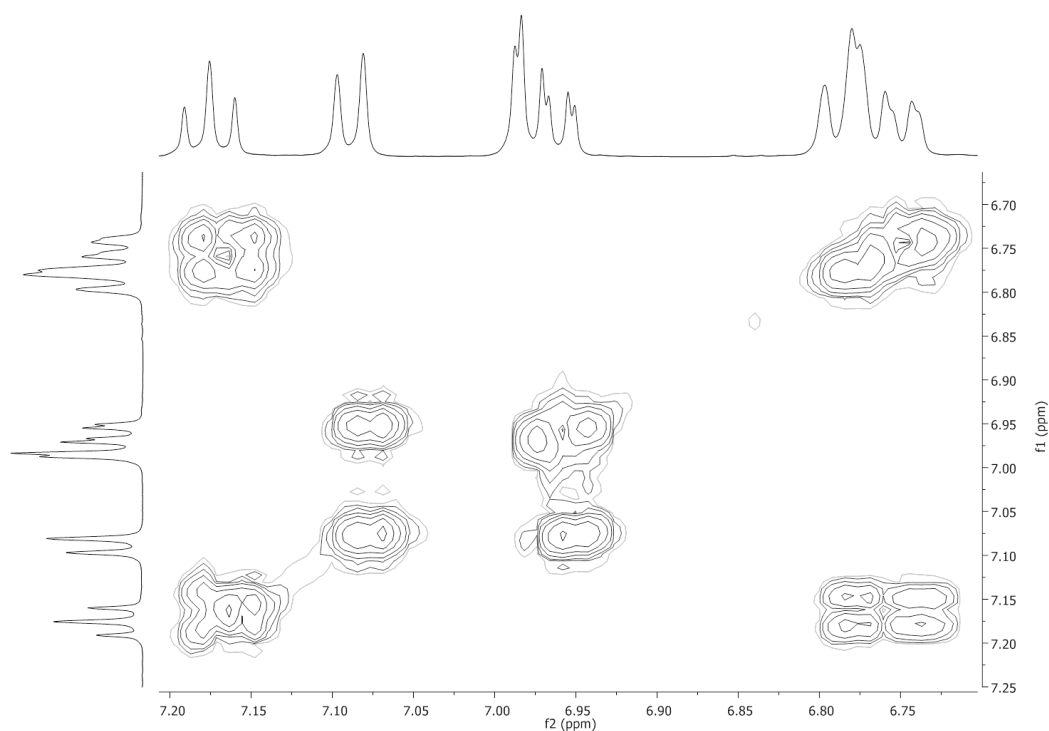


Figure 3.5. COSY spectrum of AC001, expansion of aromatic region

The first spin system involves the signal at 7.18 ppm (1H) and the broader signal at 6.80-6.74 ppm (3H). The second system involves the signal at 7.09 ppm (1H) and the signal at 6.99-6.95 ppm (2H). To assign the peak at 7.18 ppm the resonance contributors of each aromatic ring were examined to predict which protons were the most deshielded, (**Figure 3.6**).

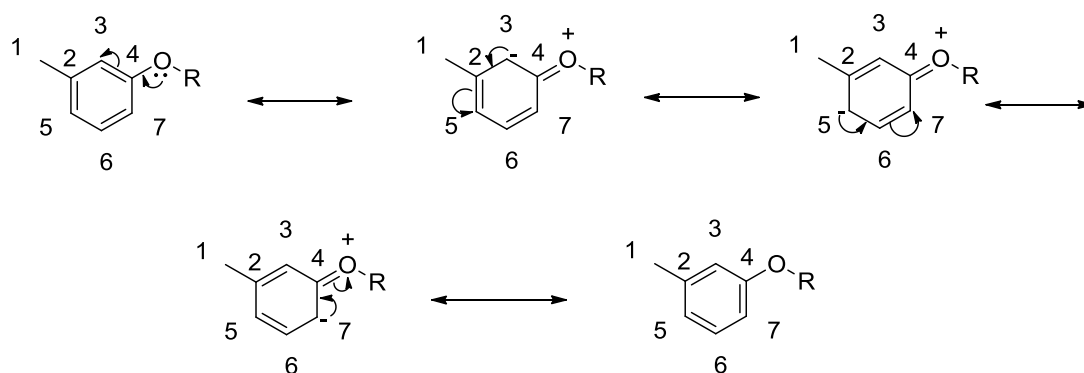


Figure 3.6. Resonance contributors of the ether substituted aromatic ring.

None of the resonance contributors carry a negative charge on C6, where as a negative charge can be found on C3, C5 and C7. Therefore H6 is the most deshielded as it has the lowest electron density, and will appear the most downfield of H3, H5, H6 and H7. Based on the first order approximation of signal splitting H6 could be expected to appear as a doublet of doublets, as it is split by the inequivalent protons H5 and H7. However, the difference in the coupling constants of H5 and H7 is small. Therefore, while the signal for H6 is expected to be a doublet of doublets (see splitting tree **Figure 3.7**), it may instead appear as an apparent triplet. The signal at 7.18 ppm appears as an apparent triplet supporting its assignment as H6.

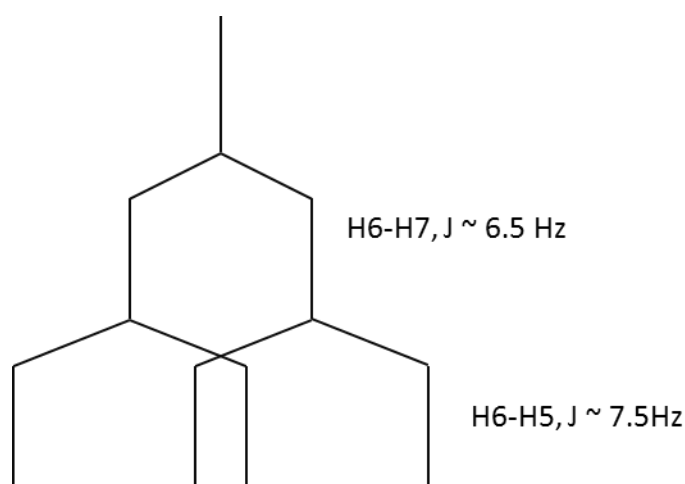


Figure 3.7. First order approximation splitting tree for H6.

From the COSY spectrum (**Figure 3.5**), it is clear that the H6 signal is in the same spin system as the signal integrating for three at 6.80-6.74 ppm. These three protons are therefore assigned as H3, H5 and H7, all appearing as one overlapping signal. All are shielded by the electron donating effect of the ether group and adopt similar chemical shifts. It is not possible to distinguish between these protons.

For the second aromatic ring several possible resonance contributors can be drawn due to electron delocalisation from the piperazine or the chlorine atom. These structures are shown in **Figure 3.8** and **Figure 3.9**.

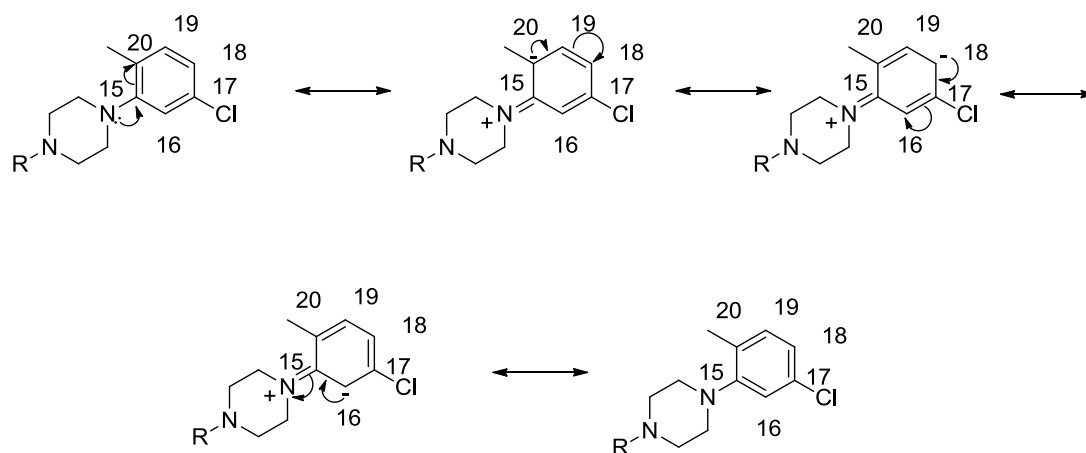


Figure 3.8. Resonance contributors, delocalisation of the piperazine ring nitrogen lone pair.

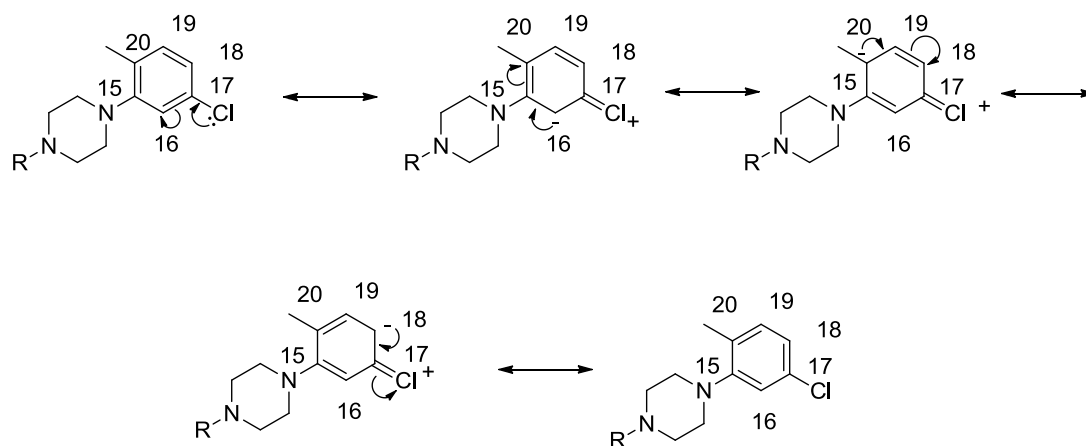


Figure 3.9. Resonance contributors from the delocalisation of the chlorine lone pair.

None of the resonance contributors place a negative charge on C19 and hence the most deshielded proton in this spin system is H19. H19 is expected to appear as a doublet, split by the neighbouring H18. Of the remaining aromatic proton signals, the one appearing at 7.09 ppm appears as a doublet and integrates for one proton. This signal is therefore assigned to H19.

Two aromatic protons remain to be assigned, H16 and H18. In the COSY spectrum it can be seen that the H19 signal (7.09 ppm) couples to the multiplet signal integrating for two at 6.99-6.95 ppm. This signal is therefore assigned to H16 and H18, appearing as one overlapping signal.

The next two proton signals appear at 4.16-4.14 ppm (1H) and 4.02-4.00 ppm (2H) (^1H NMR spectrum expansion in **Figure 3.10** and COSY spectrum expansion in **Figure 3.11**).

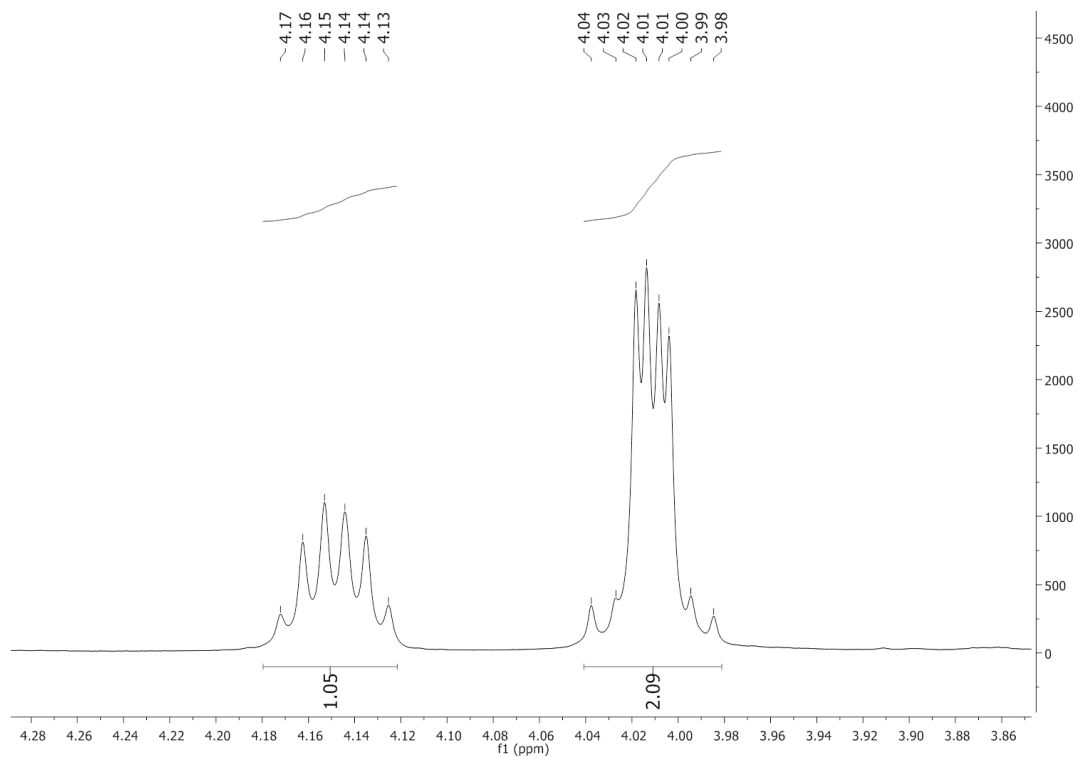


Figure 3.10. Expanded image of 4.35-3.90 ppm region of AC001 ^1H NMR spectrum.

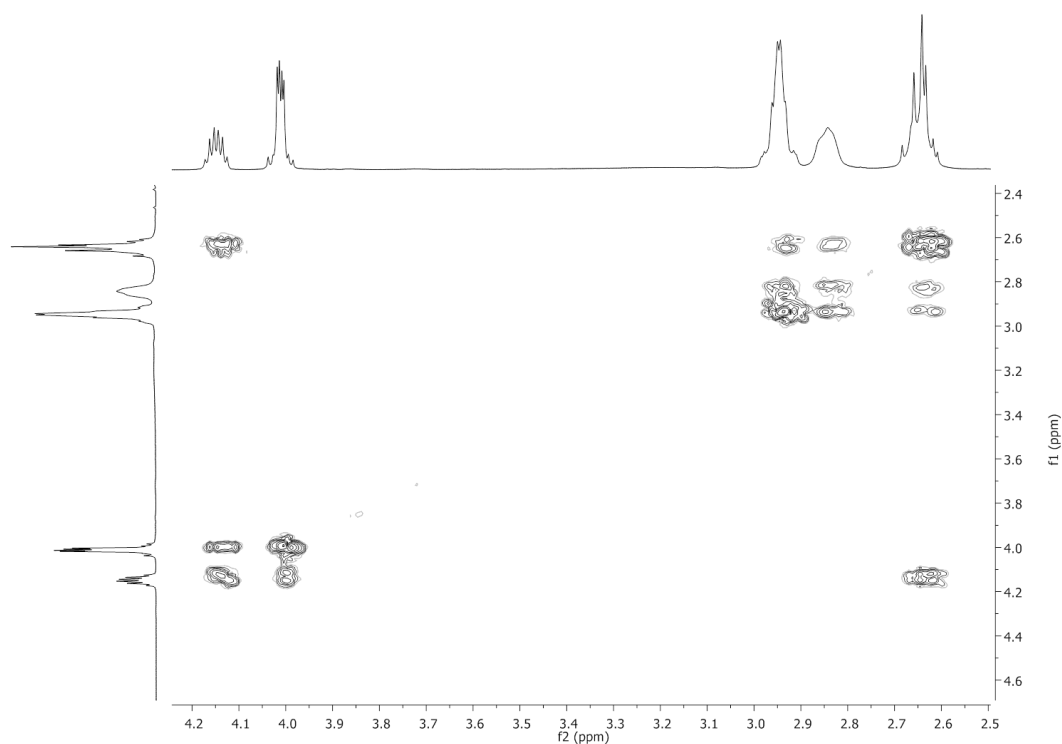


Figure 3.11. Expanded image of 4.18-2.50 ppm region in AC001 COSY spectrum.

The multiplet centred at 4.15 ppm integrates for a single proton and is heavily split. The proton on the chiral centre, H9, is a likely candidate for this signal. Due to the chiral centre, the protons at C8 and C10 are diastereotopic and will all split H9 independently. H9 may also be split by the alcohol proton. The small differences in the diastereotopic protons results in a difference in coupling constants with H9, hence the observed heavy splitting pattern.

H9 is coupled to the multiplet at 4.02-4.00 ppm and to the multiplet at 2.66-2.62 ppm. The multiplet at 4.02-4.00 ppm is assigned as the two H8s, which are deshielded by the adjacent ether oxygen. The splitting for this signal is again complex as the diastereotopic protons split each other via geminal coupling, and both are split separately by H9. Two separate doublet of doublets would be expected (**Figure 3.12**), however an overlapping multiplet is observed.

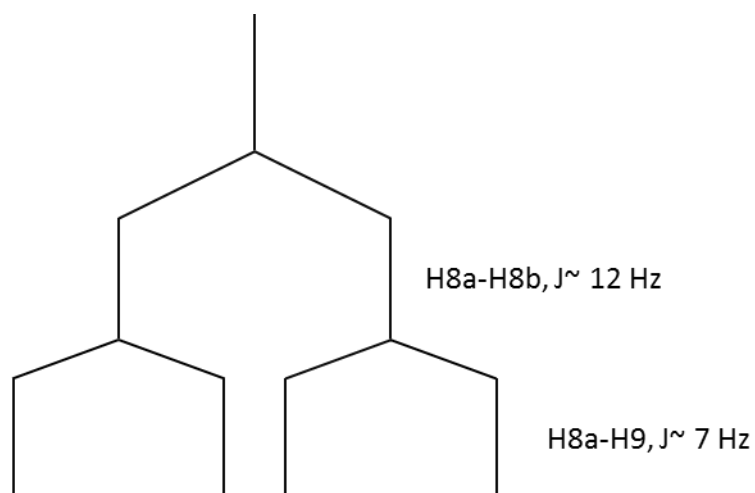


Figure 3.12. Splitting tree for one of the diastereotopic H8 protons.

The next three signals appear between 3.00 ppm and 2.60 ppm (**Figure 3.13**). These account for the piperazine (H11-H14) and H10 adjacent to the piperazine ring. Based on the integrations, the simplest assignment would appear to be that H11 and H12 account for one of the signals integrating for four, H13 and H14 account for the other signal integrating for four, and H10 accounts for the signal integrating for two. However, examination of the COSY spectrum shows this is not the case (**Figure 3.14**), as all three signals are coupled together. The piperazine protons H13 and H14 are too far removed from H10 to couple to it (5 bonds), so the simple assignment is incorrect.

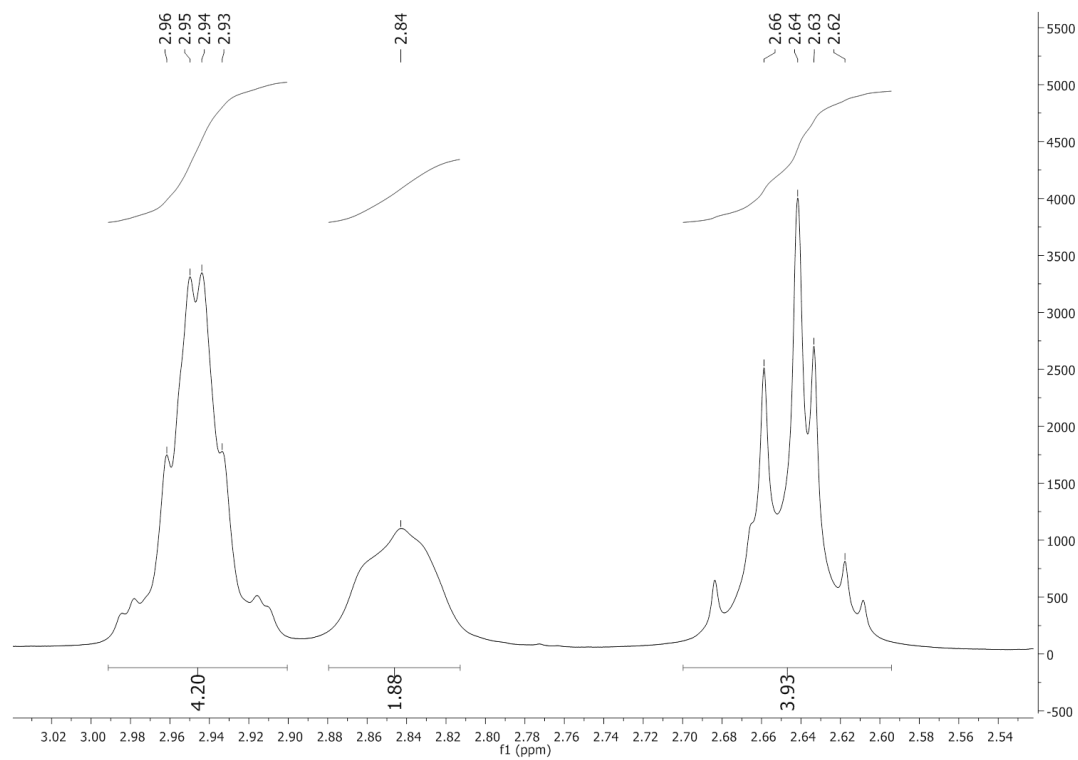


Figure 3.13. Expanded view of the 3.15 ppm to 2.50 ppm region of the ^1H NMR spectrum.

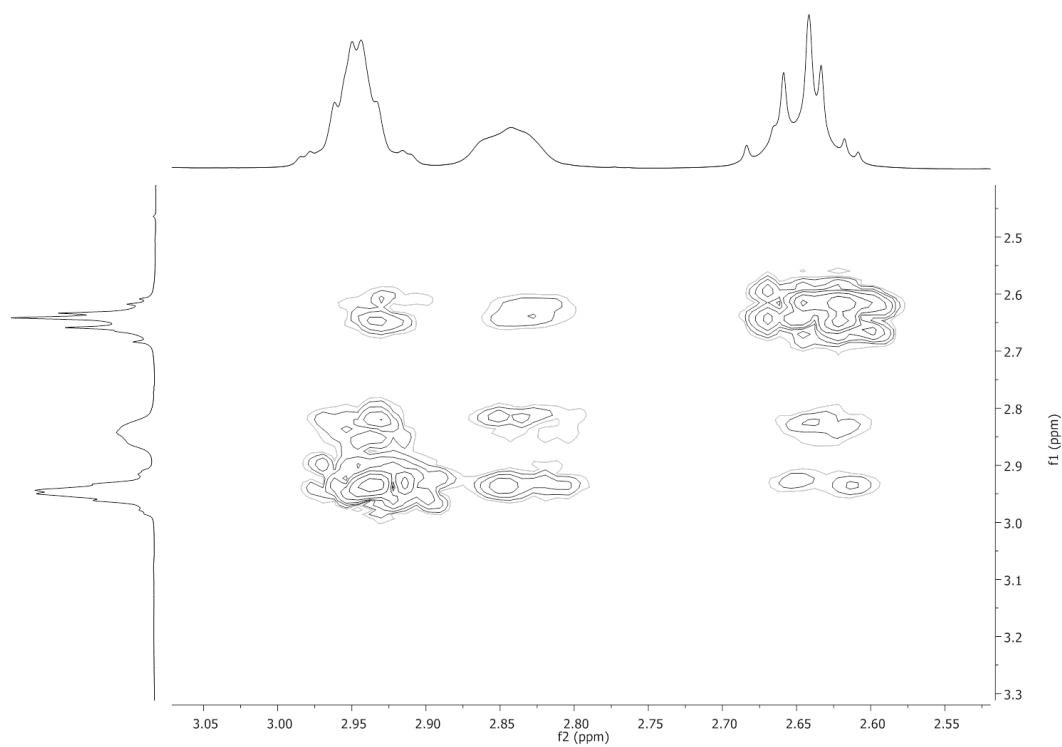


Figure 3.14. COSY spectrum of the 3.05 ppm to 2.55 ppm region.

In order to assign the ^1H NMR signals in this region of the spectrum the piperazine ring was considered to be in a locked chair confirmation as shown in **Figure 3.15**.

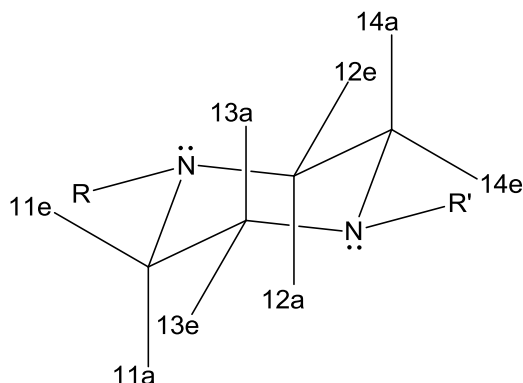


Figure 3.15. Piperazine ring with axial and equatorial protons shown. The R substituent represents the alcohol substituted carbon chain, and R' is the disubstituted aromatic ring. a = axial, e = equatorial.

The signals for H13a/H13e and H14a/H14e are overlapping at 2.95 ppm, integrating to 4H. These protons are more deshielded than H11a/H11e and H12a/H12e as the nitrogen adjacent to H13a/H13e and H14a/H14e can donate electron density into the neighbouring aromatic ring, resulting in a partial positive charge on the nitrogen atom. Electron density is therefore withdrawn from the H13 and H14, resulting in a higher chemical shift for these protons.

It is proposed that the ^1H signal for H11e and H12e occurs at 2.84 ppm, integrating for 2H. This signal couples to the signal for H13a/H13e and H14a/H14e (2.95 ppm) in the COSY as expected (**Figure 3.14**). We suggest that H11a and H12a are more shielded than H11e and H12e, perhaps due to a partial anomeric type effect from the nitrogen lone pair. We therefore assign H11a and H12a to the signal at 2.64 ppm. This signal couples to the signal for H11e/H12e at 2.84 ppm as expected. The signal at 2.64 ppm integrates for four protons. We therefore consider this signal to consist of the two H10 protons, as well as H11a and H12a protons. The signal at 2.64 ppm also couples to H9 (4.15 ppm) in the COSY spectrum (**Figure 3.11**), as would be expected for H10.

This assignment is strengthened by the fact that in the HSQC, the signals at 2.84 ppm (H11e/H12e) and 2.64 ppm (H11a/H12a) couple to the same equivalent ^{13}C signal (53.7 ppm), indicating that the protons are bonded to the same carbon, C11/C12 (**Figure 3.16**). The HSQC also shows the signal at 2.64 ppm (H10) couples to the ^{13}C signal at 60.7 ppm (C10).

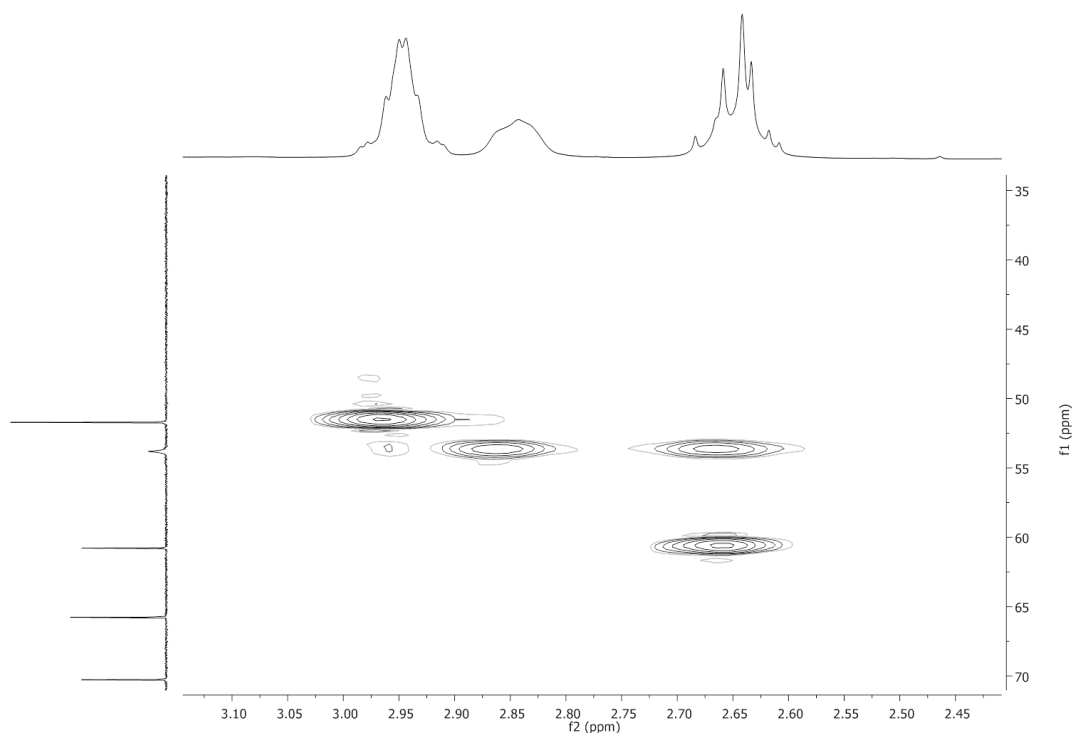


Figure 3.16. HSQC showing the protons in the signal at 2.64 ppm and 2.84 ppm couple to the same carbon signal at 53.7 ppm.

The two remaining proton signals in the ^1H NMR account for the two methyl groups, H1 and H21 (**Figure 3.17**). Using the HMBC it can be seen that the two methyl proton signals couple to separate aromatic spin systems. This is expected as C1 is part of one aromatic spin system, while C21 is part of the other.

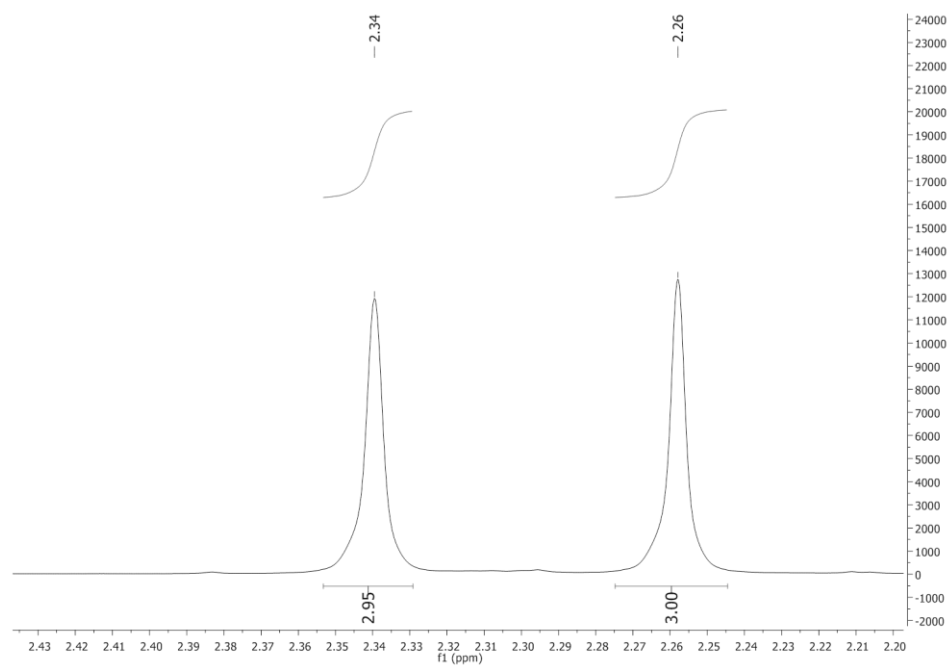


Figure 3.17. Methyl proton signals of AC001 ^1H NMR spectrum.

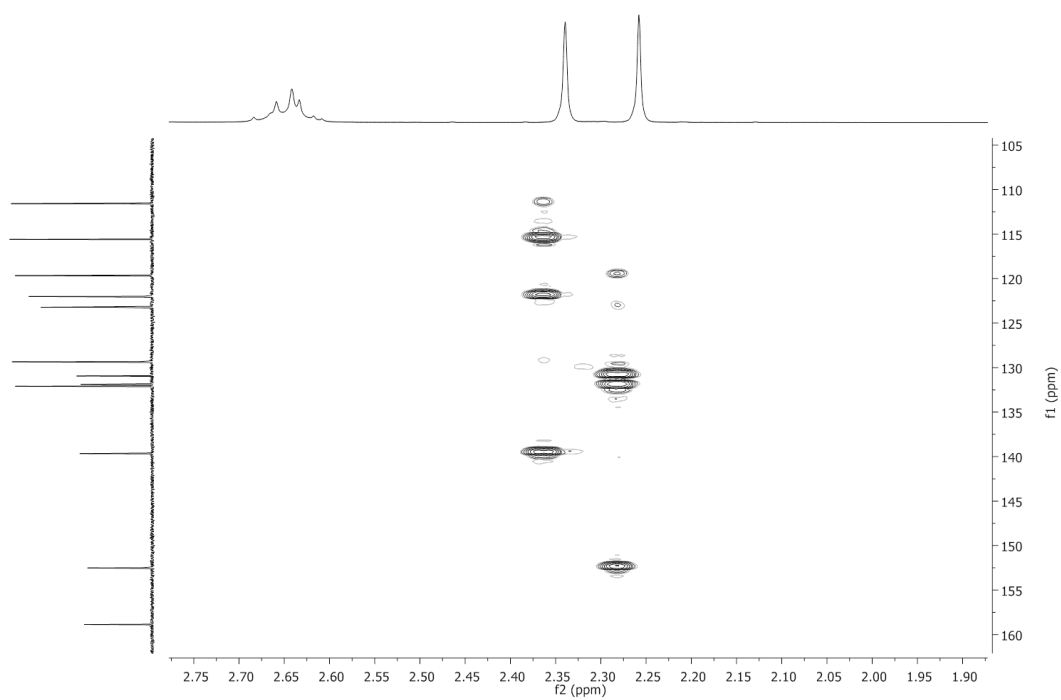


Figure 3.18. HMBC expansion of the alkyl region.

As H6 (7.17 ppm) had been well characterised and identified in the proton spectrum analysis it was used as a reference to assign the methyl proton signals. The HSQC identifies C6 as the signal at 139.8 ppm, coupling to H6 (7.18 ppm). In the HMBC a clear coupling can be seen between the carbon signal at 139.8 ppm (C6) and the more deshielded of the two methyl signals (2.34 ppm). It is suggested that H6 and the methyl protons at 2.34 ppm are bonded to the same aromatic ring. Therefore the signal at 2.34 ppm was assigned as the H1 methyl protons, leaving the signal at 2.26 ppm to account for the H21 protons.

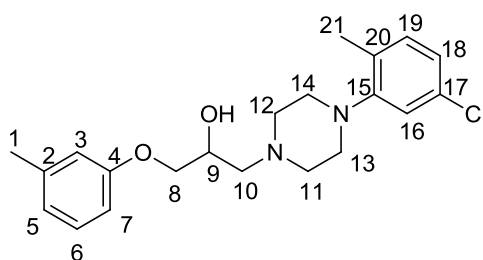


Figure 3.19. AC001 with numbered protons and carbons.

A full carbon spectrum for AC001 is shown in **Figure 3.20**. The quaternary carbon signals were first to be assigned. Using an overlaid ^{13}C and DEPT135 spectra (**Figure 3.21**) the quaternary carbons were identified as the signals at 158.9 ppm, 152.5 ppm, 139.7 ppm, 131.9 ppm and 130.9 ppm.

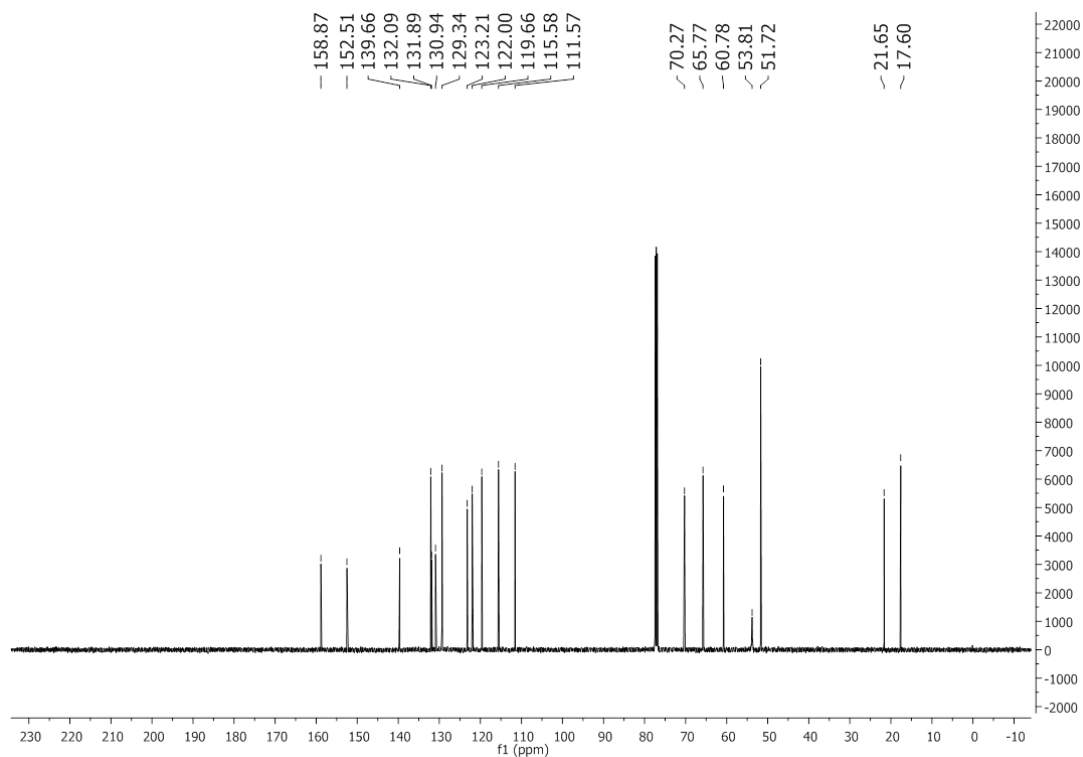


Figure 3.20. Full ^{13}C NMR spectrum of AC001.

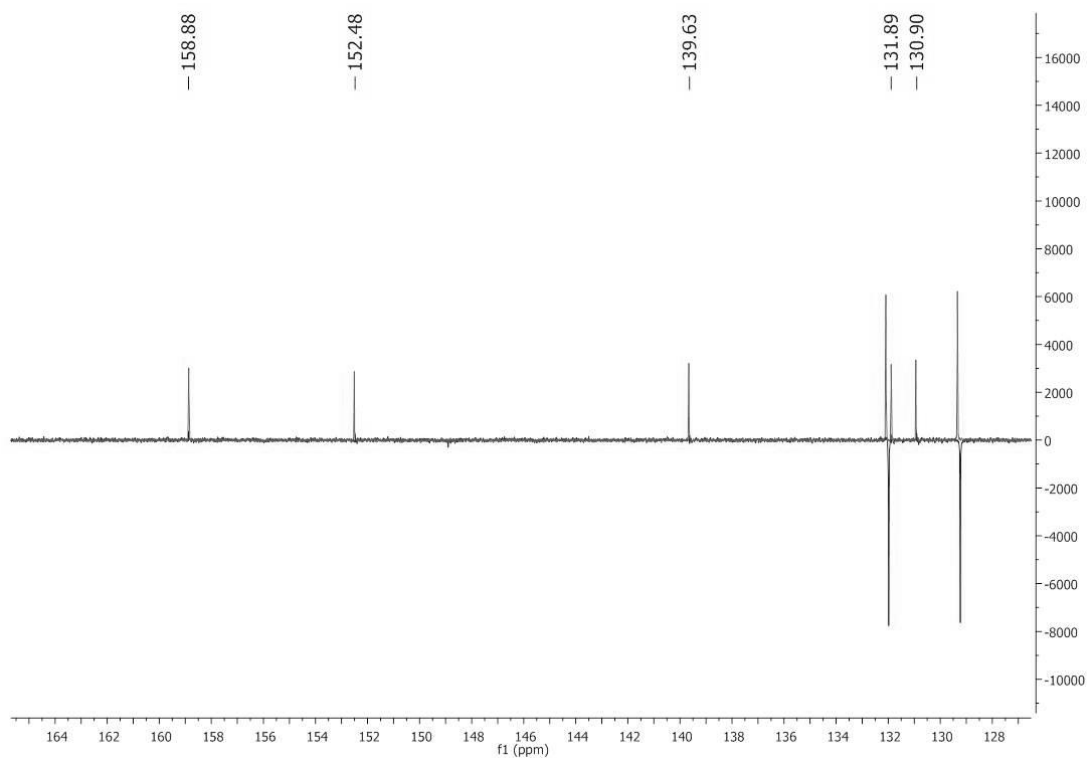


Figure 3.21. Overlaid DEPT135 spectrum and ^{13}C NMR spectrum

The most deshielded quaternary carbon is C4. It is adjacent to an electronegative oxygen that withdraws electron density from C4 via induction. This oxygen also donates electron density into the aromatic ring via resonance. This results in a partial positive charge on the oxygen which will further withdraw electron density from C4. The signal at 158.9 ppm is assigned to C4.

The next most deshielded carbon is C15. This is the aromatic carbon adjacent to the piperazine ring. Delocalisation of the piperazine nitrogen lone pair into the aromatic ring, results in a partial positive charge on the nitrogen and a deshielding of C15. The signal at 152.5 ppm is assigned to C15.

Using the HMBC, it is suggested that the carbon signal at 139.6 ppm is part of the disubstituted aromatic spin system. This signal is therefore assigned to C2, as it was the only remaining quaternary carbon in this spin system.

This leaves the assignment of C20 and C17 to the two quaternary signals at 131.9 ppm and 130.9 ppm. C20 has a partial negative charge due resonance contributions from the piperazine ring and the chloro group (**Figure 3.8** and **Figure 3.9**), where C17 does not experience this effect. C20 therefore is more shielded than C17 and is expected to appear at 130.9 ppm. The signal at 131.9 ppm is therefore assigned to C20.

C6, C8, C9 and C19 are identified by HSQC as the signals at 129.3 ppm, 70.3 ppm, 65.8 ppm and 132.1 ppm respectively. Individual identification of the aryl signals for C3, C5 and C7 is not possible. However, in the HSQC spectrum the overlapping H3, H5 and H7 ¹H signals couple to the ¹³C signals at 122.0 ppm, 115.6 ppm and 111.6 ppm. C18 and C16 were assigned to 123.2 ppm and 119.7 ppm. In the resonance hybrid representing this aromatic ring a partial negative charge is found on C18, shielding it. The C18 signal is therefore at 119.7 ppm, while C16 is at 123.2 ppm.

The methyl carbon signals were then assigned using the HSQC. The signal for H1 at 2.34 ppm is coupled to the carbon signal at 21.7 ppm. This is assigned to C1. Similarly, the signal for H21 is coupled to a carbon signal at 17.6 ppm. This represents C21 (**Figure 3.22**).

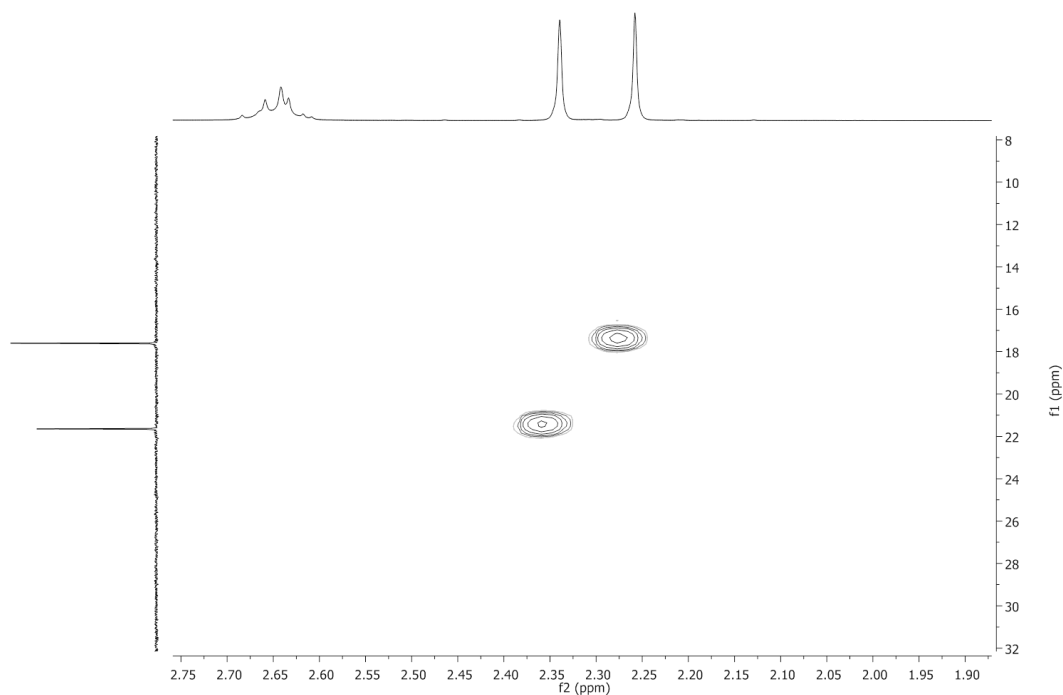


Figure 3.22. HSQC to identify methyl carbons.

The three remaining unassigned ¹³C signals appear at 51.7 ppm, 53.8 ppm and 60.8 ppm. H13 and H14 appear at 2.95 ppm, these couple to the carbon signal at 51.7 ppm in the HSQC. This is the C13/C14 signal. The proton signal at 2.86 ppm and 2.64 ppm are both caused by piperazine protons on carbons 11 and 12. Both of these proton signals couple to the carbon signal at 53.7 ppm in the HSQC, which we assign to C11/C12. The final carbon signal at 60.8 ppm is assigned to C10 which appears as a CH₂ in the DEPT135. This couples to the H10 ¹H NMR signal (2.64 ppm) in the HSQC.

3.2.1.3 Synthesis of 37-40

A set of piperazine containing compounds were synthesised based on a compound identified from the flexible docking of the Maybridge database into the human nNOS homology model (chapter two, section 2.6.1), (**Figure 3.23**).

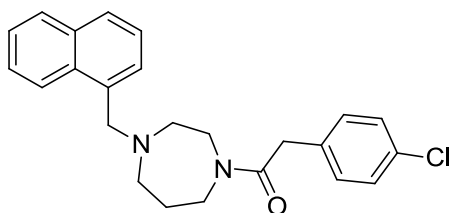


Figure 3.23. **34**, identified from the flexible dock of Maybridge with the nNOS homology model.

The compound appeared promising as it contained a naphthyl moiety and an aromatic chloro substituted ring. These could potentially form π stacking interactions with the heme moiety and the Tyr711 residue in the human nNOS binding site. The structure was also synthetically accessible and was not commercially available. Given the high rank of **34** (ranked 17) in the docked list, it was decided to synthesis several derivatives of this compound (**Figure 3.24**)

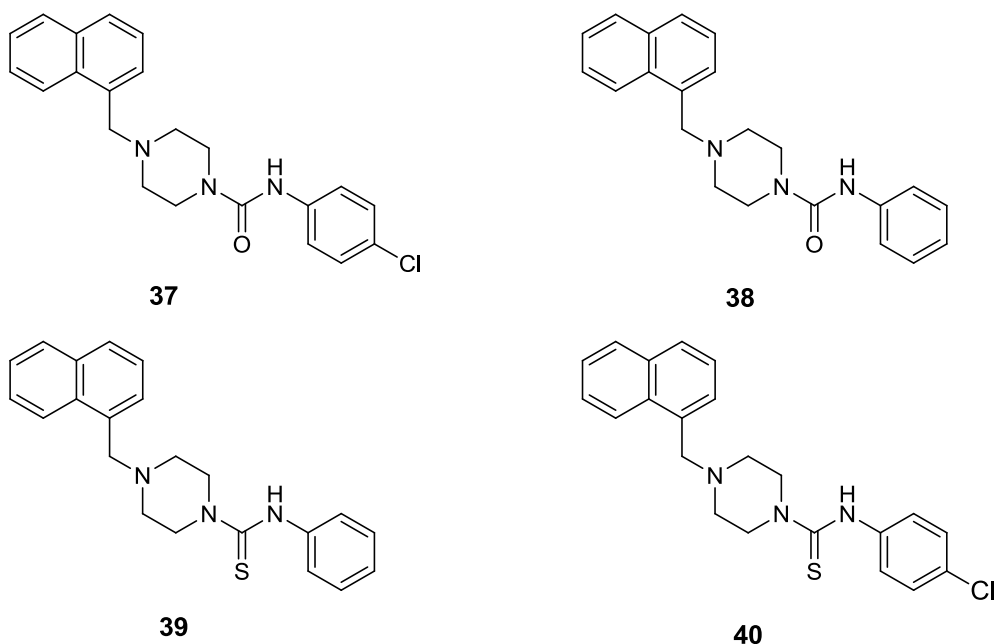
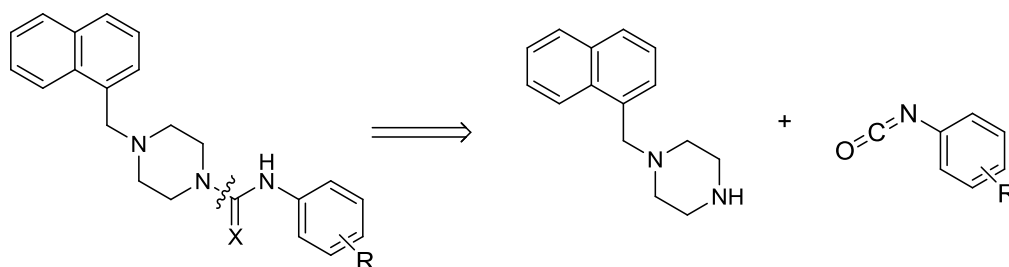


Figure 3.24. Derivatives of **34** which were chosen for synthesis, **37-40**.

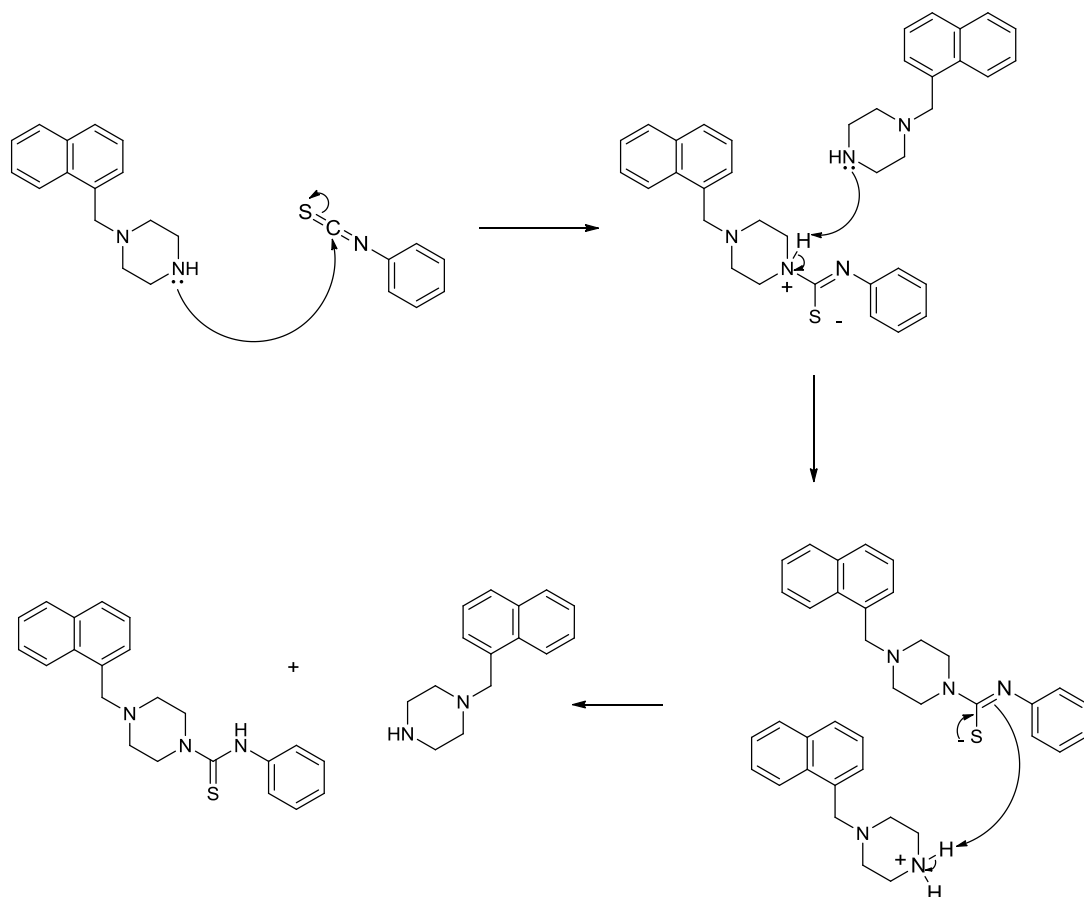
The core was modified to a six membered piperazine ring, rather than the seven membered ring found in **34**. This piperazine ring was more synthetically accessible than the seven membered ring. A secondary amine was added adjacent to the carbonyl group. It

was envisaged that this could act as a potential HB donor and interact with the acidic residues in the nNOS pocket (Glu597, Asp602). The inclusion of the amide also allowed for bond formation via well reported synthetic methodologies. The chlorine moiety from the screening hit was retained, and a version of the compound without the chlorine was synthesised to explore the importance of the substituent for activity. Finally, two derivatives were synthesised where the carbonyl oxygen was substituted with sulphur to examine the effect NH acidity may have on inhibitory activity. Thiourea groups are stronger acids than urea groups.⁸⁶ It is therefore expected that the sulphur containing derivatives would form stronger HB interactions with anionic species such as the Glu597 and Asp602 in the arginine binding site. The synthetic targets were docked into the arginine nNOS binding site, and received robust cDOCKER scores, thus validation this synthetic approach (discussed in chapter two, section 2.6.1). The retrosynthetic analysis for these compounds, **37-40**, is shown in **Scheme 3.3**.



Scheme 3.3. Retrosynthetic analysis of piperazine compounds, X = O, S ; R = *p*-Cl, H.

The isocyanate, isothiocyanate and the naphthyl substituted piperazine were commercially available. The forward reaction involved stirring the two reactants together in a 1:1 ratio in dry DCM under a flow of nitrogen, followed by purification via column chromatography. A proposed mechanism using **39** as an example is shown in **Scheme 3.4**.



Scheme 3.4. Proposed mechanism for the formation of **39**.

The formation of the thiourea moiety was facilitated by nucleophilic attack of the secondary piperazine nitrogen at the carbonyl carbon of the isothiocyanate. The resulting intermediate was deprotonated by a second piperazine species, followed by formation of the thiourea product. A similar mechanism is proposed when using the isocyanate in place of the isothiocyanate.

41 and the four synthetic derivatives of **34** were successfully synthesised in moderate to good yields. Interestingly, the chloro substituted derivatives of **34** were isolated in higher yields than the respective non-chloro substituted derivatives. This may be due to the inductive electron withdrawing ability of the chloro group, which may increase the electrophilic character of the isocyanate or isothiocyanate reaction centres. The yields obtained for **37**, **38**, **39** and **40** were 81%, 66%, 58% and 76% respectively.

3.2.1.4 Structural characterisation of 39

The structure of AC007 with numbered carbons and protons is shown in **Figure 3.25**.

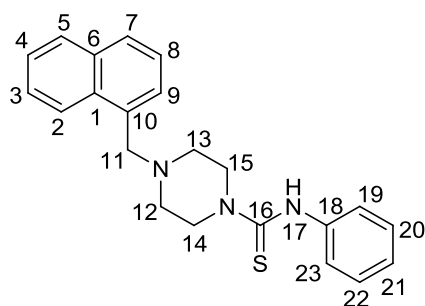


Figure 3.25. AC007 with numbered protons and carbons.

The full ^1H spectrum of AC007 is shown in **Figure 3.26**. An expanded view of the aromatic region of AC007 is shown in **Figure 3.27**, where the relative integrations in this region add up to 13 protons. AC007 has only 12 aromatic protons. The signal at 7.16 ppm (1H) does not couple to a carbon signal in the HSQC. This signal is also distinctively broad, and is therefore assigned as the NH proton, H17. All of the remaining signals shown in **Figure 3.27** are caused by protons on either the naphthyl group or on the phenyl ring.

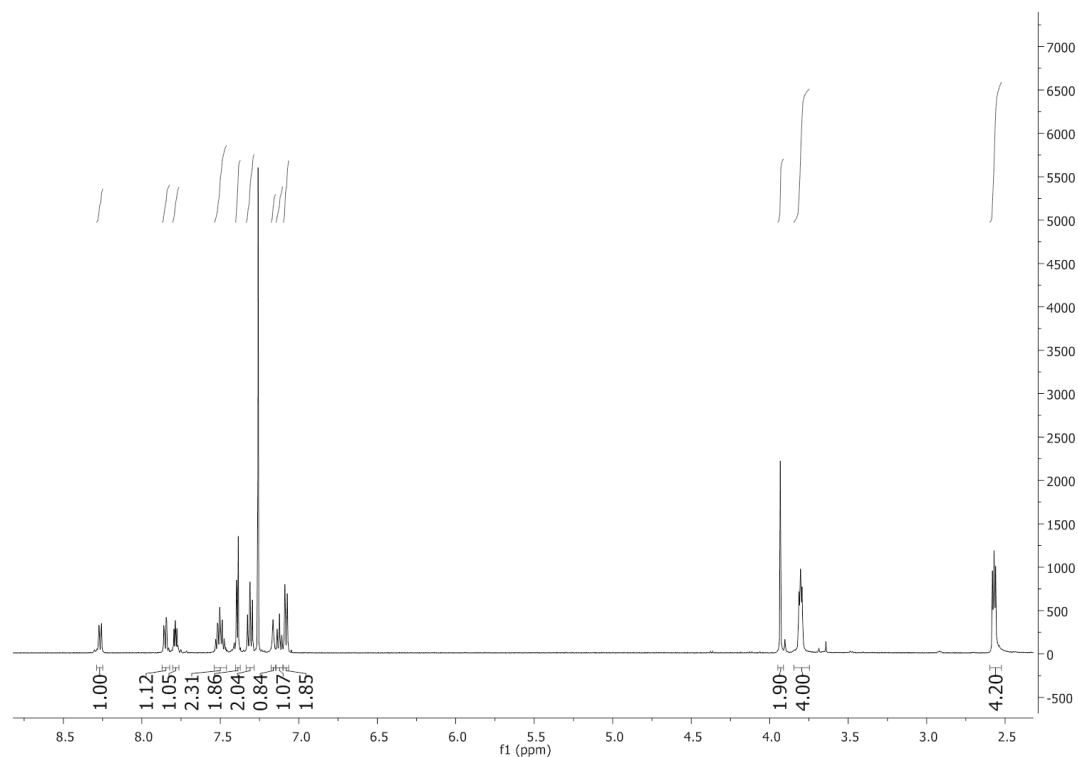


Figure 3.26. Full ^1H NMR spectrum of AC007.

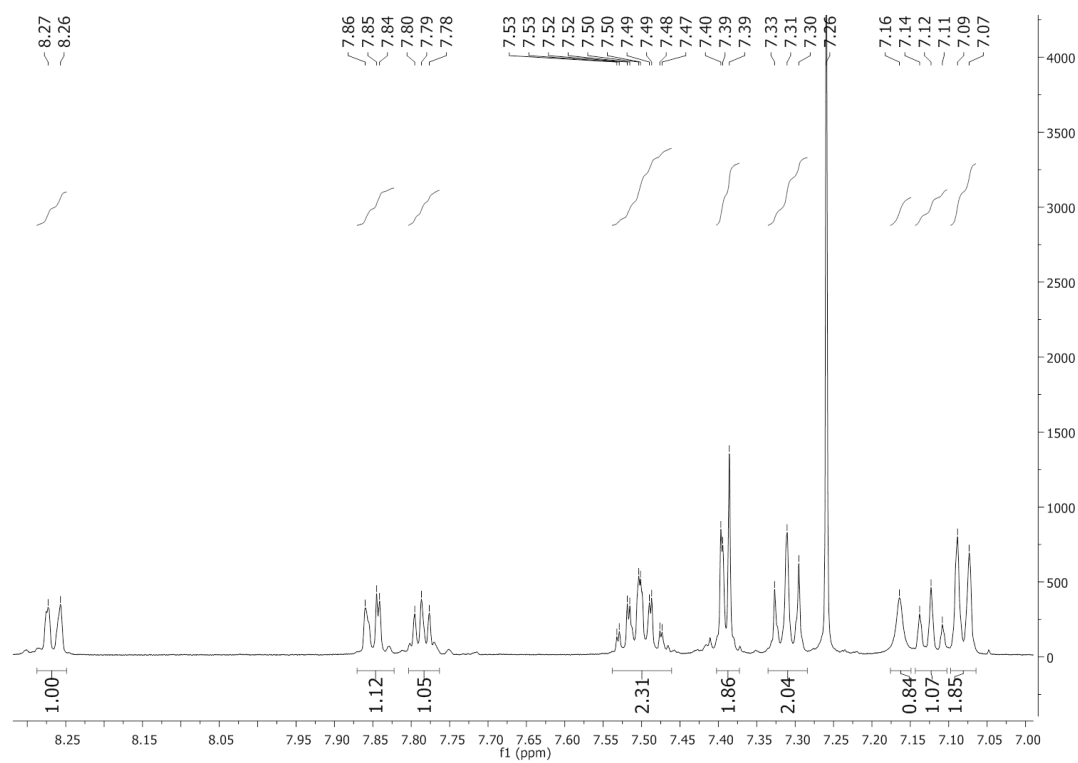


Figure 3.27. Expanded aromatic region of ^1H NMR spectrum of AC007.

Examination of the COSY spectrum (**Figure 3.28**) reveals two distinctive spin systems in the aromatic region, as expected due to the separation of the naphthyl and phenyl moieties.

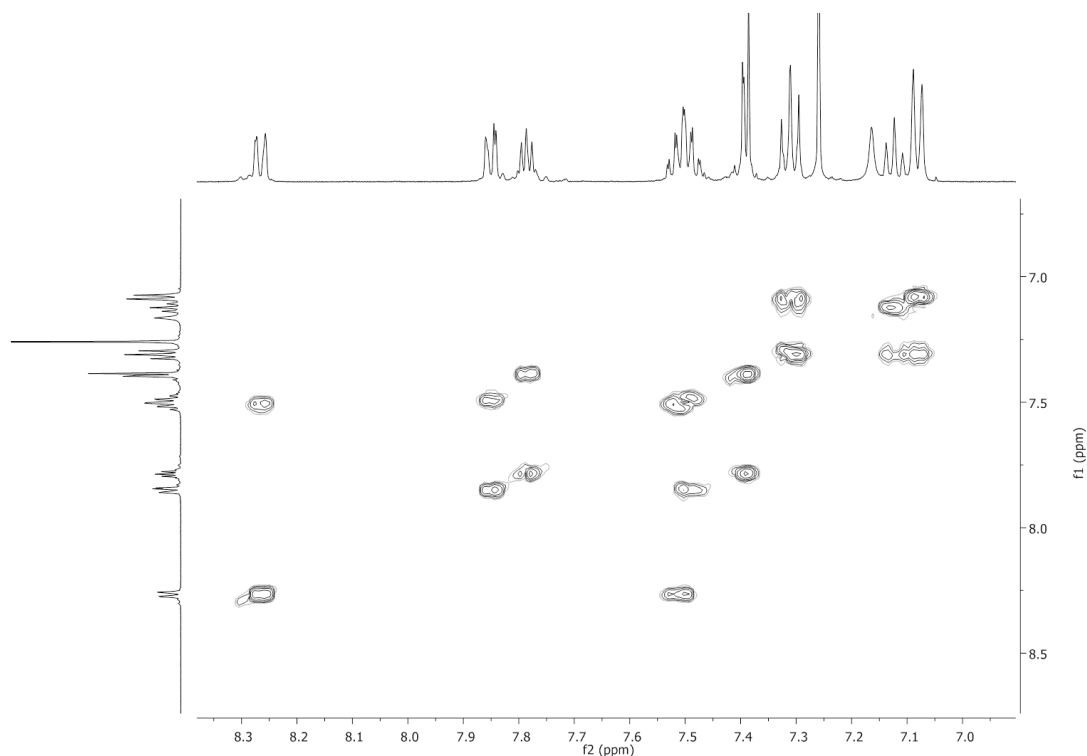


Figure 3.28. COSY spectrum of AC007, expansion of the aromatic region.

The signals at 7.08 ppm (2H), 7.12 ppm (1H) and 7.31 ppm (2H) couple to form one spin system, while the remaining signals form another, larger system. The larger system is expected to represent the naphthyl group, with the signals of the smaller system at 7.08 ppm, 7.12 ppm and 7.31 ppm attributed to H19-H23 of the phenyl ring.

Due to the monosubstitution pattern of the phenyl ring, it is expected that H19 and H23 are equivalent, and that H18 and H22 are equivalent. This leads to an assignment of H21 as the signal at 7.12 ppm, integrating for 1H. To distinguish between the signals for H19/H23 and H18/H22 the resonance contributors from the electron donating nitrogen were considered (**Figure 3.29**).

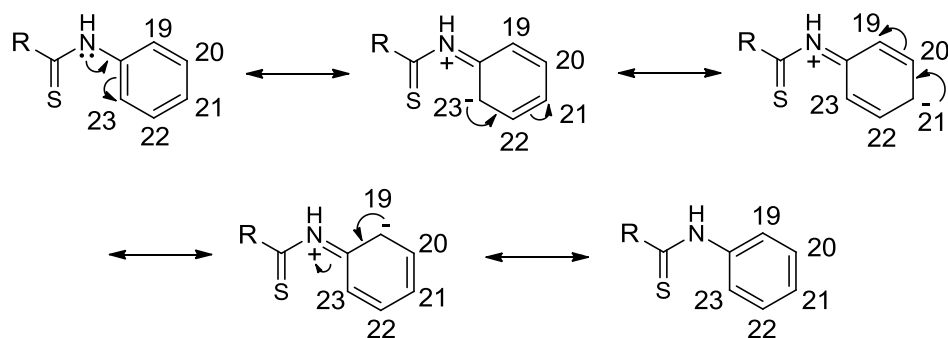


Figure 3.29. Resonance contributors of phenyl ring on AC007.

A negative charge can be found on C19 and C23, while none of the contributors show a negative charge on C20 or C22. H19 and H23 are therefore more shielded than H20 and H22 and are responsible for the signal at 7.08 ppm (2H). The remaining aromatic signal in this spin system at 7.31 ppm (2H) is accounted for by H20 and H22. Due to the conjugated nature of the aromatic system, the splitting of the three proton signals in the phenyl ring does not occur according to first order approximation rules. H21 appears as an unsymmetrical doublet, with H22/H20 and H19/H23 appearing as unsymmetrical triplets with some peak shouldering in evidence.

The second and larger aromatic spin system is caused by the naphthyl moiety. This ring system contains seven protons, which matches the integration of the remaining signals in the aromatic region (**Figure 3.27**). Due to the highly conjugated nature of this group it is difficult to assign individual protons to each signal.

The signals for the non-aromatic protons, H11-H15, are shown in **Figure 3.30**. H11 is easily identified as it is expected to appear as a singlet integrating for two, while the two sets of piperazine protons (H12/H13 and H14/H15) are expected to appear as triplets integrating for four. H11 is assigned to the peak at 3.93 ppm. Due to the proximity of the electron withdrawing thiourea group, it is expected that H14/H15 are more deshielded than H12/H13. The signal at 3.80 ppm (4H) is therefore assigned to H14/H15, leaving the signal at 2.57 ppm to account for H12/H13.

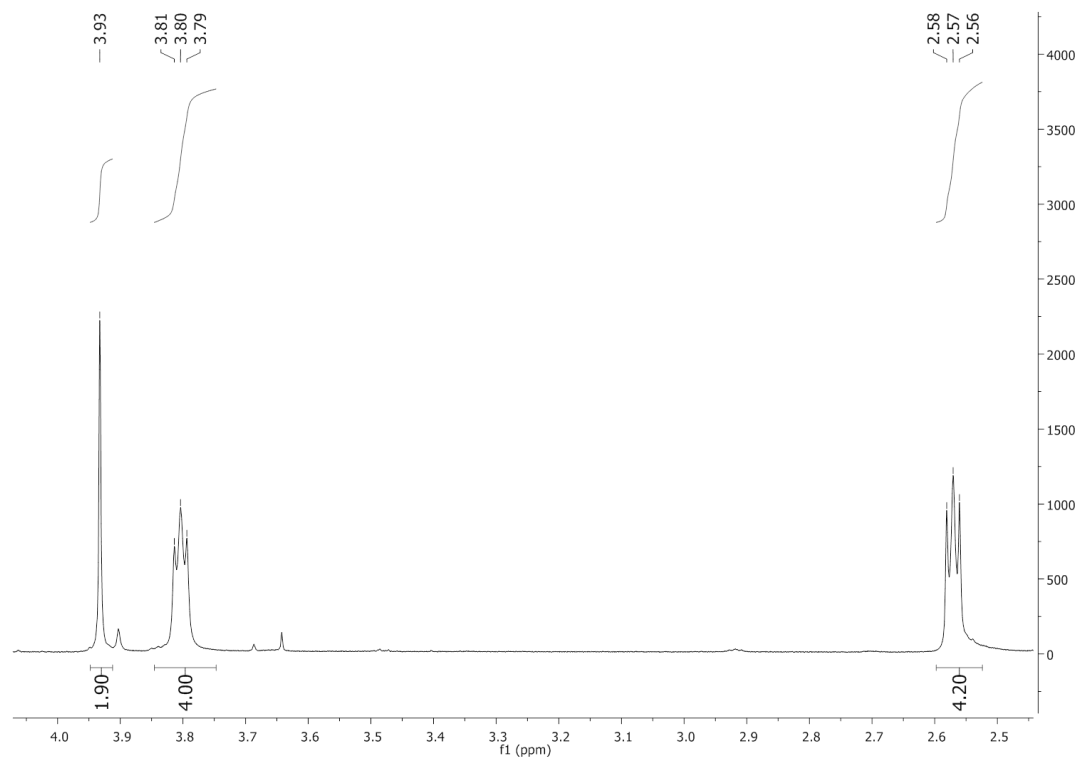


Figure 3.30. Non-aromatic signals for AC007, ¹H NMR spectrum.

The full ¹³C spectrum of AC007 is shown in **Figure 3.31**. Using DEPT135 spectroscopy the five quaternary carbons (C1, C6, C10, C16 and C18) were identified as the signals at 183.3 ppm, 140.1 ppm, 133.9 ppm, 133.2 ppm and 132.4 ppm. The only non-aromatic carbon in this group is C16. This is assigned to the signal at 183.3 ppm. C18, on the phenyl ring, was identified via HMBC interactions with H23/H19 (7.08 ppm) and H22/H20 (7.31 ppm), **Figure 3.32**.

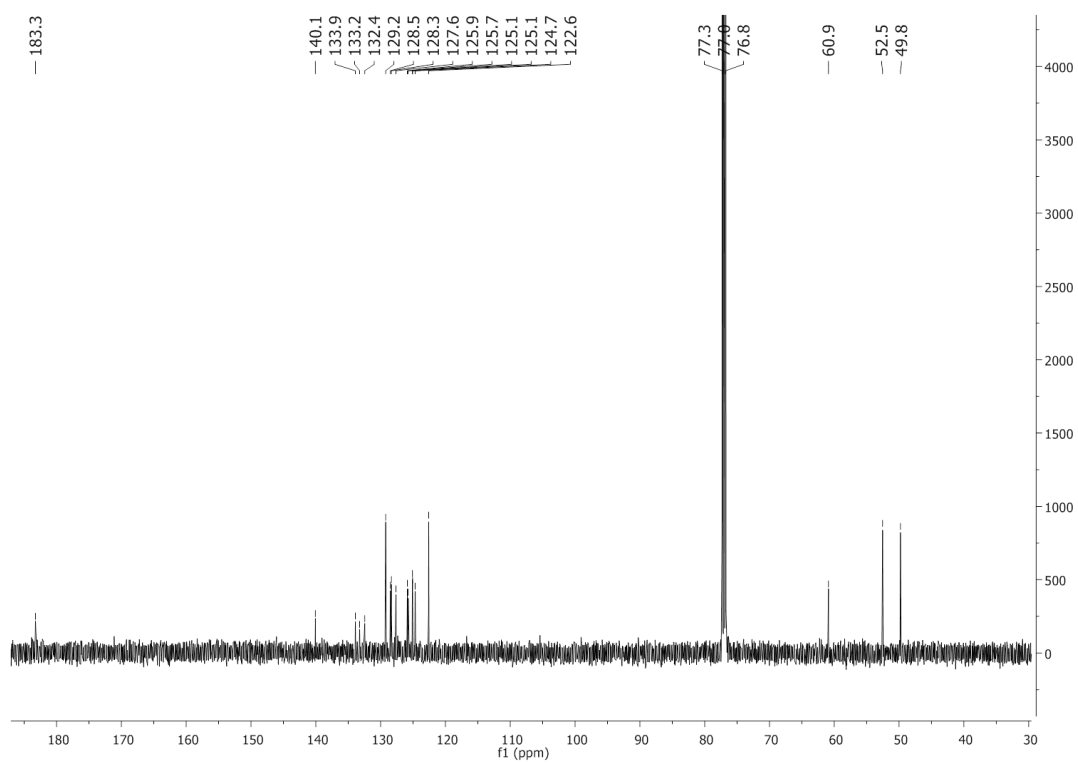


Figure 3.31. ^{13}C NMR spectrum of AC007.

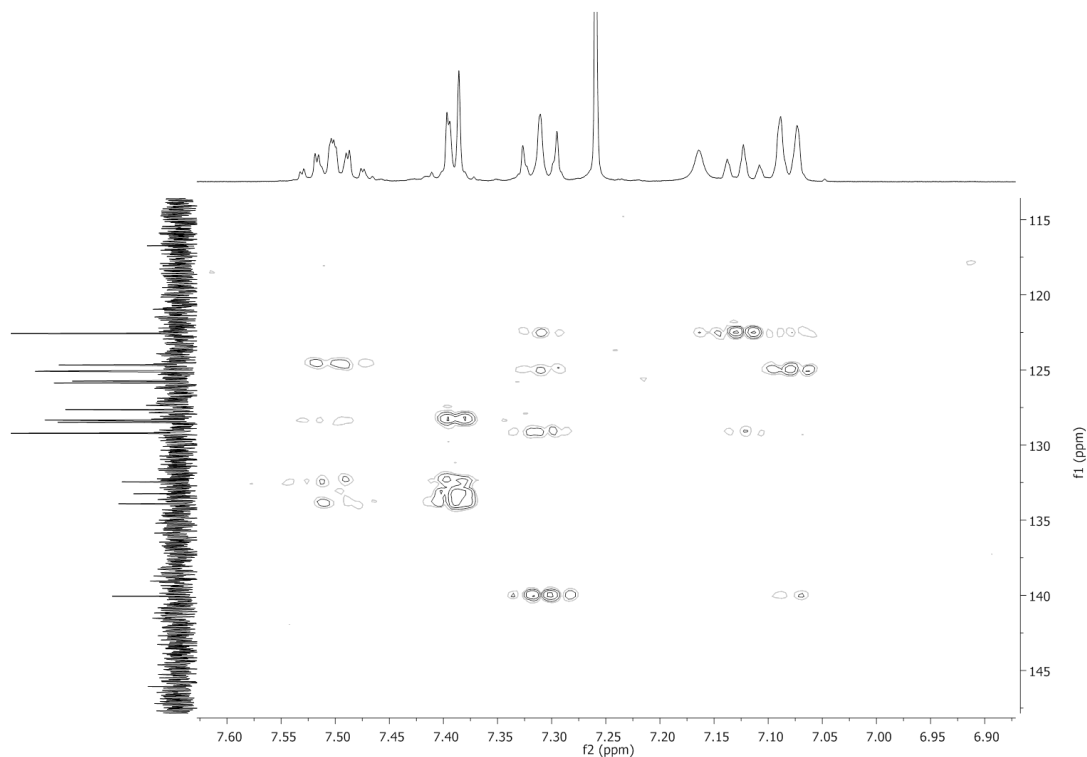


Figure 3.32. HMBC for AC007 showing coupling between the proton signals at 7.31 ppm and 7.08 ppm and the carbon signal at 140.0 ppm.

The signals for H22/H20 and H23/H19 both couple to the quaternary carbon signal at 140.1 ppm in the HMBC, this signal was therefore assigned to C18. Interestingly, the HMBC correlation between H20/H22 and C18 is stronger than the correlation between H19/H23 and C18, despite H19/H23 being closer to C18. This is due to the fact that HMBC correlations follow a Karplus type relationship, with angle of the coupling species relative to each other playing a key role in the strength of the correlation.^{87,88} The remaining quaternary carbon signals, at 133.9 ppm, 133.2 ppm and 132.4 ppm are attributed to the three naphthyl quaternary carbons, C1, C6 and C10. These are difficult to assign individually due to the conjugated nature of the system.

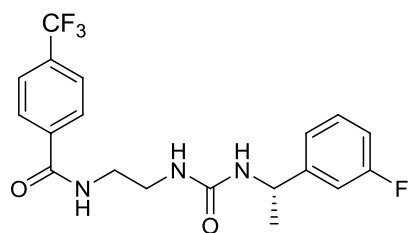
The aromatic carbons C19/C23, C20/C22 and C21 were identified via HSQC coupling with their protons. These signals occur at 122.6 ppm, 129.2 ppm and 125.1 ppm respectively. The remaining seven aromatic ¹³C signals correspond to C2, C3, C4, C5, C7, C8 and C9. These seven signals appear at 128.5 ppm, 128.3 ppm, 127.5 ppm, 125.9 ppm, 125.7 ppm, 125.1 ppm and 124.7 ppm.

The final remaining carbon signals for AC007 are the non-aromatic carbons, C11-C15. These were again identified using HSQC, with C11 assigned to the peak at 60.9 ppm, C12/C13 assigned to 52.5 ppm and C14/C15 to 49.8 ppm.

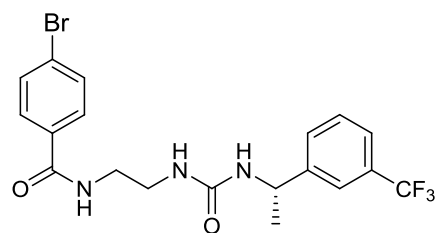
All targets **37-40**, were successfully synthesised and characterised via NMR, mass spectrometry and IR spectrum. Compounds **37, 38, 40** were assigned in a similar fashion to **39**, with many of the same signals and splitting patterns being retained across the four compounds. The Cl substituted derivatives, **37** and **40**, had one less ^1H NMR signal due to the replacement of H21 by the chlorine. Both **37** and **40** also had one additional quaternary ^{13}C NMR signal each, identified at 130.5 ppm and 129.9 ppm respectively via DEPT135 spectroscopy. Replacement of the sulphur with oxygen, as in **37** and **38**, caused a change in the chemical shifts of the H19/H23 signals. The H19/23 signal for the sulphur containing **39** appears at 7.08 ppm, while in the oxygen derivative, **38**, the H19/H23 signal appears at 7.30-7.27 ppm. The more deshielded signal in **38** is attributed to the more electronegative oxygen of this compound withdrawing electron density from the nitrogen, thus reducing the effect of the donation of its lone pair into the aromatic ring.

3.2.2 Urea containing compounds

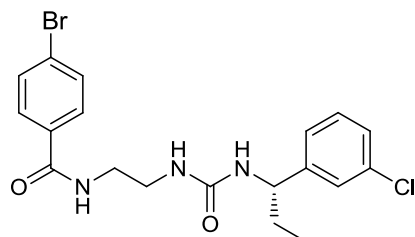
A class of urea containing compounds were synthesised based on the structures shown **Figure 3.33**. The compounds in **Figure 3.33** ranked highly in the screening of the published human nNOS crystal structure with the commercial databases, chapter two, section 2.9.2. The ranks of each of the compounds in the docking list are also shown.



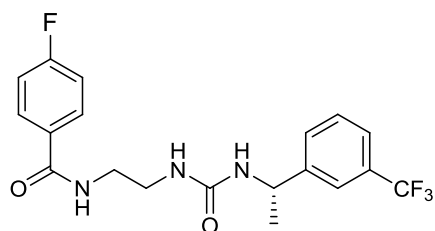
Compound ranked 6th



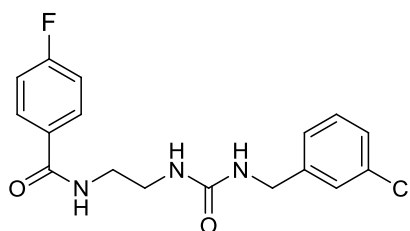
Compound ranked 9th



Compound ranked 10th



Compound ranked 11th



Compound ranked 48th

Figure 3.33. Urea containing compounds which ranked highly in the crystal structure screen of the Maybridge and Zinc databases.

A class of compounds that were similar in structure to those in **Figure 3.33** were designed and selected as synthetic targets. These synthetic targets are shown in **Figure 3.34**.

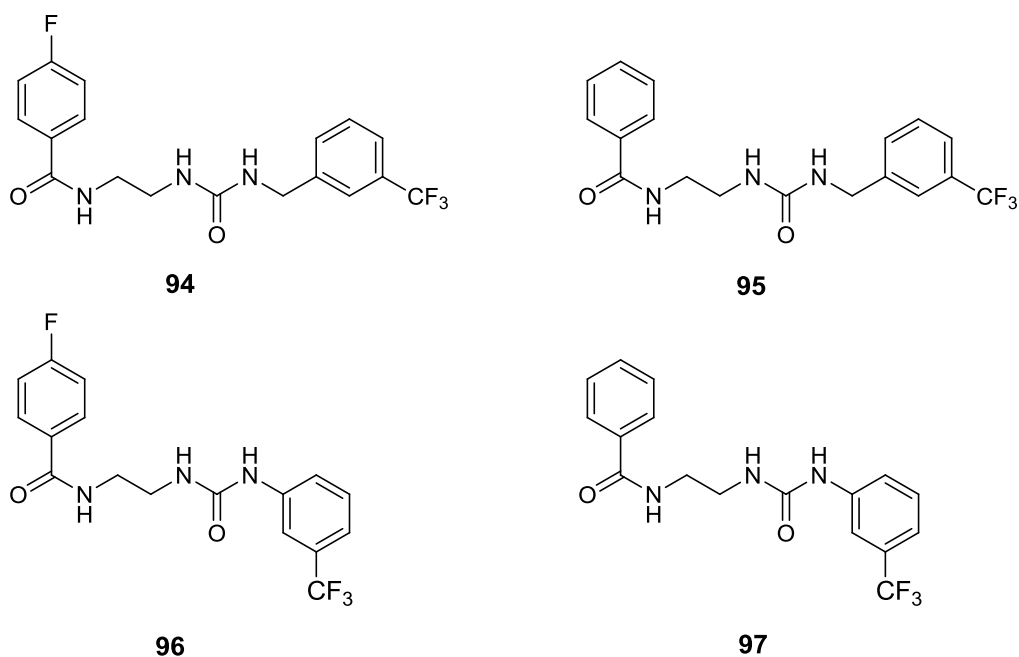


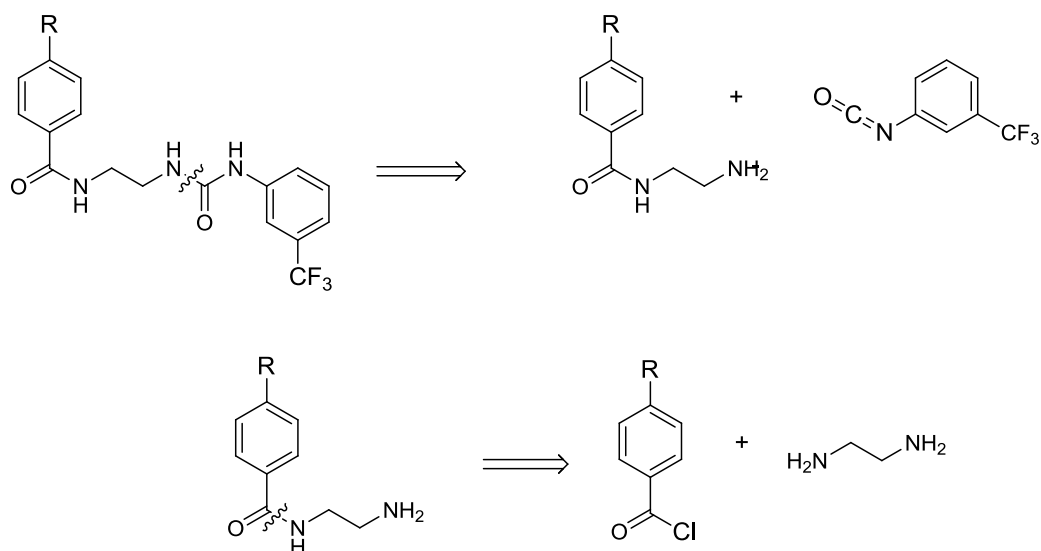
Figure 3.34. Class of urea containing synthetic targets, **94-97**.

For ease of synthesis, the chiral centre from some of the docking hits was removed from the target molecules. It was envisaged that if nNOS inhibitory activity was observed with this family of compounds, the chiral centre would be re-introduced to determine its effect on activity. One of the docking hits (ranked 48th, **Figure 3.33**) did not have this chiral centre and so it was felt that its removal for synthetic feasibility was justified and may still result in an nNOS inhibitory compound. Furthermore, docking of the target compounds (**Figure 3.34**) into the human nNOS crystal structures resulted in favourable Chemgauss4 scores, as previously described in chapter two, section 2.9.

It was hoped that the inclusion of HB donors close to both aromatic rings would allow the compounds to bind into the active site in a variety of poses. The HB donor beside either ring could form interactions with Glu597 or Asp602, while the adjacent aromatic ring would pi stack with the nNOS heme moiety. The other aromatic ring could potentially interact with Tyr711, facilitating the formation of a HB between the donor and the heme propionate groups, as is often observed for the aminopyridine class of inhibitors (See chapter one, section 1.4).

3.2.2.1 Synthesis of 96 and 97

The retrosynthetic analysis for **96** and **97** is shown below (**Scheme 3.5**). Breaking the urea functional group resulted in two accessible synthetic equivalents. The benzamide could be generated from ethylenediamine and the commercially available acyl chloride.



Scheme 3.5. Retrosynthetic analysis for **96** and **97**, R = *p*-F (w). R = H (x)

The synthetic scheme for **96** and **97** is detailed in **Figure 3.35**. The ethylenediamine was monoprotected with the BOC protecting group. This reaction was carried out at 0 °C to minimize the formation of the diprotected species. Following purification, the monoprotected amine was reacted with the aryl acyl chloride. Subsequent deprotection using TFA in DCM generated the free amine. Reaction of this amine with the isocyanate resulted in the formation of the urea linkage. Following purification, via column chromatography, **96** was isolated as a white solid in a 39% yield, while **97** was isolated as a white solid in a 36% yield. These were characterised via NMR, IR, mass spectrometry and melting point analysis.

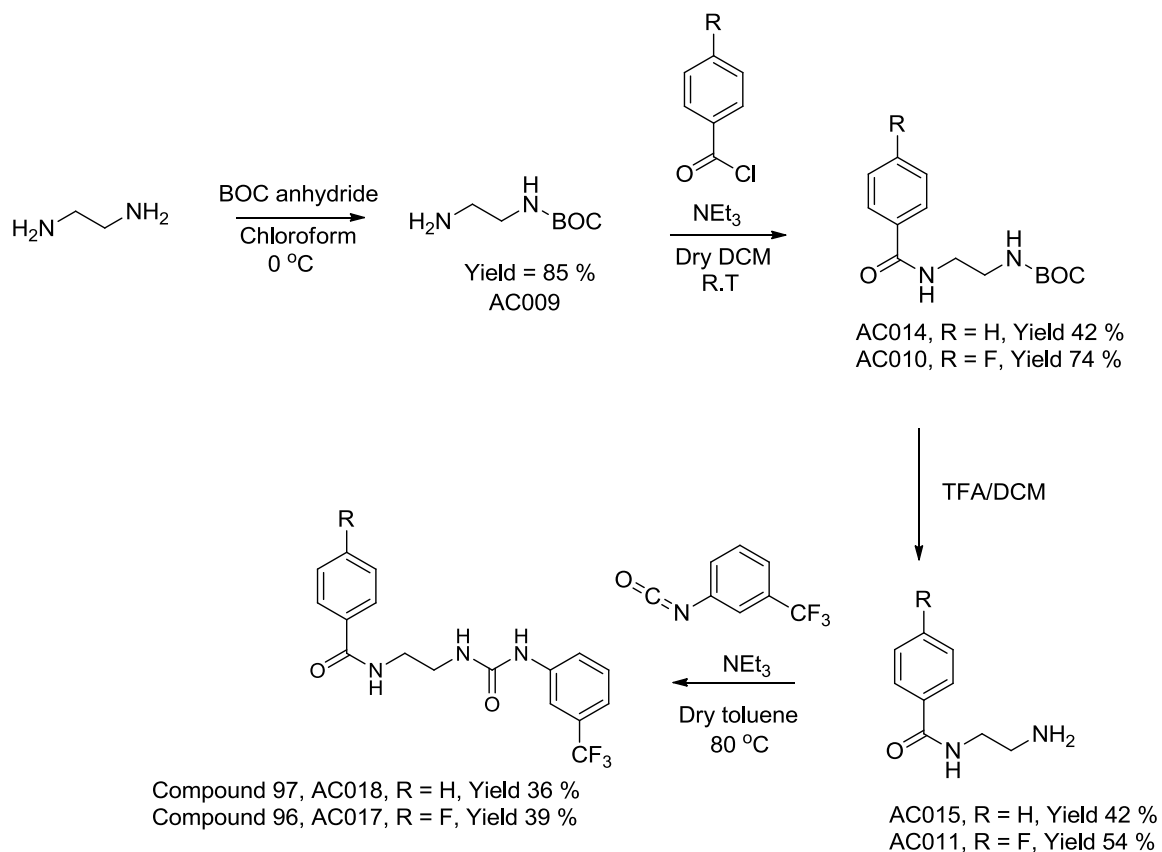


Figure 3.35. Synthetic scheme used for the synthesis of **96** (R = F) and **97** (R = H)..

3.2.2.2 Structural characterisation of **97**

The structure of **97** with numbered hydrogens and carbons is shown in **Figure 3.36**.

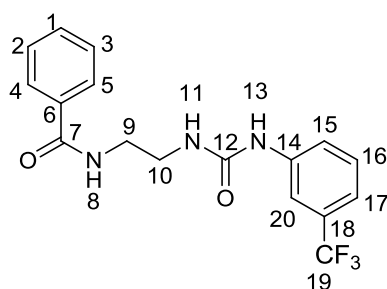


Figure 3.36. Numbered protons and carbons of **97**.

The full ^1H spectrum of 97 is shown in **Figure 3.37**, and an expansion of the 9.0 ppm-6.30 ppm region shown in **Figure 3.38**. Using HSQC, the three NH ^1H NMR signals were identified as appearing at 8.96 ppm (1H), 8.54 ppm (1H) and 6.40 ppm (1H). None of these proton signals show a one bond correlation to a carbon signal in the HSQC. In the HMBC, the two NH proton signals at 8.96 ppm and 6.40 ppm couple to the same quaternary carbon signal (155.4 ppm). This is assigned to C12. This therefore leaves H8 as the ^1H NMR signal at 8.54 ppm. H13 is expected to be more deshielded than H11 due to electron donation by N13 into the aromatic ring. H13 is assigned to the signal at 8.96 ppm, leaving H11 to be assigned to 6.40 ppm. All remaining signals in the 9.0 ppm to 6.30 ppm region (**Figure 3.38**) are caused by hydrogens on the two aromatic rings of 97.

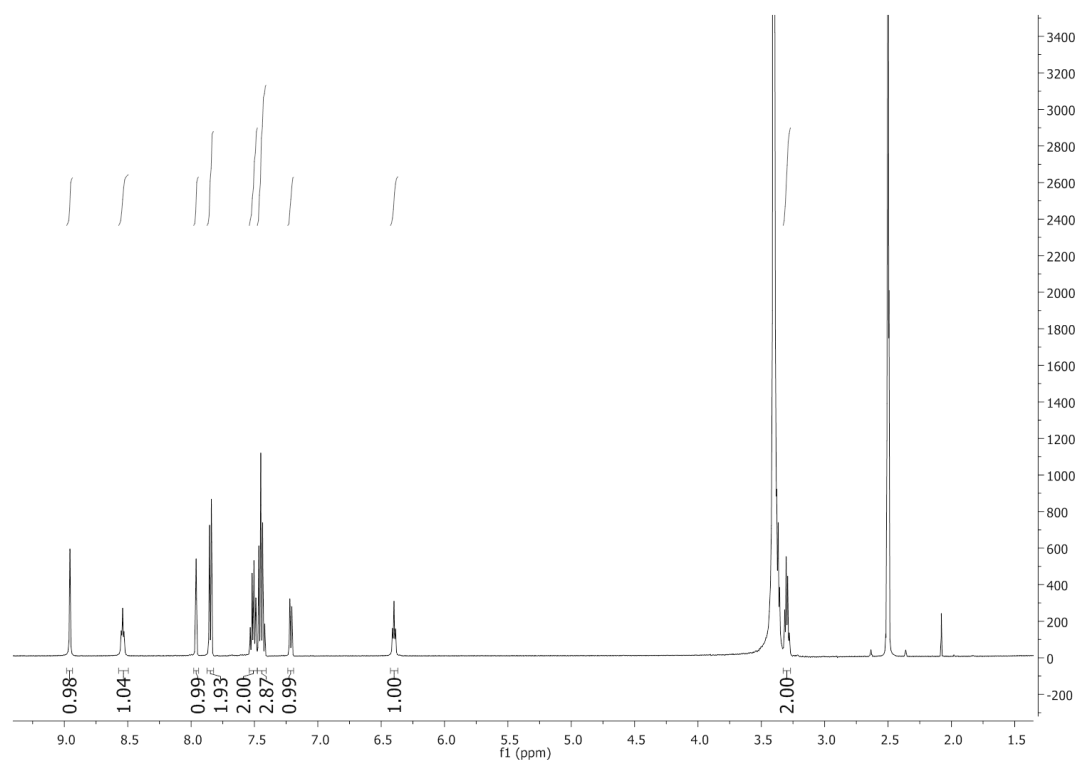


Figure 3.37. ^1H NMR spectrum of 97.

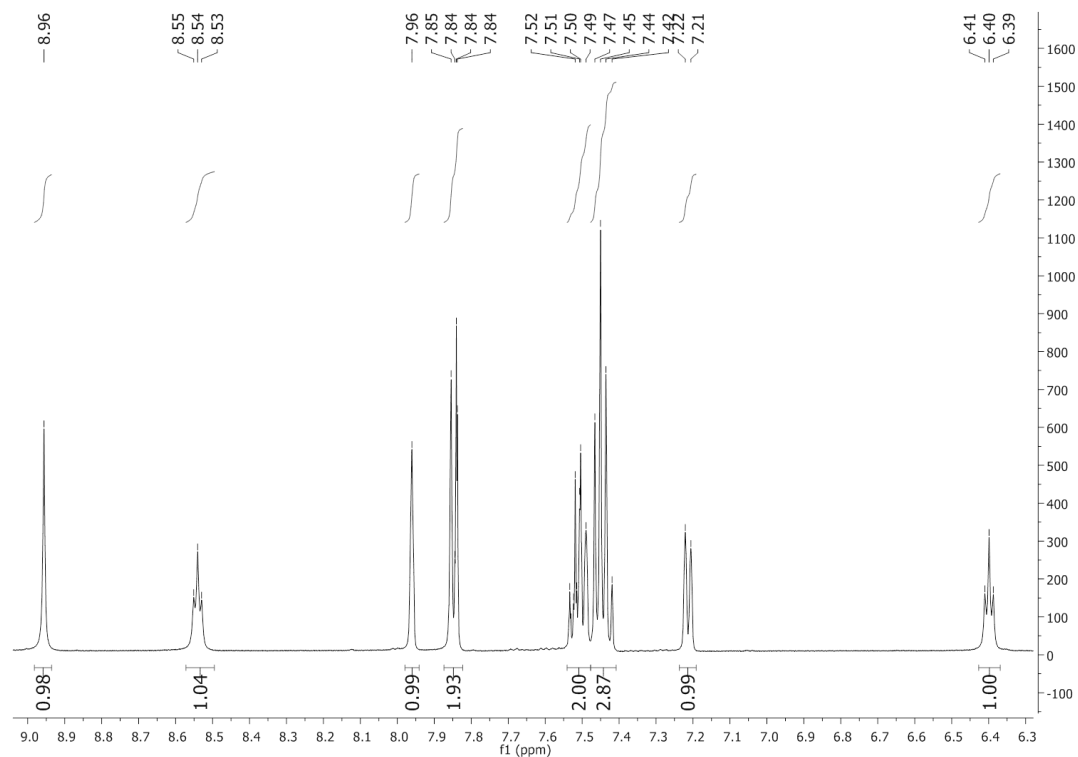


Figure 3.38. Expansion of the 9.0 ppm to 6.3 ppm region of the 97^1H NMR spectrum.

With C12 assigned to 155.4 ppm, C7 was assigned to the carbon signal at 166.7 ppm. Analysis of the HMBC (**Figure 3.39**) revealed that C7 coupled to the proton signal at 8.54 ppm (H8) and to the multiplet at 7.86-7.83 ppm (2H). This multiplet was assigned as H4 and H5, appearing as one signal.

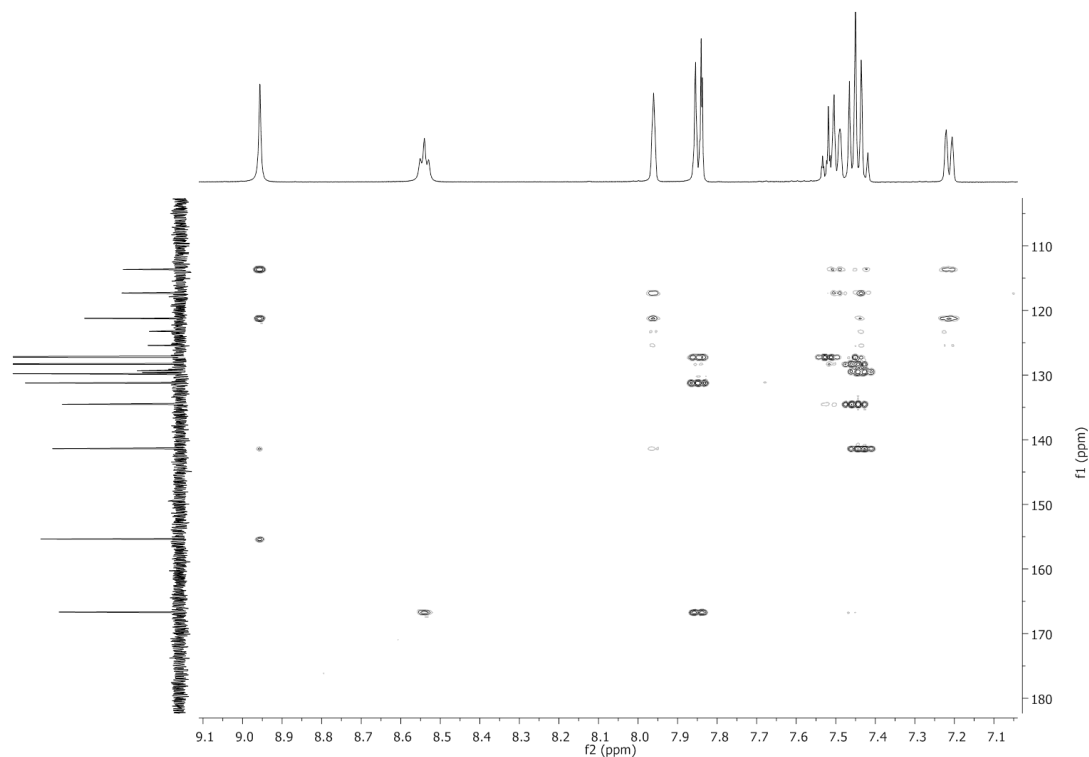


Figure 3.39. HMBC of 97 showing the signals at 166.7 ppm correlating to the ^1H signals at 8.54 ppm and 7.86-7.83 ppm.

H20 is the only aromatic proton which could be expected to appear as a singlet and hence is assigned to the singlet peak at 7.96 ppm (1H). Examination of the COSY spectrum (**Figure 3.40**) reveals that the signal for H20 is coupled to the signal at 7.51 ppm (2H) and at 7.21 ppm (1H).

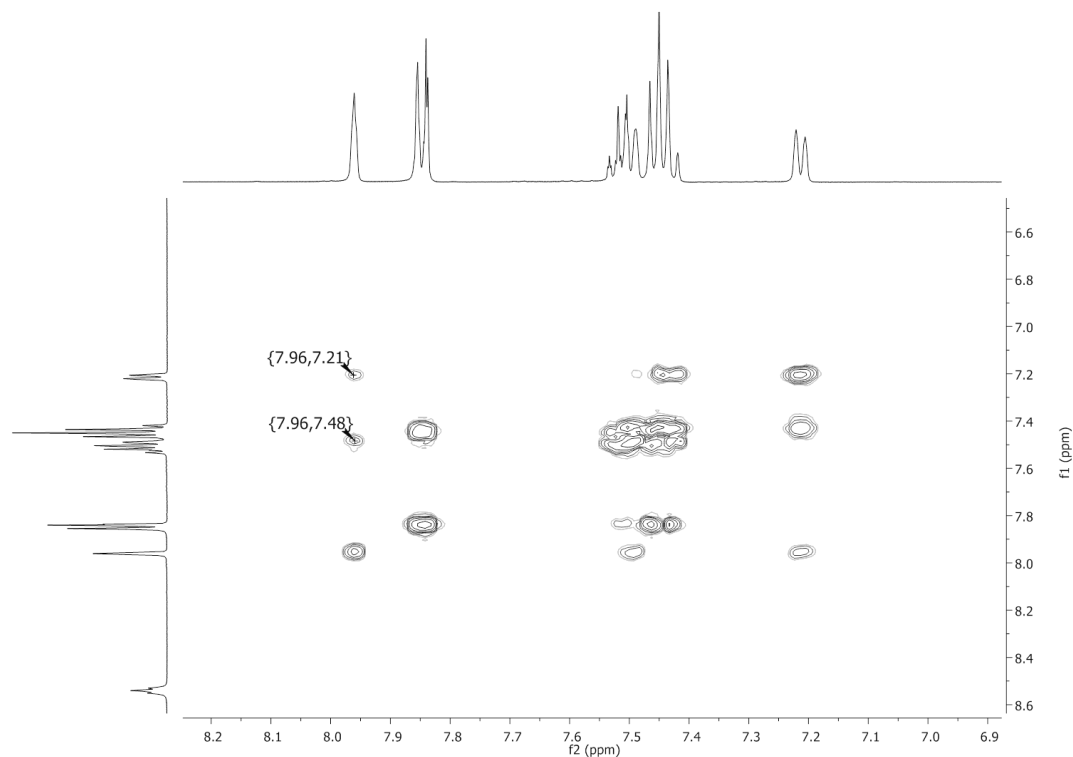


Figure 3.40. Aromatic region of 97 COSY NMR spectrum.

The resonance contributor which places a negative charge on C17 is the most stable contributor for this system due to the separation of the positive and negative charges (**Figure 3.41**). H17 is therefore more shielded than H15 and H16 and is assigned to the signal at 7.21 ppm (1H).

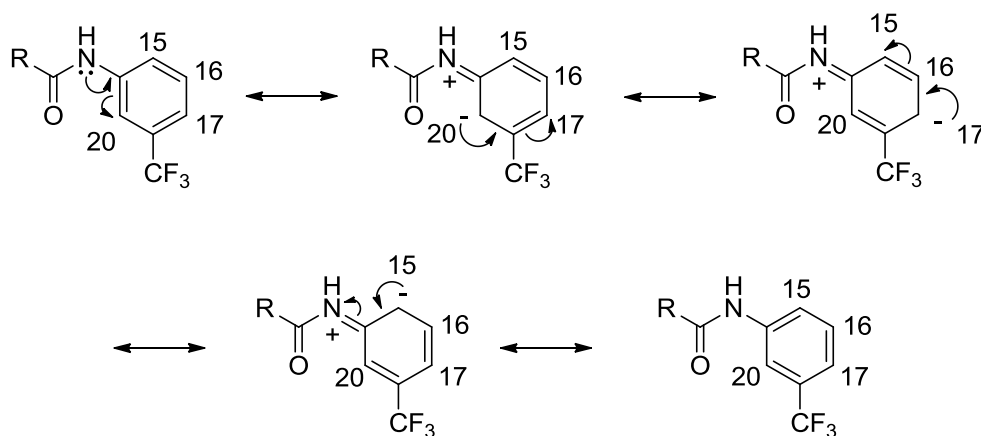


Figure 3.41. Resonance structures of CF_3 substituted aromatic ring of 97.

A clear ^1H - ^1H correlation can be seen between the signals at 7.96 ppm (H20) and the signal at 7.21 ppm (H17) in the COSY spectrum. A ^1H - ^1H correlation is therefore expected between the signal for H20 and the signal for H15. It is expected that no correlation, or at best a very weak correlation, will be observed between H16 and H20 due to the 5 bond distance between them. H15 is therefore assigned to the signal at 7.51 ppm (2H).

The signal at 7.51 ppm (2H) is coupled to several ^1H NMR signals in the COSY spectrum. These include the signals at 7.96 ppm (H20), 7.85 ppm (H4, H5) and the multiplet at 7.48-7.41 ppm. This extensive coupling suggests that the signal at 7.51 ppm is an overlapping signal, caused by one proton on the CF_3 substituted ring, and by one proton on the other, monosubstituted, phenyl ring. It is expected that the ^1H NMR signal for H2 and H3 will appear as an equivalent signal. Therefore, if H2 and H3 were responsible for the single at 7.51 ppm, along with H15, the signal at 7.51 ppm would integrate for 3H. This is not the case as the 7.51 ppm signal only integrates for 2H. Therefore, H1 is assigned as the second proton responsible for the signal at 7.51 ppm (2H).

The remaining aromatic proton signal at 7.48-7.41 ppm (3H) is assigned to the three remaining aromatic protons, H16, H2 and H3. This signal is coupled to the ^1H signals at 7.21 ppm (H17), 7.51 ppm (H15 and H1) and to the multiplet 7.86-7.83 ppm (H4 and H5) in the COSY spectrum.

The final two groups of protons to be assigned are H9 and H10. One of these signals can be clearly seen in the ^1H spectrum at 3.30 ppm (2H) as an apparent quartet (**Figure 3.37**). Both H9 and H10 would be expected to appear as a doublet of triplets. As can be seen in the HMBC spectrum (**Figure 3.42**), the proton signal at 3.30 ppm couples to the carbon signal at 155.4 ppm. This carbon signal is attributed to C12, the more shielded of the two carbonyl carbons. The proton signal at 3.30 ppm is therefore assigned to the hydrogen adjacent to C7, i.e. H10.

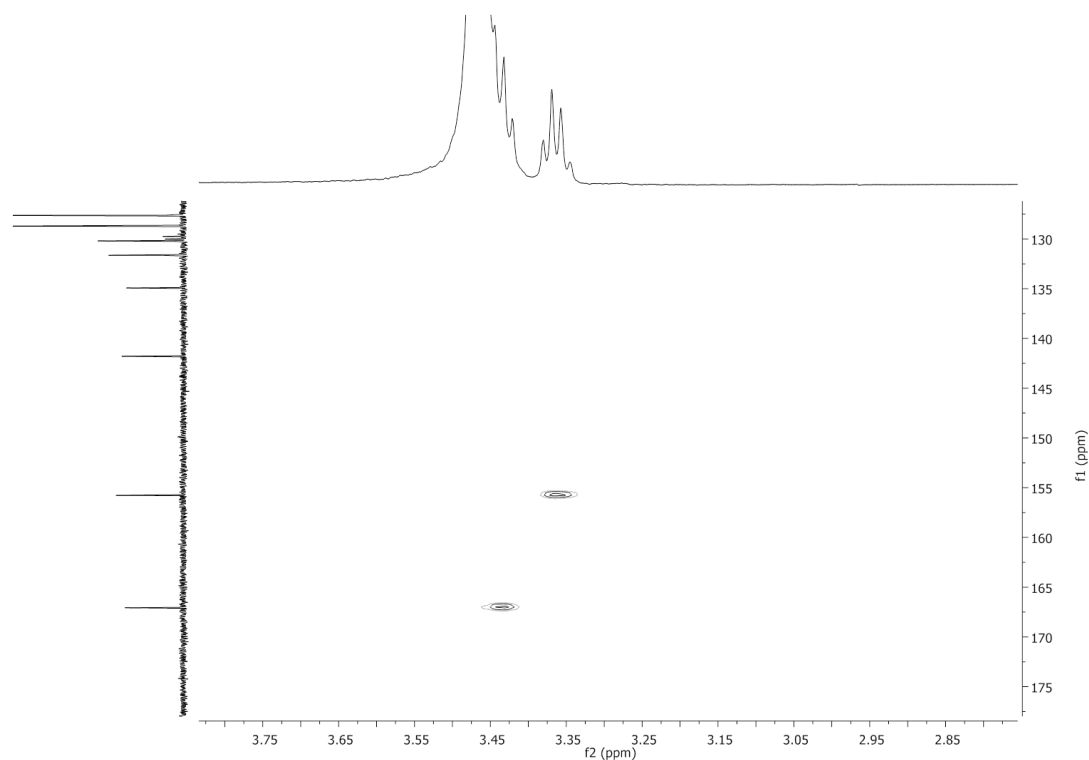


Figure 3.42. HMBC spectrum of 97 showing coupling of H9 and H10 to their neighbouring carbonyl carbons.

The expected signal for H9 is masked by the water present in the deuterated DMSO. A correlation, similar to the one described between H10 and C12 described above, can be seen between the ^{13}C NMR signal for C12 and a shoulder which appears under the H_2O peak in the HMBC (**Figure 3.42**). H9 is assigned to this shoulder at 3.37 ppm. The presence of two CH_2 groups in 97 is confirmed by analysis of the DEPT135 spectrum, which clearly shows two CH_2 signals close to the DMSO solvent signal at 39.5 ppm and 38.7 ppm (**Figure 3.43**).

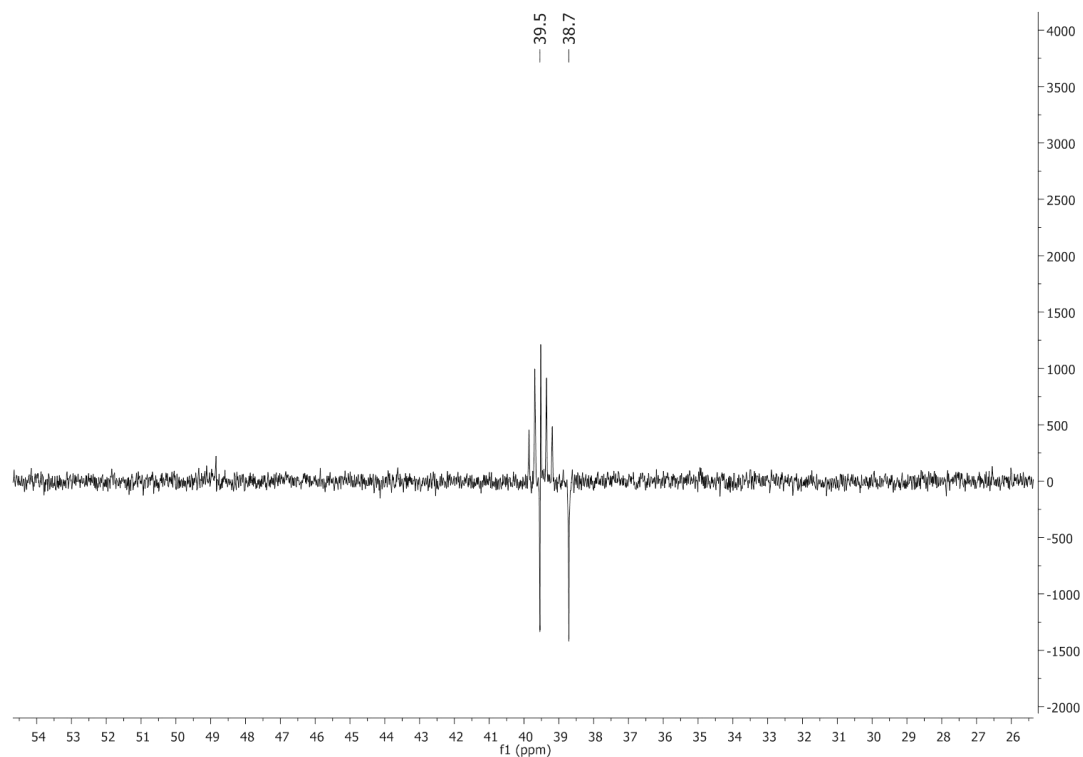


Figure 3.43. DEPT135 spectrum of 97, proving the presence of two CH₂ groups in 97.

A full ¹³C NMR spectrum for 97 is shown in **Figure 3.44**. Using DEPT135 spectroscopy the quaternary carbons signals are identified at 166.5 ppm, 155.4 ppm, 141.4 ppm, 134.4 ppm, 124.3 ppm and 129.5 ppm.

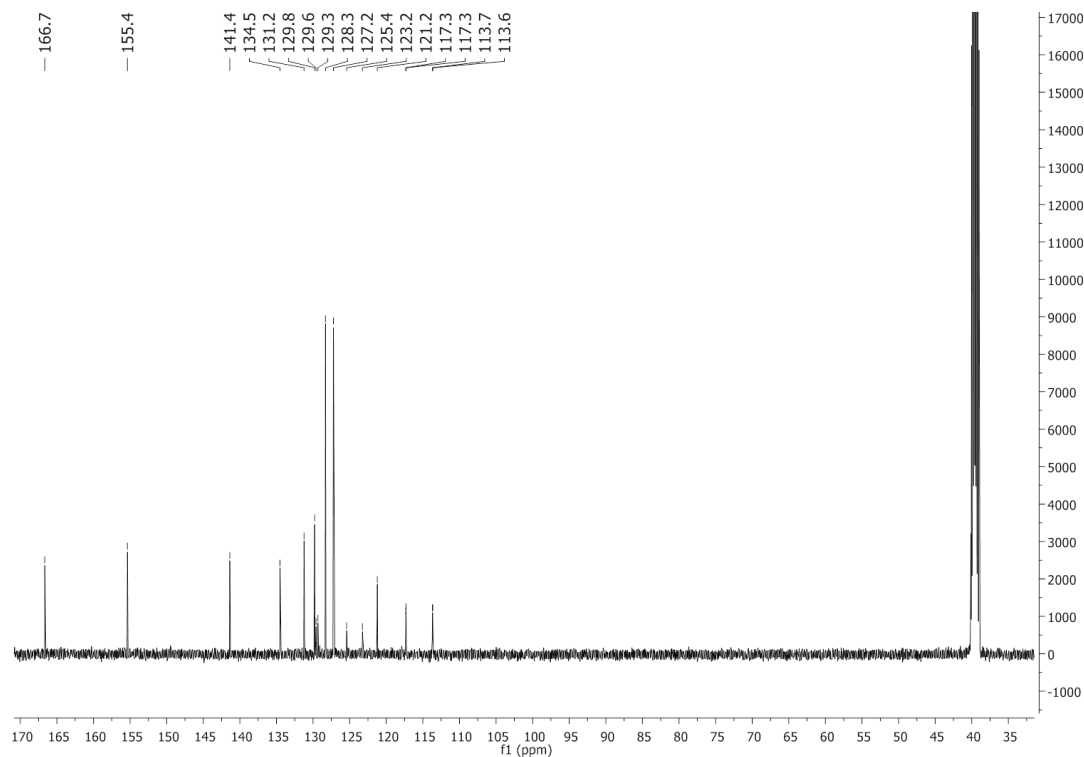


Figure 3.44. ^{13}C NMR spectrum of 97.

The carbonyl carbons are assigned based on their relative shieldings, with C12 being more shielded than C7. C12 is assigned to the peak at 155.4 ppm and C7 to 166.7 ppm. C14 is attributed to the signal at 141.4 ppm, with HMBC correlations observed with H13 (8.98 ppm) and H20 (7.96 ppm). The quaternary signal at 134.4 ppm is coupled to the ^1H signals at 7.48-7.41 ppm (H16,H2,H3) and 7.50 ppm (H1 and H15). C6 is therefore assigned to the signal at 134.4 ppm.

The two remaining quaternary carbons, C18 and C19, are adjacent to a fluorine atom that causes the signals for both carbons to be split into quartets with large coupling constants. C19 appears as a quartet with a J value of 272.2 Hz at 124.3 ppm. C18 also appears as a quartet at 129.5 ppm, with a J value of 31.2 Hz.

Using HSQC (**Figure 3.45**), the ^{13}C signals for C20 and C17 are assigned to the peaks at 113.7 ppm and 117.3 ppm respectively (H20 at 7.96 ppm, H17 at 7.21 ppm). These ^{13}C signals are split into quartets by the fluorine atoms, with the C20 signal having a J value of 3.9 Hz and the C17 signal having a J value of 4.1 Hz. H4 and H5, 7.86-7.81 ppm, are coupled to the ^{13}C signal at 127.2 ppm in the HSQC, and this signal is thus assigned to C4 and C5.

The HSQC also reveals that the signal at 7.50 ppm (2H), which is attributed to H1 and H15, couples to two carbon signals at 131.2 ppm and 121.2 ppm. C15 is expected to be more shielded than C1 due to the electron donating group *ortho* to C15. C15 is assigned to the signal at 121.2 ppm, while C1 is assigned to the signal at 131.2 ppm.

Similarly, the ^1H signal at 7.48-7.41 ppm (H2, H3 and H16) is coupled to two ^{13}C signals at 128.3 ppm and 129.8 ppm. These signals are caused by C2/C3 and C16. To differentiate between the carbon signals the HMBC was used to observe a correlation between the ^1H signal for H4 and H6 (7.86-7.83 ppm, 2H) and the ^{13}C signal at 128.3 ppm. C2 and C3 are therefore assigned to the signal at 128.3 ppm, with C16 assigned to the remaining aromatic ^{13}C signal at 129.8 ppm.

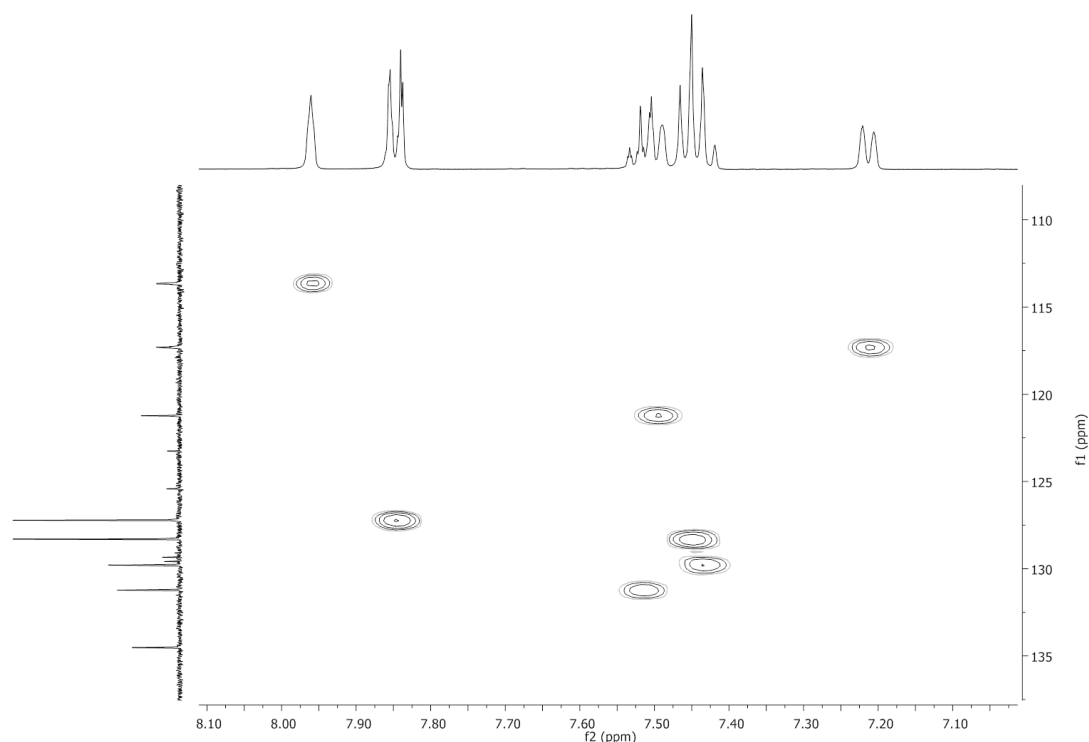


Figure 3.45. Expanded view of the aromatic region of the HSQC for 97.

The signals for C9 and C10 are expected to appear near 40 ppm in the ^{13}C spectrum. Both of these signals are obscured by the solvent peak. However, the HSQC of the region shows two clear CH_2 correlations (**Figure 3.46**). The presence of the two CH_2 groups is proven by the DEPT135 spectrum as previously discussed (**Figure 3.43**). The signal at 38.7 ppm is assigned to C10, leaving the signal at 39.5 ppm to be assigned to C9.

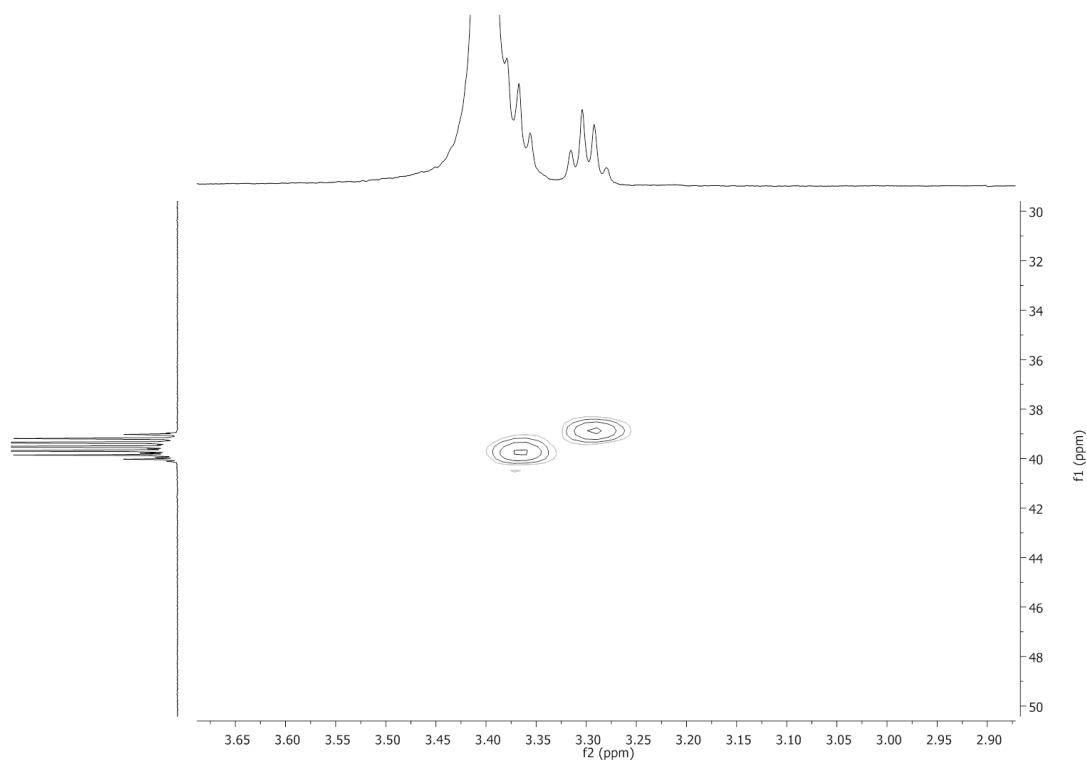


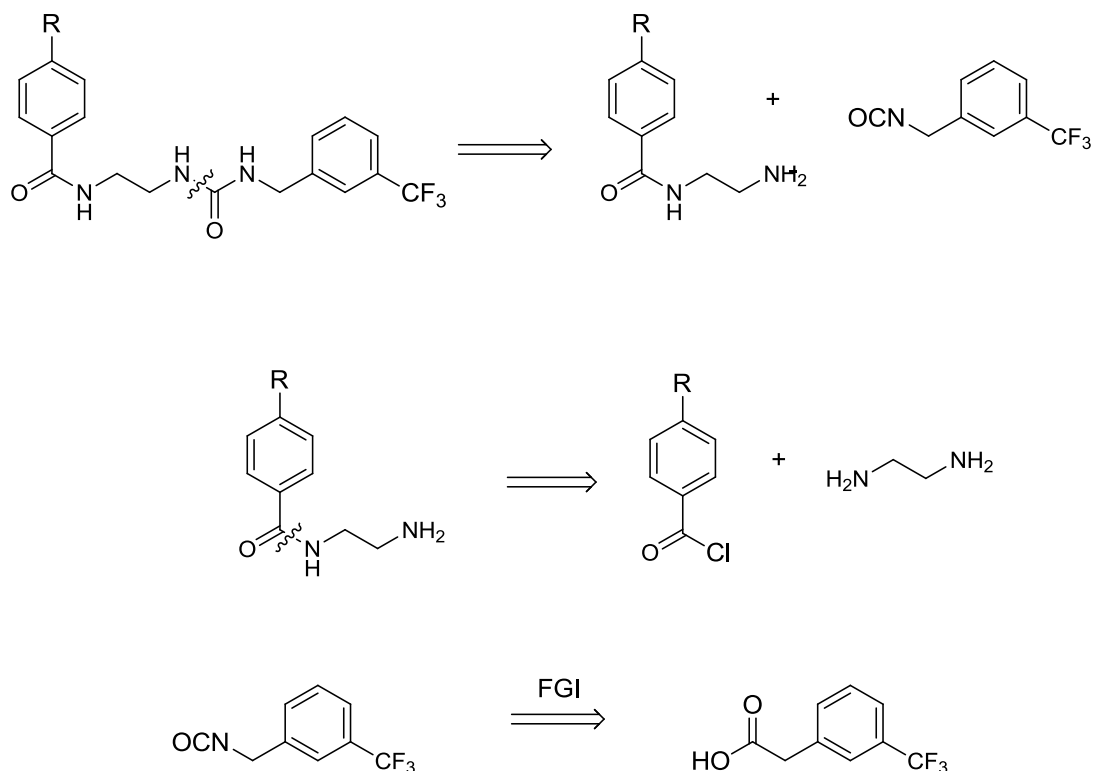
Figure 3.46. HSQC showing two clear and separate CH₂ correlations, proving the presence of C9 and C10 in **97**.

The NMR data of **96** was assigned using a similar approach to the one described above for **97**. The key differences in the spectra of **96** compared to **97** are caused by the addition of a fluorine atom onto the aromatic ring at C1. The ¹H NMR spectrum of compound **96** has one less signal proton signal than the ¹H spectrum of **96** due to this substitution.

In the ¹³C NMR of **96**, the signal for C1 (seen as a singlet at 131.2 ppm in **97**) becomes quaternary and is shifted to 164.3 ppm. This signal becomes a doublet ($J = 248.3$ Hz), split by the fluorine. Similarly, the ¹³C signals for C2/C3 and C4/C5 of **96** both appear as doublets and are shifted to 115.6 ($J = 21.7$ Hz) and 130.3 ppm ($J = 8.0$ Hz) respectively. In the ¹³C spectrum of **97** C2/C3 appears as a singlet at 128.3 ppm and C4/C5 also appears as a singlet at 127.2 ppm.

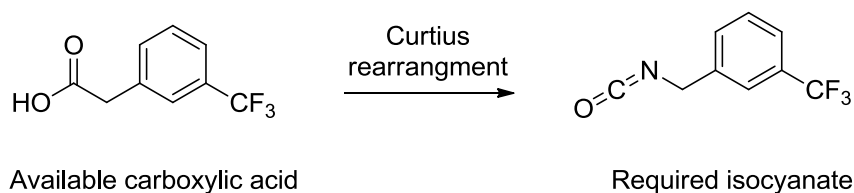
3.2.2.3 Synthesis of compounds 94 and 95

Compound **94** and **95** were synthesised in a different manner than **96** and **97**. The retrosynthetic analysis for **94** and **95** is shown in **Scheme 3.6**.



Scheme 3.6. Retrosynthetic analysis for **94** and **95**, R = p-F (w), R = H (x)

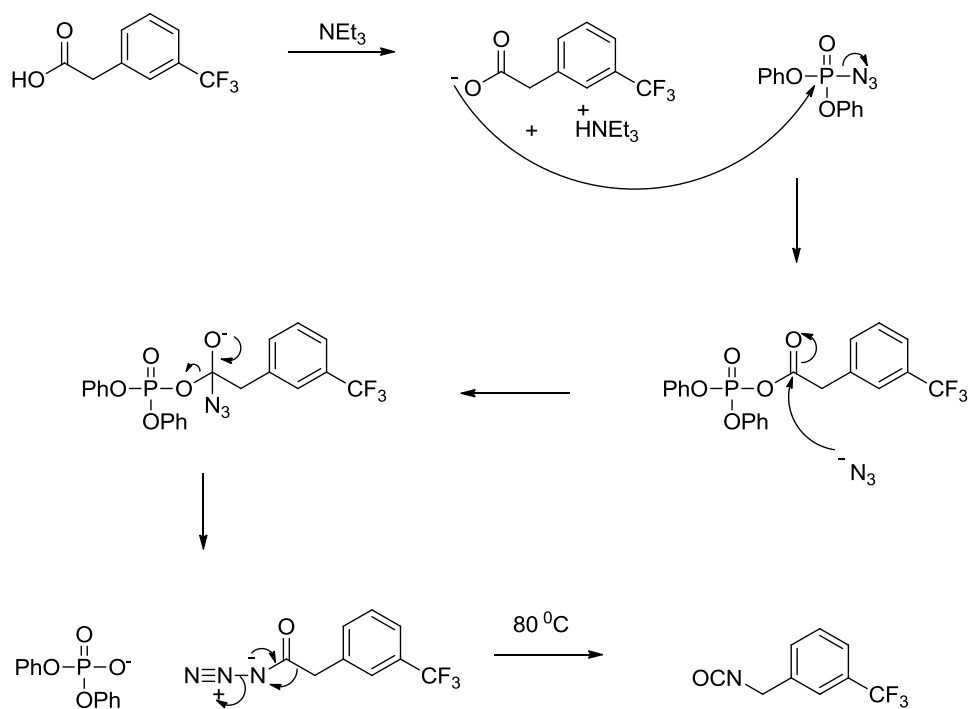
Reaction of the aryl acyl chloride and ethylenediamine followed the same retrosynthetic methodology as has been previously discussed for **96** and **97**, section 3.2.2.1. However, while the appropriate isocyanate starting material was commercially available for the synthesis of **96** and **97**, the required isocyanate for **94** and **95** was not available. The synthesis of this isocyanate was achieved by subjecting the carboxylic acid derivative of the starting material to a Curtius rearrangement (**Scheme 3.7**).



Scheme 3.7. Conversion of carboxylic acid to require isocyanate, **99**, via Curtis rearrangement.

This conversion is a two-step process, where the carboxylic acid group is converted to an azide using diphenyl phosphoryl azide (DPPA). DPPA represents a more stable and less toxic azide source than the “classic” sodium azide.⁸⁹ Once the azide is formed, the reaction is heated to cause a Curtius rearrangement. This results in elimination of nitrogen gas and formation of the isocyanate group. A proposed mechanism is provided in **Scheme 3.8**.

The azide formation step involves the reaction of the carboxylic acid with diphenyl phosphoryl azide in the presence of a base, such as triethylamine, at room temperature. This results in the formation of a phosphate intermediate which is attacked by the azide ion. The phosphate group is eliminated, leaving the desired acetyl azide product. The phosphate anion deprotonates the conjugate acid of the triethyl amine to form diphenyl hydrogen phosphate, which can be removed via column chromatography or by tritration with hexane once the reaction is complete. Once azide formation is complete, the reaction is heated to 80 °C to eliminate nitrogen gas and leave the isocyanate product.



Scheme 3.8. Isocyanate, **99**, formation from carboxylic acid and DPPA via an azide intermediate.

The isocyanates products are water sensitive and can react with moisture to form carbamic acid, which can then undergo spontaneous decarboxylation. Due to this instability the isocyanate products are not routinely isolated. Formation of the isocyanates product can be confirmed by ¹H NMR analysis of the crude reaction mixture, and identification of the proton signals alpha to the isocyanate group. An example of such a spectrum is shown in **Figure 3.47**.

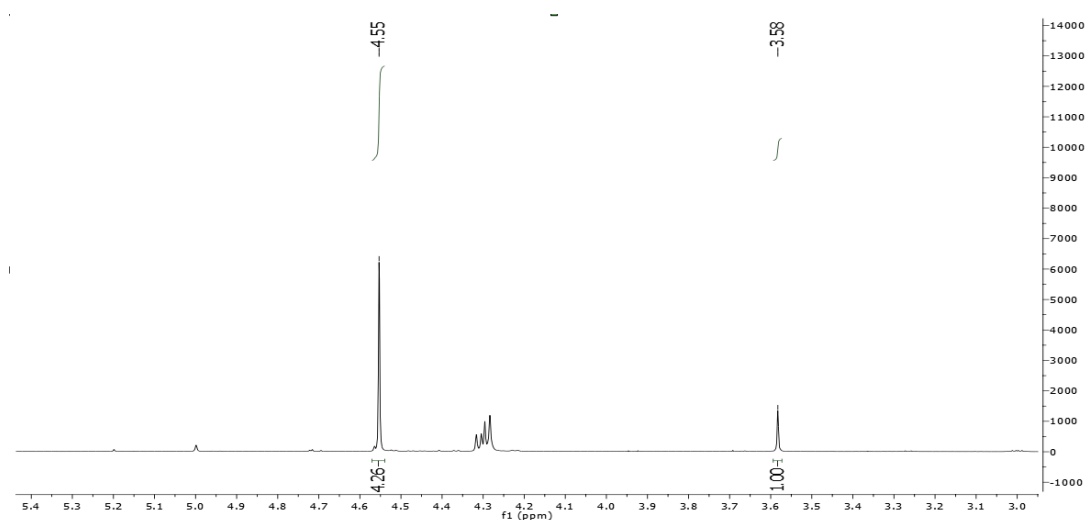
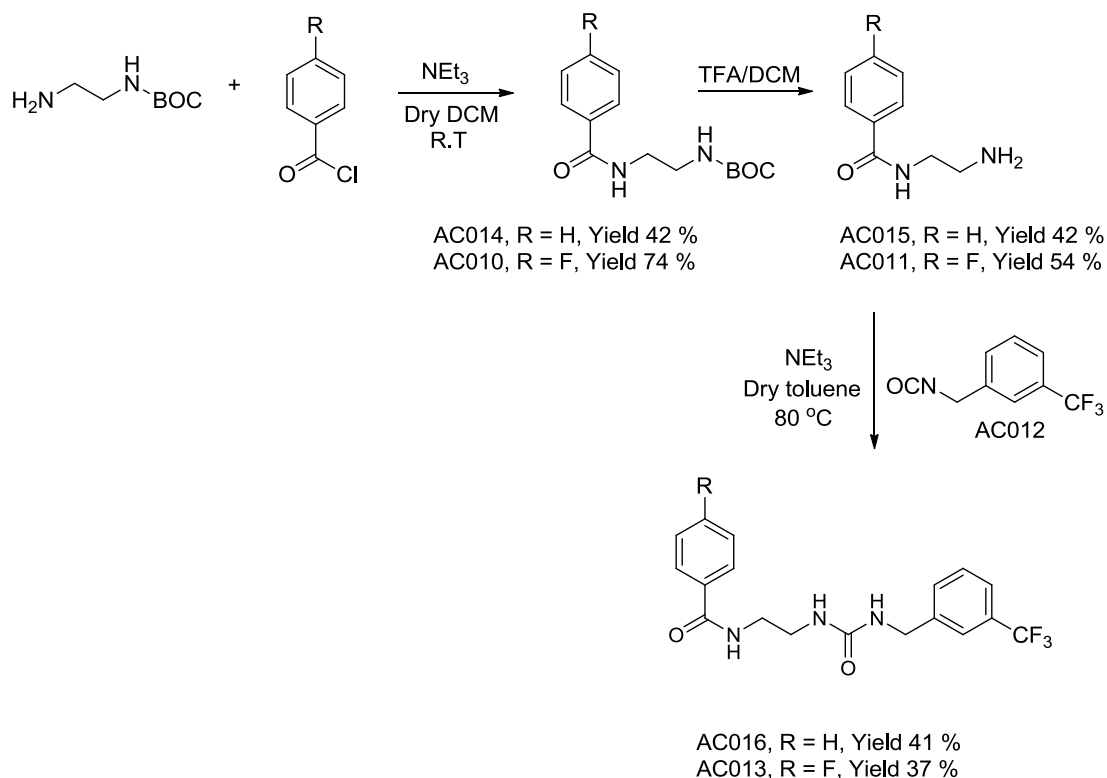


Figure 3.47. ^1H NMR spectrum demonstrating formation of **99**.

The singlet at 3.58 ppm in **Figure 3.47** represents the protons alpha to the carboxylic acid in the starting material. The appearance of a new singlet at 4.55 ppm represents the formation of the isocyanate. The protons alpha to the isocyanate are more deshielded than the equivalent protons in the carboxylic acid species. Using the relative integrations of the two peaks, an estimate of the amount of isocyanate that has formed can be calculated.

With the necessary isocyanate on hand, the synthesis of **94** and **95** was conducted according to the synthetic scheme outlined in **Scheme 3.9**. The steps are similar to the forward reaction scheme detailed for **96** and **97**, but the synthesised isocyanate, **99**, was used for **94** and **95** while the commercially available isocyanate was utilised for the synthesis of **96** and **97**.



Scheme 3.9. Synthetic scheme used for the synthesis of **94** (R = F) and **95** (R = H).

3.2.2.4 Structural characterisation of compound **94** and compound **95**

Much of the ^1H and ^{13}C NMR assignment for **94** and **95** was similar to the assignments for **96** and **97**, with the relative integrations and positions of the protons appearing as expected. The splitting of the ^{13}C signals of the carbons adjacent to the fluorine groups was similar to the splitting patterns of **96** and **97**. The most obvious change in the NMR spectra of compounds **94** and **95** was the inclusion of an extra CH_2 group. The ^1H NMR signal for this group appears at 4.33 ppm and 4.35 ppm, and the ^{13}C NMR signal appears at 42.7 ppm and 43.0 ppm for compound **94** and compound **95** respectively.

Using the synthetic methodologies described above, the urea containing synthetic targets as outlined in **Figure 3.34** were successfully synthesised in a range of yields. They were purified and characterised via a range of analytical techniques, most notably NMR spectroscopy. The intricacies of these NMR assignments have been discussed in detail for **97** with notable NMR signal shifts described for the other three target compounds in this

class. These four compounds, elucidated from computational screening of the nNOS crystal structure, were now on hand for biological evaluation.

3.2.3 Modified arginine and thioether compounds

The third class of compounds which were synthesised comprised of the arginine/diaminopyridine which was discussed in chapter 2, section 1.4.4.3, and a triazole compound which ranked 34th in the crystal structure screen, but was not available for purchase. Both of these compounds are shown in **Figure 3.48**.

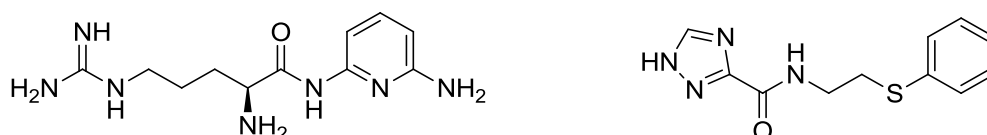
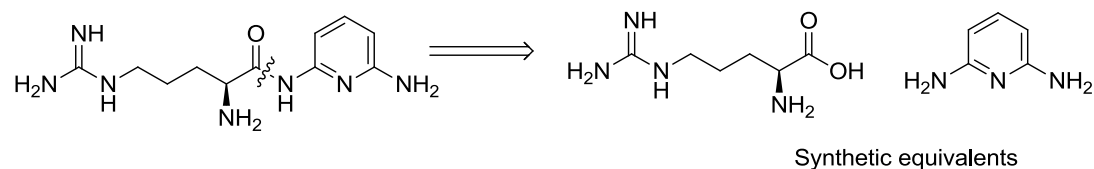


Figure 3.48. Third class of synthetic targets, **98** and **88**.

3.2.3.1 Attempted synthesis and characterisation of arginine/aminopyridine, compound 98

The retrosynthesis of arginine/aminopyridine compound is outlined in **Scheme 3.10**.



Scheme 3.10. Retrosynthetic analysis for **98**.

The forward reaction using the two synthetic equivalents shown in **Scheme 3.10** was complicated by the presence of multiple primary amino groups, and the moderately nucleophilic guanidinium moiety on the arginine. A protecting group strategy was used to

address these issues. One of the primary amines on the 2,6-diaminopyridine was protected with BOC. The primary amine on the arginine was protected with the same group. The guanidinium side chain was protected with the less common 2,2,4,5,7-pentamethyl-2H-benzofuran-5-sulfonyl (Pbf) protecting group (**Figure 3.49**).⁹⁰

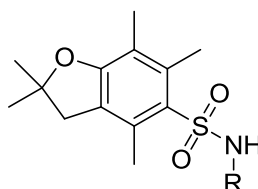
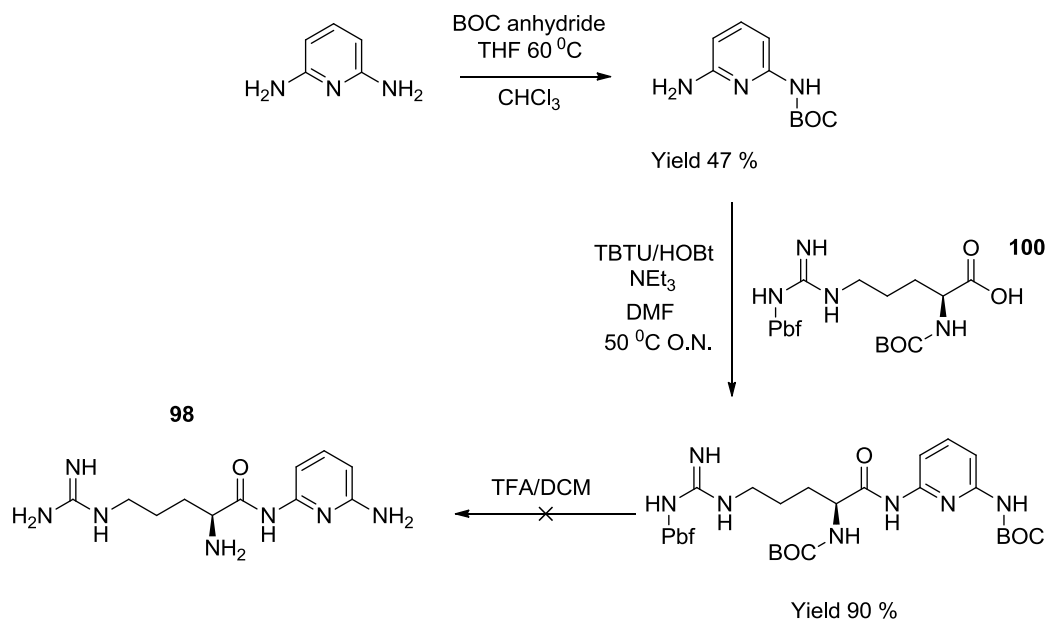


Figure 3.49. A Pbf protected amine.

The Pbf group is used in peptide bond forming reactions involving arginine as the guanidinium side chain has some nucleophilic character. This can result in self-cyclization with the arginine carbonyl group, and potential intermolecular nucleophilic attack with other species in the reaction mixture.⁹¹ The use of Pbf with the BOC protecting groups was advantageous, as the two groups are acid labile and so could be removed in one cleavage step, once peptide bond formation was achieved.⁹¹ The synthetic scheme for formation of **98** is shown in **Scheme 3.11**.



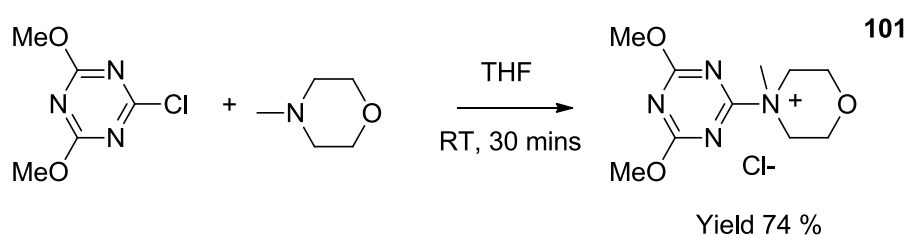
Scheme 3.11. Forward reaction scheme for **98**.

The diprotected arginine species, compound **100**, was commercially available, while the aminopyridine was mono protected as described in the chapter 5, section 5.6.3. The peptide coupling was trialled with a variety of coupling reagents before the conditions in **Scheme 3.11** were identified. The conditions trialled included 4-(4,6-dimethoxy-1,3,5-triazin-2-yl)-4-methyl-morphorlyin chloride (DMTMM) and 2-(1H-benzotriazole-1-yl)-1,1,3,3-tetramethyluronium tetrafluorborate/hydroxybenzotriazole (TBTU/HOBT) in DCM and DMF. The various conditions trialled and the results of these experiments are outlined in **Table 3.1**.

Table 3.1. Coupling conditions trialled for the synthesis of **98**.

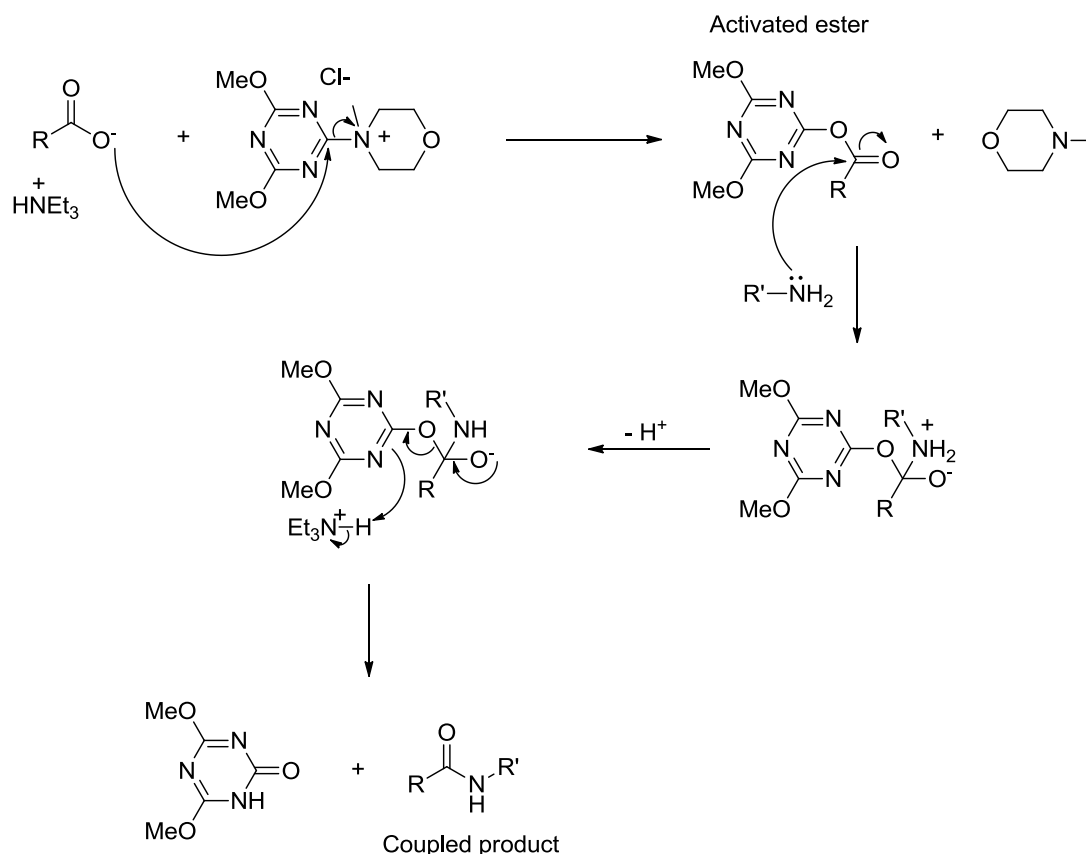
Coupling reagent	Solvent	Temperature	Result
DMTMM	DCM	R.T	Complex mixture
DMTMM	DMF	R.T	Complex mixture
TBTU/HOBT	DCM	R.T	Complex mixture
TBTU/HOBT	DMF	R.T	Complex mixture
TBTU/HOBT	DCM	50 °C	Complex mixture
TBTU/HOBT	DMF	50 °C	90% yield

DMTMM is a triazine based peptide coupling reagent and was freshly synthesised from 2-chloro-4,6-dimethoxy-1,3,5-triazine (CDMT) and *N*-methyl-morpholine (NMM) in a 1:1 ratio as outlined in **Scheme 3.12**. This coupling reagent is not as popular as others due to its relatively short shelf life and instability in organic solvents, particularly DCM, which is a popular solvent for peptide bond formation.⁹² DMTMM can decompose through loss of the methyl group on the quaternary nitrogen, rendering it inactive as a peptide coupling reagent.⁹²



Scheme 3.12. DMTMM, **101**, synthesis.

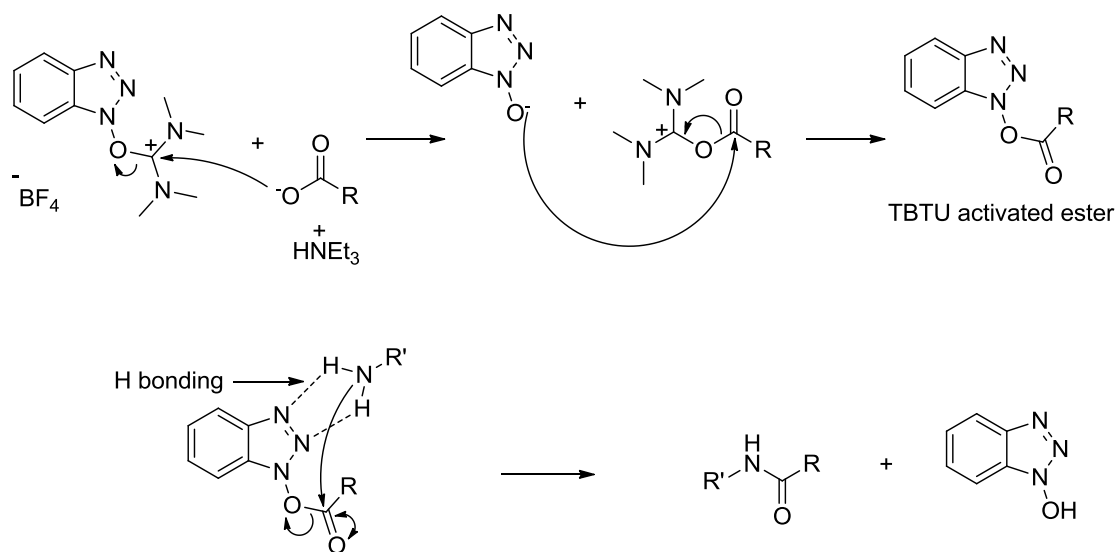
It was anticipated that DMTMM would form an activated ester species when reacted with the carboxylic acid of the diprotected arginine. This should then react with the protected 2,6 diaminopyridine to form the product as shown in **Scheme 3.13**.



Scheme 3.13. Activated ester formation and peptide bond formation using DMTMM.

This coupling approach with DMTMM did not yield the expected product, it instead resulted in a complex mixture. It is not uncommon in peptide coupling reactions to trial a variety of coupling conditions. Prediction of which set of conditions will be successful is difficult, and often a wide screen of reagents is necessary to form the desired product.⁹³

HOBt/TBTU in DMF proved to be successful for this reaction. HOBt prevents racemisation, and has been reported to form the OBt activated ester. It is possible that OBt activated esters have increased reactivity due to their ability to stabilize the approach of the amine through H-bonding.⁹⁴ The formation of the activated ester from TBTU and subsequent amine coupling is shown in **Scheme 3.14**.



Scheme 3.14. Formation of activated ester from TBTU and subsequent coupling of the amine.

Coupling of the diprotected arginine and the mono protected diaminopyridine gave the triprotected species (**Figure 3.50**) in a 90% yield. The coupling of the two partners was confirmed via NMR and mass spectrometry. Three distinctive protecting group signals for the two BOC groups and the Pbf group were observed at 1.43 ppm (9H), 1.44 ppm (6H) and 1.48 ppm (9 H). The alkyl chain signals were also in evidence, with complex splitting due to the diastereotopic nature of the protons. The total combined integration for the alkyl signals observed was seven. The aromatic signals for the pyridine ring were clearly visible at 7.36 ppm (t, 1H), 7.19 ppm (d, 1H) and 6.13 ppm (d, 1H).

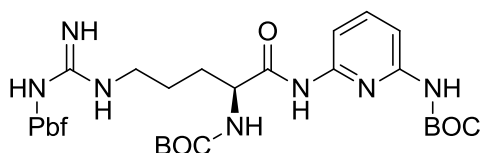


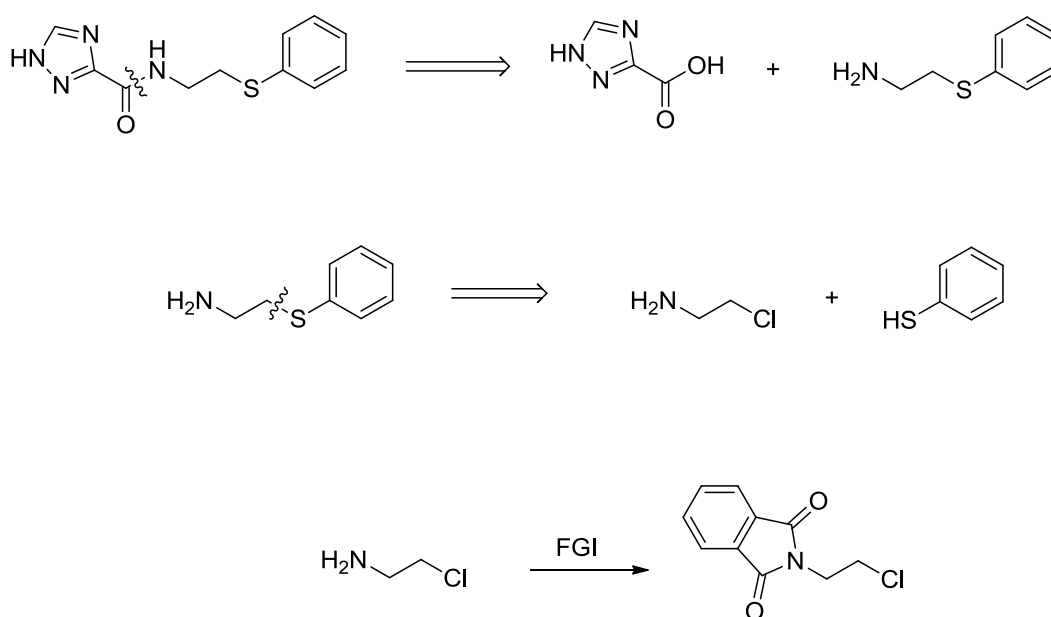
Figure 3.50. Triprotected product, **102**, obtained from TBTU coupling.

Once the coupling had been completed, the deprotection of **102** was attempted using TFA. While the coupling of the protected species was successful and the triprotected product was obtained in high yields, the subsequent deprotection using TFA did not yield the

expected product. The protecting group signals for both BOC groups and the Pbf group were not present in the ^1H NMR, demonstrating that they had been removed. However, the expected CH_2 signals for the arginine chain were absent, and the aromatic region did not contain the expected 1:1:1 ratio of aromatic proton peaks for the aminopyridine ring protons. It is possible that the use of high concentrations of TFA, which are required for Pbf removal, resulted in degradation of the product. Also, the deprotection of the nucleophilic guanidinium group on the arginine side chain may have contributed to unpredictable side reactions. The deprotected species, compound 98, was therefore not successfully synthesised.

3.2.3.2 Attempted synthesis and characterisation of thioether, compound 88

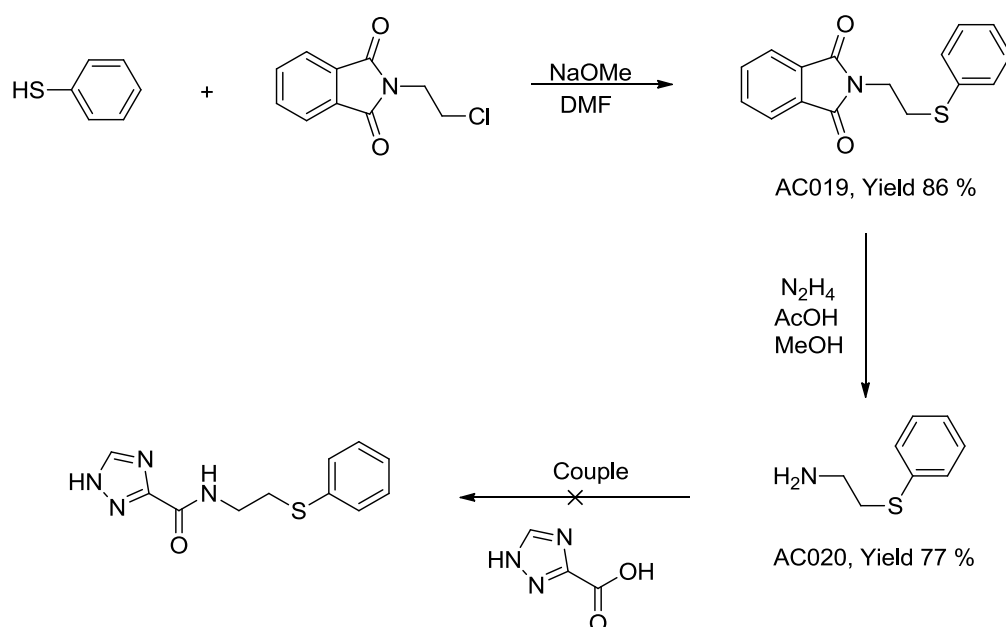
The synthesis of a triazole containing sulphur ether, shown in **Figure 3.48** was also attempted. The retrosynthetic analysis of this compound is shown in **Scheme 3.15**.



Scheme 3.15. Retrosynthetic analysis of **88**.

Breaking of the peptide bond gives the commercially available triazole carboxylic acid, and the thioether compound with a free primary amine. The thioether could be generated from

thiophenol and 2-chloroethanamine. While this amine was available, it was thought that treatment of this compound with base could result in self-reaction via nucleophilic attack of the deprotonated amino group at the carbon alpha to the chloro leaving group. To prevent this possible complication, the free amine was protected using a phthalimide group. Once the thiophenol and the phthalimide protected amine had reacted, the protecting group could be removed via treatment with hydrazine in the presence of methanol and acetic acid. This amine could then be coupled with the triazole species. A proposed synthetic scheme is outlined in **Scheme 3.16**.



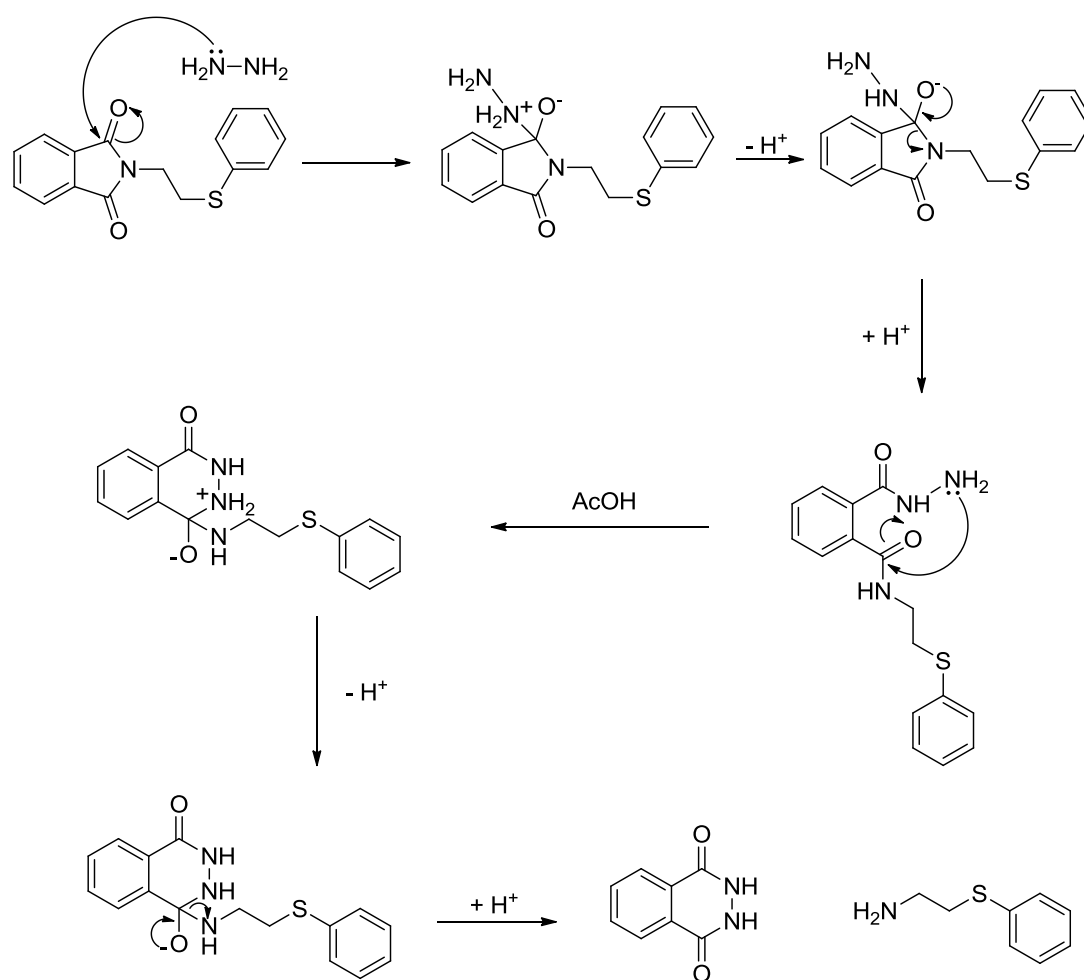
Scheme 3.16. Synthetic scheme for **88**.

The attack of the thiophenol on the carbon alpha to the chlorine yields the desired product in an 86% yield. Clear ^1H NMR signals were observed for the two CH_2 groups at 3.72 ppm (t, 2H) and at 3.05 ppm (t, 2H). The ^{13}C NMR signals for the two carbonyl carbons appears as one equivalent signal at 167.7 ppm. A HMBC correlation is observed between the CH_2 signal at 3.72 ppm and this carbon signal. This correlation, along with the presence of the expected number of aromatic signals, indicated formation of the desired product.

The deprotection using hydrazine generated the primary amine in a 77% yield. The two CH_2 signals were again visible in the ^1H NMR at 2.90 ppm and 2.80 ppm. A characteristically

broad amine ^1H NMR signal was observed at 1.49 ppm, along with the expected aromatic ^1H NMR signals in a 2:2:1 ratio.

A proposed mechanism for the hydrazine deprotection, which is similar to the phthalimide removal in the Gabriel synthesis, is outlined in **Scheme 3.17**.^{95,96} The dione side product is insoluble in methanol and so can be removed via filtration.



Scheme 3.17. Phthalimide removal in the presence of hydrazine and acetic acid.⁹⁶

Coupling of this amine with the triazole carboxylic acid was then attempted using a variety of conditions (**Table 3.2**). The coupling reaction could not be completed successfully, and **88** was not isolated for biological testing.

Table 3.2. Coupling conditions trialled for the synthesis of 88.

Coupling reagent	Solvent	Temperature	Result
DMTMM	DCM	R.T	Complex mixture
DMTMM	DMF	R.T	Complex mixture
TBTU/HOBt	DCM	R.T	Complex mixture
TBTU/HOBt	DMF	R.T	Complex mixture
TBTU/HOBt	DCM	50 °C	Complex mixture
TBTU/HOBt	DMF	50 °C	Complex mixture
DCC	DMF	R.T	Complex mixture
DCC	DCM	R.T	Complex mixture

It is possible that the triazole has some nucleophilic properties, and may attack the activated ester upon its formation. Triazole has been observed to act as a nucleophile in the presence of organocatalysts.⁹⁷ Protection of the triazole NH may address this issue; however it is possible that the all nitrogens of the triazole possess some nucleophilic properties. Protection of one nitrogen may therefore not eliminate potential side reactions when attempting to couple the triazole carboxylic acid with the desired amine.

3.3 Synthesis conclusion

A variety of non-commercially available potential human nNOS inhibitors had been identified by the computational screening studies that were conducted in chapter two. Two classes of compounds were synthesised based on some of the high ranking structures from these screens. The first class, with five members, had a piperazine core and was synthesised using a range of methodologies, including epoxide ring opening and nucleophilic attack on isocyanates and isothiocyanate. The five synthetic targets, all of which were novel compounds, were successfully synthesised in a range of yields.

The second class of compounds contained a urea linkage that was synthesised via amine attack on isocyanates. Two of the required isocyanates were first synthesised via azide formation and Curtius rearrangement. The four members of this second class of compounds were isolated as white solids, and their structural characterisation has been

discussed in detail. The core structure of this class of compounds was well represented in the hit list which was generated from docking with the human nNOS crystal structure. It is hoped that this strong computational performance would translate to inhibitory activity in a human nNOS assay.

Synthesis of a third class of compounds, containing a *de novo* designed mixed arginine-aminopyridine and a computationally identified triazole thioether, was also attempted. Key intermediates of these two synthetic targets were successfully isolated, but the production of the final target compounds was not achieved.

The successfully synthesised compounds from class one and class two were now available for testing in a human nNOS inhibition assay. These compounds were novel and had been identified via a variety of computational screening methods. In order to test their inhibitory activity, a human nNOS assay was now required.

4 NOS Expression, Assay Development and Compound Evaluation

4.1 Introduction

The vast majority of nNOS inhibitor evaluation is currently performed using the rat isoform of the enzyme, with inhibitor selectivity routinely being determined by testing with bovine eNOS and murine iNOS.^{32,49,52,57,98,99} This use of different isoforms is not an accurate system for determining the effectiveness of compounds against human nNOS. This work aimed to address these issues by expressing all three human isoforms of NOS in *E. coli* cells, and to use the recombinant proteins in a robust and reproducible NOS assay system. Additionally, the NOS proteins will be co-expressed with human calmodulin (CaM), a protein which is vital to NOS function.^{10,100} It was expected that this co-expression approach, not reported thus far in the literature, would improve NOS activity in subsequent assay systems. The avoidance of human NOS enzymes by the scientific community suggests that the expression and purification of these enzymes is non-trivial. As such, it was anticipated that the development of a reliable human NOS recombinant expression system would be challenging and would present a range of difficulties that would have to be overcome.

To address the challenges that would be associated with human NOS production, the approach outlined in **Figure 4.1** was used. Each stage of this process required careful optimisation and consideration of the experimental approach. The overall experimental design first involved the amplification of the NOS DNA, followed by transformation of a suitable expression host with the amplified DNA. The growth and lysis conditions at this stage were scrutinised closely, as were the optimum affinity purification conditions. If the NOS/CaM protein complex could be isolated from these experiments, it would then be used in a Griess assay system. Each stage of this process and the difficulties faced will be described in this chapter.

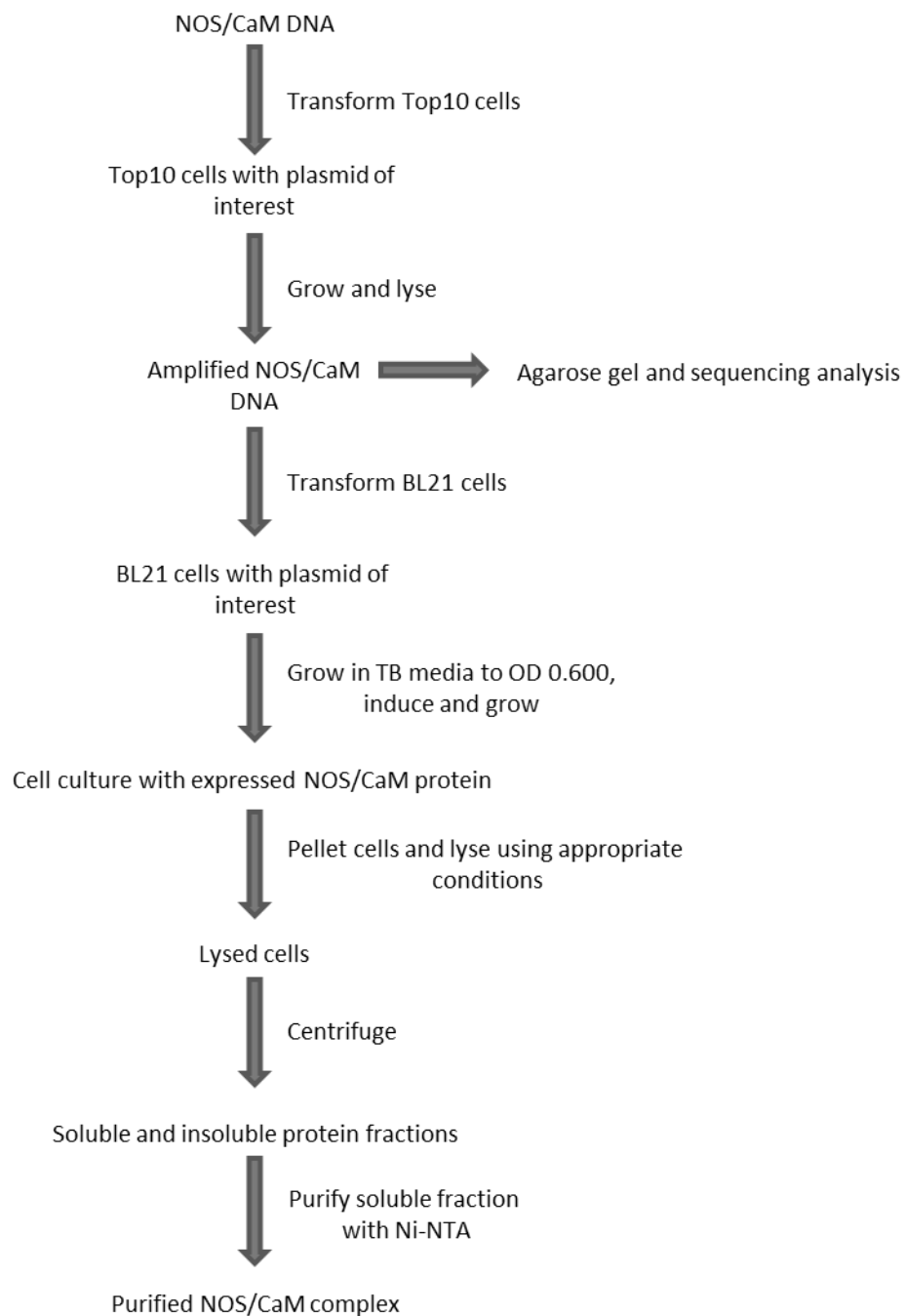


Figure 4.1. Flowchart describing the general steps for NOS/CaM expression.

4.2 DNA sequencing and verification of insert

The first stage of the expression protocol was to transform TOP10 *E. coli* cells with the plasmid containing the human NOS (either eNOS, iNOS or nNOS) and calmodulin genes. This was done to amplify the DNA and ensure sufficient DNA stocks were available for analysis and future experimental work. TOP10 *E. coli* cells were used for this step because they have high transformation efficiency (1×10^9 colony form units (cfu) / μg of plasmid DNA) and have been genetically modified to knock out a number of *E. coli* genes that code for restriction enzymes. If present, these restriction enzymes could degrade the plasmid DNA.¹⁰¹

The TOP10 cells were transformed with the DNA as per chapter five, section 5.2.2.1. Following transformation, the clones were analysed via agarose gel electrophoresis to ensure that the transformation process was successful, and to ensure that the NOS and calmodulin gene sequences were the correct length. Five clones were grown for each gene and the plasmid DNA removed from them. The NOS and CaM genes were excised using restriction digestion and ran on agarose gels. The resulting gels for the five colonies of iNOS, eNOS, nNOS and calmodulin are shown in **Figure 4.2** to **Figure 4.5**. The expected band sizes for each digested plasmid are in **Table 4.1**. (See chapter five, section 5.2.1 for plasmid maps).

Table 4.1. Expected DNA band sizes (bp).

	iNOS	eNOS	nNOS	CaM
Band Size 1 (plasmid)*	4041 kb	3803 kb	4386 kb	4274 kb
Band Size 2 (insert)	2840 kb	3221 kb	3381 kb	540 kb

* Plasmid vector with NOS or CaM gene excised

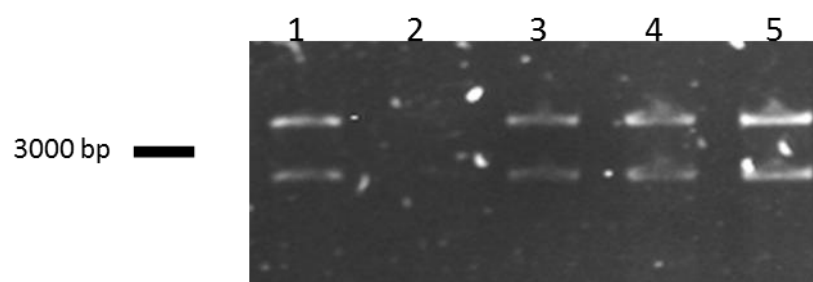


Figure 4.2. Agarose gel analysis of five DNA samples containing the iNOS plasmid. The upper band represents the plasmid vector with the iNOS gene excised, while the lower band represents the iNOS gene. Digested product was observed in four clones, while the clone in lane two was not successfully transformed.

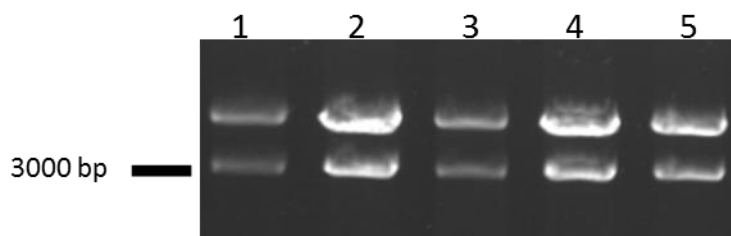


Figure 4.3. Agarose gel analysis of five DNA samples containing the eNOS plasmid. The upper band represents the plasmid vector with the eNOS gene excised, while the lower band represents the eNOS gene. The eNOS gene was observed in all five samples.

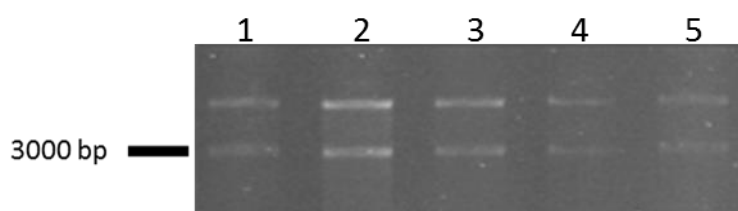


Figure 4.4. Agarose gel analysis of five DNA samples containing the nNOS plasmid. The upper band represents the plasmid vector with the nNOS gene excised, while the lower band represents the nNOS gene. The nNOS gene was observed in all five samples.

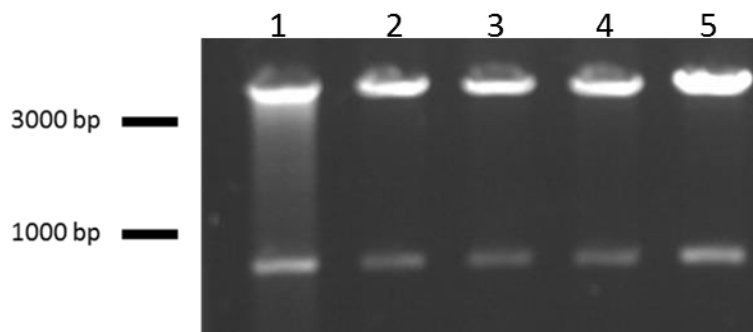


Figure 4.5. Agarose gel analysis of five DNA samples containing the CaM plasmid. The upper band represents the plasmid vector with the CaM gene excised, while the lower band represents the CaM gene. The CaM gene was observed in all five samples.

All band sizes were as expected, with one band for the insert and one for the cleaved vector observed in each construct. The only exception was for the iNOS clone in lane two of **Figure 4.2**. This clone was not successfully transformed with the iNOS DNA. This type of random failure of transformation can occur in these experiments. This was why five transformed clones, and not just one, were analysed for each construct. As the other four clones of iNOS were successfully transformed, this single failure was not a concern. The results presented in the agarose gel analysis demonstrate that DNA of target genes was successfully amplified, and that genes of the correct size were present in each construct. To ensure that the bands represented the NOS and CaM genes, sequencing analysis was carried out.

The suspected NOS and CaM genes were sequenced as per chapter five, section 5.2.2.6. All genes matched their reported sequences with 100% accuracy, with the exception of a single mutation in the human nNOS gene. However, this mutation (R1297S) did not occur close to the arginine binding site and was unlikely to affect inhibitor binding to human nNOS.¹⁰² Full alignments of the four sequenced genes with their published sequences (taken from Uniprot <http://www.uniprot.org/>) are available in appendix, chapter 8.

The human NOS and CaM genes had been successfully verified via sequencing, and the DNA constructs had been amplified using the TOP10 *E. coli* cells. With this DNA in hand attention was turned to expression of the target proteins in a bacterial system.

4.3 nNOS expression and purification

As human nNOS was the key target for this project, efforts were initially focused on the development of an effective expression and purification strategy for this isoform. Initial expression trials were based on the published rat nNOS expression protocol, and personal communication with the leading groups in the field.¹⁰³ It was anticipated that these initial expression conditions would need to be significantly modified to improve the expression, solubility and purification of the target protein. It was of key importance to optimize this procedure so that the maximum amount of human nNOS could be captured from each experiment. This would improve the likelihood of developing a successful assay protocol. It was hypothesised that if a successful human nNOS expression and purification protocol could be developed; then the same conditions could be applied to human eNOS and iNOS.

4.3.1 Establishing a jackpot clone

The two most popular strains for *E. coli* recombinant expression are the BL21 strain, and the M15 strain. The M15 strain contains an extra plasmid, prep4. This plasmid codes for kanamycin resistance. If M15 cells were used for expression, the media would have to be treated with three types of antibiotic when the cells were transformed with the NOS and CaM plasmids. Namely, kanamycin for the prep4 plasmid, ampicillin for the NOS plasmid and chloramphenicol for the CaM plasmid. This may decrease overall NOS expression levels as the cells would need to expend a large amount of resources in expressing the proteins which confer antibiotic resistance. BL21(DE3) cells were therefore chosen for the expression work. Use of this strain would mean that the media would only need two antibiotics, ampicillin and chloramphenicol. Kanamycin would not be required as BL21(DE3) cells do not contain a prep4 plasmid. BL21 cells were also used in the published rat nNOS expression protocol.¹⁰³

BL21(DE3) cells were initially transformed with human nNOS DNA and four clones were assessed to determine their ability to express the protein. The four clones were grown in 3 mL of LB media to an OD₆₀₀ of 0.600 at 37 °C. These were then induced with 1 mM Isopropyl β-D-1-thiogalactopyranoside (IPTG) and grown overnight at 37 °C. The cells were

then pelleted and solubilised in 400 μ L of sample buffer (chapter five, section 5.2.3). The levels of human nNOS present in each sample were then analysed via Western blot using equal volume loadings (40 μ L) for each sample (**Figure 4.6**). A specific anti-human nNOS antibody was used to probe the samples at a concentration of 1:1000 in PBST. The clone which expressed the largest amount of the target protein was termed the “jackpot” clone.

Human nNOS (MW ~160 kDa) was successfully expressed in three out of four clones. Similar to the DNA amplification experiments, failure of individual clones to express the target protein is not an issue if other clones are expressing the protein. Relatively high levels of human nNOS were detected in the samples from clones two and three. No expression was observed in clone one and a trace amount of nNOS was detected in clone four (**Figure 4.6**). BL21(DE3) cells had now been successfully transformed with the human nNOS gene and the protein was expressing successfully. The expression experiments could now be scaled up to in the hope of generating sufficient quantities of protein for the assay work. A glycerol stock was made from clone three for storage of the jackpot clone.

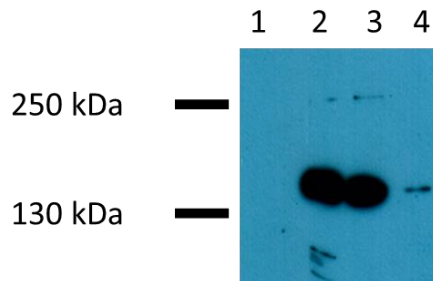


Figure 4.6. Jackpot clone trials for human nNOS. Clone one in lane one shows no detectable level of nNOS expression. Clones two and three show good levels of expression, while clone four shows very little expression. (1:1000 anti-human nNOS). Expected band size of human nNOS 160 kDa. All lanes loaded with equal volumes of whole cells lysed in sample buffer.

4.3.2 Initial large scale expression conditions

With a strongly expressing clone identified, large scale expression trials were attempted. The scale of expression needed to be relatively large (~ 2 L cultures) to generate enough functional protein for use in the Griess assay. The development of an optimised, large scale expression procedure was to prove challenging, and required a large degree of refinement.

The glycerol stock for clone three (**Figure 4.6**) was grown on agar plates and individual colonies were transferred to LB media containing appropriate antibiotic (50 µg/µL ampicillin). After overnight growth, the LB culture was used to inoculate fresh TB media containing 50 µg/µL ampicillin and supplemented with 2 µM riboflavin and 1 mM aminolevulinic acid. These additives acted as FAD/FMN and heme precursors respectively.^{104,105} The cells were grown to an OD₆₀₀ of 0.600, induced with 1 mM IPTG and grown overnight for 42 hours at room temperature. These are the growth times and temperatures that are reported for rat nNOS expression post induction.¹⁰³ Once the cells were grown, they needed to be lysed so that any expressed human nNOS could be purified. Lysis of the cells was conducted using a lysis buffer.

All buffers for human nNOS lysis and purification were adjusted to pH 8. This is within one unit of biological pH, which should aid in protein folding. A pH closer to 7 was not used as while it could aid in protein folding, the isoelectric point (pI) of human nNOS is 7.1. Use of a buffer with a pH too close to this pI value may result in severe protein aggregation due to loss of secondary structure folding interactions. pH 8 was used for buffers instead of pH 6 as the pK_a of the histidine side chain is roughly 6.¹⁰⁶ If a pH of 6 had been selected, this could have resulted in the protonation of the His-tag histidine imidazole rings. This would render the nNOS protein unable to bind to the Ni-NTA resin, making it unsuitable for purification by column chromatography. Calcium chloride was also added to all buffers as this expression strategy involved the co-expression of nNOS and calmodulin. The CaCl₂ would allow the calmodulin to bind to the nNOS protein during these co-expression experiments.

In the initial lysis buffer, the ionic strength was provided by NaCl, while the Na₂HPO₄ was used to buffer the pH. β-Mercaptoethanol was used to disrupt potential disulphide bonds, while the Triton X-100 was a detergent used to solubilize cell membranes. Proteases were inhibited using the Sigma inhibitor cocktail and phenylmethylsulfonyl fluoride (PMSF).

Lysozyme was included to help break open the cells, while the glycerol was present to help stabilize human nNOS. The inclusion of glycerol for target protein stabilisation is routine in these types of experiments. BH₄ is a key co-factor of nNOS that is not provided by *E. coli* and the inclusion of CaCl₂ has been explained above. The components and their final concentrations are outlined in **Table 4.2**.

Table 4.2. Initial nNOS lysis buffer (pH 8).

Component	Concentration
Na ₂ HPO ₄	50 mM
NaCl	300 mM
B-Mercaptoethanol ^a	10 mM (140µL/100mL)
Triton X-100	1%
Sigma inhibitor cocktail ^a	1 tablet/100ml
PMSF ^a	1 mM (0.0435g in 2.5ml IPA, 1mL/litre)
Lysozyme	2 mg/ml
Glycerol	20%
Tetrahydrobiopterin	10 µM
CaCl ₂	2 mM

^aAdded just before use

The lysis process was conducted as per chapter five, section 5.2.3.2. For purification, the Ni-NTA resin was pre-equilibrated with 10 mM imidazole in stock purification buffer (50 mM Na₂HPO₄, 300 mM NaCl, 20% glycerol and 2 mM CaCl₂) to reduce the interactions of non-specific proteins with the resin. The resin was loaded into a polypropylene column and the flowthrough was collected. The resin was then washed with the stock purification buffer containing 20, 40 and 60 mM imidazole and the proteins eluted from the column with 250 mM imidazole. The fractions were analysed for human nNOS content via Western blot analysis, shown in **Figure 4.7**.

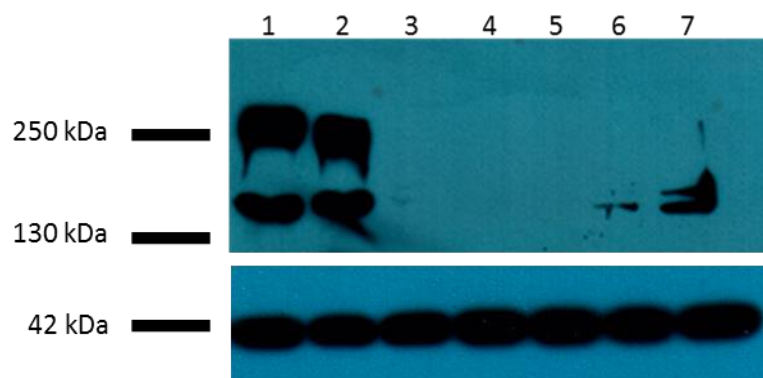


Figure 4.7. Western blot demonstrating initial human nNOS expression and purification conditions. Lane one contains the pellet sample, lane two the cleared lysate and lane three the column flowthrough. Lane four, five and six contain samples from 20, 40 and 60 mM imidazole washing and finally lane seven contains the elution sample. (1:1000 anti-human nNOS). The lower panel is actin loading control, expected M.W of actin was 42 kDa.

Expression was successful as clear bands at the correct molecular weight for human nNOS (160 kDa) could be seen in lanes one, two, six and seven. The higher molecular weight species in lanes one and two was possibly an aggregate or a dimer of human nNOS. This blot demonstrated that significant portions of the expressed protein had become trapped in the insoluble fraction (lane one). This was not desirable as any NOS protein which was in the insoluble fraction could not be purified and had to be discarded. The soluble fraction (lane two) was taken forward for Ni-NTA purification. The nNOS in the soluble fraction bound strongly to the Ni-NTA resin as no band is observed in the flowthrough lane (lane three). This confirmed that affinity purification is a suitable purification technique for this protein. The 20 mM and 40 mM imidazole washes (lanes four and five) did not remove any of the nNOS protein, while a small amount was washed off the column with 60 mM imidazole (lane six). Finally, the elution fraction in lane seven shows a clear nNOS band, indicating that the protein was indeed removed from the resin using a 250 mM imidazole elution. To ensure that these results were robust an actin loading control blot was also produced, proving that the total protein concentration was the same in each lane.

The results generated by the above experiment were encouraging. They demonstrated that the jackpot clone, as established in section 4.3.1, could be used for a larger scale expression. Human nNOS was successfully expressed and was purified using affinity chromatography. However, several issues needed to be addressed from this initial

expression, lysis and purification procedure. The solubility of the target protein was an issue, with a significant portion of human nNOS remaining in the insoluble fraction following cell lysis. The amounts of aggregated species were also of concern. To try and improve this situation, and to increase the amount of protein captured from the resin in the elution step, a variety of expression, lysis and purification experiments were conducted. The results of these experiments are outlined in the following sections.

4.4 nNOS expression and cell growth conditions

Solubility of a recombinantly produced protein can vary greatly depending on the growth and induction conditions used. A number of these conditions were examined for this system to assess their impact on human nNOS solubility. These conditions included;

1. Induction conditions
2. The effect of growth medium
3. The effect of temperature
4. Expression and solubility levels at various time points post induction

These conditions were chosen for experimentation as they are well reported as having a major impact on recombinant protein production and solubilisation.¹⁰⁷ It was hoped that varying these conditions would address the issues surrounding human nNOS production as described above.

Equal volume loading was used for the Western blot analysis of the optimisation trials. When two conditions were to be compared, e.g. IPTG versus no IPTG, the cultures were grown in identical conditions with identical volumes of media. Following the growth and expression procedures the same volume of lysis buffer was used to resuspend the pelleted cells in both conditions. These cells were then lysed and centrifuged, resulting in an insoluble and a soluble fraction for both conditions. The insoluble material was resuspended in PBS. An equal volume of all material, both soluble and insoluble, was then loaded onto the gels.¹⁰⁸ This allows for comparison of nNOS protein levels across lanes of the Western blots that will be presented in the following sections.

4.4.1 IPTG induction

Recombinant protein production makes use of the host cell's transcription and translation machinery to produce the target protein. This process can strain the host cell, as resources are rapidly consumed in the production of the recombinant protein, to the detriment of native protein production. If the recombinant production begins too early in the cell culture's growth cycle, the cells may die from the strain. Also, if the recombinant protein of interest is toxic to *E. coli* cells, production of large volumes of the target early in the cell growth cycle may lead to total cell death.¹⁰⁷

To prevent this from occurring, the expression from the genes for the recombinant protein can be controlled via inducible expression.¹⁰⁹ A promoter is located upstream from the gene of interest, in this case human nNOS. This promoter is "turned off" in its native state due to the binding of an inhibitory protein to the promoter sequence. This inhibitor prevents mRNA polymerase from transcribing the human nNOS gene. Gene expression can be "turned on", or induced, by addition of IPTG. This binds to the promoter sequence and causes the inhibitor protein to be cleaved from the promoter sequence. The mRNA polymerase can then bind to the promoter, and the human nNOS gene can be transcribed.^{110,111}

In theory, production of the human nNOS protein should therefore not occur before addition of IPTG. However, many gene constructs under the control of the lac operator exhibit "leaky" expression of the target protein, i.e. expression of the protein in the absence of an inducing agent.¹¹² If significant leaky expression occurs then addition of IPTG may make little difference to the level of soluble protein produced. If leaky expression occurs, at a very low level, omission of IPTG may result in extremely poor soluble protein yields. The effect of IPTG addition therefore needed to be investigated for the nNOS expression system.

Two cultures of human nNOS were grown to an OD₆₀₀ of 0.600 as described in section 4.3.2. Protein expression was induced in one of these cultures with 1 mM IPTG, while the other was not induced. These were grown for 42 hours at room temperature. The cultures were lysed and the soluble and insoluble fractions for each were analysed (**Figure 4.8**). No purification steps were carried out as the goal of this experiment was to examine the effect of IPTG on protein solubilisation. Purification was therefore not required.

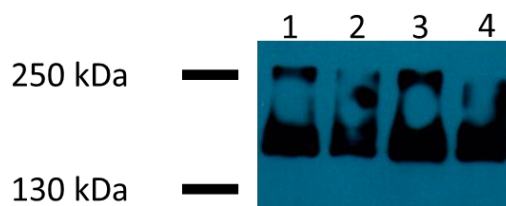


Figure 4.8. Human nNOS induction trials. Lanes one and two contain uninduced (without IPTG) pellet and cleared lysate, respectively. Lanes three and four contain induced (with IPTG) pellet and cleared lysate, respectively (1:1000 anti-human nNOS antibody). All lanes loaded with equal volumes.

For the induced samples (lane three and four), it appeared that more of the protein moved into the soluble fraction when compared to the uninduced samples. This suggested that induction with IPTG was preferable for human nNOS expression. A degree of “leaky” expression (expression of the target protein without IPTG addition) was observed in this system. This is commonly found with pQE-30 plasmid as the T5 promoter is recognised by *E. coli* mRNA polymerase.¹¹⁰ This leaky expression could be controlled or eliminated by switching to a T7 promoter which is not recognized by *E. coli* mRNA polymerase, or by the use of M15[prep4] cells for expression.^{111,113} The prep4 plasmid held by these cells produces excess lac repressor to help silence the T5 promoter prior to induction. As nNOS was already expressing successfully even with the leaky expression, none of these solutions were required.¹¹³

An IPTG concentration screen can be conducted to determine the optimum concentration for protein expression. However, as 1 mM is the recommended concentration for induction of expression from a pQE-30 vector (Qiagen manual) and because 1 mM IPTG worked well in the nNOS system, this trial was deemed unnecessary. The existing system was observed to function correctly, and induction with 1 mM IPTG resulted in a better solubilised target protein when compared to the uninduced samples.

4.4.2 Growth Media

The effect of the growth media on target protein expression and solubility was then examined. TB media is richer in nutrients than LB media, allowing cultures to reach a higher

density than is possible in LB media. However, solubilisation of the target protein is equally important. The solubility of a target protein can be affected by the media in which the host is grown and so the relative levels of soluble protein resulting from each media must also be examined.¹¹⁴

To determine the most suitable media for human nNOS production a culture was grown in each media to an OD₆₀₀ of 0.600, induced with 1 mM IPTG, grown for 42 hours at room temperature and lysed as before. Both media cultures were supplemented with 2 µM riboflavin and 1 mM aminolevulinic acid. No purification was carried out. The resulting blot is shown in **Figure 4.9**.

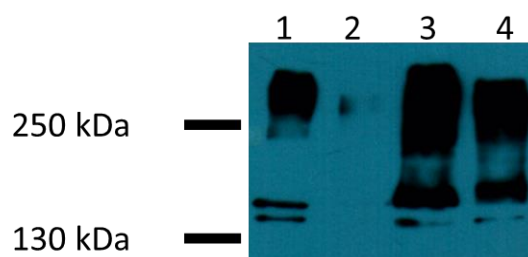


Figure 4.9. LB vs TB growth media trial for human nNOS expression. Lanes one and two contain pellet and cleared lysate samples of cultures grown in LB media. Lanes three and four contain pellet and cleared lysate samples of cultures grown in TB media (1:1000 anti-human nNOS antibody). Expected weight of human nNOS 160 kDa. All lanes loaded with equal volumes.

When expression was induced in LB media almost all of the protein was retained in the insoluble fraction (lane one), and a large portion of it aggregated, rendering it useless for functional assays. For the TB media, large portions of the protein do remain insoluble (lane three). However, a significant portion of the protein is observed in the TB soluble fraction (lane four) and is notably better than the LB soluble fraction (lane two). TB media has been specifically engineered to improve recombinant protein stability and yield, so its superior performance was as expected.¹⁰⁷ It was important to compare its performance to the performance of LB, as LB was the media of choice for rat nNOS expression, and is also one of the most popular media for recombinant protein expression.¹¹⁵ Due to the increased solubility observed with TB, it was chosen as the media for human nNOS protein expression.

4.4.3 Growth temperature

With media and induction conditions optimised, growth temperature post induction was examined. Growing *E. coli* cells at 37 °C post induction may cause the cells to produce the target very quickly, resulting in the formation of insoluble aggregates of misfolded protein called inclusion bodies. Lower growth temperatures post induction may prevent the formation of these aggregates and aid in recombinant protein solubilisation.¹¹⁴

Two separate cultures were grown to an OD₆₀₀ of 0.600 in TB media supplemented with 2 µM riboflavin and 1 mM aminolevulinic acid, and induced with 1 mM IPTG. One culture was grown at 37 °C for 42 hours and one was grown at room temperature for 42 hours. The resulting cells were lysed and analysed via Western blot (**Figure 4.10**).

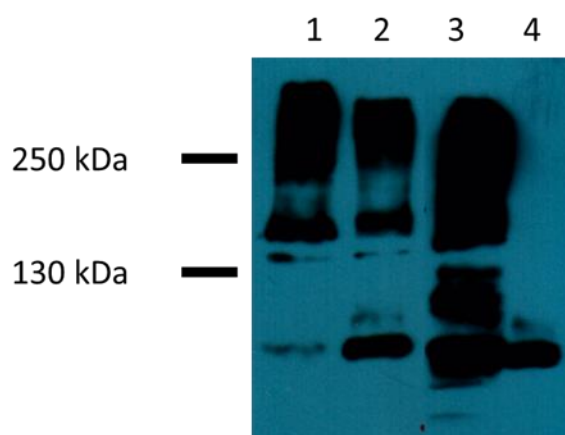


Figure 4.10. Temperature trial for human nNOS expression. Lanes one and two contain pellet and cleared lysate samples from TB cultures grown at room temperature. Lanes three and four contain pellet and cleared lysate samples from TB cultures grown at 37 °C (1:1000 anti-human nNOS antibody). Expected weight of human nNOS 160 kDa. All lanes loaded with equal volumes.

Growth at 37 °C resulted in severe aggregation of human nNOS, evidenced by the “streaky” bands in lane three. The vast majority of the protein was also rendered insoluble under these conditions as no band was observed at the correct molecular weight in lane four. At 37 °C there was considerable degradation of the NOS protein as a large number of bands were seen below the 160 kDa marker.

Cultures grown at room temperature were noted to have some degree of aggregation. However, a much greater portion of the human nNOS was found in the room temperature soluble fraction (lane two) in comparison to the 37 °C soluble fraction (lane four). Room temperature was chosen as the better option for human nNOS production.

4.4.4 Cell growth time course

The final optimisation experiment for the expression and growth conditions focused on optimising the time taken to grow the cell cultures post induction. So far, all cultures had been grown for 42 hours, as this was the growth time used for rat nNOS.¹⁰³ Long time courses for culture growth may result in greater cell densities and thus higher protein yields. This must be balanced against the possible formation of inclusion bodies, as the cellular concentration of recombinant protein increases.

A TB culture was induced at an OD₆₀₀ of 0.600 and grown at room temperature. Samples were taken at 8, 12, 24 and 42 hours (h) post induction. Pellet and cleared lysate of each sample were analysed as before (**Figure 4.11**). Time points as far as 42 hours were taken in order to compare with the reported expression time for rat nNOS expression.¹⁰³ Longer time points were not analysed as one of the goals of the experiment was to decrease the overall growth time, if possible, and to improve processing times for human nNOS recombinant production. Also, after 42 hours at room temperature, TB cultures were observed to have reached maximum confluency as measured by OD₆₀₀ measurements. Further growth time was therefore not required.

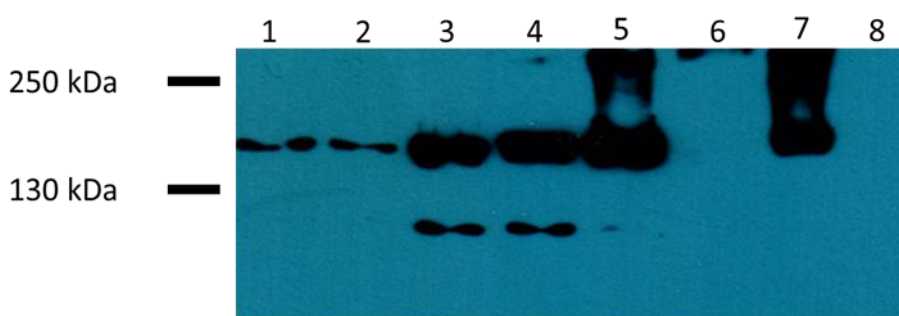


Figure 4.11. Time course for human nNOS expression. Lanes one and two contain pellet and cleared lysate sample from culture which was grown for 8 h post induction. Lanes three and four are from 12 h post induction, five and six from 24 h post induction and seven and eight are pellet and cleared lysate samples taken 42 h post induction (1:1000 anti-human nNOS antibody). Expected weight of human nNOS 160 kDa. All lanes loaded with equal volumes.

At any time point past 24 hours it was seen that nearly all of the nNOS protein had migrated to the insoluble fraction. Although previous experiments had shown some level of protein solubilisation after 40 hours, this experiment suggested that 12 hours was the optimal growth time for the cultures. Any shorter resulted in lower levels of nNOS expression, while longer time points showed severe aggregation and insolubility. This was considerably shorter than the growth time suggested in the rat nNOS expression procedure.¹⁰³ The 12 hour growth period resulted in better solubilised protein, and also increased the speed at which large quantities of the protein could be produced for functional assay testing.

4.4.5 nNOS expression and cell growth conditions conclusion

The experiments described above were designed to probe the cell growth and protein expression conditions, in the hope of improving the solubility and overall yields of human nNOS. The initial conditions used were based on those previously published rat nNOS recombinant expression conditions.¹⁰³ This used LB media, grown at room temperature for 42 hours, with expression being induced with 1 mM IPTG. Following examination of these conditions, and trials of alternatives, the optimum conditions for human nNOS expression were found to be growth in TB media, at room temperature for 12 hours, using 1 mM IPTG

for induction. These resulted in a significant improvement in protein solubility, and in efficiency of protein production. The new conditions were carried forward for the next set of experiments, which involved optimising the lysis and purification conditions for human nNOS recombinant expression.

4.5 nNOS lysis and purification conditions

As alluded to in section 4.3.2, optimal lysis and purification buffer conditions are difficult to predict for recombinant protein experiments. These buffers play a key role in the solubility and overall yield of target proteins, and therefore merit careful examination. Four separate buffers were analysed for human nNOS expression. The results with each buffer are presented in the following section.

4.5.1 Lysis buffer screen

Four separate, yet identical one litre nNOS cultures were grown according to the new optimal growth conditions, section 4.4.5. Upon cell harvesting the pellets were resuspended in equal volumes of one of four possible lysis buffers (**Table 4.3**). All four buffers contained protease inhibitor tablet, 1% Triton X-100, 10 mM β -mercaptoethanol, 1 mM PMSF, 2 mg/mL lysozyme, 10 μ M BH_4 and 20% glycerol, 2 mM CaCl_2 but varied in their ionic strength and buffer components as outlined in **Table 4.3**. Each culture was lysed with rolling and sonication as before, and purified via affinity chromatography. The purification buffers were made up of the stocks as shown in **Table 4.3**, with the appropriate amount of imidazole added. The ability of each of the four lysis buffers to solubilise human nNOS was assessed via Western blot, **Figure 4.12-Figure 4.15**.

Table 4.3. Buffer conditions screened for nNOS solubilisation. All buffers at pH 8.

Buffer A	Buffer B	Buffer C	Buffer D
300 mM NaCl	500 mM NaCl	500 mM NaCl	500 mM NaCl
50 mM Na_2HPO_4	50 mM Na_2HPO_4	50 mM Tris.HCl	50 mM HEPES

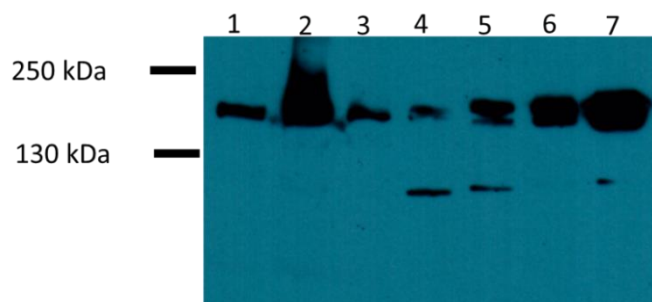


Figure 4.12. Lysis and purification buffer A. Lane one contains the pellet sample, lane two the cleared lysate, lane three the column flowthrough. Lanes four, five and six contain samples of the 20, 40 and 60 mM imidazole column washes, respectively. Lane seven contains a sample of the elution fraction, eluted with 250 mM imidazole. (1:1000 anti-human nNOS antibody). All lanes loaded with equal volumes.

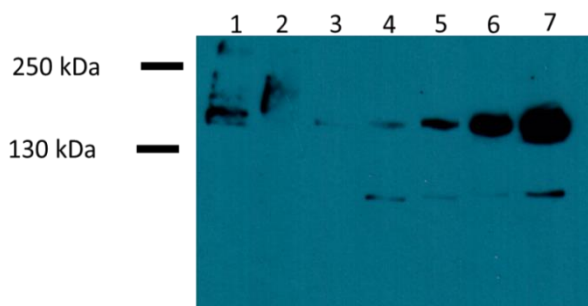


Figure 4.13. Lysis and purification buffer B. Lane one contains the pellet sample, lane two the cleared lysate, lane three the column flowthrough. Lanes four, five and six contain samples of the 20, 40 and 60 mM imidazole column washes, respectively. Lane seven contains a sample of the elution fraction, eluted with 250 mM imidazole. (1:1000 anti-human nNOS antibody). All lanes loaded with equal volumes.

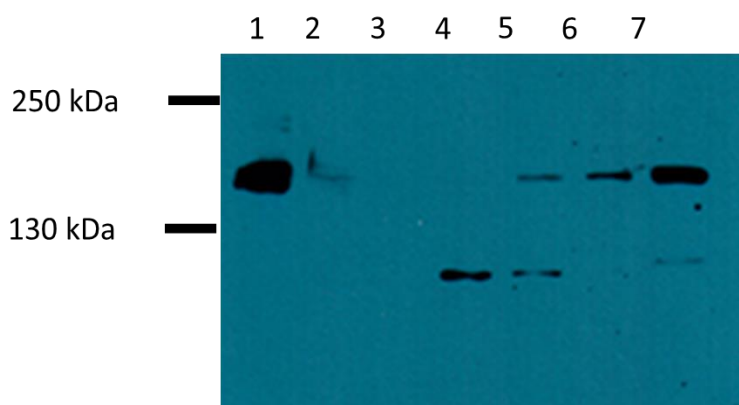


Figure 4.14. Lysis and purification buffer C. Lane one contains the pellet sample, lane two the cleared lysate, lane three the column flowthrough. Lanes four, five and six contain samples of the 20, 40 and 60 mM imidazole column washes, respectively. Lane seven contains a sample of the elution fraction, eluted with 250 mM imidazole. (1:1000 anti-human nNOS antibody). All lanes loaded with equal volumes.

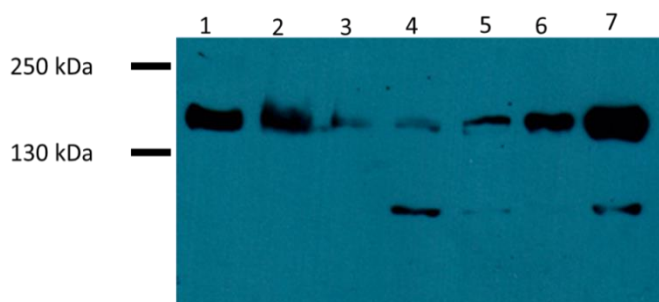


Figure 4.15. Lysis and purification buffer D. Lane one contains the pellet sample, lane two the cleared lysate, lane three the column flowthrough. Lanes four, five and six contain samples of the 20, 40 and 60 mM imidazole column washes, respectively. Lane seven contains a sample of the elution fraction, eluted with 250 mM imidazole. (1:1000 anti-human nNOS antibody). All lanes loaded with equal volumes.

Buffer A was the lysis buffer which had been used for the initial experiments with human nNOS (section 4.3.2). Buffer B was the same buffer but with twice the NaCl concentration. This would investigate how increased ionic strength affected human nNOS solubilisation. Ionic strength of lysis and purification buffers plays a key role in recombinant protein solubilisation and, similar to many aspects of recombinant expression, is difficult to predict.¹¹⁶ Buffer C was chosen as this was previously reported for rat nNOS production

from *E. coli*.¹⁰³ Buffer D was chosen with an ionic strength between A and B. HEPES was also used in Buffer D as the Griess assay system that was to be used for compound testing employed a HEPES buffer. It may be advantageous to use a HEPES based buffer for lysis, purification and in the functional assay to avoid unpredictable interferences that may be caused by mixed buffer systems.

Buffers A (300 mM NaCl, 50 mM Na₂HPO₄, 20% glycerol) and D (500 mM NaCl, 50 mM HEPES, 20% glycerol) were the most successful, with use of each resulting in a strong nNOS band in the elution fraction. Both also showed efficient nNOS solubilisation when compared to buffers B (600 mM NaCl, 50 mM Na₂HPO₄, 20% glycerol) and C (500 mM NaCl, 50 mM Tris.HCl, 20% glycerol). Buffer B, as reported for rat nNOS production, and buffer C were therefore deemed to be ineffective in this system.

Buffer D was chosen over buffer A for future nNOS expression experiments as the former contained sodium phosphate. This resulted in the formation of insoluble calcium phosphate when the calcium chloride was added. This white, insoluble material was not removed by the purification or dialysis steps. It was feared that the resulting turbidity could interfere with the absorption readings during the Griess assay. Also, buffer A showed some degree of human nNOS aggregation in the cleared lysate lane, as evidenced by the streaking of the band in the Western blot. The Griess assay system which was to be used for compound evaluation employed a HEPES buffer. Buffer D was also a HEPES based buffer and so may be more compatible with the assay system. For these three reasons buffer D was chosen over buffer A as the optimal lysis and purification buffer.

4.5.2 Ni-NTA purification screen

The growth, expression and lysis conditions had now been examined and improved. The final aspect of the protocol that required examination was the purification conditions used for affinity chromatography. All human NOS constructs used in this work were expressed with a histidine affinity tag (His-tag). This sequence of six histidine residues binds strongly to Ni-NTA affinity columns. Some non-specific *E. coli* proteins will also bind to this column despite not having a His-tag. These can be removed from the column using low concentration imidazole washes. The purified target protein can then be eluted using a

high concentration imidazole wash.¹¹⁷ The exact figures for “low” and “high” imidazole concentrations differ from protein to protein, with some recombinant proteins binding strongly to the Ni-NTA column, while some bind more transiently. Imidazole wash screens therefore had to be conducted to determine the optimal conditions for human nNOS purification.

The Western blot shown in **Figure 4.15** demonstrates that some of the human nNOS protein was removed from the Ni-NTA column even when relatively low imidazole concentrations (20 mM) washes were used. Any loss of the target protein was undesirable. However, the overall purity of the eluted sample also had to be considered. The use of extremely low imidazole concentrations (<20 mM) may result in more of the target protein being retained on the column and ultimately captured in the elution fraction. However, the use of such low imidazole concentrations may also result in large amounts of non-specific protein being retained on the column and co-eluted with the human nNOS in the elution fractions. Further purification experiments were conducted to ascertain the imidazole concentrations that gave the best balance between protein purity and overall nNOS recovery.

Cultures were grown and purified as described for buffer D in section 4.5.1. To minimize binding of nonspecific proteins to the column, the Ni-NTA was equilibrated with the stock buffer containing 10 mM imidazole prior to purification. The lysed nNOS containing cells were incubated with the Ni-NTA resin as per chapter five, section 5.2.3.3. The resulting Ni-NTA column was then washed with stock purification buffer containing increasing concentrations (20, 40, 50, 60, 70, 80 and 100 mM) of imidazole. All remaining proteins were then eluted from the column with a 250 mM imidazole wash. A Western blot and Coomassie analysis of these experiments are shown in **Figure 4.16**.

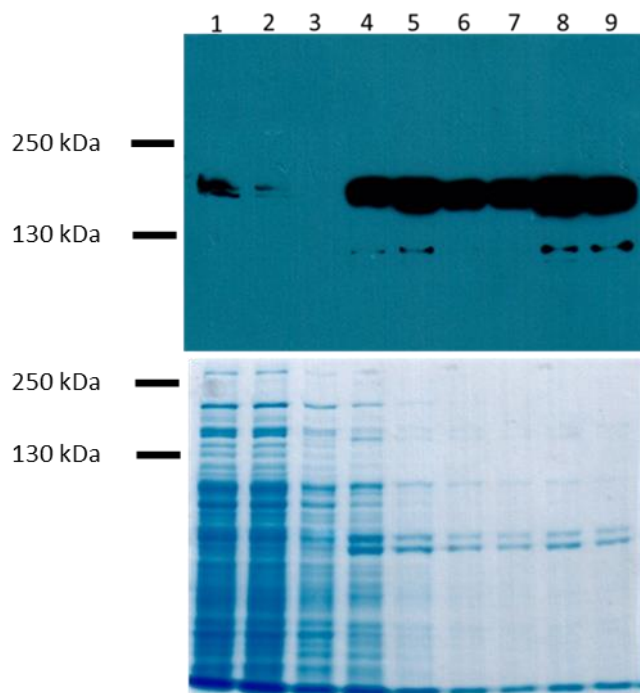


Figure 4.16. Imidazole screen for human nNOS expression. Lane one contains a cleared lysate sample pre Ni-NTA incubation and lane two contains the column flowthrough. Lanes three to nine contain column washes using increasing imidazole concentrations as follows: 20 mM, 40 mM, 50 mM, 60 mM, 70 mM, 80 mM, 100 mM and 250 mM. Also shown in the lower gel is the corresponding Coomassie stain of the same samples with the same layout (1:1000 anti-human nNOS antibody). All lanes loaded with equal volumes.

It can be seen that nNOS protein is removed from the column at 40 mM imidazole concentration and higher. It may therefore be desirable to only wash the Ni-NTA with low (< 20 mM) imidazole concentrations. However, upon examination of the Coomassie gel, it can be seen that the 40 mM wash removes a large amount of non-specific proteins. The loss of target protein with the 40 mM wash was therefore deemed acceptable in order to achieve greater protein purity. The final conditions chosen were to wash the column with 10 column volumes of 40 mM imidazole. This provided a reasonable balance between purity and yield of human nNOS protein.

4.5.3 nNOS lysis buffer and purification conditions conclusion

The initial lysis buffer conditions, as described in section 4.3.2, did solubilize human nNOS, and resulted in the isolation of some the target protein in the elution fraction. However, this buffer did not fully solubilize human nNOS and a portion of the protein remained trapped in the insoluble fraction. Following experimentation with a variety of lysis buffers, a new buffer system was chosen for the human nNOS system. This demonstrated superior solubilisation of the recombinantly expressed protein, and also used the same buffer components as those to be used in the Griess functional assay. The development of this new lysis buffer system was therefore a considerable success.

With the optimised lysis buffer in hand, the purification wash steps and procedures were examined. Optimal column wash conditions were identified, which balanced target protein yield with overall purity. This represented the final step in the optimisation of the human nNOS expression conditions. These conditions were then applied to the co-expression experiments, where human nNOS and human calmodulin were to be expressed in the same cell culture.

4.6 nNOS co-expression with calmodulin

Calmodulin is a key co-factor for all NOS enzymes, and is vital for their function.^{10,100} Calmodulin may be expressed and purified separately and added to NOS preparations, however this is time consuming and wasteful as it requires two separate expression and purification experiments to isolate the calmodulin and NOS proteins separately. It has been observed for human iNOS that co-expression with calmodulin aids in protein folding and helps to ensure maximal NOS activity.¹¹⁸ Human eNOS has also been expressed with and without calmodulin. It was reported that expression with calmodulin resulted in an increased yield of human eNOS and in a more active protein.¹¹⁹ Based on the trends observed for the other two isoforms, it was hypothesised that co-expression of human nNOS with calmodulin could increase protein yield and activity. Such an approach has not been previously reported and may result in significant improvement in human nNOS production.

Human nNOS was co-expressed with human calmodulin using the protocol that had been developed in section 4.4 and 4.5. The calmodulin construct did not have a His-tag and so would not bind to the Ni-NTA resin during the purification process. To avoid losing the calmodulin at this stage, 2 mM CaCl₂ was included in all growth media, lysis and purification buffers. In the presence of calcium calmodulin binds to the eNOS and nNOS proteins forming an active complex which produces NO.¹ This mechanism is one of the *in vivo* regulatory controls of the NOS proteins, ensuring that they are not constantly active. As iNOS is inducibly expressed this regulatory control is not as important, i.e. iNOS binds calmodulin even in the absence of calcium.¹ In theory, inclusion of CaCl₂ should facilitate nNOS/calmodulin complex formation and allow the two proteins to be captured together from the Ni-NTA resin. This remained to be experimentally verified prior to this study.

4.6.1 Co-expression with optimised conditions

To achieve the co-expression of the two proteins, BL21(DE3) *E. coli* cells were transformed with the DNA for both genes as per chapter five, section 5.2.3.1. The veracity of both the nNOS and the calmodulin containing plasmids had been previously established using restriction digestion and DNA sequencing (see section 4.2). Small (3 mL) cultures of these co-transformed BL21(DE3) cells were grown, the plasmid DNA extracted and analysed via agarose gel. No restriction digestion was performed on the isolated DNA as the nNOS and calmodulin constructs contained many of the same restriction sites. Digestion would therefore have resulted in poorly resolved bands of a range of sizes which would not have been helpful. Instead, the isolated DNA was examined for presence of full length plasmids. An example of such an analysis is shown in **Figure 4.17**. The expected length of the full length nNOS and calmodulin constructs was 7767 bps and 4936 bps respectively.

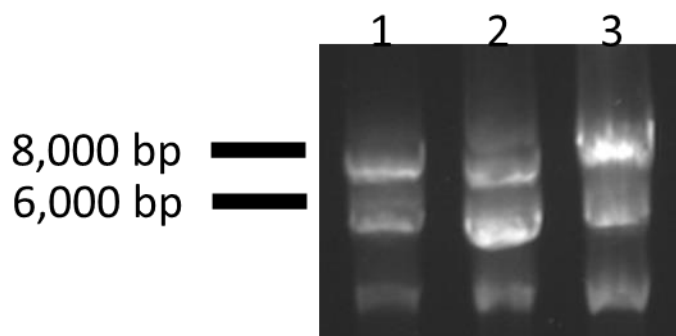


Figure 4.17. Undigested plasmid DNA isolated from three clones transformed with both nNOS and calmodulin plasmids.

The band below the 8,000 bp marker represented the human nNOS construct while the band below the 6,000 bp marker represented human calmodulin. The lowest band was potentially supercoiled DNA. Streaky bands, such as those as observed in **Figure 4.17**, are characteristic of supercoiled DNA.¹²⁰ The supercoiled DNA was not an issue as bands of the expected size for the two genes were also observed. These would provide sufficient sequence information for nNOS and calmodulin transcription. The transformation was therefore deemed a success and a glycerol stock was made for storage from the culture that provided the DNA sample in lane two of **Figure 4.17**.

The glycerol stock was used to grow a large culture and to express the two target proteins according to the optimised human nNOS expression methodology which was developed in section 4.4 and 4.5. The cells were lysed and purified and the various fractions were analysed via Western blot, Coomassie and mass spectrometry. The results of the Western blot and Coomassie are shown in **Figure 4.18**.

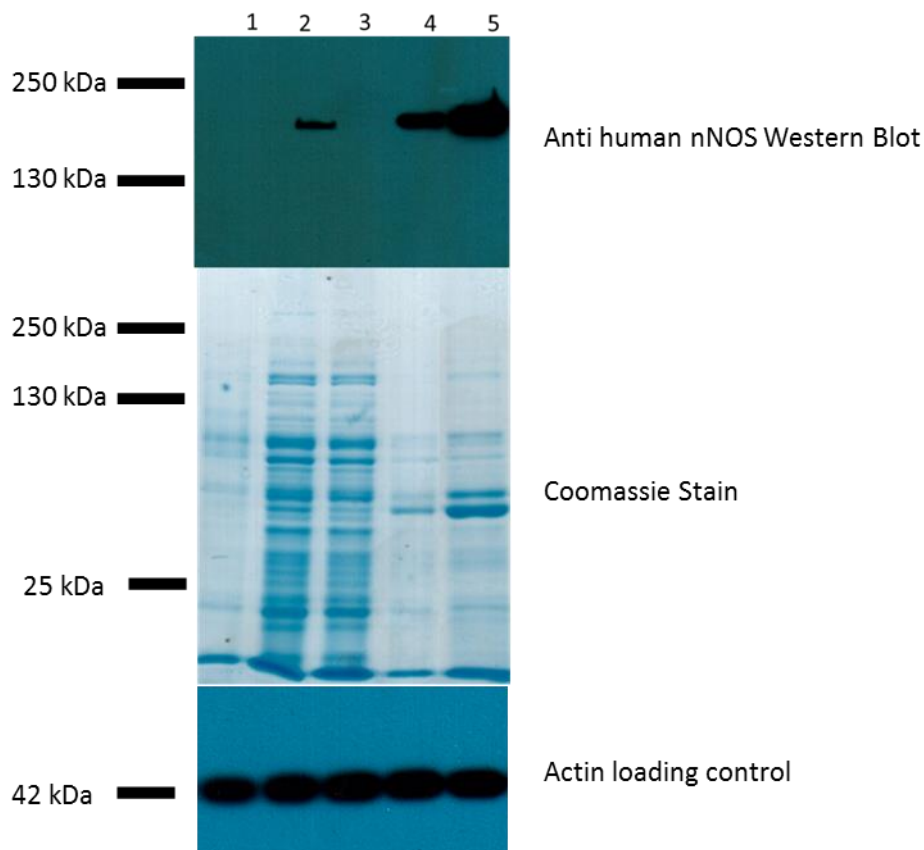


Figure 4.18. Optimised human nNOS/calmodulin co-expression protocol. Lane one contains the pellet sample, lane two contains the cleared lysate sample, lane three the column flowthrough, lane four a 40 mM imidazole wash and finally elution with 250 mM imidazole (1:1000 anti-human nNOS antibody). Expected size of calmodulin 17 kDa, expected size of human nNOS 160 kDa. Representative blot, n=5.

As expected the Western blot confirmed the presence of human nNOS at 160 kDa. The optimised nNOS protocol was consistently producing nNOS, with all of the nNOS protein in the soluble fraction (lane two) and none remaining insoluble (lane one). The nNOS bound well to the affinity column and a loss of protein was observed with the 40 mM imidazole wash as expected (lane four). This 40 mM wash did remove impurities from the column, as can be seen in the corresponding coomassie lane. The heaviest nNOS band is observed in the elution lane (lane five). To ensure that these results were robust an actin loading control blot was also produced, proving that the same concentration of protein was present in each lane.

The co-expression strategy had resulted in improved nNOS expression and solubilisation, as well as human nNOS co-expressed with human calmodulin. The presence of calmodulin was confirmed by excising a number of bands from lane five of the coomassie gel between 15 kDa and 20 kDa (M.W of calmodulin 17 kDa). Following in gel digestion, human calmodulin was identified using an ion trap mass spectrometer and the Mascot search engine.¹²¹ Using the Swiss Prot database and *Homo sapien* as the species, Mascot protein scores greater than 37 were deemed to be significant ($p < 0.05$).

The Mascot score for the calmodulin band was 86, with sequence coverage of 22% and three human calmodulin peptides being identified. Mass spectrometry was also used to confirm the presence of human nNOS in lane five of the coomassie in **Figure 4.18**. After in gel digestion, a Mascot score of 67, with sequence coverage of 19% and three human nNOS peptides were identified. These mass spectrometry results served to verify the Western blot results and demonstrated that human nNOS was indeed being expressed in the bacterial system. This final confirmation was important as the expression of human nNOS in *E. coli* cells had not yet been reported in the literature.

4.7 nNOS protocol development conclusion

An optimised human nNOS/human calmodulin co-expression system was developed. Briefly, BL21(DE3) cells co-transformed with human nNOS and human calmodulin were induced with 1 mM IPTG, grown in TB media (supplemented with 2 μ M riboflavin and 1mM aminolevulinic acid) at room temperature for 12 hrs and harvested in a 500 mM NaCl, 50 mM HEPES, 20% glycerol buffer at pH 8 containing the components outlined in **Table 4.4**.

Table 4.4. Components to be added to the buffer for human nNOS lysis and purification buffers.

Component	Concentration
β mercaptoethanol ^a	10 mM (140 μ L/100mL)
Triton X-100	1%
Sigma inhibitor cocktail ^a	1 tablet/100ml
PMSF ^a	1 mM (0.0435g in 2.5ml IPA, 1mL/litre)
Lysozyme	2 mg/ml
Glycerol	10%
Tetrahydrobiopterin	10 μ M
CaCl ₂	2 mM

^a Added immediately before use

Purification was then conducted with Ni-NTA, washing with 10 column volumes of 40 mM imidazole and eluting the recombinantly expressed proteins with one column volume of 250 mM imidazole. The imidazole washes were made up in the stock buffer of 500 mM NaCl, 50 mM HEPES and 20% glycerol, with CaCl₂ added.

Human nNOS has been successfully co-expressed with human calmodulin using a bacterial system. When the initial expression conditions were used, a large amount of the human nNOS protein remained insoluble and unusable for functional assays (**Figure 4.7**). A variety of experiments were conducted surrounding the cell growth, cell lysis and human nNOS purification procedures to solve these issues. Such an optimisation study is not reported in the literature for human nNOS, and it resulted in a considerable improvement in the solubility, purity and overall yield of the target protein. The new process was also considerably faster than the protocol reported for rat nNOS, with the former using a 12 hour growth time, and the latter a 42 hour growth time.¹⁰³ The NOS protein was also co-expressed with human calmodulin for the first time.

The novel and efficient system which had been developed for human nNOS was next applied to the expression of human iNOS and human eNOS. Currently, functional assays in the field of NOS inhibition most often use bovine eNOS, rat nNOS and murine iNOS for comparison of inhibitor efficacy across isoforms. This approach is sub optimal due the mixture of species which are used in the assay systems. In addition, the reported assay systems also do not use the human isoforms of the proteins, which is an obvious disadvantage when looking to address human diseases. It was hoped that application of the

human nNOS procedure to the human iNOS and human eNOS isoforms would result in an all human assay system that could accurately assess the efficacy of potential NOS inhibitors.

4.8 Human iNOS and human eNOS expression

Human iNOS and human eNOS were the next targets for the expression and assay development work. Once an inhibitor of human nNOS was identified, these two isoforms were to be used to determine the specificity of the inhibitor for nNOS. Both human iNOS and human eNOS were to be co-expressed with human calmodulin. This was to ensure uniformity with the nNOS expression procedure, and to reduce variance between the isoforms in the assay system. The approach taken for the co-expression procedure involved using the previously developed human nNOS protocol for human iNOS and human eNOS. This would hopefully result in a rapid and reliable system for the expression and isolation of all three isoforms. Use of the same conditions would also allow for production of all three isoforms at the same time. This approach could then be used for the rapid expression of the NOS proteins for biological applications.

4.8.1 Co-transformation of human eNOS and human iNOS with human calmodulin

BL21(DE3) cells were co-transformed with human eNOS and CaM, and with human iNOS and CaM as per chapter five, section 5.2.3.1. These transformations were analysed via agarose gel electrophoresis for the presence of full length plasmids. The eNOS plasmid contained 7024 base pairs, the iNOS plasmid contained 6881 base pairs and the calmodulin plasmid contained 4936 base pairs. The analysis of the plasmids is shown in **Figure 4.19**.

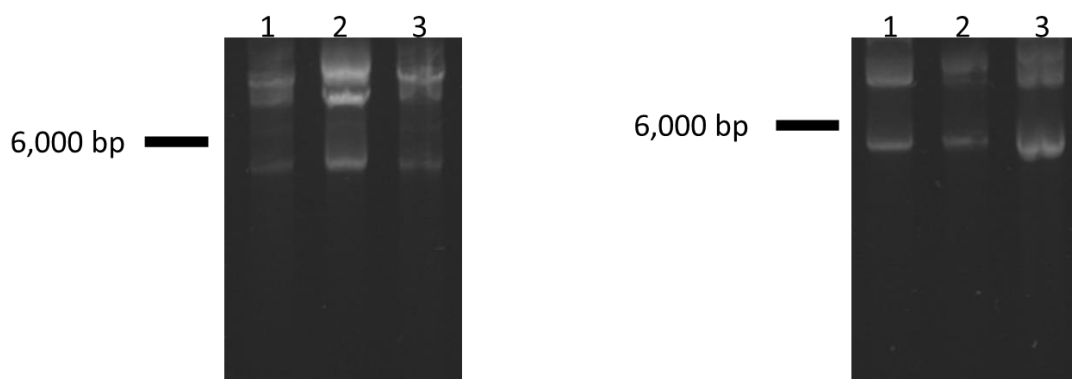


Figure 4.19. Left panel: Plasmid DNA extracted from three clones co transformed with human eNOS and calmodulin. The band below 6000 bp represents the calmodulin construct, while the band above the 6000 bp marker represents human eNOS construct. The upper most band is potentially aggregated DNA. Right panel: Plasmid DNA extracted from three clones co transformed with human iNOS and calmodulin. The band below 6000 bp represents the calmodulin construct, while the band above the 6000 bp marker represents human eNOS construct.

A band representing the respective NOS isoforms can be seen at the correct size in each agarose gel. All samples also show a band at the correct length for human calmodulin. Co-transformation of human iNOS and human eNOS with human calmodulin was therefore deemed a success. The clone in lane two of the eNOS gel and the clone in lane one of the iNOS gel were used to create glycerol stocks for the co-expression studies.

Expression and purification was then carried out as per the optimised nNOS protocol, section 4.4 and 4.5. The only difference was that the iNOS lysis and purification buffer was adjusted to pH 7.5 (rather than pH 8, which was used for eNOS and nNOS). This was because the isoelectric point (pI) of human iNOS is pH 8.2. Use of lysis buffers with a pH close to the pI of the target protein is not advisable as it can result in loss of secondary structure and protein aggregation, ultimately leading to insoluble protein samples. The pI of human nNOS and eNOS is 7.1 and 6.94 respectively. Human calmodulin has a pI of 4.09.

4.8.2 eNOS expression and purification

The glycerol stocks, derived from clone two in the left panel of **Figure 4.19**, was used to grow a culture in TB media using the nNOS conditions. The cells were lysed with the nNOS buffer and the cleared lysate purified by affinity chromatography. A range of imidazole concentrations were trialled for the purification process to determine the best wash concentrations for eNOS. All column fractions, as well as the soluble and insoluble material from the lysis steps, were analysed via Western blot for the presence of human eNOS and human calmodulin (**Figure 4.20** and **Figure 4.21**).

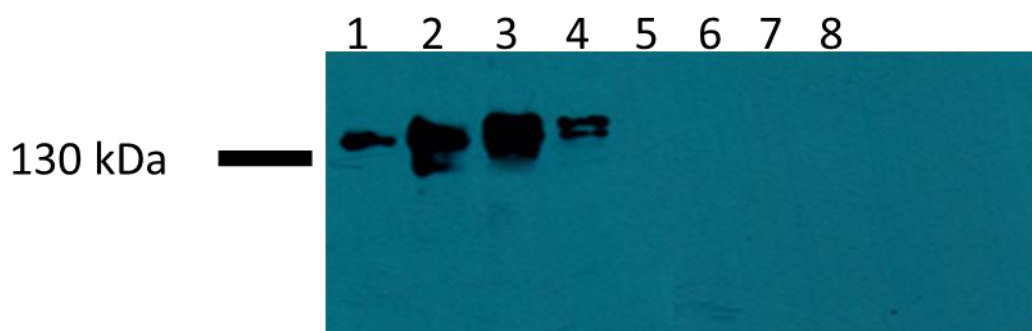


Figure 4.20. Human eNOS expression. Lane one contains a pellet sample, lane two a cleared lysate sample pre Ni-NTA incubation, lane three contains the column flowthrough. Lanes four to eight contain column washes using increasing imidazole concentrations as follows: 20 mM, 40 mM, 60 mM, 80 mM, 250 mM. (Antibody Human eNOS, 1:1000). Lane numbers correspond to lane numbers in **Figure 4.21** (eNOS M.W 133 kDa).

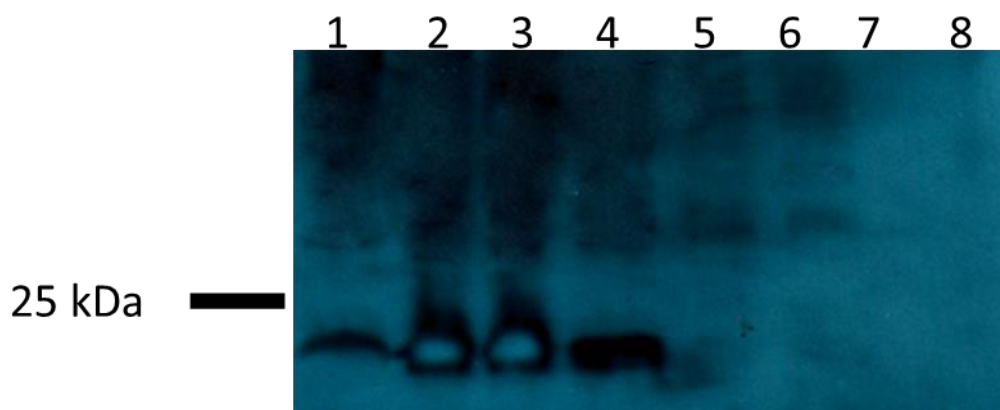


Figure 4.21. Human calmodulin co-expressed with human eNOS. Lane one contains a pellet sample, lane two a cleared lysate sample pre Ni-NTA incubation, lane three contains the column flowthrough. Lanes four to eight contain column washes using increasing imidazole concentrations as follows: 20 mM, 40 mM, 60 mM, 80 mM, 250 mM (Human calmodulin 1:500). Lane numbers correspond to lane numbers in **Figure 4.20**. Expected size of human calmodulin ~ 17 kDa.

Figure 4.20 and **Figure 4.21** represent analysis of the same samples. The blot in **Figure 4.20** was probed with the anti-human eNOS antibody, while the blot in **Figure 4.21** was probed with the anti-human calmodulin antibody. These results were encouraging as the expression and solubilisation of human eNOS was successful (**Figure 4.20**). Clear bands can be seen at the correct molecular weight for eNOS in lanes one to four. Some of the protein was trapped in the insoluble fraction (lane one), although a heavier band was seen in the soluble fraction (lane two). Bands were also seen in the flowthrough lane (lane three) and the 20 mM imidazole wash lane (lane four). However, no eNOS protein was detected in the elution lane (lane eight). The presence of human eNOS in the soluble fraction (lane two) was confirmed via mass spectrometry analysis. Human eNOS was identified with a Mascot score of 54, 9% sequence coverage and two peptides identified.

Human calmodulin was also successfully expressed in this system, with bands observed at the correct molecular weight in lanes one to four. Mass spectrometry confirmed the presence of the calmodulin protein in these fractions (Score 79, 20% coverage, three peptides identified). Both eNOS and calmodulin were observed in the same fractions, suggesting that the two proteins were forming a complex.

While the expression and solubilisation of both target proteins was successful, their purification proved challenging. The blot shown in **Figure 4.20** suggests that eNOS binds very poorly to the Ni-NTA resin as a strong band is observed in the flowthrough lane (lane three). A weaker band is seen in the 20 mM wash lane (lane four), with no detectable eNOS in lanes five to eight. This demonstrated that all eNOS was displaced from the resin with relatively low imidazole concentrations (<20 mM). This analysis is borne out in the literature, with some groups suggesting that 7.5 mM is the maximum imidazole concentration that will not cause elution of the protein from the column.¹²² The weak interaction between eNOS and the column may be due to the folding of the eNOS protein which may result in the histidine tag being buried or partially buried in an internal cavity. It would then be unavailable to interact with the Ni-NTA resin. Ni-NTA affinity chromatography was therefore not ideal for human eNOS purification.

It was postulated that the lack of affinity of human eNOS for the Ni-NTA column may have been caused by the position of the histidine tag in the gene sequence. Human nNOS, which bound strongly to the Ni-NTA column, had its His-tag on the N terminus of the protein, where as human eNOS had the his tag on the C terminus of the protein (see chapter five, section 5.2.1 for plasmid maps). The folding of human nNOS may make the N terminus histidine tag more available for interaction with the affinity resin, where as in eNOS, the C terminus may be partially buried in an internal cavity, thus rendering it inaccessible. This hypothesis would be further explored when human iNOS, with a C terminus histidine tag, was expressed and purified.

Other options for purification were considered at this stage. Size exclusion chromatography could be used to purify the eNOS/CaM complex that had clearly been successfully produced. While this may have resulted in a purified complex, this was not guaranteed. The optimisation and experimental development surrounding size exclusion chromatography would also have been quite considerable.

It was hypothesised that highly pure human eNOS may not be necessary for the Griess assay. This hypothesis was supported by the manufacturer of the Griess assay kit.¹²³ It was therefore decided to test cellular lysates containing eNOS protein in the Griess assay system. Use of these lysates would address the issues surrounding human eNOS purification via affinity chromatography. The cleared lysate sample (lane three, **Figure 4.20**) was taken forward for human eNOS assay development.

4.8.3 iNOS expression and purification

The human iNOS glycerol stock, derived from clone one in the right panel of **Figure 4.19**, was used to grow a culture in TB media as per the nNOS methodology. The cells were lysed and purified using affinity chromatography. Two imidazole washes were used, at 20 mM and 40 mM concentrations, before elution with 250 mM imidazole in the purification buffer. Lower imidazole concentrations were used in the wash steps for iNOS than were used for eNOS as it was suspected that iNOS would be removed from the Ni-NTA column at imidazole concentrations above 40 mM. This would be consistent with the trend observed for human eNOS and human nNOS. For this reason, only two imidazole concentrations were used for column washings.

The samples that resulted from this expression and purification trial were analysed via Western blot for the presence of human iNOS and human calmodulin, (**Figure 4.22** and **Figure 4.23**).

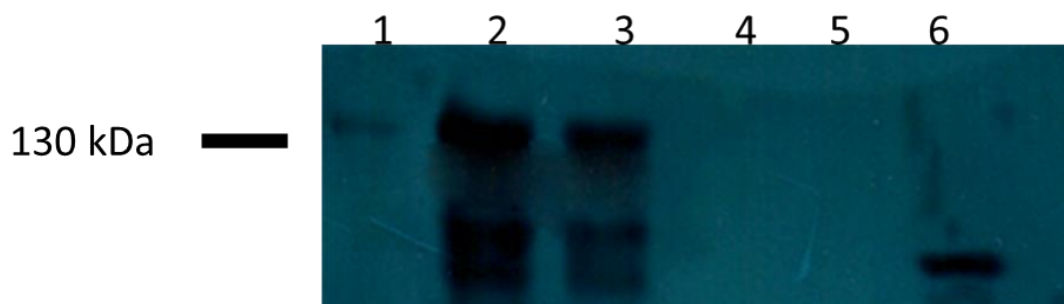


Figure 4.22. Human iNOS expression. Lane one contains a pellet sample, lane two a cleared lysate sample pre Ni-NTA incubation, lane three contains the column flowthrough. Lanes four, five and six contain column washes using 20 mM, 40 mM and 250 mM imidazole concentrations respectively. (1:5000 anti-Histidine). Lane numberings correspond to lane numbers in **Figure 4.23**. (iNOS MW 131 kDa). All samples were loaded with equal volumes.

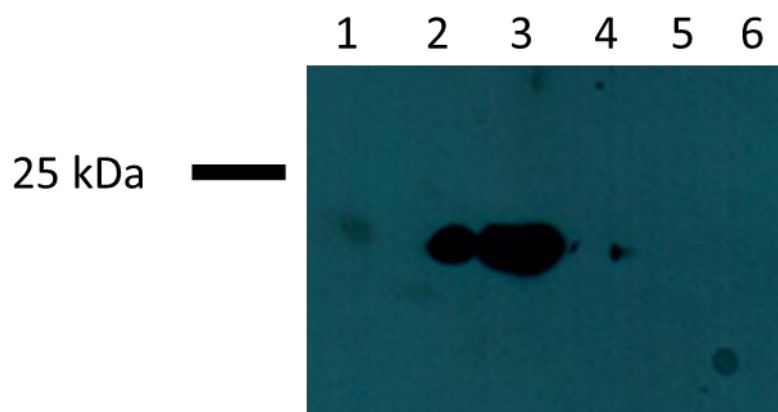


Figure 4.23. Human calmodulin co-expressed with human iNOS. Lane one contains a pellet sample, lane two a cleared lysate sample pre Ni-NTA incubation, lane three contains the column flowthrough. Lanes four, five and six contain column washes using 20 mM, 40 mM and 250 mM imidazole concentrations respectively. (1:500 anti-human calmodulin). Lane numberings correspond to lane numbers in **Figure 4.22**.

Bands of the correct molecular weight were observed in lanes two and three of **Figure 4.22**. This indicated that human iNOS was expressing and was soluble under the conditions used. However, the presence of iNOS bands in the flowthrough lane (lane three), and the absence of bands in the wash and elution lanes, suggested that human iNOS did not bind strongly to the Ni-NTA. This was similar to the results found for human eNOS previously described. This suggests that a C terminus histidine tag is not suitable for human NOS purification via affinity chromatography. The two C terminus tagged proteins, eNOS and iNOS, did not bind strongly to the column, while the N terminus tagged protein, nNOS, did bind successfully.

The presence of human iNOS was confirmed via mass spectrometry of bands around the 130 kDa M.W marker in lane two and three (score of 59, 11% sequence coverage and three peptides identified). However, the bands in **Figure 4.22** are much less distinct than those previously observed for human eNOS and human nNOS. This was because an anti-histidine antibody had to be used for human iNOS detection. Despite multiple attempts, the human iNOS specific antibody did not produce bands in Western blot analysis. It was thought that this was a problem with the antibody sample itself, as human iNOS was successfully identified using mass spectrometry. As an alternative supplier of anti-human iNOS antibody was not available, the anti-His antibody was employed.

The anti-His antibody recognises the His-tag on recombinantly produced proteins, rather than protein specific epitopes. The His-tag on the human iNOS construct was most likely partially buried inside a protein cavity as the construct was unable to bind to the Ni-NTA resin. This same tag was the epitope that the anti-His antibody recognises. Since the antibody could not fully access the partially buried His tag, the bands in the Western blot in **Figure 4.22** appear quite indistinct. The anti-histidine antibody is also notoriously “dirty” and use of it can result in indistinctive and non-specific bands as seen in **Figure 4.22**.¹²⁴ The low band molecular weight bands in lanes two, three and six of **Figure 4.22** are examples of these non-specific bands. These low molecular weight bands were analysed via mass spectrometry and no human iNOS was identified.

Human calmodulin was also expressed in this system, and was present in the same lanes as human iNOS (**Figure 4.23**). This is as expected as iNOS binds to calmodulin most strongly out of the three NOS isoforms. The band in lanes two and three of **Figure 4.23** were confirmed to represent human calmodulin via mass spectrometry.

Although expression and solubilisation of human iNOS with human calmodulin was achieved, affinity purification with Ni-NTA was not ideal for this isoform. Size exclusion chromatography was a possible alternative to affinity chromatography for iNOS/CaM purification. However, a similar approach was taken for human iNOS/CaM as was adopted for human eNOS/CaM. A cleared lysate solution, taken from lane two of **Figure 4.22**, was to be trialled in the Griess assay. It was now envisaged that the purified human nNOS/CaM complex could be used to test inhibitor efficacy, while the cleared lysate samples of eNOS/CaM and iNOS/CaM would be used to evaluate inhibitor specificity.

4.9 Human iNOS and human eNOS expression conclusion

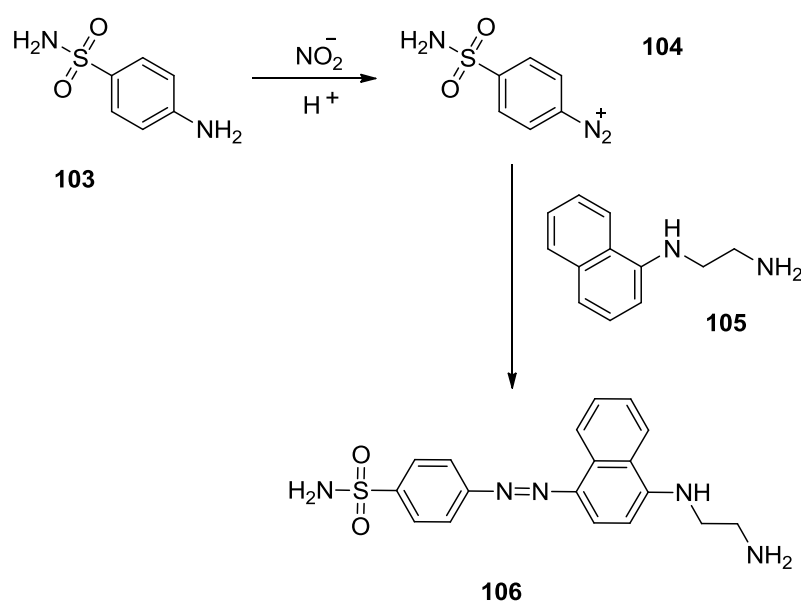
Human iNOS and human eNOS proteins were successfully expressed in the bacterial system and both were co-expressed with human calmodulin. This represented an important step towards the establishment of an all human isoform NOS assay. Purification of the isoforms via affinity chromatography proved challenging, with both iNOS and eNOS binding very weakly to the column. While purification of these isoforms may be better achieved via an alternate technique, such as size exclusion chromatography, this would be time consuming

and had no guarantee of success. The cleared lysate samples containing human iNOS and human eNOS were therefore taken forward for testing in a functional biological assay. The use of crude protein preparations in such an assay system had been previously reported, and the assay manufacturers suggested that the lack of purity of the iNOS and eNOS proteins would not be problematic.¹²³ Samples of all three human NOS isoforms were now on hand for functional assay development.

4.10 Functional assay development

4.10.1 Assay Components

The assay system which was employed for compound testing made use of the recombinantly expressed NOS proteins. When active, the NOS isoforms produce the radical nitric oxide, which is quickly degraded into nitrate and nitrite metabolites.¹²⁵ The Griess assay system provides a convenient and quantifiable method of measuring the levels of nitrites that are produced by active NOS. To calculate total NOS enzyme activity, it is necessary to ensure that all nitrates are first reduced to nitrites.¹²⁶ The nitrites are then reacted with sulphanilamide (**103**) to produce a diazonium salt (**104**), which is then further reacted with N-1-naphthylethylenediamine (**105**) to produce a bright purple azo compound (**106**) (Scheme 4.1).



Scheme 4.1. Griess reaction involving nitrite metabolites to produce azo dye.

The absorbance is then read at 540 nm, the λ max for the azo dye. The more active the NOS protein, the more nitrites are produced and the more intense the purple colour becomes. The absorbance readings then increase accordingly and can be converted to nitrite concentrations using a standard curve. In the presence of a NOS inhibitor, the

decreased activity of the NOS proteins results in a decrease in absorbance levels, and a lower nitrite concentration. Comparisons can then be made between treated and untreated NOS samples to determine the effectiveness of the inhibitor.

In addition to NOS proteins, the Griess assay used in this work required several co-factors and additional components which were supplied with the assay kit (Oxford Biomedical, part number NB78). The NOS enzymes were incubated with these, as per chapter five, section 5.2.5 prior to performing the reaction described in **Scheme 4.1**. These additives as described by the assay kit manufactures are outlined in **Table 4.5**.¹²⁷

Table 4.5. Additional components required for NOS activity using the assay system.¹²⁷

Component	Contents
Assay buffer	20 mM HEPES; 0.5 mM EDTA
NADPH Part A	NADP+, Glucose 6-phosphate, L-arginine
NADPH Part B	Glucose 6-phosphate dehydrogenase
Co-factor mix	FAD, FMN, calmodulin

The assay buffer was a HEPES based buffer, with added ethylenediaminetetraacetic acid (EDTA). The EDTA functioned as a protease inhibitor to prevent degradation of the NOS proteins by any residual *E. coli* proteases that may have been present in the samples. NADPH part A provided the NOS substrate, L-arginine, as well as NADP+ and glucose 6-phosphate. These two species react to form NADPH which is required for NOS activation. The formation of NDAPH is catalysed by glucose 6-phosphate dehydrogenase, provided in NADPH part B. Finally, the co-factor mix supplies FAD and FMN, which are key components of the electron transport chain in NOS enzymes. Calmodulin is also provided by this cofactor mix, although this additional calmodulin may not be required for the system used in this project, as all NOS enzymes were co-expressed with calmodulin.

Other assay systems are available for isolated NOS functional assay testing. One of the most popular systems involves measuring the conversion of radiolabelled L-arginine to L-citrulline to determine the level of NOS activity.¹²⁸ Due to the costs, hazards and regulatory constraints associated with using radioactive material, this assay was not employed for this project. Assays which measure the conversion of hemeoglobin to methemeoglobin are also reported.¹²⁹ This is a side reaction of the nitrite formation cycle. This system was initially considered for this project; however it would have had to be conducted in a 1 mL

cuvette, thus dramatically increasing the quantities of human NOS protein that would have been needed for each assay test. The Griess assay was conducted in a 96 well plate which minimized enzyme wastage.

4.11 Standard curve construction

Along with the assay components described above, the Griess assay kit also contained nitrite standards, which were used to construct a standard curve for conversion of absorbance at 540 nM to nitrite concentration. The same standard curve could be used when testing all NOS isoforms. The standards supplied with the kit were diluted according to manufacturer's instructions (**Table 4.6**). The resulting solutions were read at 540 nM and a standard curve constructed (**Figure 4.24**).

Table 4.6. Dilutions and final nitrate concentrations of the nitrate standards for standard curve.

Standard	Final nitrate concentration (μM)	Deionised H ₂ O (μL)	Diluted standard (μL)
B0	0	1000	0
S1	0.5	995	5
S2	1	990	10
S3	5	950	50
S4	10	900	100
S5	25	750	250
S6	50	500	500
S7	100	0	250

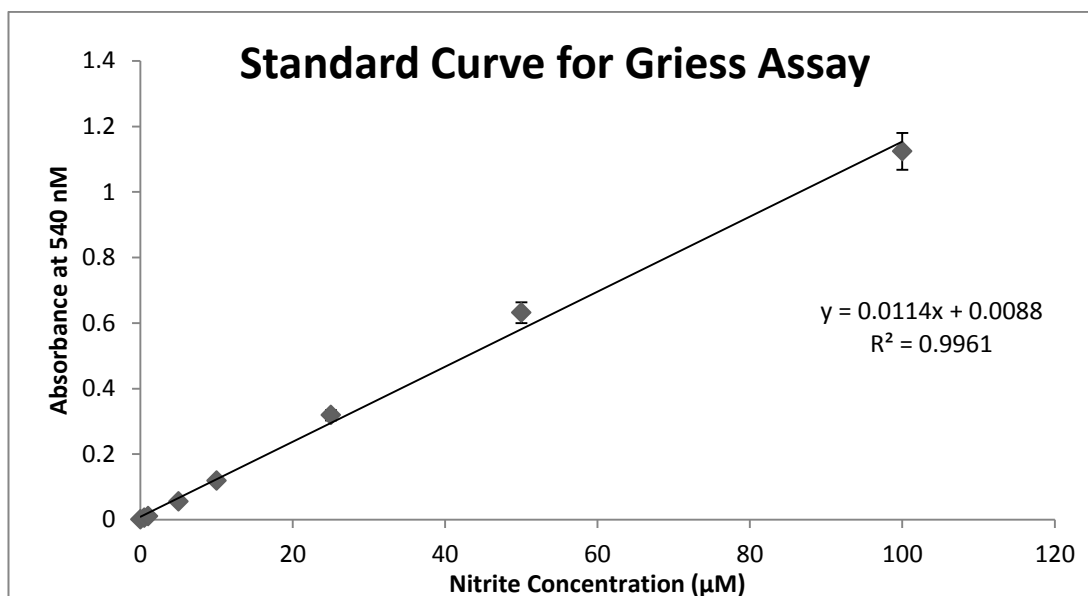


Figure 4.24. Standard Curve for Griess assay system. Representative graph, n=3.

The standard curve had a robust R^2 value of 0.9961, indicating that the curve would be reliable for the conversion of absorbance to nitrite concentration in the NOS assays. With the standard curve constructed the attention was turned to the establishment of the functional assay using the recombinantly produced NOS proteins. This was divided into two separate experiment groups. The assay for nNOS was developed first as it was the key target of the project, and it was the NOS enzyme of highest purity. The assay system using the crude lysates of eNOS and iNOS was then examined.

4.12 NOS assay development

As with all assay systems, it was important to use the proper controls in the NOS inhibition assay. The positive control in all assays was to be an untreated NOS sample. If activity was observed in these untreated wells, it would prove that the NOS assay was functional and producing NO. The second control was a negative control. This involved treating the recombinantly produced NOS samples with a known inhibitor. The inhibitor chosen for this task was L-NNA (**Figure 4.25**). This was chosen as it was relatively inexpensive and available in large quantities. It is also a known non-specific inhibitor of the NOS proteins, and so could be used as the negative control in all three NOS isoform assays. Wells containing the

NOS proteins were treated with 50 μM of this known inhibitor. This concentration was chosen as the reported IC_{50} of L-NNA for rat nNOS was 6.0 μM .⁴⁵ To ensure a response was seen with human NOS proteins, a final concentration of 50 μM was used in the assay systems.

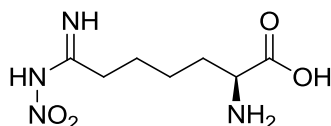


Figure 4.25. L-NNA, the NOS inhibitor used as a negative control in the assay system.

The final control which was included in each assay run was a vehicle control. The vehicle refers to the solvent used to dissolve the potential inhibitory compounds that were to be tested against the human NOS isoforms. The vehicle chosen was DMSO as it was to be used to dissolve the small molecules for biological evaluation. Therefore, each assay plate would include a set of wells containing the NOS protein treated with DMSO. The enzyme activity levels in the wells treated with potential inhibitors would be compared to the activity level in the vehicle treated wells. This would ensure that any change in activity caused by the DMSO vehicle could be negated prior to statistical analysis.

4.13 Human nNOS Griess assay development

As previously mentioned, human nNOS was the enzyme system first studied for assay development. It was envisaged that once the controls had been established for the nNOS system, the same principles and experimental methodology could be applied to the iNOS and eNOS systems. The human NOS proteins used in all of these assays had been co-expressed with human calmodulin as described.

4.13.1 Positive and negative controls

The positive and negative controls for human nNOS were first established. In a 96 well plate, one set of wells contained untreated human nNOS and the necessary assay components. A separate set of wells contained human NOS, the assay components and 50 μM L-NNA dissolved in water. Water was used to dissolve L-NNA as it proved to moderately insoluble in DMSO. A set of wells containing no protein, the assay components and 50 μM L-NNA was also tested to ensure that nitrates were not being formed in the absence of human nNOS. The assay was conducted as per chapter five, section 5.2.5 and the absorbances of each sample read at 540 nm. The absorbances were converted to nitrite concentration using the standard curve (**Figure 4.24**). These were then converted to percentage activity, using the positive control as the 100% activity standard. The results are shown in **Figure 4.26**.

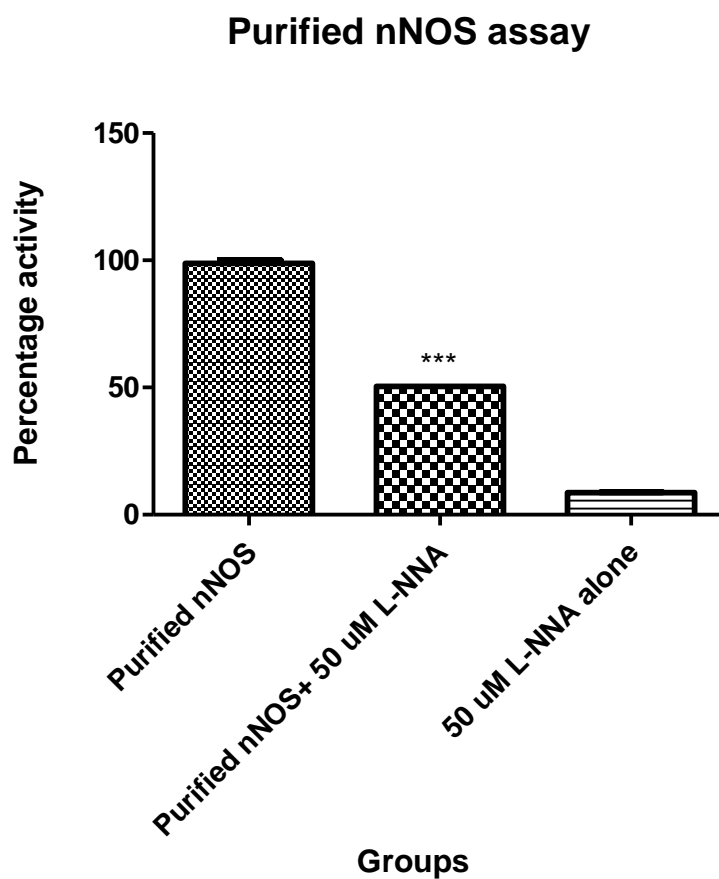


Figure 4.26. Purified human nNOS functional assay with positive control. nNOS was co-expressed with calmodulin. A three star significant difference was observed between the purified nNOS and the purified nNOS treated with L-NNA ($p=0.0008$). Representative graph, $n=5$.

The human nNOS was functional, with the presence of nitrates being immediately obvious due to the purple colour that developed in the plate upon addition of the Griess reagents. The absorbance readings confirm this activity, with a clear decrease in percentage activity observed for the L-NNA treated samples. To the eye, the purple colour in the treated protein well was far less intense than in the untreated wells. When using a t test ($p<0.05$) a three star significant difference was found between the treated and untreated wells. The purified human nNOS was therefore functional and was successfully inhibited by the known inhibitor, L-NNA. Small amounts of nitrates are observed in the absence of the nNOS protein, indicating that the NOS protein was responsible for the vast majority of the nitrite production. These small amounts of nitrites would also be present in the control samples and hence do not affect the final result.

This was a very encouraging result, and represented the first report of functional human nNOS that has been co-expressed with human calmodulin in a bacterial system. The protein was also clearly inhibited by L-NNA, indicating that the enzyme was functioning as expected. This result also represented the achievement of one of the key goals of this project, to establish a functional and reproducible human nNOS assay.

4.13.2 Vehicle control

Vehicle control testing was also conducted. While L-NNA is sparingly water soluble, it was probable that many of the *in silico* derived hits would not be soluble in aqueous solutions. As with many biological assays, DMSO was to be the solvent of choice for compound delivery due to its ability to solubilize most organic compounds. The assay was conducted as before, using untreated human nNOS and nNOS treated with L-NNA. A second sample was also tested with 0.5% DMSO to examine the effect of the vehicle on the enzyme function. The results of this are shown in **Figure 4.27**.

Functional human nNOS DMSO vehicle testing

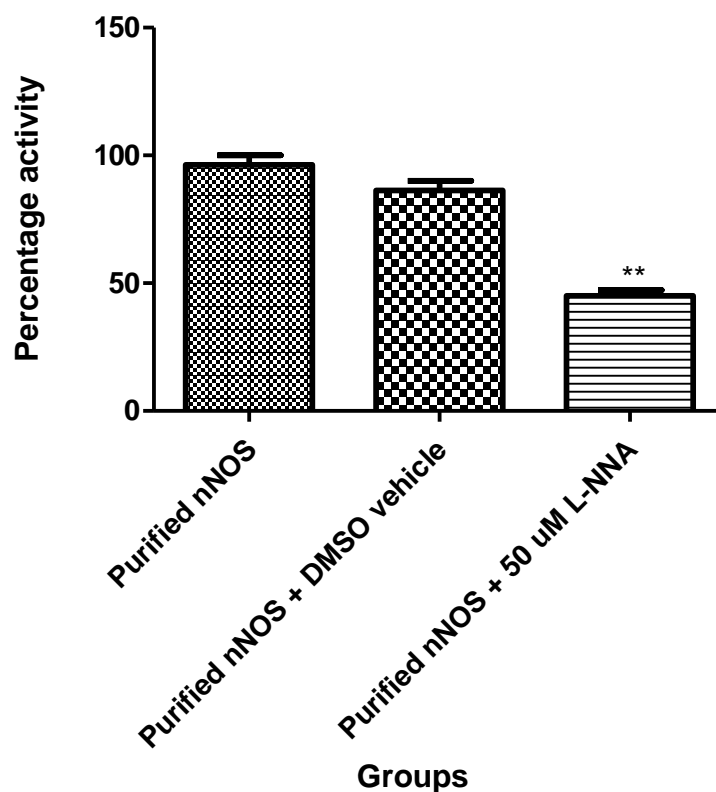


Figure 4.27. Functional nNOS DMSO vehicle testing. The purified nNOS treated with L-NNA showed a two star significant difference from the vehicle treated nNOS ($p=0.0071$). There was no significant difference between purified nNOS and purified nNOS treated with the DMSO vehicle. Representative graph, $n=3$.

Human nNOS was again observed to be functional and was inhibited by L-NNA. On examination of the histogram (**Figure 4.27**) there did appear to be a small decrease in nitrite concentration between the untreated and the vehicle treated sample groups, but importantly, this was not statistically significant. DMSO was therefore a suitable vehicle for this assay.

This result represented the final control experiment for this system. A human nNOS assay system for screening of computationally derived potential human nNOS inhibitors had now been established. The screening of compounds against human nNOS always included a positive, negative and vehicle control to ensure that the enzyme and assay was functioning correctly.

4.13.3 Dose response studies with human nNOS

While it was clearly demonstrated that L-NNA had inhibited human nNOS as expected, it was decided to further explore the human nNOS/L-NNA interaction. There was one previous report of human nNOS being treated with L-NNA.⁴⁵ This paper reported the IC₅₀ of L-NNA for their human nNOS protein as 4.4 μ M \pm 1.0 μ M. The system reported in this paper differed significantly from the work of this project. The publication did not optimise the nNOS expression/purification procedure, did not co-express with human calmodulin and used a methemeoglobin assay for measurement of nNOS activity. As such, it was necessary to complete a dose response study for our optimised system.

To determine the IC₅₀ of L-NNA for the human nNOS isoform co-expressed with calmodulin, identical wells containing the protein complex were treated with increasing doses of the inhibitor. The concentrations used were 0.5 μ M, 5 μ M, 10 μ M, 50 μ M and 100 μ M. All concentrations were introduced to the appropriate wells in an equal volume. Following incubation as per chapter five, section 5.2.5, the absorbances were read at 540 nM and a dose response curve was constructed. This is shown in **Figure 4.28**.

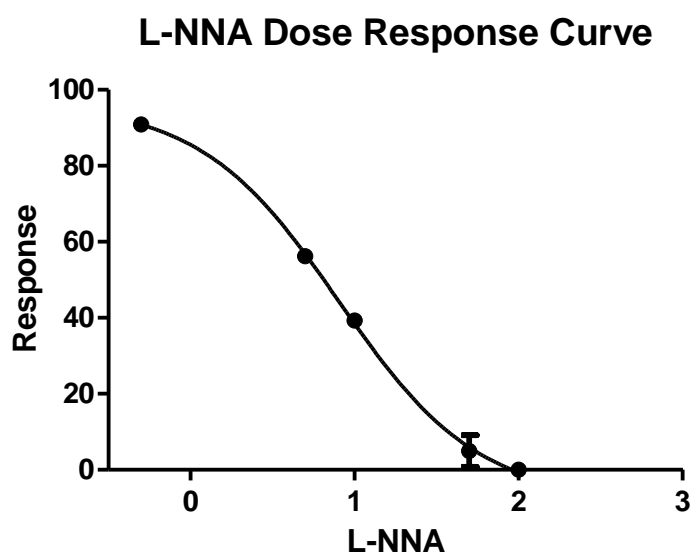


Figure 4.28. Normalised graph of L-NNA concentration versus nNOS response (Representative graph, n=3).

The IC_{50} of L-NNA for human nNOS in this work was found to be $8.0 \mu\text{M} \pm 2.0 \mu\text{M}$. This is in the same range as the previously reported IC_{50} value discussed above. The increase in IC_{50} observed in this system may be due to the fact that the human nNOS was co-expressed with calmodulin. Based on reported human iNOS and human eNOS trends, this co-expression approach is likely to increase the activity of human nNOS, thus requiring a higher concentration of L-NNA to achieve a 50% reduction in enzyme activity.

This result further demonstrated that the human nNOS assay system established in this work was functional and would respond to relatively small changes in inhibitor concentration. It was also the first dose response curve constructed with human nNOS that had been co-expressed with calmodulin in a bacterial system.

4.13.4 nNOS lysate assay

The expressed and purified human nNOS was now known to be functional based on the previous experiments. As the assays of human iNOS and human eNOS were to be conducted with cleared lysates rather than purified enzyme samples, it was decided to test if the assay system was functional using cleared nNOS lysates. As the purified nNOS was clearly functional, failure of the assay with the nNOS lysate would indicate that the assay system was, in fact, not suitable for use with impure protein samples.

An nNOS culture was grown, induced and lysed using the optimised human nNOS methodology. Half of the cleared lysate was frozen in aliquots before purification, while the other half was purified using affinity chromatography. Aliquots of the impure and the purified nNOS were then tested simultaneously, with both a positive and negative control being analysed for the pure and impure samples. The absorbances were read for all samples, and the results are shown in **Figure 4.29**.

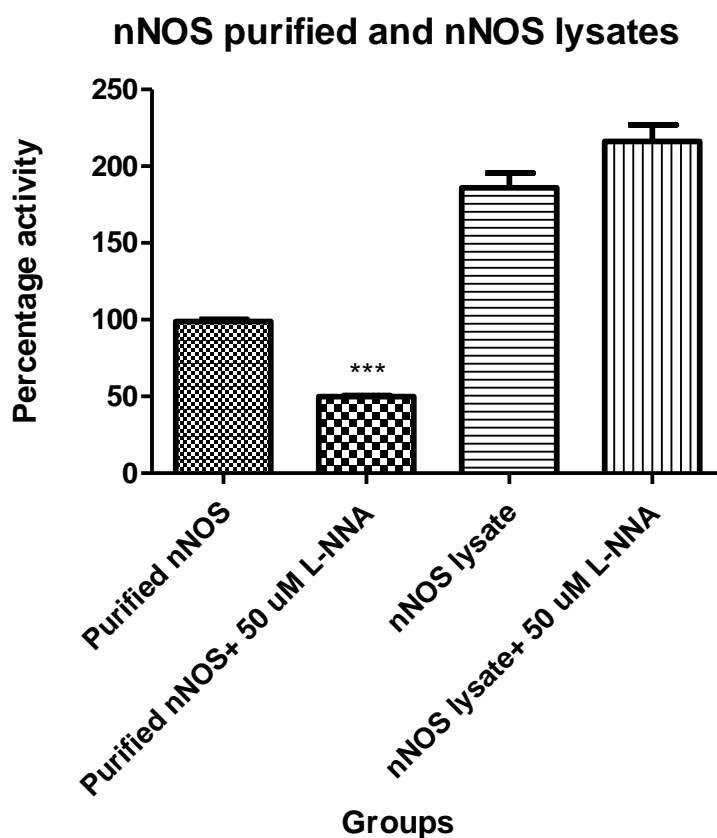


Figure 4.29. Testing of nNOS lysates for suitability in human nNOS assay. A three star significant difference ($p=0.0008$) was seen between the purified nNOS and the partially purified nNOS treated with 50 μ M L-NNA. Presence of precipitates in assay wells of the lysate samples interferes with absorption readings. Representative graph, $n=2$.

The purified samples worked as before, and a clear inhibition was seen with L-NNA. There was a three star significant difference between the purified untreated and the purified treated samples as shown in **Figure 4.29**. The wells containing the lysate samples did turn purple upon addition of the Griess reagents, however, the samples contained a large amount of precipitated material (most likely non-specific *E. coli* protein) which may have interfered with the absorbance readings. This resulted in a large increase in absorbance readings that were not attributable to human nNOS activity. There was a slight difference between treated and untreated samples but this was not statistically significant.

The inability to use nNOS lysates for the assay system was not overly concerning as the purified human nNOS had been previously demonstrated to function as expected.

However, the problems encountered with the nNOS lysates suggested that development of the eNOS and iNOS assay using cleared lysates would be difficult.

4.14 eNOS and iNOS assay development

As has been previously described, affinity purification of the human eNOS construct was not successful as the histidine tag did not bind strongly to the Ni-NTA resin. Cleared cell lysates containing human eNOS were therefore trialled in the Griess assay. Similar to the nNOS assay, the positive control was an untreated sample of the eNOS containing lysate, while the negative control was eNOS containing lysate treated with 50 μ M L-NNA. The assay was conducted as before, the absorbances measured and the results graphed. (**Figure 4.30**).

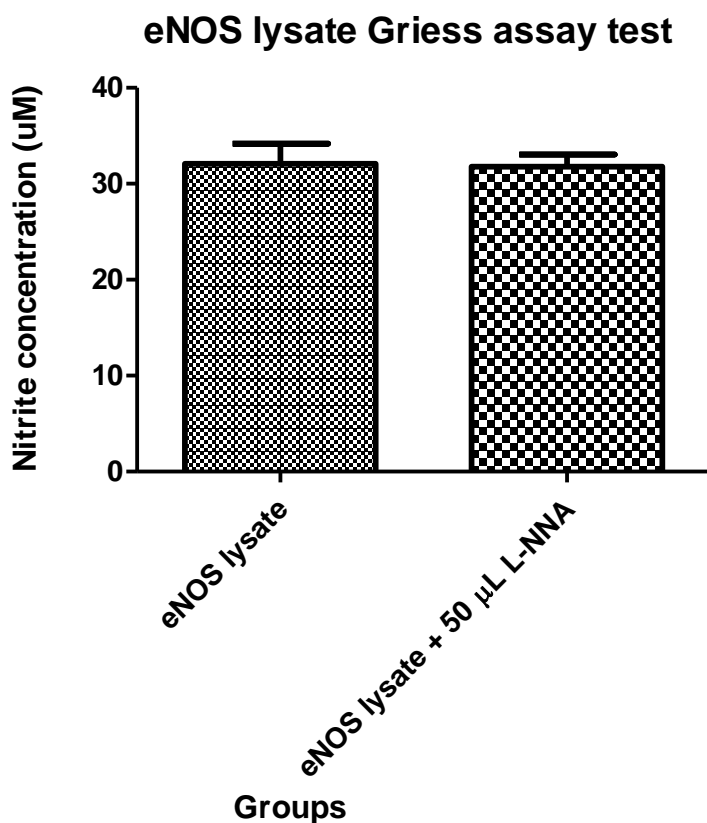


Figure 4.30. Testing of eNOS lysates for suitability in human eNOS assay. Presence of precipitates in assay wells interferes with absorption readings. Representative graph n=2.

Similar to the nNOS lysate tests, a large amount of precipitate was observed in the assay wells of both the treated and untreated sample, which interfered with the absorbance readings. No difference was observed between the treated and untreated wells due to this interference. A purple colour was observed in the wells when the Griess reagents were added, which indicates the presence of nitrites in the lysate. This purple colour was less intense in the wells treated with L-NNA. It was thought that the eNOS protein was functional and capable of being inhibited, but the large amounts of interferents present in the assay wells meant the activity did not translate to reliable absorbance readings.

A similar outcome was observed when iNOS lysates were tested for activity (**Figure 4.31**).

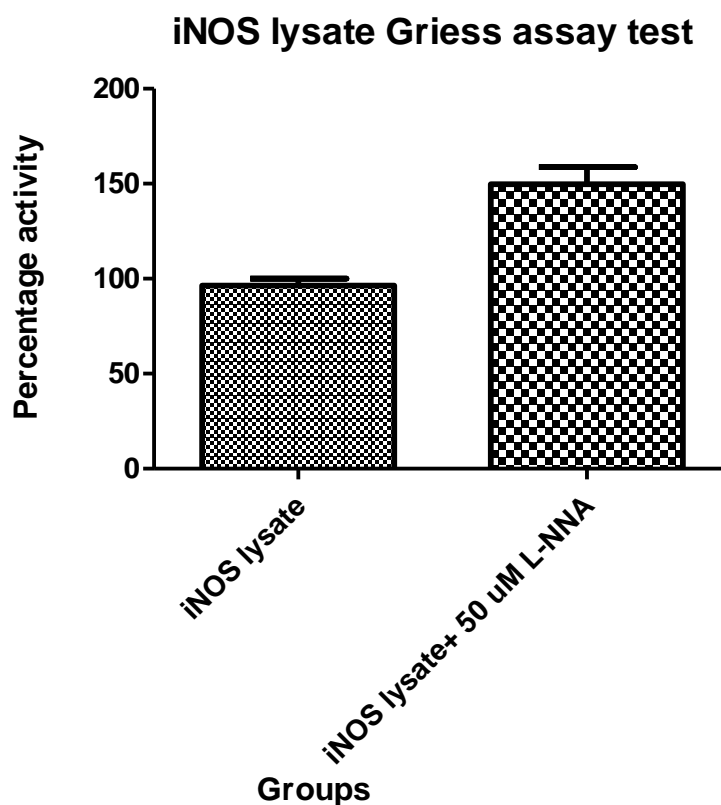


Figure 4.31. Testing of iNOS lysates for suitability in human iNOS Griess assay. Presence of precipitates in assay wells interferes with absorption readings. Representative graph, n=2.

In this instance, the iNOS treated with the L-NNA inhibitor showed an apparently higher level of enzyme activity than the untreated samples. This may have been due to the lack of uniformity between protein lysate samples, resulting in more non-specific protein in the treated sample than was present in the untreated sample. A purple colour was observed in the untreated wells, while a less intense colour was seen in the treated wells. This suggests that the enzyme was functional and was being inhibited by the compound, but this could not be translated into reliable and reproducible absorbance readings due to the presence of large amounts of precipitates in both the treated and untreated wells.

The lysates containing human eNOS and human iNOS were thought to be producing nitrites, suggesting that the enzymes were functional. However, the presence of large amounts of contaminating *E. coli* protein in the cell lysates cast doubt over the accuracy of

the absorbance readings. This observation agreed with what was seen when lysates were used in the nNOS assay system. The work to date had succeeded in recombinantly producing the three human nNOS isoforms, and all three were seen to be functional in the Griess assay, as evidenced by the appearance of a purple colour in the wells. However, only the affinity chromatography purified human nNOS produced reliable and robust results in the assay system, while the assays for the other two isoforms were less successful.

4.15 Assay development conclusion

The assay system was successfully developed for human nNOS which was the key target of this work. The assay was observed to function correctly using nNOS purified via affinity chromatography and was clearly inhibited by the known inhibitor, L-NNA. Despite manufacturer's suggestions (personal communication), the Griess assay system employed here was not suitable for use with nNOS lysates as large amounts of precipitate in the assay wells caused the absorbances to give inaccurate readings. This was due to the non-specific proteins that were present in the lysate of the impure proteins.

For iNOS and eNOS, the purification via Ni-NTA affinity chromatography was not possible due to poor interaction with the affinity column. Therefore, the enzymes were tested as crude lysates in the assay system. Similar to nNOS lysates, this proved to be ineffective due to the precipitates clouding the wells and interfering with the absorbance readings. It is suspected that the enzymes are functional as a purple colour develops for both isoforms upon treatment with the Griess reagents. This suspected activity could not be translated into a robust and reproducible assay system for iNOS and eNOS.

The assay for human nNOS, which was the key target for this work, was functioning correctly. It was therefore decided to focus on the search for inhibitors of this target, and return to the development of the eNOS and iNOS assays at a later date. Future work may focus on development of the human eNOS and human iNOS assay using the successful expression protocols described above.

4.16 Compound testing

The compounds derived from the various computational screens in chapter two were purchased, or synthesised as discussed in chapter three. The selected compounds have been subdivided into sections based on which computational method was used for their identification. All have been sequentially numbered and the structures of each compound are shown in the tables in chapter two. For each assay, the untreated human nNOS samples was designated as 100% active, and the inhibitory activities of the compounds were calculated relative to this. All assays included an L-NNA control. This known inhibitor was used at a concentration of 50 μ M. A DMSO vehicle control was also included in every assay. All compounds for screening were dissolved in DMSO and used at a final concentration of 50 μ M. The percentage of DMSO in each treated well, including the vehicle control, was 0.5%.

All statistical analysis was carried out using Graphpad.¹³⁰ Differences between the vehicle control and treated samples were tested for statistical significance using a two tailed t test, with a p value of less than 0.05 being deemed significant. Histograms and statistical analysis of all compounds tested are shown in the following sections. Each assay was carried out twice in duplicate to ensure that statistical analysis was robust.

4.16.1 Homology modelling flexible docking compounds

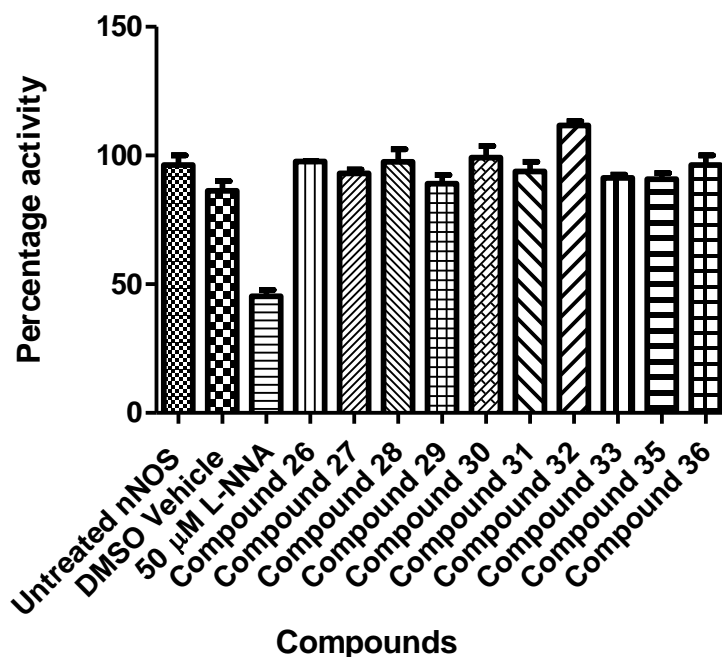


Figure 4.32. Biological evaluation of compounds **26-33**, **35** and **36**, identified via flexible docking of Maybridge compounds with human nNOS homology model. Two star significant difference between untreated nNOS and nNOS treated with 50 μ M L-NNA ($p=0.0076$). One star significant difference between DMSO vehicle and compound **32** ($p=0.0253$). Representative graph, $n=2$.

Compounds **26-33**, **35** and **36** in **Figure 4.32** are *in silico* hit compounds identified from docking of the Maybridge database with the 3PNF-HM. The structures of the compounds can be found in chapter two, **Table 2.15**. The known inhibitor, L-NNA, decreased activity as expected, but unfortunately, none of the evaluated compounds showed any inhibitory activity towards human nNOS. Interestingly, the wells treated with **32** showed an increase in nitrite concentration relative to the vehicle control, indicating that **32** may increase the activity levels of human nNOS. It is doubtful that **32** (**Figure 4.33**) provides a source of NO in a similar manner to arginine. This compound does not possess the guanidinium side chain which is necessary for NO formation via the proposed NOS catalytic cycle (**Scheme 1.2**). Therefore **32**'s ability to enhance NO production may be based on an allosteric interaction with the nNOS enzyme. Compounds of this nature, which increase nNOS activity, have not been reported in the literature. While this was an interesting result, this project was

focused on identifying an nNOS inhibitor and so the exact mechanism of action of the compound was not explored.

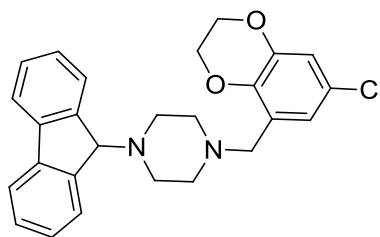


Figure 4.33. Compound **32** identified via screening of the Maybridge database with the 3PNF homology model.

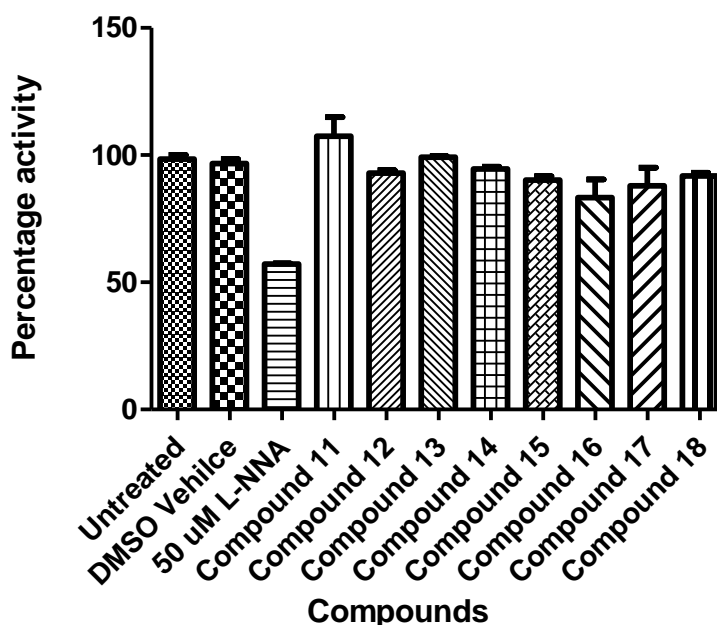


Figure 4.34. Biological evaluation of **11-18** identified via flexible docking of Zinc compounds with human nNOS homology model. Two star significant difference between untreated nNOS and nNOS treated with 50 μ M L-NNA ($p=0.0014$). Representative graph, $n=2$.

Compounds **41-48** in **Figure 4.34** were identified via flexible docking of the Zinc database using the 3PNF-HM. The structures of **41-48** are shown in **Table 2.16**. Again, the assay performed as expected with the known inhibitor acting to decrease nNOS activity levels. Unfortunately, this set of compounds showed no activity for human nNOS. Nitrite levels were not seen to increase or decrease for any of the compounds tested. This trend was

retained when the synthesised piperazine containing **37-40** were evaluated (synthesised in chapter three, section 3.2.1.3), with no decrease in nNOS activity observed (**Figure 4.35**). The data generated from the testing of these compounds was useful, despite the lack of an inhibitor. It provided a set of 21 experimentally validated inactive compounds for human nNOS. These types of compounds are not reported in the literature and provide a valuable resource for refinement of computational models.

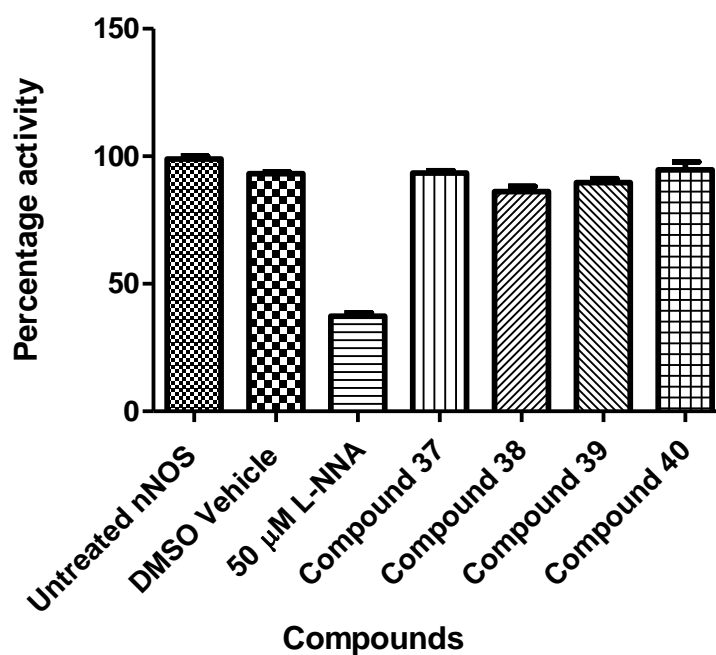


Figure 4.35. Biological evaluation of synthesised **37-40** identified via flexible docking of Maybridge compounds with human nNOS homology model. Three star significant difference between untreated nNOS and nNOS treated with 50 μ M L-NNA ($p=0.0008$). Representative graph, $n=2$.

4.16.2 Pharmacophore one compounds

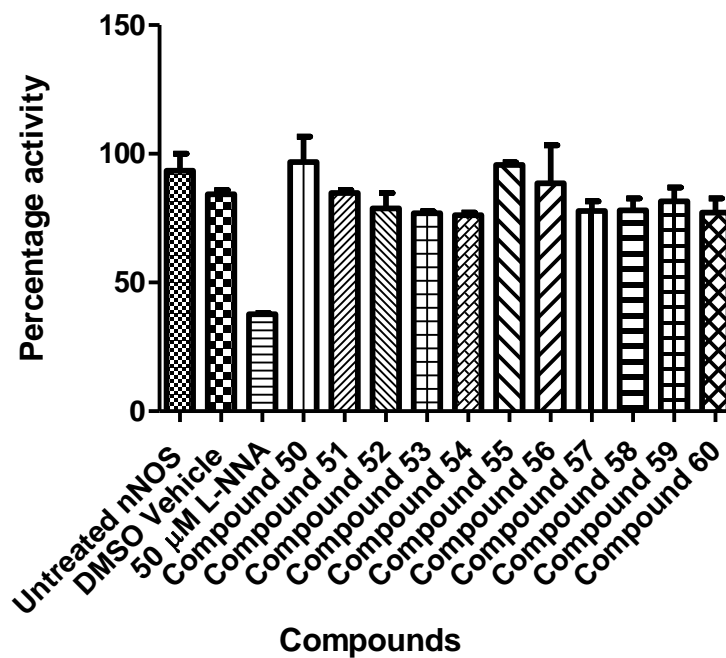


Figure 4.36. Biological evaluation of 50-60 derived from pharmacophore one. One star significant difference between untreated nNOS and nNOS treated with 50 μ M L-NNA ($p=0.0134$). Representative graph, $n=2$.

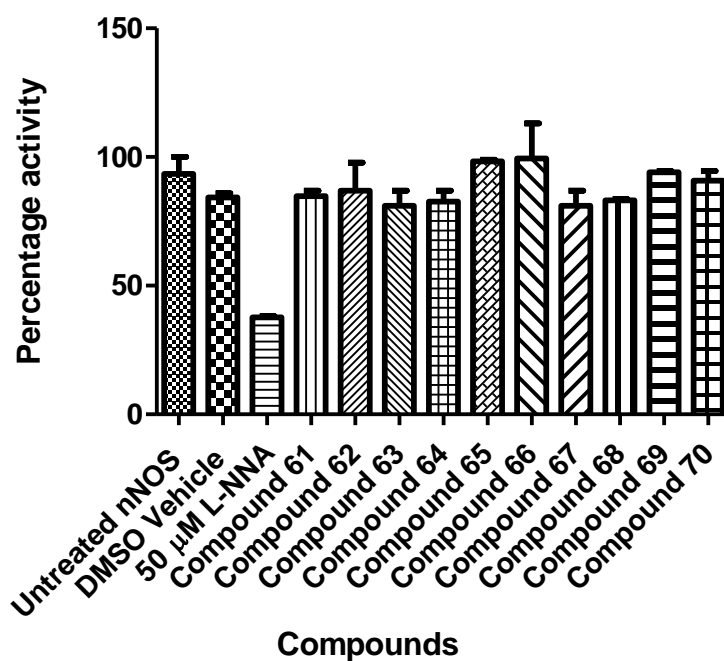


Figure 4.37. Biological evaluation of 61-70 derived from pharmacophore one. Two star significant difference between untreated nNOS and nNOS treated with 50 μ M L-NNA ($p=0.0134$). Representative graph, $n=2$.

The structures of 50-70 can be found in Table 2.21, chapter two. The results from their biological evaluation are shown in Figure 4.36 and Figure 4.37. Similar to the homology model derived compounds, no novel human nNOS inhibitors were identified from this screen. The compounds which proved inactive were combined with the inactive compounds from section 4.16.1 and were used to further refine the pharmacophoric models as described in chapter two, section 2.8.3. This further increased the numbers of experimentally validated human nNOS inhibitors which were useful for this work.

4.16.3 Pharmacophore two compounds

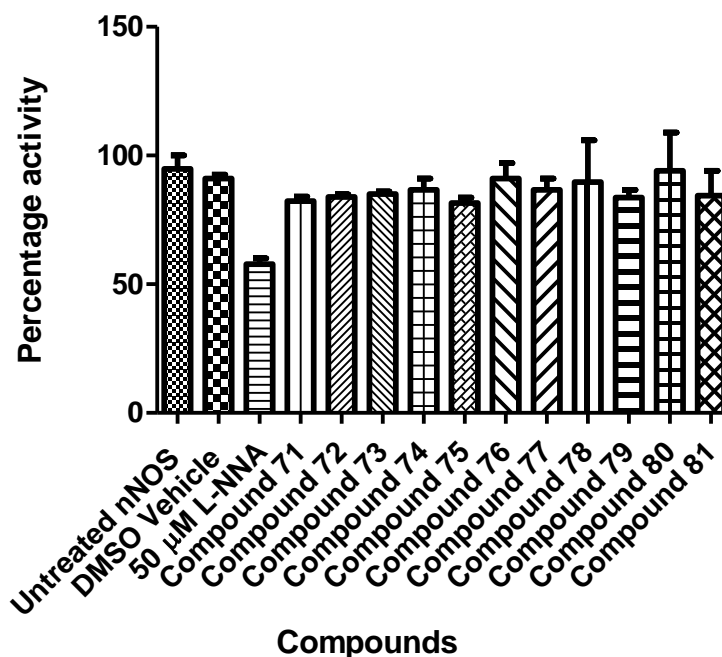


Figure 4.38. Biological evaluation of **71-81** identified from pharmacophore two. Two star significant difference between untreated nNOS and nNOS treated with 50 μ M L-NNA ($p=0.0224$). Representative graph, $n=2$.

As demonstrated in **Figure 4.38**, **71-81** were seen to be inactive against human nNOS. While this was not ideal, the pool of experimentally validated inactives against human nNOS was further increased.

The use of a pharmacophore to search for human nNOS inhibitors was a novel and logical approach, and represented a viable option for this project. The inabilities of this approach to identify a new class of inhibitors lead to the use of the human nNOS crystal structure for screening purposes.

4.16.4 Crystal structure docking compounds

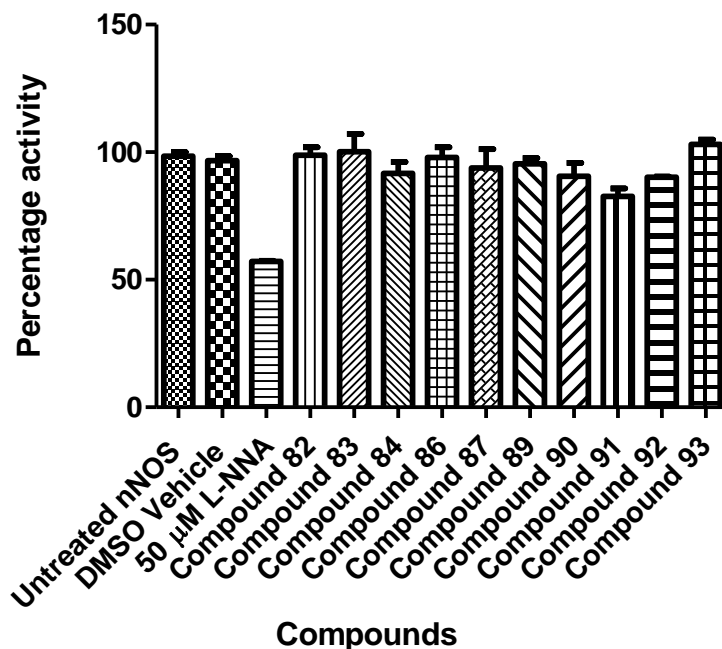


Figure 4.39. Biological evaluation of **82-84, 86, 87, 89-93** identified via the crystal structure screen. Two star significant difference between untreated nNOS and nNOS treated with 50 μ M L-NNA ($p=0.0014$). Representative graph, $n=2$.

Docking of the human nNOS crystal structure with commercial datasets (Zinc and Maybridge) was conducted in the latter stages of the project as the first reports of crystallised human nNOS were released in early 2015.⁸³ The use of high throughput computational screening with this structure has yet to be reported in the literature. Compounds **82-84, 86, 87, 89-93** (structures shown in chapter two, section 2.9.2) were chosen for biological evaluation from this computational screen. The results from this assay test are shown in **Figure 4.39**.

A set of urea containing compounds were synthesised based on hits from the computational screen of the human nNOS crystal structure. The structures and synthesis of this family of compounds is outlined in chapter three, section 3.2.2. The results from the biological screening of these compounds are shown in **Figure 4.40**.

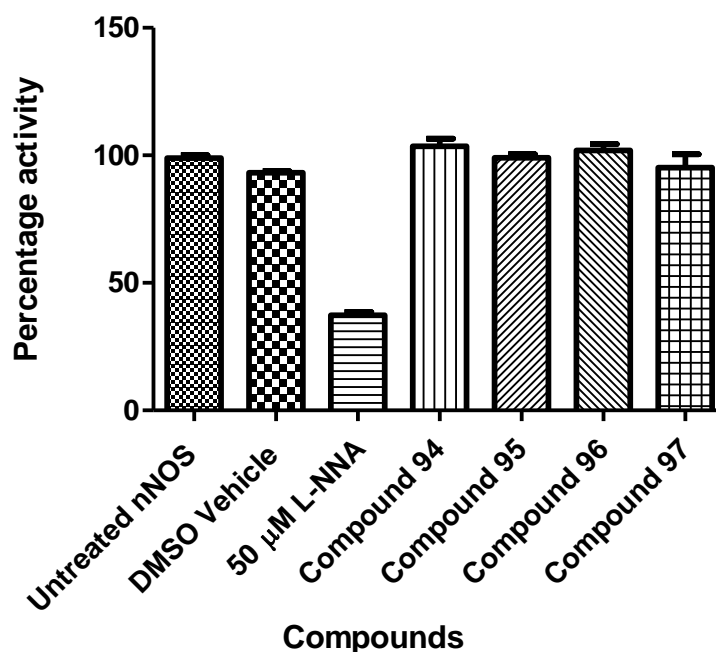


Figure 4.40. Biological evaluation of **94-97**, derived from crystal structure screen and synthesised as per chapter four, section 3.2.2. Three star significant difference between untreated nNOS and nNOS treated with 50 μ M L-NNA ($p=0.0008$). Representative graph, $n=2$.

The assay results demonstrated that the compounds tested did not have any inhibitory effect on the recombinantly produced human nNOS. The inability of these compounds to inhibit the protein, along with the inactivity observed with the compounds derived from previous *in silico* screens confirmed that human nNOS is a difficult target to computationally model and target.

4.16.5 Literature and other compounds

During the course of this project, Xu *et al.* published a computational paper that contained a set of structures that they proposed as possible human nNOS inhibitors.⁶² This publication was purely computational and did not contain biological evaluation. Some of the compounds suggested by Xu *et al.* (**Figure 4.41**) were therefore acquired and biologically evaluated.

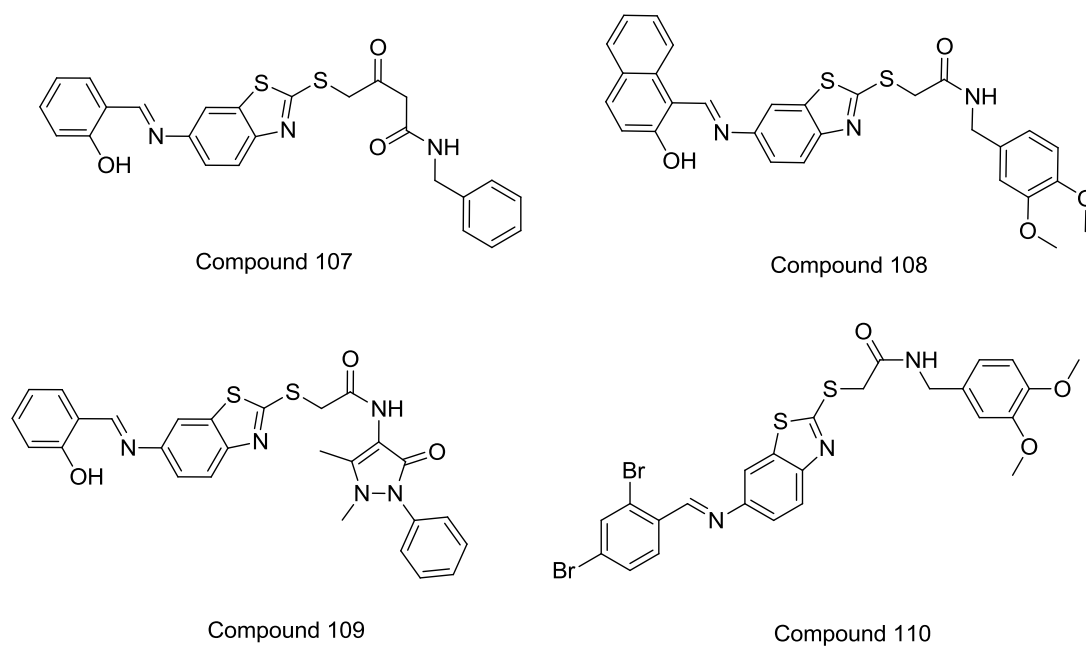


Figure 4.41. Additional literature compounds that were biologically evaluated, **107-110**.⁶²

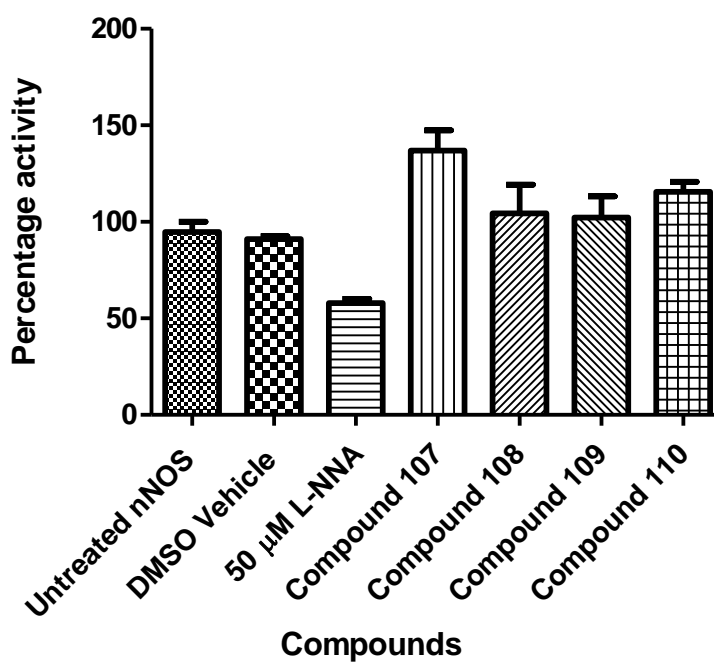


Figure 4.42. Biological evaluation of compounds identified from literature sources.⁶² One star significant difference between untreated nNOS and nNOS treated with 50 μ M L-NNA ($p=0.0224$). One star significant difference between DMSO vehicle and **107** ($p=0.0483$). Representative graph, $n=2$.

The results of the biological evaluation of compounds **107-110** are shown in **Figure 4.42**. These compounds proved inactive in the assay system. This added weight to the theory that human nNOS is a difficult target to model and predict as the computational work of two separate research projects had failed to identify a human nNOS inhibitor.

Interestingly, compound **107** was seen to increase nNOS activity. Similar to **32**, it is unlikely that **107** binds to nNOS in the same manner as arginine, the natural substrate. Compound **107** does not have the necessary guanidinium group required for NO production, and therefore most likely causes the increase in enzyme activity via allosteric interactions with nNOS. A combined study on the precise binding modes of **107** and **32** may elucidate the exact nature of the process which causes increased NO production from nNOS. This type of study was not attempted during this project.

4.16.6 Discussion on compound evaluation

Although no human nNOS inhibitor had been identified in these screening trials, there were a number of very positive results generated. The use of a human nNOS homology model and pharmacophore to screen commercial databases is a novel approach, and the results shown above contribute to the overall field of human nNOS inhibition. The compounds tested proved to be inactive, but now represent the first set of experimentally validated human nNOS inactive compounds. These are useful for future computational and synthetic work. Compound **32** was seen to increase the activity of human nNOS. The exact mechanism of action of this compound is not clear. Further studies on the binding mode of **32** may provide a valuable insight into the mechanism of human nNOS over activation.

Compounds developed via *in silico* methods from other groups also proved to be inactive in the assay. This, coupled with the lack of activity of the computationally derived from this work, suggests that human nNOS is a challenging target. This theory is reinforced by the fact that there are no literature reports of successful human nNOS inhibitors that were generated by CADD. This also helps to explain why there are only two well explored classes of nNOS inhibitors, as new inhibitor classes seem to be difficult to identify.

The assay system, based on recombinantly produced human nNOS, proved to be reliable, high throughput and reproducible. The routine use of human nNOS co-expressed with

calmodulin for compound evaluation is a unique feature of this project. The publication of the human nNOS crystal structure demonstrates that the field is moving towards a human isoform based system, rather than the traditional rat based systems. The assay system that was utilised in this project can therefore be considered to be at the “cutting edge” of the field, and ensures that future assay testing experiments will be relevant.

The assay system is also high throughput. Compound screening can be achieved by one experienced operator, and represents a considerable strength of this assay system. Other assay systems, such as the radio labelled arginine assay for NOS activity, require expensive (and potentially hazardous) materials and cannot be used in a high throughput manner like the system developed in this work. Furthermore, alternate assay systems require the addition of calmodulin to ensure maximal nNOS activity. This is not necessary for the assay system described here as the human nNOS is co-expressed with human calmodulin. It is felt, therefore, that the procedures developed in this work represent an affordable, robust and rapid method of testing inhibitory compounds against human nNOS that has yet to be matched in the literature.

4.17 Conclusion

This work focused on reproducible expression of all three human isoforms of the NOS proteins in *E. coli* cells. The conditions for expression, lysis and purification were optimised for human nNOS, the key target of this work. The resulting system, as outlined above, provides a fast, inexpensive and reproducible route to partially purified human nNOS. In addition, this system allows for the co-expression of human calmodulin with the nNOS protein. The two recombinant proteins stay complexed throughout the purification process and are both present in the elution fractions from a Ni-NTA column. This is a novel and potentially extremely useful system as the complexation of nNOS and calmodulin should result in a maximally efficient NOS enzyme.

This purified complex was successfully utilised in a Griess assay system. Both a treated protein sample and a sample with the known NOS inhibitor, L-NNA, were trialled. A clear activity difference was observed between the treated and untreated samples, indicating that the nNOS was functional, and that its inhibition leads to a decrease in absorbance at 540 nm. The IC_{50} of L-NNA in this system was calculated as $8.0 \mu\text{M} \pm 2.0 \mu\text{M}$. DMSO was also identified as a suitable vehicle for the system as it did not interfere with readings when used at 0.5% of the total assay volume. A cost effective, in house system was therefore available for testing of the potential nNOS inhibitory compounds that had been identified from the *in silico* screen.

Human iNOS and human eNOS were also successfully expressed from the *E. coli* cells. Both were co-expressed with human calmodulin. However, purification of these NOS isoforms via affinity chromatography proved problematic, with the histidine tag on the isoforms not binding well to the column resin. This may have been due to the folding of the iNOS and eNOS protein, which potentially results in the tag being unable to bind to the resin. Both the iNOS and eNOS constructs had the histidine tag on the C terminus, where the nNOS construct had the tag on the N terminus of the protein. As all three isoforms fold in a similar manner, movement of the tag from C to N terminus in the eNOS and iNOS constructs may result in less transient tag/resin binding.

Despite the difficulties in the purification process, the identification of the iNOS and eNOS proteins in the crude lysates prompted testing of these samples in the Griess assay. Although a purple colour did develop in the wells for both isoforms, the formation of large

amounts of precipitated, non-specific protein resulted in inaccurate absorbance readings that could not be translated into nitrite concentrations.

Although a working assay system was not developed for human iNOS and human eNOS, the expression of both isoforms was successful. In future work, an alternate purification method, such as size exclusion chromatography, may result in purified samples of iNOS and eNOS, which could then be used in the manner described for nNOS.

The successfully developed assay for human nNOS was used to biologically evaluate a wide range of compounds, both purchased and synthesised. While none of the compounds proved active against human nNOS, the assay system proved itself to be high throughput and reproducible. The tested compounds provide a valuable resource for future computational screens, and the assay system which was developed represents a novel, useful and transferable method for evaluation of human nNOS inhibitors. Two compounds (32 and 107) were also observed to increase nNOS activity levels, potentially providing an additional avenue of research into the exact mechanisms of NOS over activation.

5 Materials and Methods

5.1 Chemicals and reagents

All chemicals, reagents and solvents were purchased from Sigma, Fischer or Lennox unless otherwise stated. Restriction enzymes were obtained from either Promega or Fermentas. Plasmid DNA isolation and purification kits were purchased from Invitrogen and Thermo Scientific. DNA size markers for agarose gels were supplied by Fermentas.

Protein purification was carried out using Ni-NTA agarose purchased from Qiagen. SDS gels were made using acrylamide supplied by Promega. ECL Western blot substrate was purchased from Pierce. Molecular weight markers were purchased from Thermo Scientific. Blotting paper was supplied by Whatman purchased from GE Healthcare. PVDF membranes were also purchased from GE Healthcare. Antibodies were obtained from Sigma (anti-histidine) and Thermo Scientific (anti-iNOS, eNOS and nNOS). Anti-calmodulin antibody was obtained from Pierce. The Griess assay kit (part number NB 78) and necessary co-factors (part number NS70) were sourced from Oxford Biomedical Research.

5.2 Biological Materials and Methods

5.2.1 Vectors and host strains

Human NOS DNA was gifted by Dr. Hartmut Kleinert (Johannes Gutenberg University of Mainz). The three isoforms were supplied in pQE30 vectors, incorporating a C terminus histidine tag for eNOS and iNOS and an N terminus histidine tag for nNOS. The vector also coded for ampicillin resistance and had an inducible T5 lac operon promoter, (**Figure 5.1** to **Figure 5.3**).

Expression was initially attempted with the NOS isoforms alone and then co-expression trials were conducted with calmodulin. The calmodulin DNA was gifted by Dr. Clinton Nishida, UCSF. This was supplied in a modified pACYC vector which coded for chloramphenicol resistance (**Figure 5.4**).

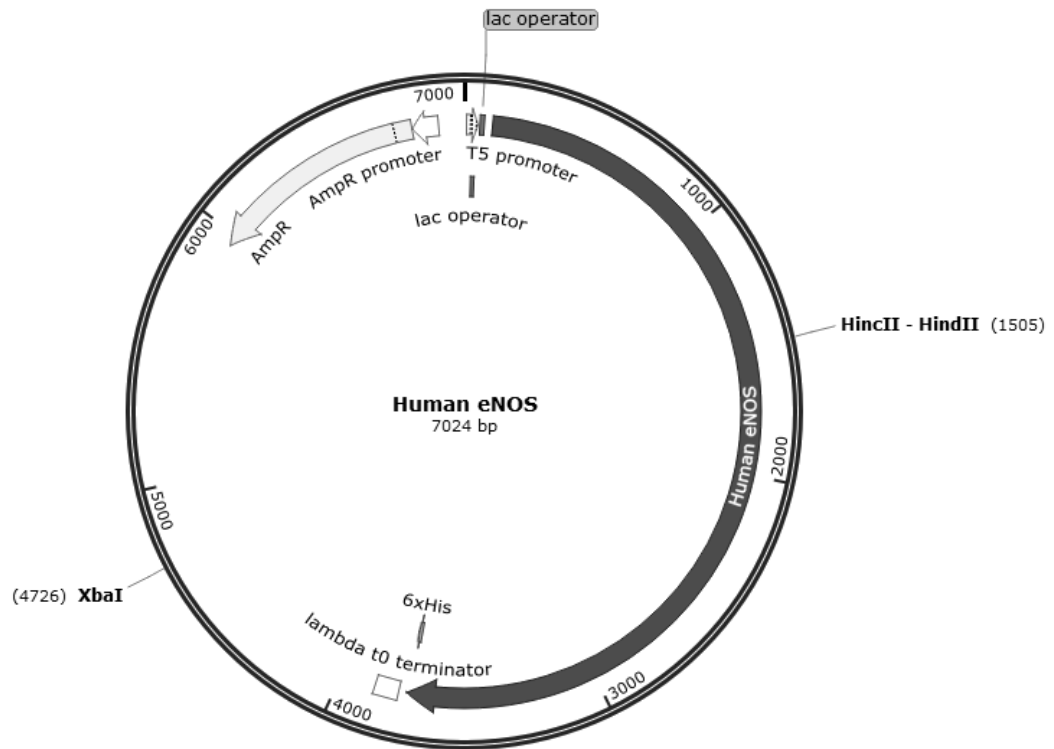


Figure 5.1. pQE30 Human eNOS construct.

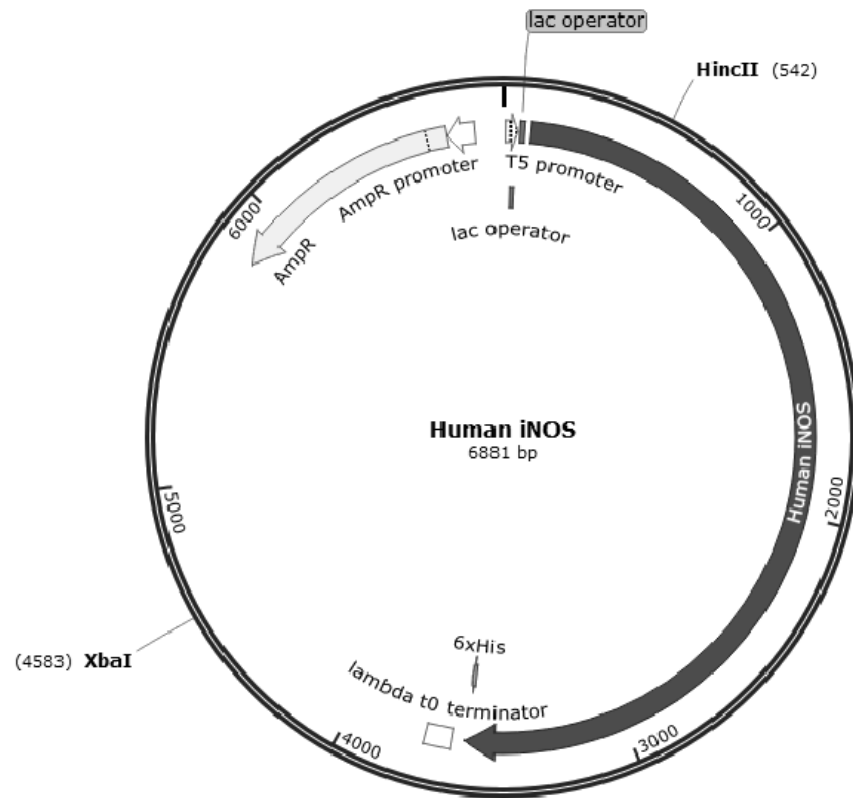


Figure 5.2. pQE30 Human iNOS construct.

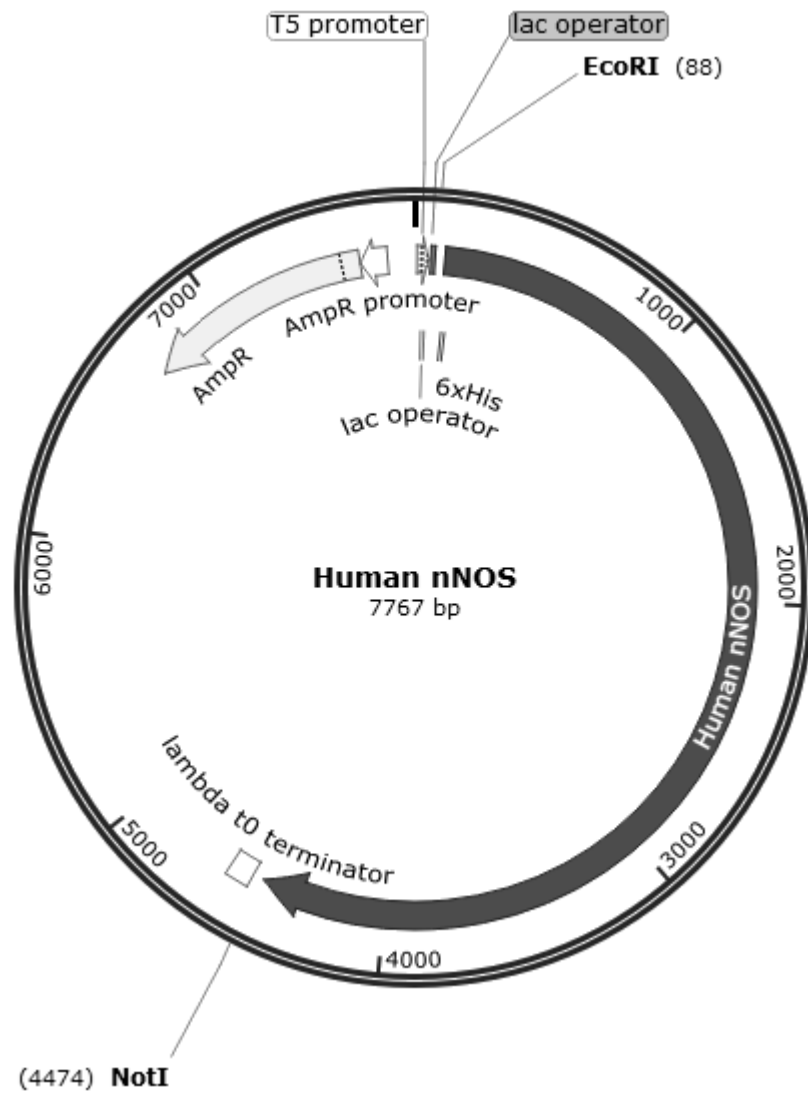


Figure 5.3. pQE30 Human nNOS construct.

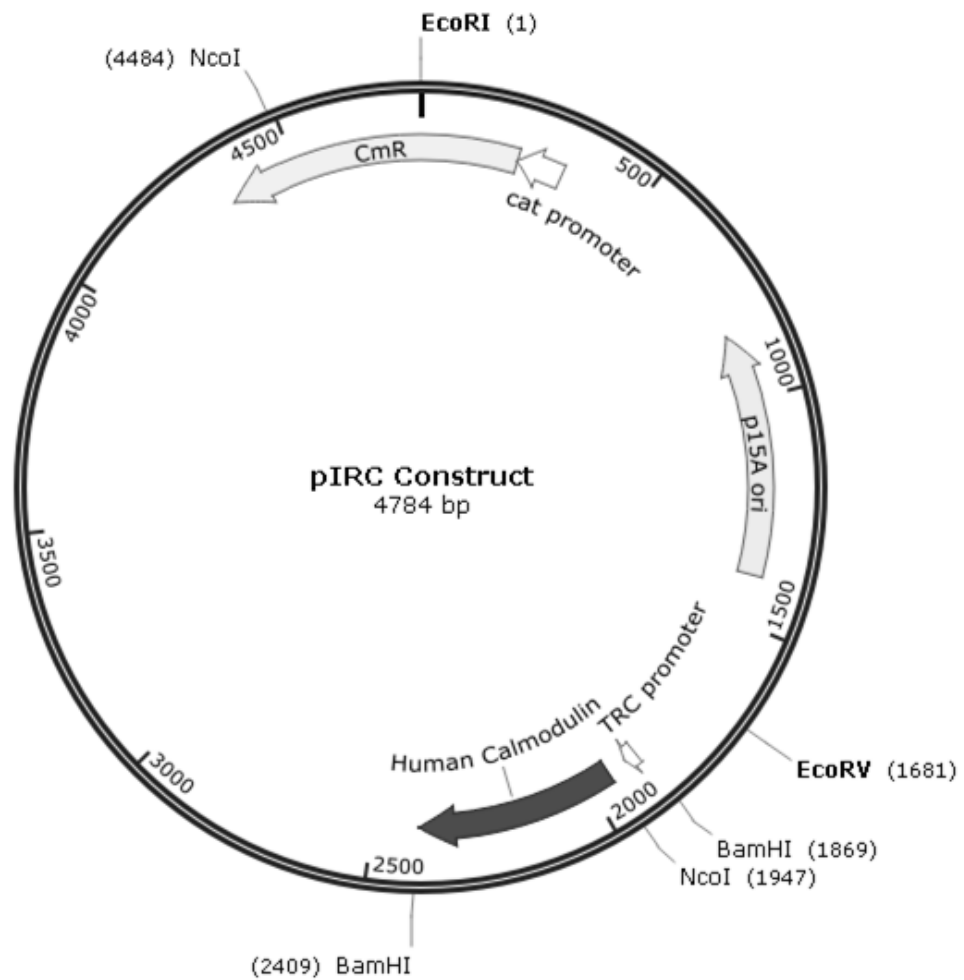


Figure 5.4. pIRC Human calmodulin construct.

DNA amplification was carried out using TOP10 *E. coli* cells, supplied by Invitrogen. Expression was conducted in BL21(DE3) *E. coli* cells supplied by Invitrogen.

5.2.2 DNA amplification and verification

5.2.2.1 Transformation of competent *E. coli*

TOP10 *E. coli* cells were used to amplify all DNA samples received from other labs. The transformation of these cells was carried out as per manufacturer's instructions. A 5 μL sample of the required DNA at a concentration of 5 $\text{ng}/\mu\text{L}$ was pipetted into 50 μL of competent TOP10 cells which had been thawed on ice. The mixture was incubated on ice for 30 minutes before being heat shocked at 42 $^{\circ}\text{C}$ for 30 seconds. The cells were immediately placed back onto ice and 250 μL of pre warmed super optimal broth with catabolite repression (SOC) media was added (5% tryptone (w/v), 0.5% yeast extract (w/v), 2.5 mM KCl, 10 mM MgCl_2 , 10 mM MgSO_4 , 20 mM glucose). Cells were incubated at 37 $^{\circ}\text{C}$ for 1 hour with shaking, then plated on LB agar plates (1% tryptone (w/v), 0.5% yeast extract (w/v), 0.5% NaCl (w/v), 1% agar (w/v), pH 7) with 50 $\mu\text{g}/\mu\text{l}$ of ampicillin (and 25 $\mu\text{g}/\mu\text{l}$ chloramphenicol when co-expressing calmodulin) for selection and left at 37 $^{\circ}\text{C}$ overnight.

5.2.2.2 Miniprep and subsequent analysis

Colonies that grew on selection agar plates were transferred into 3 mL LB media (1% tryptone (w/v), 0.5% yeast extract (w/v), 1% NaCl (w/v), pH 7). Colonies were incubated in media overnight at 37 $^{\circ}\text{C}$. A 2 mL sample of each respective culture was spun at 6800 RCF for 2 minutes. DNA was then extracted from the bacteria using the plasmid purification kit supplied by Thermo Scientific (K0503), as per manufacturer's instructions. A 5 μl sample of purified plasmid was then digested, using the appropriate restriction enzyme, to assess the presence of the desired insert (**Table 5.1**).

Table 5.1. Restriction digest mixtures.

Component	iNOS plasmid	eNOS plasmid	nNOS plasmid	Calmodulin plasmid
Miniprep DNA	5 μ L	5 μ L	5 μ L	5 μ L
Fast Digest buffer	2 μ L	2 μ L	2 μ L	2 μ L
Restriction enzyme 1	1 μ L Hinc II	1 μ L Hinc II	1 μ L EcoR1	1 μ L BamH1
Restriction enzyme 2	1 μ L xbaI	1 μ L xbaI	1 μ L Not1	1 μ L BamH1
Water	11 μ L	11 μ L	11 μ L	11 μ L
Expected Band size 1	4041 bases	3803 bases	4386 bases	4224
Expected Band size 2	2840 bases	3221 bases	3381 bases	540

5.2.2.3 Agarose gel analysis

The DNA digests generated via the miniprep procedure were analysed via agarose gel to ensure that the NOS and calmodulin genes were present. A 0.8% agarose gel was used with SYBR Safe DNA gel stain supplied by Invitrogen (S33102) to visualize the DNA. Agarose (0.4 g) was heated in 50 mL 1 x TAE buffer (40 mM Tris-acetate, 1 mM EDTA, pH 8.4) until dissolution occurred. The solution was cooled and 5 μ L of SYBR safe was added. Gels were poured and allowed to set at room temperature. DNA loading dye was supplied by Thermo Scientific and was used in a 1:10 dilution with the DNA sample. Gels were electrophoresed at 120 volts and visualised using UV light. GeneRuler 1 kb DNA ladder supplied by Thermo Scientific (SM0313) was used to assess the size of the electrophoresed DNA. Samples containing inserts of the correct size were noted and used for midi preparations.

5.2.2.4 Midiprep culture of plasmid

Samples which contained the plasmid of interest were propagated in 50 mL LB media with 50 µg/ml of ampicillin and 25 µg/ml of chloramphenicol when co-expressing calmodulin. Media was inoculated with 1 mL of miniprep culture and grown at 37 °C for 48 hours. Plasmid was then purified using the S.N.A.P. Midiprep kit supplied by Invitrogen (K1910-01), as per manufacturer's instructions. DNA was eluted using 750 µL sterile Milli-Q water. DNA concentration was assessed by reading absorbance at 260 nm. DNA was then stored at -20 °C.

5.2.2.5 Preparation of glycerol stocks

For long term storage of plasmids, liquid cultures of *E. coli* transformed with the plasmid of interest were frozen at -80 °C. Briefly, 150 µl of a 50 ml culture of desired *E. coli* was combined with 850 µl of sterile glycerol and mixed thoroughly. Cells were then stored at -80 °C.

5.2.2.6 Gene sequencing

All gene sequencing was performed by Eurofins labs, Germany. DNA samples (15 µL) with concentrations of 50 ng/µL were prepared for each of the four constructs from the Midiprep samples. The T5 promoter was used as a primer for the NOS genes. Also, due to the length of the NOS genes, internal primers were chosen every 300 base pairs. These internal primers were 20 base pairs long. For calmodulin gene sequencing the primer chosen was the first 20 base pairs of the calmodulin gene. Internal primers were not required. Results of gene sequencing were compared to the published sequences using the Clustal Omega alignment tool from the EMBL website. All alignments are provided in appendix.

5.2.3 Co-expression and isolation of NOS and calmodulin proteins

5.2.3.1 *Competent cells, their transformation and expression screening*

Expression studies were carried out in BL21(DE3) cells supplied by Invitrogen. These were supplied as “One Shot” fully competent cells. These were first transfected with the NOS constructs. NOS DNA was isolated from the TOP10 cells using Miniprep as previously described. This DNA was transformed into the BL21(DE3) cells using the same protocol as described in section 5.2.2.1. Cells were transfected using 2 μL of DNA construct at a DNA concentration of 5 $\text{ng}/\mu\text{L}$. The transfected cells were spread onto LB agar plates containing 50 $\mu\text{g}/\mu\text{L}$ of ampicillin and were incubated at 37 $^{\circ}\text{C}$ overnight.

Individual colonies were chosen and grown in 5 mL of LB media containing 50 $\mu\text{g}/\mu\text{L}$ of ampicillin (LB-amp) with shaking at 37 $^{\circ}\text{C}$. The OD_{600} of the cultures was measured periodically using LB-amp media as a blank. When an OD_{600} of 0.600 was reached (after roughly four hours) protein expression was induced by addition of 1 mM IPTG. The cultures were grown overnight at 37 $^{\circ}\text{C}$ with shaking. The resulting cells (1 mL) were pelleted by centrifugation at 4000 x g. The supernatant was discarded and the pellets were resuspended in 100 μL of 5 x Laemmli sample buffer (300 mM Tris-HCl, 50% (v/v) glycerol, 10% (w/v) SDS, 0.02% (w/v) bromophenol blue, 10% (v/v) β -mercaptoethanol, pH 6.8). These samples were loaded directly onto SDS gels and analysed via Western blot to confirm expression of NOS proteins. Glycerol stocks were made of the colonies which were observed to express well.

BL21(DE3) cells were also used when calmodulin and NOS genes were to be co-expressed in the same cell. When transforming two constructs at once, 2 μL of each construct was used, each at a concentration of 5 $\text{ng}/\mu\text{L}$. The agar plates in this case contained 50 $\mu\text{g}/\mu\text{L}$ of ampicillin and 25 $\mu\text{g}/\mu\text{L}$ of chloramphenicol.

Expression testing was conducted in the same manner as described above, however the LB media used for culture growth contained 50 $\mu\text{g}/\mu\text{L}$ of ampicillin and 25 $\mu\text{g}/\mu\text{L}$ of chloramphenicol (LB-amp/chlor). Expressing clones were identified via Western blot analysis and glycerol stocks prepared.

5.2.3.2 Large scale expression of NOS proteins and lysis of cells

Glycerol stocks containing strongly expressing clones were streaked on LB agar plates containing the appropriate antibiotics. In the case of NOS expression alone the antibiotic used was ampicillin (50 µg/µL). When co-expressing NOS and calmodulin the antibiotics used were ampicillin (50 µg/µL) and chloramphenicol (25 µg/µL). The streaked plates were incubated overnight at 37 °C and individual colonies chosen. The individual colonies were grown in 50 mL of appropriate LB media (LB-amp or LB-amp/chlor) at 37 °C overnight with constant shaking. The cultures were then diluted back to an OD₆₀₀ of 0.65 in TB media (1.2% (w/v) tryptone, 2.4% (w/v) yeast, 0.4% (v/v) glycerol, 17 mM KH₂PO₄, 72 mM K₂HPO₄, pH 7.0). Fresh antibiotic was added to the media to final concentrations of 50 µg/µL and 25 µg/µL for ampicillin and chloramphenicol respectively. Riboflavin and aminolevulinic acid were added to final concentrations of 2 µM and 1 mM respectively. IPTG was added to a final concentration of 1 mM to induce protein expression, and the cultures were left to shake (200-250 RPM) at room temperature for 12 hours.

The cultures were centrifuged at 4,000 x g for 15 minutes using a Sorvall RC5C Plus ultracentrifuge with rotor SLA-3000 precooled to 4 °C. The resulting supernatant was discarded and the pellet resuspended in lysis buffer (3-5 mL per gram of wet cell pellet weight) containing the components outlined in **Table 5.2**.

Table 5.2. Lysis buffer components. ^a

Component	Concentration
Hepes	50 mM
NaCl	500 mM
β mercaptoethanol ^b	10 mM (140 μ L/100mL)
Triton X-100	1%
Sigma inhibitor cocktail ^b	1 tablet/100ml
PMSF ^c	1 mM (0.0435g in 2.5ml IPA, 1mL/litre)
Lysozyme	2 mg/ml
Glycerol	20%
Tetrahydrobiopterin	10 μ M
CaCl ₂	2 mM

^a pH adjusted to 8.0 @ 4 °C (for iNOS experiments the pH was adjusted to 7.5)

^b added just before use

^c a phenylmethylsulfonyl fluoride (PMSF) stock was first made up in isopropyl alcohol and an appropriate volume of this stock solution was added to the lysis buffer.

The pellet was resuspended by vigorous vortexing and repeated pipetting. The culture was passed through an 18 gauge needle and was then incubated at 4 °C for an hour on a mechanical roller. The PMSF containing alcohol solution was re-added after 30 minutes, and again following the hour rolling.

Following the hour incubation the suspensions were sonicated using a probe sonicator (Bandelin Electrical, UW2200, 20% power, with a cycle time of six, 30 seconds). This was repeated three times. The sonicated solutions were passed through a 25 gauge needle into appropriate sized centrifugation tubes. Centrifugation was then carried out at 14,000 x g for 20 minutes at 4 °C. Pellet and cleared lysate were separated and the pellet was resuspended in PBS. This was retained for SDS-PAGE analysis. A small sample of cleared lysate was also retained for SDS-PAGE analysis with the majority taken forward for Ni-NTA purification.

5.2.3.3 Purification and storage of recombinant protein

Ni-NTA resin (2 mL per 400 mL of original culture) was used for protein purification. The Ni-NTA resin was first pre equilibrated with binding buffer (50 mM HEPES, 500 mM NaCl, 20% (v/v) glycerol, 10 μ M BH₄ and 2 mM CaCl₂). For nNOS the binding buffer also contained 10 mM imidazole. For eNOS and iNOS no imidazole was used in the binding buffer. Ni-NTA resin was centrifuged (700 x g, 4 °C) for one minute. The top layer was removed and replaced with an equal volume of binding buffer. The tube was mixed thoroughly and re-centrifuged. This was repeated three times. The Ni-NTA resin was added to the cleared lysate samples and left mixing at 4 °C for 90 minutes.

The resin was then collected using 5 mL plastic, disposable columns. For nNOS, the resin was washed once with 10 column volumes of binding buffer containing 40 mM imidazole. Bound protein was then eluted in one column volume of binding buffer with 250 mM imidazole. For eNOS and iNOS, washings were conducted using binding buffer with no imidazole present. Elution was carried out in the same manner as for nNOS.

Dialysis was carried out to remove imidazole from protein samples. Each 1 mL of purified protein was dialysed against 500 mL of dialysis buffer (50 mM HEPES, 500 mM NaCl, 20% (v/v) glycerol, 2 mM CaCl₂) for 2 hours at 4 °C. This was repeated twice more to yield a final imidazole concentration of less than 2×10^{-9} M. The samples were then concentrated to half their original volume using centrifugal concentration (Amicon Ultra) with a molecular weight cut off of 10 kDa. The concentrated samples were added to an equal volume of ice cold, fresh dialysis buffer supplemented with 10 μ M BH₄ and were aliquoted in volumes of 35 μ L into pre cooled Eppendorf tubes. The samples were immediately frozen at -80°C for use in future assay work.

5.2.4 Expression verification: One dimensional electrophoresis, Western blot and mass spectrometry

5.2.4.1 Pierce protein assay

A standard protein curve was prepared using BSA at 0, 50, 100, 200, 400, 600, 800, 1000, 1250, 1500, 1750 and 2000 µg/ml. Samples were diluted as required and 10µl used for the assay in duplicate. 10µl of each standard or sample was used in duplicate in a 96 well plate along with 150 µl Pierce Protein Assay reagent (PN22660). The plate was incubated at room temperature for 5 minutes. The plate was then analysed using a BIO-TEK EL800 plate reader at 630nm. Protein concentration of the samples was deduced from the standard curve.

5.2.4.2 SDS-PAGE Analysis

Before electrophoresis samples were denatured in 1 x Laemmli sample buffer. Separation of proteins on the basis of molecular weight was achieved using sodium dodecyl sulphate polyacrylamide gel electrophoresis (SDS-PAGE). The gels used contained 8% acrylamide. The resolving portion of the gel was made by mixing 4.6 mL water, 2.7 mL acrylamide, 2.5 mL TRIS base in water pH 8.8, 0.1 mL 10% SDS in water, 0.1 mL 10% ammonium persulphate in water and 0.006 mL of tetramethylethylenediamine (TEMED). The stacking portion of the gel was made by mixing 1.4 mL water, 0.33 mL acrylamide, 0.25 mL TRIS base in water pH 6.6, 0.02 mL 10% SDS in water, 0.02 mL 10% ammonium persulphate in water and 0.002 mL TEMED. The denatured samples were loaded and electrophoresed at 19 mA per gel for approximately two hours. The running buffer consisted of 0.1% (w/v) SDS, 25 mM Tris-Base and 192 mM glycine, pH 8.3. A protein ladder supplied by Thermo Scientific (SM1811) was used to assess the molecular weight of electrophoresed proteins.

5.2.4.3 Coomassie staining

SDS-PAGE gels were stained with Coomassie brilliant blue stain (Thermo Scientific PageBlue). Gels run in a reducing environment were first washed three times in deionised water for ten minutes. Gels were then covered with 20 mL of Coomassie brilliant blue and placed on a rocker for 60 minutes at room temperature. Gels were destained using deionised water. Three initial de staining steps were carried out for ten minutes each, followed by an overnight de stain. Further water washes were carried out if necessary, until gels with strongly contrasting bands were obtained.

5.2.4.4 Western blot

More sensitive and specific detection of protein was achieved using Western blot. Proteins were transferred from polyacrylamide gels to polyvinylidene fluoride (PVDF) in transfer buffer (10 mM CAPS, pH 11, 10% (v/v) methanol) for 90 minutes at a constant 140 mA, using a semi-dry transfer unit. The membranes were then blocked using 10% Marvel milk in PBST (10 mM NaH₂PO₄, 0.14 M NaCl, 3 mM KCL, 0.05% (v/v) Tween-20, pH 7.4) for two hours at room temperature or overnight at 4 °C. The antibody of choice was then introduced. Anti-histidine antibody was used at a 1:5000 concentration in PBST. Incubation was carried out for two hours at room temperature. The membrane was then washed five times, for five minutes, with PBST.

NOS specific antibodies were used in 1:1000 concentration in PBST. The membrane was incubated with the primary antibody overnight at 4 °C. The membrane was washed three times for five minutes in PBST. The secondary antibody used was goat anti-rabbit. This was incubated with the membrane for one hour, at room temperature at a concentration of 1:2000. The membrane was then washed five times for five minutes with PBST. Calmodulin specific antibody was used at 1:500 concentration in PBST. The secondary antibody used with the calmodulin antibody was rabbit anti-mouse, which was used in 1:1000 concentration.

The washed blots were developed by incubation of the membrane for three minutes with enhanced chemiluminescent (ECL) Western blot substrate (Pierce). Signals were detected

using photography film supplied by Kodak or Santa Cruz. Exposure times varied depending on what antibody was used. The preferred exposure time for anti-histidine antibody proved to be between 30 and 45 minutes. For the NOS specific antibodies exposure time was 15 minutes. These films were developed and molecular weight markers were manually added using the PVDF membrane as a guide.

5.2.4.5 Stripping and re-probing PVDF membranes

In order to utilise different antibodies on the same PVDF membrane, the initial primary antibody used must be removed. PVDF membranes were stripped of antibody using 5mL of Restore Western blot Stripping Buffer (21059) supplied by Thermo Scientific and incubated with rotation for 5 minutes at room temperature. Residual stripping solution was removed by washing three times for five minutes with PBST. In order to ascertain if complete removal of the antibody had occurred, membranes were incubated with ECL and developed as described above. Where no signal was detected, complete removal of the enzyme conjugate could be assumed. Successfully stripped membranes were then re-blocked with 10% (w/v) non-fat dried milk prepared in PBST for a minimum of 30 minutes at room temperature. Successfully stripped membranes could then be probed with alternative antibodies. Membranes were probed a maximum of three times.

5.2.4.6 Mass spectrometry

Successful expression of NOS and calmodulin proteins was confirmed via mass spectrometry analysis. Following Coomassie staining of gels the bands which were suspected to be NOS proteins were cut from the gel and prepared for analysis using the protocol of Shevchenko *et al.*¹³¹ Bands of interest were manually cut from the gel surface sliced into small cubes and placed into 500 µl Eppendorf tube. The gel fragments were incubated with 100 µL of 100 mM ammonium bicarbonate/acetonitrile for 30 minutes. Acetonitrile (500 µL) was added and incubation continued until destaining of the gel fragments was completed.

Trypsin digestion solution was prepared using 20 µg sequencing grade trypsin supplied by Promega (V511C). Trypsin (20 µg) was resuspended in 1.5 mL 10 mM ammonium bicarbonate containing 10% (v/v) acetonitrile. Each gel piece was incubated on ice with 50 µL of the trypsin solution for two hours. Additional digestion solution was added to any gel pieces that were not saturated with solution. The gel pieces were prevented from drying out by addition of 10 µL of 10 mM ammonium bicarbonate in 10% acetonitrile to the top of each sample. The gel pieces were then incubated at 37 °C overnight. Protein was extracted from the gel plugs using 100 µL extraction buffer (1:2 (v/v) 5% formic acid: acetonitrile). Samples were incubated at 37 °C for 15 minutes with shaking. The solution containing extracted peptides was then removed from each sample and placed in a fresh Eppendorf tube. Samples were vacuum dried using an Eppendorf concentrator 5301 and stored at -20 °C until mass spectrometry analysis.

All peptide identifications were carried out using the Ion Trap 6340 LC/MS/MS system supplied by Agilent. Digested samples were resuspended in 20 µl 0.1% (v/v) trifluoroacetic acid (TFA) in Milli-Q water. Samples were then filtered using spin filters supplied by Fisher (MPA-150-020W), pore size 0.22 µm. Trypsin digest (5 µL) was loaded onto a C18 chip (G4240-62006) supplied by Agilent at a rate of 0.6 µl/min in 0.1% formic acid (FA). The mobile phases were aqueous solutions of 0.1% (v/v) FA and an acetonitrile solution of 0.1% (v/v) FA. A 10 minute gradient was carried out to increase the acetonitrile concentration to 100% linearly. Charged ions were generated using an electrospray ionisation source. Spray voltage was set to 2000 V.

All peptides were submitted to the Mascot search engine to identify proteins and searched against the Swiss-Prot database.¹²¹ Trypsin was set as the digestion enzyme and up to two missed cleavages were allowed. Peptide mass tolerance was set at ± 2 for precursor ions and a tolerance of ± 1 for fragment ions. Variable modifications allowed for were carboxymethyl (C) and oxidation (M). Taxonomy was selected as Homo sapien. When using the Swiss-Prot, database individual ion scores >37 indicate protein identity or extensive homology ($p < 0.05$). Only peptides matched with a score >37 were accepted as significant.

5.2.5 Griess assay

The effectiveness of potential human nNOS inhibitors was tested using a Griess assay kit supplied by Oxford Biomedical research (NB78). Also purchased from the same supplier was the nitric oxide synthase co-factor kit, (NS70). This co-factor kit contained 25 μM FAD, 25 μM and 2.5 μM calmodulin. The Griess assay kit contained the following components (Table 5.3).

Table 5.3. Griess assay kit components.

Component	Contents
Reaction buffer	20 mM HEPES; 0.5 mM EDTA
NADPH part A	NADP ⁺ , Glucose 6-Phosphate, L-arginine
NAPDH part B	Glucose 6-phosphate dehydrogenase
Nitrate reductase	Nitrate reductase
Nitrate reductase Buffer	Aqueous buffer
Colour solution A	Sulfanilamide in 3N HCl
Colour solution B	N-(1-Naphthyl) ethylenediamine dihydrochloride
Nitrite standard	500 pmol / μL NaNO ₂

5.2.5.1 Standard curve construction

The manufacturer provided nitrite standard samples was used to produce a standard curve. The standard was diluted using MQ water to produce a series of solutions with nitrite concentrations ranging from 0 to 100 μM . The absorbance of these solutions was read at 540 nM. Absorbance was plotted against nitrite concentration to generate a standard curve.

5.2.5.2 Sample testing

Frozen protein samples prepared as described above (Section 5.2.3.3) were defrosted on ice for compound testing. Each vial of 35 μL allowed for one compound to be tested in duplicate. All compounds to be tested were made up in DMSO. Eppendorf tubes were labelled as required; each set of tests included a positive and a negative control, as well as a vehicle control. The positive control was untreated NOS protein, the negative control was NOS protein treated with 50 μM of L-NNA and the vehicle control was treated with 1.25 μL of DMSO.

To each Eppendorf 200 μL of reaction buffer, 10 μL of NADPH A and 10 μL of NADPH B were added, along with 30 μL of purified NOS protein and 10 μL of NOS cofactor mix. Compounds to be tested were added to the appropriate tubes in 1.25 μL of DMSO to a final concentration of 50 μM . These tubes were shaken gently and then incubated at 37 $^{\circ}\text{C}$ for six hours.

Following incubation the tubes were chilled on ice for five minutes before adding 10 μL of nitrate reductase. Following a brief vortex these were then left at room temperature for 20 minutes and then centrifuged at 12,500 rpm for five minutes at 4 $^{\circ}\text{C}$. A 100 μL aliquot from each tube was then added in duplicate to a 96 well plate. Colour solution A (50 μL) was added to each well, followed by 50 μL of colour solution B (**Table 5.3**). The plate was covered with a clear lid and left rocking gently for five minutes. The absorbance readings were measured at 540 nm. The absorbances were converted to concentration using the standard curve. The effectiveness of the compounds was compared to the vehicle for statistical significance using Graphpad.¹³⁰ Differences between the vehicle control and treated samples were tested for statistical significance using a two tailed t test, with a p value of less than 0.05 being deemed significant.

5.3 Computational theory

In silico drug design has proven to be a popular and productive tool for identification of small molecule inhibitors of various enzymes and binding sites. There are many techniques which can be applied in this field. This work made use of a selection of these including docking, homology modelling, pharmacophore development and large database screening. Efforts were also made to predict various ADMET properties of computational hit compounds. The following section describes the theory behind these techniques.

5.3.1 Molecular mechanical calculations

The strength of ligand-enzyme interactions are of key importance for *in silico* design experiments. These interactions are scored based on how strongly the ligand is predicted to bind to the enzyme. Owing to the size and complexity of the molecules involved it is computationally difficult to examine all interactions at an atomistic level. Instead, approximations called force fields are used.¹³² These force fields also play a role in other processes such as energy minimization operations. They are therefore of fundamental importance and will be discussed in some detail.

5.3.2 Force fields

Force fields are a simplified method of predicting the overall energy of a given nuclear configuration, such as a ligand protein interaction. The total energy (E_{tot}) can be written as a function of the nuclear coordinates.¹³³ Electrons are not explicitly considered and the field they generate is not actually calculated, but rather represented by an “effective” potential treated by classical mechanics.¹³³ Electrons can be explicitly considered by use of quantum mechanical calculations. These are extremely accurate and precise calculations but are resource intensive and so are not suitable for the types of virtual screening applications that were used in this project.

Different force fields calculate the total energy of the molecules in slightly different ways. A popular and widely used force field is Chemistry at HARvard Macromolecular mechanics, or CHARMM.¹³⁴ This is incorporated into Biovia's Discovery Studio suite of software. The force field equation for CHARMM is shown in Equation 2.

Equation 2. CHARMM force field equation.⁶⁹

$$U(\vec{R}) = \sum K_b (b - b_0)^2 + \sum_{angles} K_\theta (\theta - \theta_0)^2 + \sum_{Urey-Bradley} K_{UB} (S - S_0)^2 + \\ \sum_{dihedrals} K_\varphi (1 + \cos(n\varphi - \delta)) + \sum_{impropers} K_\omega (\omega - \omega_0)^2 + \\ \left\{ \varepsilon_{ij}^{min} \left[\left(\frac{R_{min}^{ij}}{r_{ij}} \right)^{12} - 2 \left(\frac{R_{min}^{ij}}{r_{ij}} \right)^6 \right] + \frac{q_i q_j}{4\pi\varepsilon_0 \varepsilon r_{ij}} \right\} + \sum_{residues} U_{CMAP}(\varphi, \psi)$$

Each term of the equation represents a different parameter which needs to be considered for configuration energy. These terms can be loosely divided into bonding and non-bonding terms. The bonded terms are $v(b)$ bond stretching (Equation 3), $v(\theta)$ angle bending (Equation 4), $v(\varphi)$ torsion potentials (Equation 5), and $v(\omega)$ improper torsions (Equation 6). The energy contribution of all bonded terms is calculated by comparing the observed state of the molecule to an "ideal" value. The difference is then multiplied by a constant. Deviation away from the "ideal" value results in an energy penalty. The larger the deviation, the larger the penalty, the more energetic that particular state becomes. The non bonding interactions are accounted for by $v_{nb}(r_{ij})$. The non bonded functions include Van der Waals forces and electrostatic interactions.¹³³

5.3.2.1 Bonded Functions

Each HB in a molecule is assigned a reference length by the particular force field. Deviation of bond length away from this reference length results in an energy penalty for that particular version of the molecule. The energy penalty is calculated based on Hooke's law as shown in Equation 3.

Equation 3. Bond length term of the CHARMM equation.⁶⁹

$$v(b) = K_b(b - b_0)^2$$

Where b_0 is the reference bond length, b is the observed bond length and K is the force constant for bond stretching. This constant is unique to each particular bond type. The larger the deviation from the reference bond length the larger the energy penalty.

The second bonded interaction is the angle bending term. This parameter is viewed in a similar manner to the bond stretching term already described. EachHB is assigned a reference angle and deviation from this angle results in an energy penalty proportional to the size of the deviation. This is quantified as shown in Equation 4.

Equation 4. Bond angle term of the CHARMM equation.⁶⁹

$$v(\theta) = K_\theta(\theta - \theta_0)^2$$

Where θ is the observed angle, θ_0 is the reference angle and, K is the force constant needed to bend the bond angle.

BothHB stretching and angle bending are sometimes referred to as hard degrees of freedom, i.e. large amounts of energy are required to stretch or bend a bond. The majority of structure variation from bonded terms is due to torsional interactions of the molecule. As a bond is rotated 360° from its starting position, the energy associated with the bond will change. The energy will increase if the bond is forced into an unfavourable torsion and will decrease if the bond adopts a favourable torsion. Favoured and disfavoured torsions vary between bond types. The energy associated with particular torsions are calculated using a cosine series expansion as shown in Equation 5.

Equation 5. Torsional potential term of the CHARMM equation.⁶⁹

$$v(\varphi) = K_\varphi (1 + \cos(n\varphi - \delta))$$

Where $v(\psi)$ is the torsion energy, K_ϕ is the barrier height, defining how much energy is needed to rotate the bond. This is constant and bond specific. The n term is the number of minimum energy points adopted during a full 360° rotation and finally δ is the phase factor, which is the torsional angle with the lowest energy. An example of the graphs generated using this function is shown in **Figure 5.5**.¹³⁵

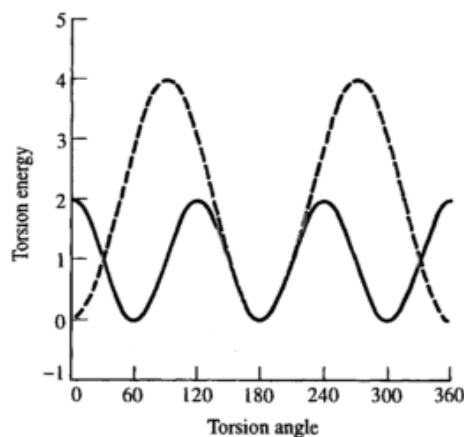


Figure 5.5. Graph demonstrating the torsion energies possessed by bonds at various angles.¹³⁵ The x-axis represents the bond torsional angles, while the y-axis represents the energy at that torsional angle.

The graph shows the energies of two different bonds. The bond represented by the dotted line adopts its minimum energy at three rotational points, 0° , 180° and 360° . The solid line also has three minimum energy points at 60° , 180° and 300° . The energy barrier for this bond is lower than that of the dotted line, meaning that it will be easier for this bond to rotate out of its ideal torsional configuration.

Improper torsions are used to define bond angle torsions in planar groups which have out of plane bending motions, such as sp^2 hybridized carbons in carbonyl groups and in aromatic rings. A reference angle, ω , is assigned to motifs which commonly exhibit out of plane bending. This assigned value dictates to what degree the bond is expected to bend out of the plane. Deviation from this reference angle is assigned an energy penalty relative to the size of the deviation (Equation 6).

Equation 6. Improper torsions equation.⁶⁹

$$v(\omega) = K_{\omega}(\omega - \omega_0)^2$$

The final type of bonded interaction is a broad class called cross terms. This refers to how movement in one part of the molecule may result in a conformational change somewhere else. For example, as a bond angle tightens the bonds which create this angle may stretch in an attempt to minimize the steric clash between the two bonded atoms. A diagram of such an interaction is shown in **Figure 5.6**.



Figure 5.6. Illustration of cross terms.

The “normal” species represents the bonding environment when there is no steric interference between atoms one and three. The “abnormal” species demonstrates how the bond length between atoms two and three and two and one can increase to mitigate steric interactions between atoms one and three. In Urey-Bradley force fields, such as CHARMM, the change in energy caused by these types of movements are represented by a harmonic function of the distance between the one and three atoms as shown in Equation 7.

Equation 7. Energy change associated with a 1,3 cross term in a CHARMM.⁶⁹

$$v(s) = K_{UB}(S - S_0)^2$$

K is the force constant and S_0 is the “ideal” distance between the one and three atoms and S is the adopted distance between the one and three atoms.

This can actually be classified as a non-bonded term as it examines the energy changes caused by the interactions of the two non-bonded atoms one and three as in **Figure 5.6**. The other two major non bonded terms considered in CHARMM are electrostatic interactions and Van der Waals forces which are discussed in Section 5.3.2.2.

5.3.2.2 Non bonded functions

Electrostatic interactions are caused by permanent dipoles within molecules due to the differences in electronegativity between various atoms. These permanent dipoles result in attractive or repulsive forces between ligands and receptors. The unevenly distributed charges within a molecule are often represented mathematically by functional point charges. The electrostatic attraction or repulsion between two atoms/molecules can then be calculated as a sum of these point charges using a variation of Coulomb's law as shown in Equation 8.

Equation 8. CHARMM describing electrostatic interactions.⁶⁹

$$\frac{q_i q_j}{4\pi\epsilon_0\epsilon r_{ij}}$$

Where q_i and q_j are the magnitudes of the charge on each molecule, ϵ_0 is the permittivity of free space which is a constant. The ϵ term is the permittivity of the solvent in which the molecules are immersed and r_{ij} is the distance between the two molecules.

Van der Waals interactions are accounted for using a Lennard-Jones 12-6 potential which incorporates both attractive and repulsive interactions.¹³⁶ The CHARMM term is shown in Equation 9.

Equation 9. Lennard Jones term for CHARMM.⁶⁹

$$\epsilon_{ij}^{min} \left[\left(\frac{R_{min}^{ij}}{r_{ij}} \right)^{12} - 2 \left(\frac{R_{min}^{ij}}{r_{ij}} \right)^6 \right]$$

The R^{12} term describes the repulsive force that exists at short distances between atoms due to the overlapping electronic orbitals, while the R^6 term describes the attractive force that exists between transient dipoles. The two equations shown in Equation 8 and Equation 9 are combined as one function in the CHARMM equation.

The final term in the CHARMM equation is known as the spline function (Equation 10).

Equation 10. Spline function in CHARMM.⁶⁹

$$v(s) = U_{CMAP}(\varphi, \psi)$$

This function is used primarily for operations involving biomolecules, such as protein minimization calculations. It adds the energy associated with the backbone dihedral angles to the overall energy as represented in Equation 2. It also allows for correction of small errors in the protein backbone.⁶⁹

5.3.3 Protein minimizations

Force fields are clearly an integral part of scoring interactions between targets and potential interactors. Force fields can also be applied to another vital computational process, energy minimization tasks.

This project made use of Discovery Studio and its built energy minimization algorithm which is based on the CHARMM force field. This program uses a combination of two minimization methods, steepest descent followed by conjugate gradient. The steepest descent method moves the atoms of the protein structure to cause the most rapid decline in energy possible. This allows the protein to adopt a local minimum. This can then be refined using a conjugate gradient to find the global minimum of the protein. This type of analysis is particularly important when examining areas of the protein which are highly flexible such as loops.

5.4 Other computational tools

5.4.1 Clustering

Clustering involves grouping molecules with similar properties into subsets, or clusters, so that each member of the set has similar properties, while molecules in different subsets are as dissimilar as possible. Similarity is assigned based on RMSD of the heavy atoms, or Tanimoto distances for fingerprints.¹⁶⁷ Each cluster is assigned a cluster centre. This is a single molecule which best represents the properties of all the members of the set. This type of analysis is useful as it allows a large dataset to be represented by a smaller, more manageable dataset.¹⁶⁸

5.4.2 Pharmacokinetic predictions

Discovery Studio can predict an array of ADMET properties for small molecule datasets. This allows for elimination of compounds with unfavourable pharmacokinetic profiles early in the drug development process. The ADMET predictions are derived from Bayesian models of experimentally validated compounds. Three of these properties were used in this work. The first of these was a prediction of how easily screened compounds would pass blood brain barrier (BBB) following oral administration. This is scored from zero to four and is based on the ratio of the concentration of compound in the brain to the concentration of compound in the blood (**Table 5.4**).¹⁶⁹

Table 5.4. BBB levels and descriptions.

Level	Value	Description
0	Very high	Brain: Blood ratio greater than 5:1
1	High	Brain: Blood ratio between 1:1 and 5:1
2	Medium	Brain: Blood ratio between 0.3:1 and 1:1
3	Low	Brain: Blood ratio less than 0.3:1
4	Undefined	Outside 99 percent confidence ellipse

The absorption level property predicts human intestinal absorption after oral administration. This is defined by the percentage of the compound which is absorbed into the bloodstream. A compound is defined as well absorbed if at least 90% of it enters the bloodstream. A value of zero is good, one is moderate, two is low and three is very low absorption.¹⁷⁰

The solubility level descriptor predicts the aqueous solubility of a compound in water at 25 °C. Compounds are assigned a solubility level from zero to six relative to a selection of known drugs (**Table 5.5**).¹⁶⁹

Table 5.5. Solubility descriptors from Discovery Studio.

Level	Description
0	Extremely low solubility, lower than 95% of drugs
1	Very low solubility, at border line of 95% of drugs
2	Low solubility, at lower end of 95% of drugs
3	Good, slight soluble to soluble
4	Optimal solubility
5	Very soluble, risks rapid elimination
6	Unknown

5.5 Computational Methods

5.5.1 Structure based design

5.5.1.1 Homology model construction

Initial structure based screening trials were conducted using a human nNOS homology model. The templates used for this were rat nNOS crystal structures (PDB codes 3RQJ and 3PNF, with resolution of 1.84 Å and 1.94 Å respectively).^{65,73} One homology models were developed from each template.

The human nNOS protein sequence was retrieved from the Uniprot database and aligned to the sequence of each template using Discovery Studio software from Biovia. One hundred homology models were then constructed using the default settings of Modeller.¹⁴⁹ Owing to the small, inflexible loops of nNOS no loop refinement was performed. The models were ranked using the DOPE scoring function and the top scoring model for the 3PNF and the 3RQJ templates were taken. These were energy minimized to remove potential atom clashes and were then validated. The homology models are referred to as 3PNF-HM and 3RQJ-HM.

5.5.2 Homology model structural verification

The structural robustness of the homology models was verified using a variety of tools on the UCLA website (<http://services.mbi.ucla.edu/SAVES/>). These included Verify 3-D, Errat and Procheck. For a full and detailed discussion of the functions of each of these tools please refer to section 2.2.

5.5.3 Homology model functional verification

The functionality of the models for virtual screening was tested using two main methods. Firstly, the templates used had been co-crystallized with inhibitors of rat nNOS. These inhibitors were removed and re docked into the binding site of the homology models. The ability of each docking function to re produce the original binding pose of the inhibitors was measured via RMSD.

Secondly, the ability of the model to identify active nNOS inhibitors from a set of 1000 molecules was tested. The set of 1000 molecules was termed a test set. The ChEMBL website was searched for compounds which inhibited human nNOS and the resulting list sorted based on IC₅₀ values. Compounds with an IC₅₀ of 10 μ M or lower were chosen as

active inhibitors, while those with an IC_{50} above 30 μ M were designated inactive, or decoys. This resulted in an active file with 520 compounds and an inactive file of 147 compounds. To have an active to decoy ratio of roughly 1:33 the active compounds were clustered into 33 cluster centres and the centre of each cluster taken as representative of the cluster.¹³⁹

A total of 967 decoys were needed to make up the full 1000 molecules and to achieve the desired ratio. The first 147 of these were taken directly from ChEMBL. The remaining 820 decoys were generated using the Chemdiv database and an nNOS like Bayesian filter. This filter was developed in Pipeline Pilot using the 520 active nNOS inhibitors taken from ChEMBL. The component learned what physio-chemical properties a molecule should have in order to be an nNOS inhibitor. The Chemdiv dataset was then passed through this filter and the top 820 compounds retained. These were combined with the 147 ChEMBL inactives to give a final total of 967 decoys. The active compounds were merged into this file to generate the final test set. Note that while ChEMBL classes the compounds mentioned above as human nNOS inhibitors, detailed examination of the literature from which the compounds were sourced mentions very little testing carried out on the human isoform of nNOS. The test set was therefore made up almost wholly of rat nNOS active and inactive compounds. There are insufficient reports of compounds tested on human nNOS to allow for generation of a human only test set.

Tautomers and stereoisomers of the test set were generated using Pipeline Pilot. Conformers were then generated with Omega.¹³⁹ This molecule file was then docked into 3PNF-HM and 3RQJ-HM using default FRED parameters. Both homology models were tested with and without water present. The docked lists from each of the seven FRED scoring functions each model were used to generate a set of ROCS curves. The overall best homology model and scoring function from this set of tests was chosen based on the verification results and taken forward for screening of commercial datasets.

5.5.4 Database preparation and docking

Two databases were screened for potential nNOS inhibitors using the 3PNF homology model. These were Maybridge (<http://www.maybridge.com>) and a “drug like commercially available” subset of Zinc (<http://zinc.docking.org/subsets/drugs-now>). Using Pipeline Pilot,

the largest fragment of each compound from both libraries was kept, thus removing salt counter ions which may interfere with binding. Duplicates were removed and a bump check filter was applied that removed molecules which were poorly drawn. A poorly drawn molecule was defined as a compound in which two or more atoms are 0.1 Å or less apart. A Lipinski filter was also applied to both datasets to select for drug like molecules. A blood brain barrier filter also used. Finally tautomers, stereoisomers and conformers were generated.

The binding site of the homology model was defined using the inhibitory ligand which the 3PNF template had been co crystallized with. Docking was conducted using FRED and the compounds ranked using Chemscore. Following the docking the duplicates were removed and the top 1000 compounds from Maybridge and Zinc were retained. Predicted pharmacokinetic (PK) properties such as solubility, blood brain barrier permeability and absorption level were generated for these compounds.

The same procedure was carried out using human iNOS and human eNOS crystal structures (PDB codes 3E7G and 1M9M and respectively). The top 1000 compounds from the rigid dock using the Chemscore function were retained for each isoform.

5.5.5 Flexible docking

The top 100 hits from Maybridge and Zinc rigid docking were flexibly docked into the 3PNF-HM using CDocker in Discovery Studio. The residues as outlined in **Table 2.1** were selected and allowed to be flexible. The hemeoglobin and the tetrahydrobiopterin adjacent to the binding site were also allowed to be flexible. The most promising candidates were chosen from this screen based on docking score, commercial availability, potential for chemical modification and PK properties. These were purchased in screening quantities for testing.

The same procedure was repeated for the eNOS and iNOS crystal structures with the residues as outlined in **Table 2.19** allowed to be flexible.

5.5.6 Key residue rotamers

Several publications that have focused on rat nNOS have reported that a glutamic acid at position 592 in the binding pocket plays a key role in ligand receptor interactions via HBing.^{49,52,77} The rotameric states of the corresponding glutamic acid in the human homology model (Glu597) were explored. In an effort to improve the docking protocol performance, the seven “new” rotameric states were docked with the test set as before (section 5.5.3) and ROCS scores generated. The three rotamers of ASp602 in the human homology model were also examined in this way. The rotamers were enumerated in Discovery Studio using the Ponder and Richards rotamer library.¹⁷¹

5.5.7 Crystal structures of iNOS and eNOS and their verification

Docking experiments were also conducted using human iNOS and human eNOS. Crystal structures of the human isoforms of both of these proteins are available in the PDB so generation of homology models was not necessary. Two crystal structures for iNOS and two crystal structures for eNOS were chosen. The iNOS structures were 4NOS and 3E7G with resolutions of 2.25 Å and 2.2 Å respectively.^{79,80} The eNOS crystal structures were 1M9M and 3NOS with resolutions of 1.96 Å and 2.40 Å respectively.^{80,81} Structural integrity was verified using similar techniques as were used for the nNOS homology model, i.e. Verify 3-D, Errat and Procheck. Functional tests were also performed by attempting to re dock the co-crystallised ligand into each of the protein crystal structures and by using test sets.

For eNOS and iNOS the test sets were developed using similar techniques as were used to develop the nNOS HM test set. Actives and decoys were retrieved from ChEMBL and the actives clustered into 33 centres. A total of 635 actives and 187 decoys were available for iNOS, while 282 actives and 275 decoys were available for eNOS. The decoys available on ChEMBL were supplemented by screening the ChEMBL database with an iNOS or eNOS “like” Bayesian filter. Tautomers, stereoisomers and conformers of the test sets were generated and then docked into the appropriate crystal structure. The ability of the crystal structures and the docking program to differentiate between actives and decoys was evaluated using ROCS curves. The best performing scoring function and crystal structure

were chosen for eNOS and iNOS. These were taken forward for screening of commercial databases and analysis of the selectivity of the docking protocol for nNOS inhibitors over eNOS and iNOS inhibitors.

5.5.8 Database preparation and docking of iNOS and eNOS

Method as per Section 5.5.4.

5.5.9 Published crystal structure docking

In 2015 the first structure crystal structure of human nNOS was published.⁸³ The structure was validated and rigid docking of Zinc and Maybridge was carried out using FRED 3.0.0. This new version of FRED was released during the course of this work. It returns only one scoring function, Chemgauss4.

5.5.10 Pharmacophore construction

Generation of an nNOS pharmacophore was accomplished using a training set. This was developed using the ChEMBL database. Compounds with IC_{50} values of 10 μ M or less were defined as active nNOS inhibitors, while those with IC_{50} values of greater than 20 μ M were defined as inactive. This set of parameters returned 550 active compounds from ChEMBL and 300 inactives. Actives and inactives were clustered separately into groups of 10 and copied into separate files. Tautomers and stereoisomers were generated. The actives were given the principal attribute of one, while the inactives were designated zero. Attempts to generate a pharmacophore from this training set failed. Therefore new actives were handpicked based on compound activity. This omitted extremely small and potentially unviable active compounds, such as small nitrogen heterocyclic compounds. Ten active compounds (with an IC_{50} of 10 μ M or less) and ten inactive compounds (with an IC_{50} of 30 μ M or more) were chosen for pharmacophore generation (**Table 5.6**). Also included were

compounds that had proved inactive in the Griess assay (compounds 26-35). These compounds had been developed from the homology model screen and showed no activity in the Griess assay with human nNOS. Tautomers and stereoisomers were generated for all actives and inactives, and the set used to generate the first pharmacophore.

Table 5.6. ChEMBL compounds used for first pharmacophore development.

Training Set Active Compounds ChEMBL ID (Handpicked)	Training Set Inactive Compounds ChEMBL ID (Cluster Centres)
ChEMBL1944717 (2)	ChEMBL114551
ChEMBL1825174	ChEMBL101439
ChEMBL397446	ChEMBL7889
ChEMBL293212	ChEMBL100658
ChEMBL162416	ChEMBL1800530
ChEMBL43678	ChEMBL292690
ChEMBL1955937	ChEMBL85525
ChEMBL2203178	ChEMBL431417
ChEMBL2011136	ChEMBL112246
ChEMBL233655	ChEMBL86795

ChEMBL1944717 was designated as most active for the pharmacophore generation. This compound is reported to have an IC_{50} of 12 nM for human nNOS.⁸⁴ This was one of the few ChEMBL compounds actually tested on human nNOS. The features which were permitted in the pharmacophore construction were H-bond donor and acceptor, hydrophobic, hydrophobic aromatic, positive ionisable, negative ionisable, positive charge, negative charge and ring aromatic. The minimum number of features was set to two and the maximum to six.

Six parameter sets were used to determine the optimal settings for pharmacophore generation from the training set. These parameter sets altered the number of excluded volumes, the fitting method (rigid or flexible) and the number of features that could be omitted during the generation process. Ten pharmacophores were generated with the parameter sets to give a total of 60 pharmacophores (**Table 5.7**). Pharmacophore generation was conducted using Catalyst in Discovery Studio.

Table 5.7. Pharmacophore development parameters.

Parameter set	Excluded Volumes	Rigid or Flexible	Max Omit Feature
1	0	Rigid	0
2	0	Rigid	1
3	50	Rigid	0
4	50	Flexible	1
5	0	Flexible	0
6	50	Flexible	0

5.5.11 Pharmacophore validation

Validation of the pharmacophore models was conducted using training sets. This validation was conducted as part of the pharmacophore generation protocol. The test set was used was the Bayesian haystack that had been developed for the structure based design. Following ROCS analysis the most successful pharmacophore was taken forward for screening of commercial databases.

5.5.12 Screening commercial databases with pharmacophores

The commercial databases were prepared as previously described (section 5.5.4). They were then both screened using the best pharmacophore. The returned compound lists had duplicates removed, PK properties calculated and were then compiled into a ranked table.

5.5.13 Pharmacophore evolution

Experimental evaluation of pharmacophore one *in silico* derived hits allowed for addition of new compounds to the generation set for the second pharmacophore. All inactive compounds (compound **50-70**) were added to the inactive portion of the training set and

new models generated. All new pharmacophore models were tested with the test set as described before. The actives used for the generation of pharmacophore one were used for generation of pharmacophore two, as was an active compound that had not appeared in ChEMBL on the original search (**Figure 5.7**).⁴⁵ The best performing pharmacophores were again used to screen commercial databases.

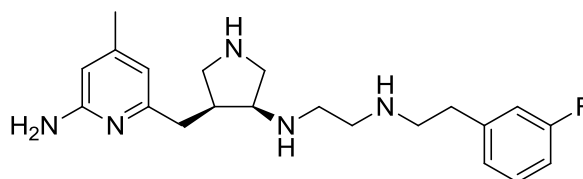


Figure 5.7. Extra active used for the generation of pharmacophore 2.⁴⁵

5.6 Chemical Materials and Methods

5.6.1 Instrumentation

Reagents and reactants were purchased from Aldrich or Alfa Aesar and used as received unless otherwise stated. DCM was distilled over CaH_2 and THF over Na wire and benzophenone. Anhydrous DMF was purchased from Sigma Aldrich. Toluene was dried over 4 Å molecular sieves.

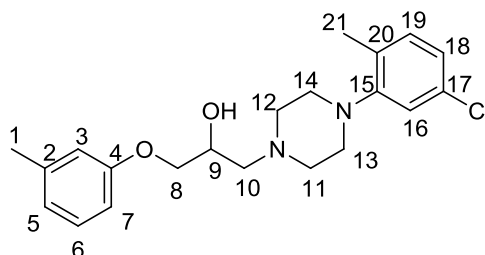
All NMR spectra were recorded on a Bruker Avance spectrometer at a probe temperature of 25 °C, unless otherwise stated, operating at 500 MHz for the ^1H nucleus and 126 MHz for the ^{13}C nucleus. Proton and carbon signals were assigned with the aid of 2D NMR experiments (COSY, HSQC) and DEPT experiments for novel compounds. Spectra were recorded in CDCl_3 unless otherwise stated, with Me_4Si used as internal standard. Chemical shifts are given in ppm downfield from the internal standard and coupling constants are given in Hz. ^{13}C NMR spectra were recorded with complete proton decoupling.

Melting point analyses were carried out using a Stewart Scientific SMP11 melting point apparatus and are uncorrected.

High resolution mass spectra (HR-MS) were performed on an Agilent-L 1200 Series coupled to a 6210 Agilent Time-of-Flight (TOF) mass spectrometer equipped with both a positive and negative electron spray source. Infrared spectra were obtained in the region 4000-400 cm^{-1} on a Nicolet Impact 400D spectrophotometer or using a Perkin Elmer 2000 FTIR spectrometer.

Flash column chromatography was performed using silica gel 60 (Merck, 0.040-0.063 mm). Analytical thin layer chromatography was carried out on aluminium sheets pre-coated with Merck TLC Silica gel 60 F254. Developed sheets were visualised using a portable UVItec CV-006 lamp ($\lambda = 254, 365 \text{ nm}$) or the appropriate stain.

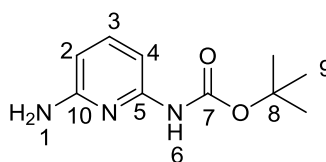
5.6.2 Synthesis of 1-(4-(5-chloro-2-methylphenyl)piperazin-1-yl)-3-(m-tolyloxy)propan-2-ol, compound 41 ⁸⁵



Using a Gilson pipette, 1-(5-chloro-2-methylphenyl)-piperazine was mixed with 2-[(3-methylphenoxy)methyl] oxirane in a 1:1 ratio and stirred briefly. The stir bar was removed and the reaction left to stand overnight. The resulting solution was a clear, viscous liquid. Purified via column chromatography (3:2 petroleum ether: EtOAc) to give a viscous, dark red oil. Yield 56%

¹H NMR: (500 MHz, CDCl₃) δ 7.18 (app t, *J* = 7.8 Hz, 1H, H6), 7.09 (d, *J* = 8.0 Hz, 1H, H19), 6.99-6.95 (m, 2H, H18, H19), 6.81 – 6.73 (m, 3H, H3, H5, H7), 4.15 (m, 1H, H9), 4.01 (m, 2H, H8), 2.95 (dd, *J* = 8.5, 5.5 Hz, 4H, H13, H14), 2.87 – 2.82 (m, 2H, H10), 2.64 (dd, *J* = 12.3, 8.2 Hz, 4H, H11, H12), 2.34 (s, 3H, H21), 2.26 (s, 3H, H1). **¹³C NMR:** (126 MHz, CDCl₃) δ 158.9 (C4), 152.5 (C15), 139.7 (C2/C17), 132.1 (C17/C2), 131.9 (C19), 130.9 (C20), 129.3 (C6), 123.2 (C16), 122.00 (Aryl C), 119.7 (C18), 115.6 (Aryl C), 111.6 (Aryl C), 70.3 (C8), 65.8 (C9), 60.8 (C11, C12), 51.7 (C13, C14), 21.7 (C21), 17.6 (C1). **Rf:** 0.55 (3:2 petroleum ether: EtOAc) **HR-MS:** calcd for C₂₁H₂₈ClN₂O₂ m/z: [M+H]⁺, 376.1861; found: 375.1861 [Diff (ppm) = -1.5]. **IR (Neat):** 3422 (OH), 2944 (N-H), 1260 (C-Cl), 1049 (C-N), cm⁻¹.

5.6.3 Synthesis of tert-butyl (6-aminopyridin-2-yl)carbamate

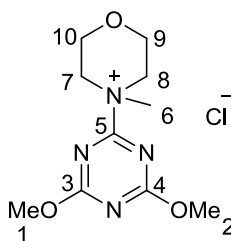


In a stirring flask of THF 1g (0.00458 moles) of di-tert-butyl dicarbonate was mixed with 0.5 g (0.00458 moles) of 2,6-diaminopyridine. This was heated to 60 °C and stirred overnight. The THF was removed under reduced pressure to give a dark brown oil. This was dissolved in

DCM and purified using flash column chromatography. The product was eluted with 7:3 EtOAc: petroleum ether. The product appeared as a light yellow solid. Yield 47%.

¹H NMR: (500 MHz, CDCl₃); δ 8.17 (s, 1H, H1), 7.39 (t, *J* = 8.0 Hz, 1H, H3), 7.20 (d, *J* = 7.9 Hz, 1H, H4), 6.15 (d, *J* = 7.9 Hz, 1H, H2), 4.55 (s, 2H, H6), 1.51 (s, 9H, H9). **¹³C NMR:** (126 MHz, CDCl₃) δ 157.4 (C5), 152.7 (C7), 150.8 (C10), 139.9 (C3), 102.9 (C2), 101.9 (C4), 80.8 (C8), 28.3 (C9). **Rf:** 0.88 (7:3 EtOAc: petroleum ether). **IR (KBr):** 2944 (N-H), 1675 (C=O) cm⁻¹. **MP** 122-124 °C. Matches literature data.¹⁷²

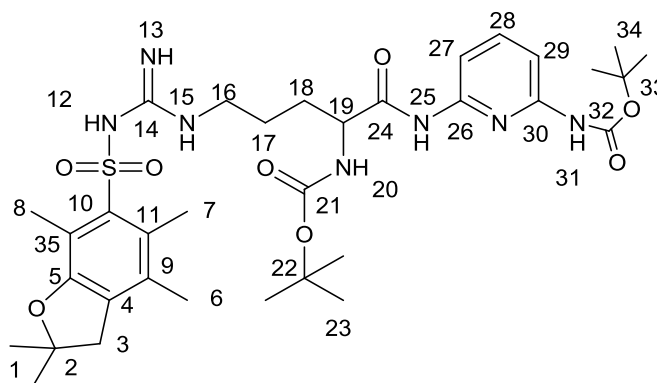
5.6.4 Synthesis of 4-(4,6-Dimethoxy-1,3,5-triazin-2-yl)-4-methyl-morpholinium chloride (DMTMM), Compound 101⁹²



Into 10 mL of freshly dried THF was placed 0.50 g (3 mmol) of 2-chloro-4,6-dimethoxy-1,3,5-triazine (CDMT). 0.52 mL (3.2 mmol) of *N*-methylmorpholine (NMM) was added and the solution stirred in an open flask for 30 minutes. A white precipitate formed as the reaction progressed. The reaction was filtered through sintered glass and the white precipitate was collected. The solid was recrystallized from hot methanol and diethyl ether. The purified DMTMM appeared as a white solid and was stored at 4 °C to ensure stability. Yield 75%.

¹H NMR: (500 MHz, D₂O) δ 4.67 – 4.62 (m, 2H), 4.17 (s, 6H), 4.16 – 4.13 (m, 2H), 3.96 – 3.82 (m, 4H), 3.55 (s, 3H). **¹³C NMR:** (126 MHz, D₂O) δ 173.9 (C3,C4), 63.9 (ring C), 62.0 (ring C), 60.0 (ring C), 57.1 (C1, C2), 55.8 (C6), 53.2 (ring C). **IR (KBr):** 1623, 1541, 1375, 1130 cm⁻¹. **MP:** 114-118 °C. Matches literature data.⁹²

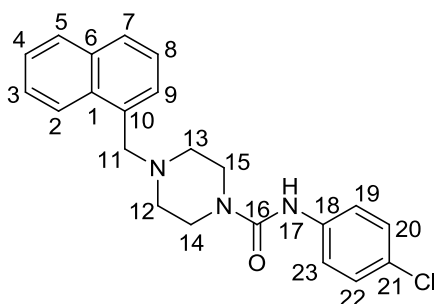
5.6.5 Synthesis of triprotected aminoguanidinium, Compound 102



Into a dry two necked round bottom under a flow of N_2 was placed 0.125 g (2.37×10^{-4} mols, 1 eq) of N_α -Boc- N_ω -(2,2,4,6,7-pentamethyl-dihydrobenzofuran-5-sulfonyl)-L-arginine (Boc-Arg-(Pbf)-OH), 0.075 g (2.37×10^{-4} mols, 1 eq) of TBTU, 0.040 g of HOBt (2.61×10^{-4} mols, 1.1 eq) and 0.65 ml (5×10^{-3} mols) of NEt_3 . These were dissolved in dry DMF and stirred at room temperature for 15 minutes. 0.051 g (2.41×10^{-4} mols, 1 eq) of tert-butyl (6-aminopyridin-2-yl)carbamate (AC002) was then added and the resulting solution stirred overnight at $50^\circ C$. The solvent was removed under reduced pressure and the mixture purified via column chromatography using 7:3 petroleum ether: EtOAc as the solvent. The product appeared as a yellow oil. Yield 90%

1H NMR: (500 MHz, $CDCl_3$); 1H NMR (500 MHz, $CDCl_3$) δ 9.42 (s, 1H, NH), 7.86 (s, 1H, NH), 7.66 (s, 1H, NH), 7.36 (app t, $J = 8.0$ Hz, 1H, H28), 7.19 (d, $J = 8.0$ Hz, 1H, H27), 6.13 (d, $J = 7.9$ Hz, 1H, H29), 5.34 (d, $J = 7.0$ Hz, 1H, NH), 4.56-4.41 (m, 2H, NH, CH (H16)), 4.35 (s, 1H, H19), 3.36 (m, 1H, H16), 2.94 (s, 2H, H3), 2.55 (s, 3H, CH_3), 2.50 (s, 3H, CH_3), 2.38 (m, 1H, H18), 2.08 (s, 3H, CH_3), 1.90 – 1.76 (m, 2H, H17), 1.60 – 1.51 (m, 1H, H18), 1.48 (s, 9H, BOC), 1.44 (s, 6H, $CH_3 \times 2$), 1.43 (s, 9H, BOC). **^{13}C NMR** (126 MHz, $CDCl_3$) δ 175.2 (C24), 158.3 (C14), 156.3 (C=O), 154.5 (C=O), 153.0 (Aryl C), 151.5 (Aryl C), 149.5 (Aryl C), 138.9 (C28), 137.9 (Aryl C), 131.8 (Aryl C), 130.7 (Aryl C), 123.8 (Aryl C), 116.7 (Aryl C), 102.0 (C29), 100.6 (C27), 85.7 (C2), 79.7 (C-Boc), 79.1 (C-Boc), 51.3 (C19), 42.1 (C3), 40.9 (C16) 28.0 (BOC CH_3), 27.6 (C1), 27.7 (BOC CH_3), 24.3 (C18), 20.0 (C17), 18.2 (CH_3), 17.0 (CH_3), 11.4 (CH_3). **Rf:** 0.46 (7:3 petroleum ether: EtOAc) **HR-MS:** calcd for $C_{34}H_{52}N_7O_8S$ m/z: $[M+H]^+$ 718.3593; found: 718.3583 [Diff (ppm) = -1.28 ppm]. **IR (Neat):** 3392 (N-H), 1696 (C=O), 1616 (C=O), 1369 (S=O).

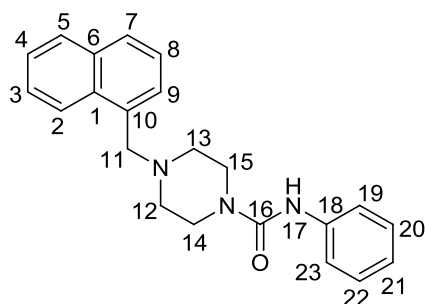
5.6.6 Synthesis of N-(3-chlorophenyl)-4-(naphthalen-1-ylmethyl)piperazine-1-carboxamide, Compound 37



Under a flow of nitrogen, 0.23 g (1 mmol) of 1-(naphthalen-1-ylmethyl)piperazine was mixed with 0.15 g (1 mmol) of 1-chloro-3-isocyanatobenzene in a sealed round bottom. To this was added dry DCM and the solution was stirred at room temperature. The reaction progress was monitored by TLC. After five hours the starting material was consumed. The DCM was removed under reduced pressure to yield the crude product. This was purified via column chromatography using 1:1 EtOAc:Pet Ether to elute the product as a white solid. Yield 81%.

¹H NMR: (500 MHz, CDCl₃) δ 8.29 (d, 1H, *J* = 7.9 Hz, Naphthyl H), 7.88 – 7.85 (m, 1H, Naphthyl H), 7.82 – 7.78 (m, 1H, Naphthyl H), 7.51-7.48 (m, 2H, Naphthyl H), 7.44-7.39 (m, 2H, Naphthyl H), 7.30 (d, *J* = 8.9, 2H, H₂₀, H₂₂), 7.23 (d, *J* = 8.9 Hz, 2H, H₁₉, H₂₃), 6.30 (s, 1H, H₁₇), 3.95 (s, 2H, H₁₁), 3.50 – 3.45 (m, 4H, H₁₄, H₁₅), 2.60 – 2.52 (m, 4H, H₁₂, H₁₃). **¹³C NMR:** (126 MHz, CDCl₃) δ 183.2 (C₁₆), 137.4 (C₁₈), 133.9 (Naphthyl C₆/C₁), 133.2 (Naphthyl C₆/C₁), 132.5 (C₁₀), 129.9 (C₂₁), 128.8 (C₂₀, C₂₂), 128.4 (Naphthyl C), 128.2 (Naphthyl C), 127.5 (Naphthyl C), 125.8 (Naphthyl C), 125.7 (Naphthyl C), 125.1 (Naphthyl C), 124.6 (Naphthyl C), 121.0 (C₁₉, C₂₃), 61.1 (C₁₁), 52.8 (C₁₂, C₁₃), 44.1 (C₁₄, C₁₅). **HR-MS:** calcd for C₂₂H₂₃ClN₃O *m/z*: [M+H]⁺; 380.1524 found: 380.1533 [Diff (ppm) = 2.1]. **IR (KBr):** 2937 (N-H), 1635 (C=O), 820.9 (C-Cl) cm⁻¹ **MP:** 205-206 °C

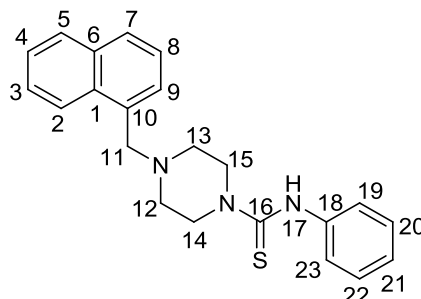
5.6.7 Synthesis of 4-(naphthalen-1-ylmethyl)-N-phenylpiperazine-1-carboxamide, Compound 38



Under a flow of nitrogen, 0.23 g (1 mmol) of 1-(naphthalen-1-ylmethyl)piperazine was mixed with 0.12 g (1 mmol) of isocyanatobenzene in a sealed round bottom. To this was added dry DCM and the solution was stirred at room temperature. The reaction progress was monitored by TLC. the starting material was consumed. The DCM was removed under reduced pressure to yield the crude product. This was redissolved in EtOAc and purified via column chromatography (50:50 EtOAc:Pet Ether) to yield the pure product as a yellow/orange solid. Yield 66%.

¹H NMR (500 MHz, CDCl₃) δ 8.30 (d, *J* = 8.1 Hz, Naphthyl H), 7.88 – 7.85 (m, Naphthyl H), 7.80 (m, 1H, Naphthyl H), 7.51 (m, 2H, Naphthyl H), 7.44 – 7.40 (m, 2H, Naphthyl H), 7.34 (dd, *J* = 8.5, 1.0 Hz, 2H, H20, H22), 7.30 – 7.27 (m, 2H, H19, H23), 7.03 (m, 1H, H21), 6.30 (s, 1H, H17), 3.95 (s, 2H, H11), 3.51 – 3.47 (m, 4H, H14, H15), 2.59 – 2.54 (m, 4H, H12, H13). **¹³C NMR** (126 MHz, CDCl₃) δ 182.2 (C16), 138.9 (C18), 133.9 (Naphthyl C6/C1), 133.2 (Naphthyl C6/C1), 132.5 (C10), 128.9 (C19, C23), 128.5 (Naphthyl C), 128.3 (Naphthyl), 127.6 (Naphthyl C), 125.9 (Naphthyl C), 125.7 (Naphthyl C), 125.1 (Naphthyl C), 124.7 (Naphthyl C), 123.1 (C21), 119.9 (C20, C22), 61.2 (C11), 52.9 (C12, C13), 44.2 (C14, C15). **HR-MS:** calcd for C₂₂H₂₄N₃O *m/z*: [M+H]⁺; 346.1914 found: 346.1923 [Diff (ppm) = 2.64]. **IR (KBr):** 2951 (N-H), 1638 (C=O) cm⁻¹. **MP:** 158-160 °C

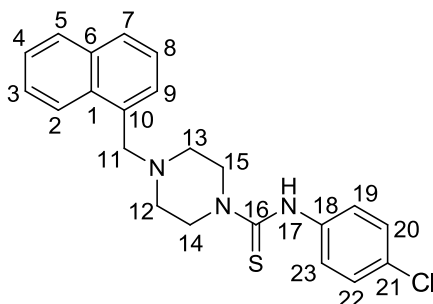
5.6.8 Synthesis of 4-(naphthalen-1-ylmethyl)-N-phenylpiperazine-1-carbothioamide, Compound 39



Under a flow of nitrogen, 0.23 g (1 mmol) of 1-(naphthalen-1-ylmethyl)piperazine was mixed with 0.14 g (1 mmol) of isothiocyanatobenzene in a sealed round bottom. To this was added dry DCM and the solution was stirred at room temperature. The reaction progress was monitored by TLC. After five hours the starting material was consumed. The DCM was removed under reduced pressure to yield the crude product. This was purified via column chromatography (95:5 DCM:MeOH) to yield the pure product as a white solid. Yield 58%.

¹H NMR (500 MHz, CDCl₃) δ 8.26 (d, *J* = 8.1 Hz 1H, Naphthyl H), 7.87 – 7.84 (m, 2H, Naphthyl H), 7.80 – 7.77 (m, 1H, Naphthyl H), 7.54 – 7.47 (m, 2H, Naphthyl H), 7.41 – 7.38 (m, 2H, Naphthyl H), 7.33-7.29 (m, 2H, H20, H22), 7.16 (s, 1H, H17), 7.12 (m, 1H, H21), 7.08 (d, *J* = 7.6 Hz, 2H, H19, H23), 3.93 (s, 2H, H11), 3.83 – 3.78 (m, 4H, H14, H15), 2.60 – 2.54 (m, 4H, H12, H13). **¹³C NMR** (126 MHz, CDCl₃) δ 183.3 (C16), 140.1 (C18), 133.9 (Naphthyl C1/C6), 133.2 (Naphthyl C1/C6), 132.5 (C10), 129.2 (C20, C22), 128.5 (Naphthyl C), 128.3 (Naphthyl C), 127.6 (Naphthyl C), 125.9 (Naphthyl C), 125.8 (Naphthyl C), 125.1 (Naphthyl C), 125.0 (C21), 124.7 (Naphthyl C), 122.6 (C19, C23), 60.9 (C11), 52.5 (C12, C13), 49.8 (C14, C15). **HR-MS**: calcd for C₂₂H₂₄N₃S *m/z*: [M+H]⁺; 362.1685 found: 362.1694 [Diff (ppm) = 2.42]. **IR (KBr)**: 2943 (N-H), 1533 (C=S) cm⁻¹. **MP**: 150-154 °C

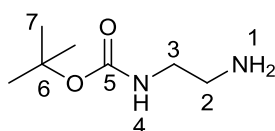
5.6.9 Synthesis of N-(3-chlorophenyl)-4-(naphthalen-1-ylmethyl)piperazine-1-carbothioamide, Compound 40



Under a flow of nitrogen, 0.23 g (1 mmol) of 1-(naphthalen-1-ylmethyl)piperazine was mixed with 0.17 g (1 mmol) of 1-chloro-3-isothiocyanatobenzene in a sealed round bottom under a flow of nitrogen. To this was added dry DCM and the solution was stirred at room temperature. The reaction progress was monitored by TLC. After five hours the starting material was consumed. The DCM was removed under reduced pressure to yield the crude product. This was purified via column chromatography (4:1 petroleum ether: EtOAc) to yield the pure product as a white solid. Yield 76%.

$^1\text{H NMR}$ (500 MHz, CDCl_3) δ 8.27 (d, $J = 8.1$ Hz, 1H, Naphthyl H), 7.89 – 7.84 (m, 1H, Naphthyl H), 7.82 – 7.78 (m, 1H, Naphthyl H), 7.51 (m, 2H, Naphthyl H), 7.40 (m, 2H, Naphthyl H), 7.28 (d, $J = 8.7$ Hz, 2H, H20, H22), 7.07 (d, $J = 8.6$ Hz, 2H, H19, H23), 3.94 (s, 2H, H11), 3.85 – 3.79 (m, 4H, H14, H15), 2.61 – 2.54 (m, 4H, H12, H13). $^{13}\text{C NMR}$ (126 MHz, CDCl_3) δ 182.9 (C16), 138.5 (C18), 133.9 (C1/C6), 133.2 (C1/C6), 132.4 (C10), 130.5 (C21), 129.2 (C20, C22), 128.5 (Naphthyl C), 128.3 (Naphthyl C), 127.7 (Naphthyl C), 125.9 (Naphthyl C), 125.8 (Naphthyl C), 125.1 (Naphthyl C), 124.7 (Naphthyl C), 124.5 (C19, C23), 60.9 (C11), 52.5 (C12, C13), 49.5 (C14, C15). **HR-MS:** calcd for $\text{C}_{22}\text{H}_{23}\text{ClN}_3\text{S}$ m/z : $[\text{M}+\text{H}]^+$; 396.1213 found: 396.1227 [Diff (ppm) = 3.5]. **IR (KBr):** 2939 (N-H), 1531 (C=S), 862 (C-Cl) cm^{-1} . **MP:** 190-192 $^\circ\text{C}$

5.6.10 Synthesis of tert-butyl (2-aminoethyl)carbamate ¹⁷³

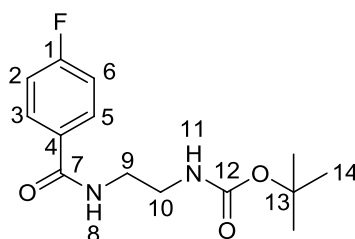


Ethylenediamine (28 mL, 400 mmol) was mixed in 300 mL of CH_3Cl . This was stirred on ice. Di-tert butyl dicarbonate (8.74 g, 40 mmol) was dissolved in 10 mL of CH_3Cl . This was added

via syringe pump at 20 $\mu\text{L}/\text{min}$. This took approximately 3.5 hours. Once all of the di-tert butyl dicarbonate was added the flask was stoppered and stirred overnight at room temperature. The reaction turned cloudy white as it progressed. Following the overnight stir the reaction mixture was washed with 6 x 100 mL of brine and 100 mL of deionised water. Following drying with MgSO_4 , the solvent was removed to yield the product as a clear oil. Yield: 85%

$^1\text{H NMR}$ (500 MHz, CDCl_3) δ 5.60 (s, 1H, H4), 2.85 (d, $J = 5.4$ Hz, 2H, H3), 2.47 (t, $J = 5.9$ Hz, 2H, H2), 1.14 (s, 9H, H7), 1.08 (s, 2H, H1). $^{13}\text{C NMR}$ (126 MHz, CDCl_3) δ 156.3 (C5), 79.3 (C6), 43.4 (C2), 41.9 (C3), 28.5 (C7). **IR (Neat):** 2928 (N-H), 1687 (C=O) cm^{-1} . Matches literature data.¹⁷³

5.6.11 Synthesis of tert-butyl (2-(4-fluorobenzamido)ethyl)carbamate

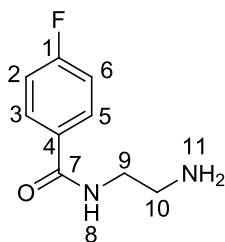


AC009 (5 ml (1 eq, 0.032 mols)) was dissolved in 40 ml of dry DCM. 4.56 mL (1 eq, 0.032 mols) of NEt_3 was added and the flask was cooled on ice. 4.66 ml (1.5 eq, 0.048 mols) of 4-fluorobenzyl chloride was added slowly to the stirring mixture. This was then removed from the ice and stirred overnight at room temperature. The reaction mixture became yellow and an insoluble material precipitated out. In the morning the reaction mixture was diluted with DCM to solubilize the precipitate. The organic layer was washed with 3x40 mL of deionised water and dried with MgSO_4 . The solvent was then removed under reduced pressure to yield a yellow/white solid. This was purified via column chromatography (1:1 EtOAc:Pet ether). Yield 74%

$^1\text{H NMR}$ (500 MHz, CDCl_3) δ 7.84 (dd, $J = 8.6, 5.4$ Hz, 2H, H3, H5), 7.30 (s, 1H, H8), 7.11 – 7.06 (m, 2H, H2, H6), 5.06 (s, 1H, H11), 3.58 – 3.50 (m, 2H, H9), 3.41 (dd, $J = 10.9, 5.8$ Hz, H10), 1.42 (s, 9H, H14). $^{13}\text{C NMR}$ (126 MHz, CDCl_3) δ 166.7 (C7), 164.7 (d, $J = 251.6$ Hz, C1), 157.8 (C12), 130.3 (d, $J = 3.1$ Hz, C4), 129.4 (d, $J = 8.9$ Hz, C3, C5), 115.5 (d, $J = 21.8$ Hz, C2, C6), 80.1 (C13), 42.4 (C9), 39.9 (C10), 28.3 (C14). **Rf:** 0.23 (1:1 EtOAc : petroleum ether) **HR-**

MS: calcd for $C_{14}H_{19}FN_2O_3Na$ m/z : $[M+Na]^+$; 305.1272 found: 305.1283 [Diff (ppm) = 3.71].
IR (KBr): 2985 (N-H Boc), 2942 (N-H, aryl), 1635 (C=O, BOC) 1606 (C=O, aryl) cm^{-1} . **MP:** 121-123 $^{\circ}C$

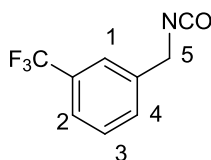
5.6.12 Synthesis of N-(2-aminoethyl)-4-fluorobenzamide



AC010 was dissolved in 1:1 mixture of DCM:TFA and stirred at room temperature for 4 hours, monitoring by TLC. When all AC009 had been consumed the solvent was removed under reduced pressure to afford a yellow oil. This was redissolved in EtOAc and petroleum ether was added slowly to crash out the product as a white solid. Yield 54%.

1H NMR (500 MHz, MeOD) δ 7.89 (dd, J = 8.6, 5.4 Hz, 2H, H3, H5), 7.06 (t, J = 8.7 Hz, 2H, H2, H6), 3.66 (t, J = 5.3 Hz, 2H, H9), 3.16 (m, 2H, H10). ^{13}C NMR (126 MHz, MeOD) δ 169.8 (C7), 166.1 (d, J = 250.9, C1), 131.1 (C4), 131.0 (d, J = 9.0 Hz, C3, C5), 116.2 (d, J = 22.1 Hz, C2, C6), 40.8 (C9), 39.0 (C10). **HR-MS:** calcd for $C_9H_{12}N_2OF$ m/z : $[M+H]^+$; 183.0928 found: 183.0930 [Diff (ppm) = 1.1]. **IR (KBr):** 3010 (N-H Boc), 2938 (N-H, aryl), 1606 (C=O) cm^{-1} .

5.6.13 Synthesis of 1-(isocyanatomethyl)-3-(trifluoromethyl)benzene, Compound 99



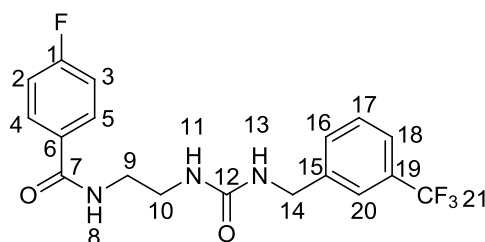
Into dry toluene under a flow of N_2 was placed 0.715 g ($3.5 \cdot 10^{-3}$ mols, 1 eq) of 2-(3-(trifluoromethyl)phenyl)acetic acid. To this was added 0.74 ml ($5.25 \cdot 10^{-3}$ mols, 1.5 eq) of triethylamine. 1.12 ml ($5.25 \cdot 10^{-3}$ mols, 1.5 eq) of diphenylphosphoryl azide was added

dropwise over the course of three hours at room temperature with constant stirring. Once addition was completed the reaction was left to stir for a further 3 hours at room temperature. It was then heated to 85 °C overnight.

The resulting orange liquid was carried straight through to the next step without further purification. Confirmation of product formation was accomplished by withdrawal of an aliquot of the reaction mixture for NMR analysis.

$^1\text{H NMR}$ (500 MHz, CDCl_3) δ 7.50 – 7.45 (m, 2H), 7.41-7.39 (m, 2H), 4.48 (s, 2H, H5).

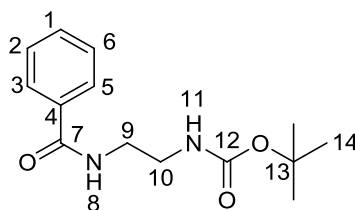
5.6.14 Synthesis of 4-fluoro-N-(2-(3-(3-(trifluoromethyl)benzyl)ureido)ethyl)benzamide, Compound 94



To a stirring solution of AC012 was added 0.49 mls (3.5×10^{-3} mols, 1 eq) of NEt_3 and 0.638 g (3.5×10^{-3} mols, 1 eq) of AC010 dissolved in dry toluene. The reaction was stirred under N_2 overnight at 85 °C. The solvent was removed *in vacuo* and the product isolated as a white solid via column chromatography (1:1 EtOAc: petroleum ether). Yield 37%.

$^1\text{H NMR}$ (500 MHz, DMSO) δ 9.49 (s, 1H, NH), 8.62 (s, 1H, NH), 7.90 (dd, 2H, $J = 8.6, 5.6$ Hz, H4, H5), 7.62 – 7.52 (m, 5H, Aryl H), 7.31 (t, $J = 8.8$ Hz, 1H, H17), 6.73 (s, 1H, NH) 4.33 (m, 2H, H14), 3.45 – 3.35 (m, 4H, H9, H10). $^{13}\text{C NMR}$: (126 MHz, DMSO) δ 166.0 (C7), 164.3 (d, $J = 248.2$ Hz, C1), 158.6 (q, $J = 36.0$ Hz, C19), 157.0 (C12), 143.1 (C15), 130.6 (q, $J = 240.7$ Hz, C21), 131.4 (d, $J = 2.9$ Hz, C6), 130.3 (d, $J = 8.0$ Hz, C4, C5), 123.7 (d, $J = 3.6$ Hz, C6), 119.8 (C16), 117.5 (C17), 115.6 (d, $J = 21.7$ Hz, C2, C3), 115.3 (m, C18, C20), 43.0 (C14), 40.7 (C9), 38.7 (C10). **Rf**: 0.45 (1:1 EtOAc: petroleum ether). **HR-MS**: calcd for $\text{C}_{18}\text{H}_{17}\text{N}_3\text{O}_2\text{F}_4\text{Na}$ m/z : $[\text{M}+\text{Na}]^+$; 407.118 found: 407.1187 [Diff (ppm) = 1.77]. **IR (KBr)**: 2947 (N-H), 1644 (C=O), 1327 (C-F) cm^{-1} . **M.P**: 142-144 °C.

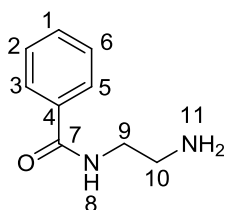
5.6.15 Synthesis of tert-butyl (2-benzamidoethyl)carbamate



Prepared as per AC010 with benzoyl chloride used in place of 4-fluorobenzyl chloride. Yield 42%

¹H NMR (500 MHz, DMSO) δ 8.48 (t, J = 4.8 Hz, 1H, H8), 7.88 (d, J = 7.4 Hz, 2H, H3, H5), 7.56 (t, J = 7.3 Hz, 1H, H1), 7.49 (t, J = 7.5 Hz, 2H, H2, H6), 6.93 (t, J = 5.4 Hz, 1H, H11), 3.35 (dd, J = 12.3, 6.3 Hz, 2H, H9), 3.16 (dd, J = 12.3, 6.2 Hz, 2H, H10), 2.03 (s, 9H, H14). **¹³C NMR** (126 MHz, DMSO) δ 166.9 (C7), 156.2 (C12), 135.0 (C2), 131.5 (C1), 128.6 (C2, C6), 127.6 (C3, C5), 78.1 (C13), 28.7 (C9), 21.1 (10), 14.5 (C14). **HR-MS**: calcd for C₁₄H₂₀N₂O₃Na m/z: [M+Na]⁺; 287.1366 found: 287.1377 [Diff (ppm) = 3.88]. **IR (KBr)** 2924 (N-H), 1663 (C=O), cm⁻¹.

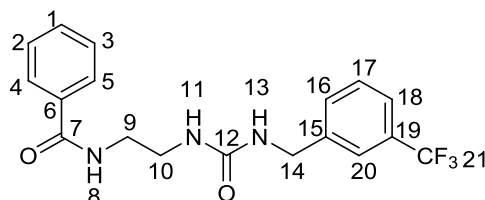
5.6.16 Synthesis of N-(2-aminoethyl)benzamide



Prepared as per AC011, dissolving AC014 in a 1:1 mixture of DCM:TFA and stirring at room temperature. Yield 42%.

¹H NMR (500 MHz, D₂O) δ 7.74 (d, J = 7.3 Hz, 2H, H3, H5), 7.57 (t, J = 7.4 Hz, 1H, H1), 7.47 (t, J = 7.7 Hz, 2H, H2, H6), 3.65 (t, J = 5.8 Hz, 2H, H9), 3.20 (t, J = 5.5 Hz, 2H, H10). **¹³C NMR** (126 MHz, D₂O) δ 171.7 (C7), 132.5 (C1), 128.8 (C2, C6), 127.1 (C3, C5), 39.3 (C10), 37.3 (C9). Matches literature data.¹⁷⁴

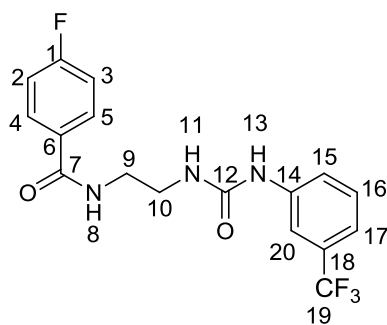
5.6.17 Synthesis of N-(2-(3-(3-(trifluoromethyl)benzyl)ureido)ethyl)benzamide, Compound 95



Prepared as per 94 by combining AC015 and AC012. Isolated as a white solid. Yield 41%.

¹H NMR (500 MHz, DMSO): δ 9.49 (s, 1H, NH), 8.59 (t, J = 4.9 Hz, 1H, NH), 7.83 (d, J = 7.2 Hz, 2H, H4, H5), 7.63 – 7.50 (m, 6H, Aryl H), 7.47 (t, J = 7.5 Hz, 1H, H1), 6.72 (t, J = 6.1 Hz, 1H, H13), 4.33 (m, 2H, H14), 3.45 – 3.35 (m, 4H, H9/H10). **¹³C NMR**: (126 MHz, DMSO) δ 167.1 (C7), 158.4 (q, J = 36.0 Hz, C19), 157.1 (C12), 143.1 (C15), 134.9 (C6) 131.5 (C4, C5), 130.6 (q, J = 270.0 Hz, C21), 128.7 (C1), 127.7 (C2,C3) 123.7 (C16), 123.7 (m, C17), 115.8 (q, J = 3.9 Hz, C20) 115.7 (q, J = 3.7 Hz, C18), 42.7 (C14), 40.7 (C9), 38.6 (C10). **Rf**: 0.42 (1:1 EtOAc:petroleum ether). **HR-MS**: calcd for C₁₈H₁₈N₃O₂F₃Na m/z : [M+Na]⁺; 388.1243 found: 388.1254 [Diff (ppm) = 3.71] **IR (KBr)**: 2938 (N-H), 1634 (C=O), 1320 (C-F) cm⁻¹ **MP**: 136-138 °C

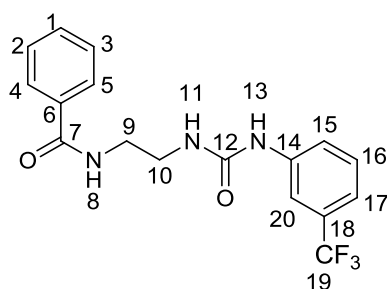
5.6.18 Synthesis of 4-fluoro-N-(2-(3-(3-(trifluoromethyl)phenyl)ureido)ethyl)benzamide, Compound 96



Prepared as per 94 by combining AC011 and 1-isocyanato-3-(trifluoromethyl)benzene. Yield 39%.

¹H NMR: (500 MHz, DMSO) δ 8.95 (s, 1H, H13), 8.58 (t, J = 5.1 Hz, 1H, H18), 7.97 (s, 1H, H20), 7.94 (d, J = 8.6, 2H, H4, H5), 7.51 (d, J = 8.2 Hz, 1H, H15), 7.45 (t, J = 8.3 Hz, 1H, H16), 7.29 (d, J = 8.5 Hz, 2H, H2, H3), 7.22 (d, J = 7.6 Hz, 1H, H17), 6.40 (t, J = 5.5 Hz, 1H, H11), 3.38 (dd, J = 11.5, 5.7 Hz, 2H, H9), 3.32 – 3.28 (m, 2H, H10). **¹³C NMR** (126 MHz, DMSO) δ 165.9 (C7), 164.3 (d, J = 248.3 Hz, C1), 155.7 (C12), 141.8 (C14), 131.4 (d, J = 2.9 Hz, C6) 130.3 (d, J = 8.0 Hz, C4, C5), 129.9 (q, J = 31.3 Hz, C18), 128.7 (C16), 124.8 (q, J = 272.3 Hz, C19), 121.6 (C15), 117.7 (q, J = 3.7 Hz, C17), 115.6 (d, J = 21.7 Hz, C2, C3), 114.1 (q, J = 3.4 Hz, C20), 40.4 (C9), 39.5 (C10). **Rf:** 0.38 (1:1 EtOAc:petroleum ether) **HR-MS:** calcd for C₁₇H₁₅N₃O₂F₄Na m/z: [M+Na]⁺; 392.0993 found: 392.1003 [Diff (ppm) = 2.64] **IR (KBr):** 2946 (N-H), 1647 (C=O), 1325 (C-F) cm⁻¹ **M.P** 186-188 °C

5.6.19 Synthesis of N-(2-(3-(3-(trifluoromethyl)phenyl)ureido)ethyl)benzamide, Compound 97

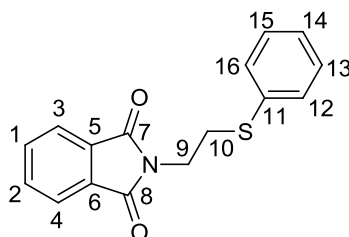


Prepared as per 94 by combining AC015 and 1-isocyanato-3-(trifluoromethyl)benzene. Isolated as a white solid. Yield 36%.

¹H NMR (500 MHz, DMSO): δ 8.96 (s, 1H, H13), 8.54 (t, J = 4.8 Hz, 1H, H8), 7.96 (s, 1H, H20), 7.86-7.83 (d, J = 7.3 Hz, 2H, H4, H5), 7.51 (m, 2H, H1, H15), 7.48-7.41 (m, 3H, H2, H3, H16), 7.21 (d, J = 7.5 Hz, 1H, H17), 6.40 (t, J = 5.5 Hz, 1H, H11), 3.37 (m, 2H, H9), 3.33-3.27 (m, 2H, H10). **¹³C NMR** (126 MHz, DMSO) δ 166.7 (C7), 155.4 (C12), 141.4 (C14), 134.4 (C6), 131.2 (C1), 129.8 (C16), 129.5 (q, J = 31.2 Hz, C18), 128.3 (C2/C3), 127.2 (C4/C5), 124.3 (q, J = 272.2 Hz, C19), 121.2 (C15), 117.3 (q, J = 4.1 Hz, C17), 113.7 (q, J = 3.9 Hz, C20) 39.5 (C9),

38.7 (C10). **HR-MS:** calcd for $C_{34}H_{32}N_6O_4F_6Na$ m/z : $[2M+Na]^+$; 725.2281 found: 725.2312 [Diff (ppm) = 4.19] **IR (KBr):** 2951 (N-H), 1639 (C=O), 1335 (C-F) cm^{-1} **M.P** 174-176 °C

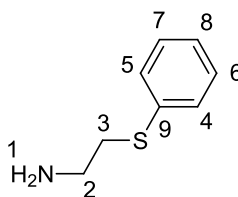
5.6.20 Synthesis of 2-(2-(phenylthio)ethyl)isoindoline-1,3-dione



Into a flask of dry DMF under a continuous flow of N_2 was placed 0.19 g (1.76×10^{-3} mols, 1 eq) of thiophenol and 0.32 mls (1.76×10^{-3} mols, 1 eq) of a 30% solution of NaOMe. This was stirred for 40 minutes at room temperature. 0.55 g (2.64×10^{-3} mols, 1.5 eq) of 2-(2-chloroethyl)isoindoline-1,3-dione was dissolved in 2 mL dry DMF in a separate flask under inert atmosphere. This was added via cannula to the stirring thiophenol mixture over the course of 15 minutes. The combined solution was stirred at room temperature overnight. The DMF was removed under reduced pressure and the residue taken up in ethyl acetate. This was washed with 3 equivalents each of 1 M HCl, brine and water. The ethyl acetate was removed and the resulting yellow oil purified via column chromatography, eluting with 17:3 petroleum ether: ethyl acetate. The product was isolated as a yellow oil. Yield 86%.

1H NMR (500 MHz, $CDCl_3$) δ 7.60 – 7.56 (m, 2H, H1, H2), 7.52 – 7.48 (m, 2H, H3, H4), 7.20 (d, $J = 7.5$ Hz, 2H, H12, H16), 7.05 (t, $J = 7.7$ Hz, 2H, H13, H15), 6.92 (t, $J = 7.4$ Hz, 1H, H14), 3.72 (t, $J = 7.1$ Hz, 2H, H9), 3.05 (t, $J = 7.1$ Hz, 2H, H10). **^{13}C NMR** (126 MHz, $CDCl_3$) δ 167.7 (C7, C8), 134.9 (C5, C6), 133.9 (C3, C5), 131.8 (C11), 129.3 (C12, C16), 128.9 (C13, C15), 126.1 (C14), 123.0 (C1, C2), 37.4 (C9), 31.3 (C10). **Rf:** 0.40 (17:3 petroleum ether: EtOAc). **HR-MS:** calcd for $C_{16}H_{14}NO_2S$ m/z : $[M+H]^+$; 284.074 found: 284.0739 [Diff (ppm) = -0.14]. **IR (Neat):** 1650 (C=O), 697 (C-S).

5.6.21 Synthesis of (phenylthio)methanamine



AC019 (0.72 g, 2.54×10^{-3} mols, 1 eq) was dissolved in methanol. To this was added 0.29 ml (5.08×10^{-3} mols, 2 eq) of glacial acetic acid and 0.05 ml (0.01 mols, 4 eq) of hydrazine monohydrate. This was stirred for 4 hours at 65 °C. The resulting white solution was filtered to remove insoluble material. The filtrate was collected and the solvent removed under reduced pressure. The white solid was re dissolved in 500 ml ethyl acetate. An extraction was carried out with 150 mL of 2 M HCl. The aqueous layer was adjusted to pH 14 with NaOH and washed with ethyl acetate. The organic layer was dried with Na₂SO₄ and the solvent removed to yield the product as yellow oil which turned to a white solid on standing. Yield 77%.

¹H NMR (500 MHz, CDCl₃) δ 7.27 (d, *J* = 7.2 Hz, 2H, H4, H5), 7.18 (t, *J* = 7.7 Hz, 2H, H6, H7), 7.09 (t, *J* = 7.4 Hz, 1H, H8), 2.90 (t, *J* = 6.4 Hz, 2H, H3), 2.80 (t, *J* = 6.3 Hz, 2H, H2), 1.49 (s, 2H, H1). ¹³C NMR (126 MHz, CDCl₃) δ 135.8 (C9), 129.7 (C4, C5), 129.0 (C6, C7), 126.2 (C8), 40.9 (C2), 38.0 (C3). **MP:** 66-68 °C. Matches literature data.¹⁷⁵

6 Conclusion

6.1 Conclusion

Human nNOS is an enzyme of key biological importance. It produces NO which is involved in a plethora of neuronal signalling events. Over production of the free radical NO has been implicated in a number of serious neurological diseases. Partial inhibition of over active nNOS offers a potential therapeutic avenue for treatment of these debilitating conditions.

The aim of this project was to make use of a range *in silico* techniques to identify novel human nNOS inhibitors. There is an over reliance on two key scaffolds for nNOS inhibition, namely modified arginines and 2-aminopyridines. The field is also overly focused on the use of rat nNOS for inhibition studies. This project aimed to move away from these scaffolds and from the rat isoform of the enzyme, and also aimed to be the first to use high throughput *in silico* screening methodologies for human nNOS inhibition. The project also attempted to co-express human calmodulin with human nNOS in *E. coli* cells, an approach not yet reported in the literature.

A human nNOS homology model was successfully constructed and validated, and was then used to flexibly dock large commercial databases for potential inhibitory compounds. The binding poses of the top hit from this screen was examined in detail. The interactions which it formed with the human nNOS homology model binding site were largely in agreement with literature precedent. Some of the top hits from this screen were purchased, while others were synthesised.

The synthesised compounds from the homology model screen were all novel, and contained a piperazine core. These were synthesised using epoxide ring opening, and nucleophilic attack on isocyanates and isothiocyanates. All targets from this class of compounds were successfully synthesised and were progressed for biological evaluation.

The structure based design approach was complimented with a ligand based design approach. A pharmacophore was developed using the ChEMBL database. This pharmacophore was validated and used to screen commercial databases. Following assay testing of the initial pharmacophore hits, a second pharmacophore was generated. This included the experimentally validated inactive human nNOS inhibitors, identified from the initial pharmacophore and homology model, in the generation set. These represent one of the only reported sets of experimentally validated inactive human nNOS inhibitors. The

second pharmacophore was successfully validated and again used for commercial database screening. A range of compounds were purchased for biological evaluation from this screen.

The publication of the human nNOS crystal structure late in this project's life cycle allowed for comparisons to be drawn between the human nNOS homology model and the crystal structure. The homology model was found to be an accurate representation of the human nNOS binding site. The crystal structure was then used to screen commercial databases as before. A number of compounds from this screen were purchased, while others were synthesised.

The synthetic targets from the nNOS crystal structure screen all contained a common urea motif. Synthesis of this motif was achieved via amine attack on isocyanates. The required isocyanate intermediates were synthesised via azide formation and Curtius' rearrangement. Again, all synthetic targets were isolated and characterised and were taken forward for biological evaluation.

Further compounds were designed by examination of the two most commonly reported structural motifs used in rat nNOS inhibition. A compound was designed that combined these two popular scaffolds, namely arginines and aminopyridines. This was done in an attempt to exploit the inhibitor properties of both scaffolds, while retaining the selectivity of the 2-aminopyridine for the nNOS isoform.

An assay system was established requiring the recombinant production of the three human NOS isoforms. The common literature approach to NOS inhibitor testing involves using rat NOS, bovine eNOS and murine iNOS. The establishment of an all human assay system would therefore be of great benefit to the field. The publication of the human nNOS crystal structure indicates that the field is moving in that direction, so the approach of this project was at the forefront of human nNOS inhibitor discovery.

The DNA sequences of the three human NOS proteins were verified and *E. coli* cells were transformed with the DNA containing plasmids. Following extensive optimisation experiments for the expression of human nNOS, a new strategy was employed that aimed to co-express the human NOS enzymes with human calmodulin, a key co-factor for NOS function. Human nNOS was successfully co-expressed with human calmodulin, and the two were purified via affinity chromatography. Human eNOS and human iNOS were also

expressed with calmodulin, although their purification via affinity chromatography proved more challenging.

An assay system was then established using the recombinant proteins. The recombinantly expressed human nNOS, the principle target of this work, was found to be active in the Griess assay. This assay system quantifies NOS activity by measuring the levels of nitrites which the enzyme produces. Treatment of active protein with Griess reagents resulted in the development of an intense purple colour, proving that the nNOS enzyme was active. The untreated protein produced higher levels of nitrites than the sample treated with the known NOS inhibitor, L-NNA. DMSO was also successfully identified as a suitable vehicle for compound delivery to the assay system. A dose response curve was constructed using the recombinantly produced human nNOS and L-NNA. The protein was seen to be inhibited more fully in the presence of higher L-NNA concentrations, and an IC₅₀ value of 8.0 µM was determined.

The assay system was then trialled using lysates containing human eNOS and human iNOS. While the proteins were seen to be functional, as evidenced by the appearance of a purple colour in the wells, the presence of large amounts of precipitated non-specific *E. coli* proteins interfered with the absorbance readings. This meant that the assay system could not accurately distinguish between treated and untreated eNOS and iNOS samples.

In all, 72 compounds, some synthesised and others purchased, were evaluated for their inhibitory activity against human nNOS in the Griess assay. No *in vitro* hits were identified which emphasizes the challenging nature of this project, as does the fact that the literature is dominated by just two inhibitor classes. Several positive outcomes were achieved that will make a significant contribution to the field of nNOS inhibition. We now have, for the first time, a set of experimentally validated compounds that can be used as human nNOS inactives in future computational studies. This will allow for the development of more accurate models for nNOS inhibition. In addition, the first co-expression system for human nNOS with human calmodulin in *E. coli* cells has been developed. The use of *E. coli* as a host for this process is significant as it allows for rapid, inexpensive production of active human nNOS. The combination of this co-expression system with the Griess assay technology has resulted in the first high throughput co-expression/assay system for human nNOS inhibitor discovery.

6.2 Future work

The computational models developed throughout this project are among the first of their kind for human nNOS. Further refinement of these models with the experimentally validated inactives would therefore be a potentially fruitful endeavour. The experimentally validated inactive human nNOS compounds are particularly useful for future pharmacophore studies.

Development of a high throughput expression and assay system for of human iNOS and human eNOS would also be of benefit to the field. Both proteins have been expressed in this work and are functional, but the purification protocols require further optimisation. Potentially, size exclusion chromatography could be used to purify this isoforms. This could then result in an all human NOS assay system. Alternatively, the His-tags of eNOS and iNOS could be moved to their N termini to try and improve the performance of affinity chromatography purification with these isoforms. The size exclusion could also be applied to human nNOS so as to obtain 100% pure protein. This could then be used for crystallisation trails.

Compounds **37** and **102** were seen to increase the level of NO production in human nNOS. Although this was not the aim of this project, these compounds may provide a mechanism for the study of nNOS over activation. The exact binding mode of these compounds with human nNOS could be elucidated by crystallization of human nNOS with compounds **37** and **102** *in situ*.

7 Bibliography

- (1) Andrew, P. J.; Mayer, B. *Cardiovasc. Res.* **1999**, *43*, 521–531.
- (2) Alderton, W. K.; Cooper, C. E.; Knowles, R. G. *Biochem. J.* **2001**, *357*, 593–615.
- (3) Shaul, P. W. *Annu. Rev. Physiol.* **2002**, *64*, 749–774.
- (4) Poulos, T. L.; Li, H. *Acc. Chem. Res.* **2013**, *46*, 390–398.
- (5) Zamora, R.; Vodovotz, Y.; Billiar, T. R. *Mol. Med.* **2000**, *6*, 347–373.
- (6) Sessa, W. C.; Forstermann, U. *Eur. Heart J.* **2012**, *33*, 829–837.
- (7) Hemmens, B.; Goessler, W.; Schmidt, K.; Mayer, B. *J. Biol. Chem.* **2000**, *275*, 35786–35791.
- (8) Li, H.; Raman, C. S.; Glaser, C. B.; Blasko, E.; Young, T. a.; Parkinson, J. F.; Whitlow, M.; Poulos, T. L. *J. Biol. Chem.* **1999**, *274*, 21276–21284.
- (9) Raman, C. S.; Li, H.; Martásek, P.; Král, V.; Masters, B. S.; Poulos, T. L. *Cell* **1998**, *95*, 939–950.
- (10) Abu-soud, H. M.; Yoho, L.; Stuehr, D. J. *J. Biol. Chem.* **1994**, *51*, 8–11.
- (11) Smith, B. C.; Underbakke, E. S.; Kulp, D. W.; Schief, W. R.; Marletta, M. A. *Proc. Natl. Acad. Sci. U. S. A.* **2013**, *110*, 3577–3586.
- (12) Li, H.; Poulos, T. L. *J. Inorg. Biochem.* **2005**, *99*, 293–305.
- (13) Giroud, C.; Moreau, M.; Mattioli, T. a; Balland, V.; Boucher, J.-L.; Xu-Li, Y.; Stuehr, D. J.; Santolini, J. *J. Biol. Chem.* **2010**, *285*, 7233–7245.
- (14) Gorren, A. C. F.; Mayer, B. *Biochim. Biophys. Acta* **2007**, *1770*, 432–445.
- (15) Curtin, A. M.; Kinsella, G. K.; Stephens, J. C. *Curr. Med. Chem.* **2015**, *22*, 2558–2579.
- (16) Francis, S. H.; Busch, J. L.; Corbin, J. D.; Sibley, D. *Pharmacol. Rev.* **2010**, *62*, 525–563.

- (17) Miki, N.; Kawabe, Y.; Kuriyama, K. *Biochem. Biophys. Res. Commun.* **1977**, *75*, 851–856.
- (18) Moncada, S.; Palmer, R. M. J.; Higgs, E. A. *Pharmacol. Rev.* **1991**, *43*, 109–142.
- (19) Kerwin, J. F.; Lancaster, J. R.; Feldman, P. L. *J. Med. Chem.* **1995**, *38*, 4343–4362.
- (20) Denninger, J. W.; Marletta, M. a *Biochim. Biophys. Acta* **1999**, *1411*, 334–350.
- (21) Olesen, J. *Neurotherapeutics* **2010**, *7*, 183–190.
- (22) Aquilano, K.; Baldelli, S.; Rotilio, G.; Ciriolo, M. R. *Neurochem. Res.* **2008**, *33*, 2416–2426.
- (23) Vallance, P.; Leiper, J. *Nat. Rev. Drug Discov.* **2002**, *1*, 939–950.
- (24) Villanueva, C.; Giulivi, C. *Free Radic. Biol. Med.* **2010**, *49*, 307–316.
- (25) Yao, J. K.; Leonard, S.; Reddy, R. D. *Schizophr. Bull.* **2004**, *30*, 923–934.
- (26) Gorren, A. C. F.; Mayer, B. *Curr. Drug Metab.* **2002**, *3*, 133–157.
- (27) Mukherjee, P.; Cinelli, M. a; Kang, S.; Silverman, R. B. *Chem. Soc. Rev.* **2014**, *43*, 6814–6838.
- (28) Chreifi, G.; Li, H.; McInnes, C. R.; Gibson, C. L.; Suckling, C. J.; Poulos, T. L. *Biochemistry* **2014**, *53*, 4216–4223.
- (29) Matter, H.; Kumar, H. S. A.; Fedorov, R.; Frey, A.; Kotsonis, P.; Hartmann, E.; Fröhlich, L. G.; Reif, A.; Pfeleiderer, W.; Scheurer, P.; Ghosh, D. K.; Schlichting, I.; Schmidt, H. H. H. W. *J. Med. Chem.* **2005**, *48*, 4783–4792.
- (30) The PyMOL Molecular Graphics System, Version 1.5.0.4 Schrödinger, LLC.
- (31) Matter, H.; Kotsonis, P.; Klingler, O.; Strobel, H.; Fröhlich, L. G.; Frey, A.; Pfeleiderer, W.; Schmidt, H. H. H. W. *J. Med. Chem.* **2002**, *45*, 2923–2941.
- (32) Ohashi, K.; Yamazaki, T.; Kitamura, S.; Ohta, S.; Izumi, S.; Kominami, S. *Biochim. Biophys. Acta - Gen. Subj.* **2007**, *1770*, 231–240.

- (33) Li, W.; Fan, W.; Elmore, B.; Feng, C. *FEBS Lett.* **2011**, *585*, 2622–2626.
- (34) Iyanagi, T.; Xia, C.; Kim, J.-J. *P. Arch. Biochem. Biophys.* **2012**, *528*, 72–89.
- (35) Ikura, M.; Barbato, G.; Klee, C. B.; Bax, A. *Cell Calcium* **1992**, *13*, 391–400.
- (36) Chattopadhyaya, R.; Meador, W. E.; Means, A. R.; Quioco, F. A. *J. Mol. Biol.* **1992**, *228*, 1177–1192.
- (37) Aoyagi, M.; Arvai, A. S.; Tainer, J. A.; Getzoff, E. D. *EMBO J.* **2003**, *22*, 766–775.
- (38) Zinzalla, G.; Thurston, D. E. *Future Med. Chem.* **2009**, *1*, 65–93.
- (39) Li, Y.; Wang, H.; Tarus, B.; Perez, M. R.; Morellato, L.; Henry, E.; Berka, V.; Tsai, A.-L.; Ramassamy, B.; Dhimane, H.; Dessy, C.; Tauc, P.; Boucher, J.-L.; Deprez, E.; Slama-Schwok, A. *Proc. Natl. Acad. Sci. U. S. A.* **2012**, *109*, 12526–12531.
- (40) Beaumont, E.; Lambry, J. C.; Gautier, C.; Robin, A. C.; Gmouh, S.; Berka, V.; Tsai, A. L.; Blanchard-Desce, M.; Slama-Schwok, A. *J. Am. Chem. Soc.* **2007**, *129*, 2178–2186.
- (41) Vítěček, J.; Lojek, A.; Valacchi, G.; Kubala, L. *Mediators Inflamm.* **2012**, *2012*, 1–22.
- (42) Tafi, A.; Angeli, L.; Venturini, G.; Travagli, M.; Corelli, F.; Botta, M. *Curr. Med. Chem.* **2006**, *13*, 1929–1946.
- (43) Moore, W.; Webber, R. K.; Fok, K. *Bioorg. Med. Chem.* **1996**, *4*, 1559–1564.
- (44) Flinspach, M. L.; Li, H.; Jamal, J.; Yang, W.; Huang, H.; Hah, J.-M.; Gómez-Vidal, J. A.; Litzinger, E. a; Silverman, R. B.; Poulos, T. L. *Nat. Struct. Mol. Biol.* **2004**, *11*, 54–59.
- (45) Fang, J.; Ji, H.; Lawton, G. R.; Xue, F.; Roman, L. J.; Silverman, R. B. *J. Med. Chem.* **2009**, *52*, 4533–7.
- (46) Ji, H.; Li, H.; Flinspach, M.; Poulos, T. L.; Silverman, R. B. *J. Med. Chem.* **2003**, *46*, 5700–5711.
- (47) Hagmann, W. K.; Caldwell, C. G.; Chen, P.; Durette, P. L.; Esser, C. K.; Lanza, T. J.; Kopka, I. E.; Guthikonda, R.; Shah, S. K.; MacCoss, M.; Chabin, R. M.; Fletcher, D.; Grant, S. K.; Green, B. G.; Humes, J. L.; Kelly, T. M.; Luell, S.; Meurer, R.; Moore, V.; Pacholok, S. G.; Pavia, T.; Williams, H. R.; Wong, K. K. *Bioorg. Med. Chem. Lett.* **2000**,

- 10, 1975–1978.
- (48) Ji, H.; Stanton, B. Z.; Igarashi, J.; Li, H.; Martásek, P.; Roman, L. J.; Poulos, T. L.; Silverman, R. B. *J. Am. Chem. Soc.* **2008**, *130*, 3900–3914.
- (49) Ji, H.; Li, H.; Martásek, P.; Roman, L. J.; Poulos, T. L.; Silverman, R. B. *J. Med. Chem.* **2009**, *52*, 779–797.
- (50) Ji, H.; Delker, S. L.; Li, H.; Martásek, P.; Roman, L. J.; Poulos, T. L.; Silverman, R. B. *J. Med. Chem.* **2010**, *53*, 7804–7824.
- (51) Huang, H.; Ji, H.; Li, H.; Jing, Q.; Labby, K. J.; Martásek, P.; Roman, L. J.; Poulos, T. L.; Silverman, R. B. *J. Am. Chem. Soc.* **2012**, *134*, 11559–11572.
- (52) Xue, F.; Li, H.; Delker, S. L.; Fang, J.; Martásek, P.; Roman, L. J.; Poulos, T. L.; Silverman, R. B. *J. Am. Chem. Soc.* **2010**, *132*, 14229–14238.
- (53) Xue, F.; Li, H.; Fang, J.; Roman, L. J.; Martásek, P.; Poulos, T. L.; Silverman, R. B. *Bioorg. Med. Chem. Lett.* **2010**, *20*, 6258–61.
- (54) Xue, F.; Fang, J.; Delker, S. L.; Li, H.; Martásek, P.; Roman, L. J.; Poulos, T. L.; Silverman, R. B. *J. Med. Chem.* **2011**, *54*, 2039–2048.
- (55) Delker, S. L.; Xue, F.; Li, H.; Jamal, J.; Silverman, R. B.; Poulos, T. L. *Biochemistry* **2010**, *49*, 10803–10810.
- (56) Reif, W. D.; McCarthy, D. J.; Cregan, E.; Macdonald, E. J. *Free Radic. Biol. Med.* **2000**, *28*, 1470–1477.
- (57) Handy, R. L.; Harb, H. L.; Wallace, P.; Gaffen, Z.; Whitehead, K. J.; Moore, P. K. *Br. J. Pharmacol.* **1996**, *119*, 423–431.
- (58) Ulhaq, S.; Chinje, E. C.; Naylor, M. a; Jaffar, M.; Stratford, I. J.; Threadgill, M. D. *Bioorg. Med. Chem.* **1998**, *6*, 2139–2149.
- (59) Rogerson, T.; Wilkinson, C.; Hetarski, K. *Biochem. Pharmacol.* **1977**, *26*, 1039–1042.
- (60) Mukherjee, P.; Li, H.; Sevrioukova, I.; Chreifi, G.; Martásek, P.; Roman, L. J.; Poulos, T. L.; Silverman, R. B. *J. Med. Chem.* **2015**, *58*, 1067–1088.

- (61) Martell, J. D.; Li, H.; Doukov, T.; Martásek, P.; Roman, L. J.; Soltis, M.; Poulos, T. L.; Silverman, R. B. *J. Am. Chem. Soc.* **2010**, *132*, 798–806.
- (62) Xu, G.; Chen, Y.; Shen, K.; Wang, X.; Li, F.; He, Y. *Int. J. Mol. Sci.* **2014**, *15*, 8553–8569.
- (63) Delker, S. L.; Ji, H.; Li, H.; Jamal, J.; Fang, J.; Xue, F.; Silverman, R. B.; Poulos, T. L. *J. Am. Chem. Soc.* **2010**, *132*, 5437–5442.
- (64) Annedi, S. C.; Maddaford, S. P.; Ramnauth, J.; Renton, P.; Rybak, T.; Silverman, S.; Rakhit, S.; Mladenova, G.; Dove, P.; Andrews, J. S.; Zhang, D.; Porreca, F. *Eur. J. Med. Chem.* **2012**, *55*, 94–107.
- (65) Xue, F.; Kraus, J. M.; Labby, K. J.; Ji, H.; Mataka, J.; Xia, G.; Li, H.; Delker, S. L.; Roman, L. J.; Martásek, P.; Poulos, T. L.; Silverman, R. B. *J. Med. Chem.* **2011**, *54*, 6399–403.
- (66) Sievers, F.; Wilm, A.; Dineen, D.; Gibson, T. J.; Karplus, K.; Li, W.; Lopez, R.; McWilliam, H.; Remmert, M.; Söding, J.; Thompson, J. D.; Higgins, D. G. *Mol. Syst. Biol.* **2011**, *7*, 1–6.
- (67) Li, H.; Xue, F.; Kraus, J. M.; Ji, H.; Labby, K. J.; Mataka, J.; Delker, S. L.; Martásek, P.; Roman, L. J.; Poulos, T. L.; Silverman, R. B. *Bioorg. Med. Chem.* **2013**, *21*, 1333–43.
- (68) Laskowski, R. a.; MacArthur, M. W.; Moss, D. S.; Thornton, J. M. *J. Appl. Crystallogr.* **1993**, *26*, 283–291.
- (69) Brooks, B. R.; III, C. L. B.; MacKerell, J. A. D.; Nilsson, L.; Petrella, R. J.; Roux, B.; Won, Y.; Archontis, G.; Bartels, C.; Boresch, S.; Caflisch, A.; Caves, L.; Cui, Q.; Dinner, A. R.; Feig, M.; Fischer, S.; Gao, J.; Hodoscek, M.; Im, W.; Kuczera, K.; Lazaridis, T.; Ma, J.; Ovchinnikov, V.; Paci, E.; Pastor, R. W.; Post, C. B.; Pu, J. Z.; Schaefer, M.; Tidor, B.; Venable, R. M.; Woodcock, H. L.; Wu, X.; Yang, W.; York, D. M.; Karplus, M. *J. Comput. Chem.* **2009**, *30*, 1545–1614.
- (70) Morris, a. L.; MacArthur, M. W.; Hutchinson, E. G.; Thornton, J. M. *Proteins Struct. Funct. Genet.* **1992**, *12*, 345–364.
- (71) Eisenberg, D.; Luthy, R.; Bowie, J. U. *Methods Enzymol.* **1997**, *277*, 396–404.
- (72) Colovos, C.; Yeates, T. O. *Protein Sci.* **1993**, *2*, 1511–1519.
- (73) Li, H.; Xue, F.; Kraus, J. M.; Ji, H.; Labby, K. J.; Mataka, J.; Delker, S. L.; Martásek, P.; Roman, L. J.; Poulos, T. L.; Silverman, R. B. *Bioorg. Med. Chem.* **2013**, *21*, 1333–1343.

- (74) McGann, M. J. *Chem. Inf. Model.* **2011**, *51*, 578–96.
- (75) Yusuf, D.; Davis, A. M.; Kleywegt, G. J.; Schmitt, S. J. *Chem. Inf. Model.* **2008**, *48*, 1411–1422.
- (76) Verkhivker, G. M.; Bouzida, D.; Gehlhaar, D. K.; Rejto, P. a; Arthurs, S.; Colson, a B.; Freer, S. T.; Larson, V.; Luty, B. a; Marrone, T.; Rose, P. W. *J. Comput. Aided. Mol. Des.* **2000**, *14*, 731–51.
- (77) Liang, G.; Neuenschwander, K.; Chen, X.; Wei, L.; Munson, R.; Francisco, G.; Scotese, A.; Shutske, G.; Black, M.; Sarhan, S.; Jiang, J.; Morize, I.; Vaz, R. J. *Med Chem Comm* **2011**, *2*, 201–205.
- (78) Labby, K. J.; Xue, F.; Kraus, J. M.; Ji, H.; Mataka, J.; Li, H.; Martásek, P.; Roman, L. J.; Poulos, T. L.; Silverman, R. B. *Bioorg. Med. Chem.* **2012**, *20*, 2435–2443.
- (79) Garcin, E. D.; Arvai, A. S.; Rosenfeld, R. J.; Kroeger, M. D.; Brian, R.; Andersson, G.; Andrews, G.; Hamley, P. J.; Mallinder, P. R.; Nicholls, D. J.; St-gallay, S. A.; Tinker, A. C.; Gensmantel, N. P.; Cheshire, D. R.; Connolly, S.; Stuehr, D. J.; Åberg, A.; Alan, V.; Tainer, J. A.; Getzoff, E. D. *Nat. Chem. Biol.* **2008**, *4*, 700–707.
- (80) Fischmann, T. O.; Hruza, a; Niu, X. D.; Fossetta, J. D.; Lunn, C. a; Dolphin, E.; Prongay, a J.; Reichert, P.; Lundell, D. J.; Narula, S. K.; Weber, P. C. *Nat. Struct. Biol.* **1999**, *6*, 233–242.
- (81) Rosenfeld, R. J.; Garcin, E. D.; Panda, K.; Andersson, G.; Aberg, A.; Wallace, A. V.; Morris, G. M.; Olson, A. J.; Stuehr, D. J.; Tainer, J. a; Getzoff, E. D. *Biochemistry* **2002**, *41*, 13915–13925.
- (82) Whitford, D. *Proteins: Structure and Function*; Wiley-Liss, 2005.
- (83) Li, H.; Jamal, J.; Plaza, C.; Pineda, S. H.; Chreifi, G.; Jing, Q.; Cinelli, M. A.; Silverman, R. B.; Poulos, T. L. *Acta Crystallogr. D. Biol. Crystallogr.* **2014**, *70*, 2667–2674.
- (84) Durón, S. G.; Lindstrom, A.; Bonnefous, C.; Zhang, H.; Chen, X.; Symons, K. T.; Sablad, M.; Rozenkrants, N.; Zhang, Y.; Wang, L.; Yazdani, N.; Shiau, A. K.; Noble, S. a; Rix, P.; Rao, T. S.; Hassig, C. a; Smith, N. D. *Bioorg. Med. Chem. Lett.* **2012**, *22*, 1237–41.
- (85) Pollard, C. B.; J.B, F. J. *Org. Chem* **1965**, *23*, 1935–1937.
- (86) Gómez, D. E.; Fabbrizzi, L.; Licchelli, M.; Monzani, E. *Org. Biomol. Chem.* **2005**, *3*, 1495–1500.

- (87) Claridge, T. D. W. *Correlations through the chemical bond II: Heteronuclear shift correlation*; Elsevier, 2009.
- (88) Karplus, M. *J. Am. Chem. Soc.* **1963**, *85*, 2870–2871.
- (89) Shioiri, T.; Ninomiya, K.; Yamada, S. *J. Am. Chem. Soc.* **1972**, *94*, 6203–6205.
- (90) Carpino, L.; Shroff, H.; Triolo, S. *Tetrahedron Lett.* **1993**, *34*, 7829–7832.
- (91) Isidro, A.; Latassa, D.; Giraud, M.; Álvarez, M.; Albericio, F. *Org. Biomol. Chem.* **2009**, *7*, 2565–2575.
- (92) Kunishima, M.; Kawachi, C.; Morita, J.; Tani, S.; Terao, K. *Tetrahedron* **1999**, *55*, 13159–13170.
- (93) El-faham, A.; Albericio, F. *Chem. Rev.* **2011**, *111*, 6557–6602.
- (94) Valeur, E.; Bradley, M. *Chem. Soc. Rev.* **2009**, *38*, 606–631.
- (95) Gibson, M. S.; Bradshaw, R. W. *Angew. Chemie Int. Ed. English* **1968**, *7*, 919–930.
- (96) Gabriel, S. *Berichte der Dtsch. Chem. Gesellschaft* **1887**, *20*, 2224–2236.
- (97) Diner, P.; Nielsen, M.; Marigo, M.; Joergensen, K. A. *Angew. Chem. Int. Ed. Engl.* **2007**, *46*, 1983–1987.
- (98) Patman, J.; Bhardwaj, N.; Ramnauth, J.; Annedi, S. C.; Renton, P.; Maddaford, S. P.; Rakhit, S.; Andrews, J. S. *Bioorg. Med. Chem. Lett.* **2007**, *17*, 2540–2544.
- (99) Lowe, J. a; Qian, W.; Drozda, S. E.; Volkmann, R. a; Nason, D.; Nelson, R. B.; Nolan, C.; Liston, D.; Ward, K.; Faraci, S.; Verdries, K.; Seymour, P.; Majchrzak, M.; Villalobos, A.; White, W. F. *J. Med. Chem.* **2004**, *47*, 1575–1586.
- (100) Brecht, D. S.; Snyder, S. H. *Proc. Natl. Acad. Sci. U. S. A.* **1990**, *87*, 682–5.
- (101) Invitrogen In *Invitrogen User Guide*; 2013; pp. 1–16.
- (102) Fedorov, R.; Vasan, R.; Ghosh, D. K.; Schlichting, I. *Proc. Natl. Acad. Sci. U. S. A.* **2004**,

- 101, 5892–5897.
- (103) Roman, L. J.; Sheta, E. a; Martasek, P.; Gross, S. S.; Liu, Q.; Masters, B. S. *Proc. Natl. Acad. Sci. U. S. A.* **1995**, *92*, 8428–8432.
- (104) Zhang, J.; Kang, Z.; Chen, J.; Du, G. *Sci. Rep.* **2015**, *5*, 8584.
- (105) Abbas, C. a; Sibirny, A. a *Microbiol. Mol. Biol. Rev.* **2011**, *75*, 321–360.
- (106) Edgcomb, S. P.; Murphy, K. P. *Proteins Struct. Funct. Genet.* **2002**, *49*, 1–6.
- (107) Francis, D. M.; Page, R. *Curr. Protoc. Protein Sci.* **2010**, 1–29.
- (108) Krause, M.; Ukkonen, K.; Haataja, T.; Ruottinen, M.; Glumoff, T.; Neubauer, A.; Neubauer, P.; Vasala, A. *Microb. Cell Fact.* **2010**, *9*, 11.
- (109) Sivashanmugam, A.; Murray, V.; Cui, C.; Zhang, Y.; Wang, J.; Li, Q. *Protein Sci.* **2009**, *18*, 936–948.
- (110) Gentz, R.; Bujard, H. *J. Bacteriol.* **1985**, *164*, 70–77.
- (111) Tabor, S. *Curr. Protoc. Mol. Biol.* **2001**, Chapter 16, Unit16.2.
- (112) Rosano, G. L.; Ceccarelli, E. a. *Front. Microbiol.* **2014**, *5*, 1–17.
- (113) Arora, K.; Mangale, S. S.; Guptasarma, P. *Anal. Biochem.* **2015**, *484*, 180–182.
- (114) Sørensen, H.; Mortensen, K. *Microb. Cell Fact.* **2005**, *4*, 1–8.
- (115) Ezraty, B.; Henry, C.; Hérisse, M.; Denamur, E.; Barras, F. *Free Radic. Biol. Med.* **2014**, *74*, 245–251.
- (116) Fink, A. L. *Fold. Des.* **1998**, *3*, R9–R23.
- (117) Knecht, S.; Ricklin, D.; Eberle, A. N.; Ernst, B. *J. Mol. Recognit.* **2009**, *22*, 270–9.
- (118) Fossetta, J. D.; Niu, X. D.; Lunn, C. a; Zavodny, P. J.; Narula, S. K.; Lundell, D. *FEBS Lett.* **1996**, *379*, 135–138.

- (119) Rodríguez-Crespo, I.; Ortiz de Montellano, P. R. *Arch. Biochem. Biophys.* **1996**, *336*, 151–156.
- (120) Points, K.; Korf, B. R.; Irons, M. B. *DNA Structure and Function*; 2012.
- (121) Perkins, D. N.; Pappin, D. J. C.; Creasy, D. M.; Cottrell, J. S. *Electrophoresis* **1999**, *20*, 3551–3567.
- (122) Montellano, P. R. O. D. E.; Nishida, C.; Rodriguez-crespo, I.; Gerber, N. *Drug Metabolism Depos.* **1998**, *26*, 1185–1189.
- (123) Ghigo, D.; Riganti, C.; Gazzano, E.; Costamagna, C.; Bosia, A. *Nitric Oxide* **2006**, *15*, 148–153.
- (124) Debeljak, N.; Feldman, L.; Davis, K. L.; Komel, R.; Sytkowski, A. J. *Anal. Biochem.* **2006**, *359*, 216–223.
- (125) Beckman, J. S.; Koppenol, W. H. *Am. J. Physiol.* **1996**, *271*, 1424–1437.
- (126) Hevel, J. M.; Micheal, M. A. *Methods Enzymol.* **1994**, *233*, 250–258.
- (127) Oxford Biomedical Griess assay kit specification sheet
http://www.oxfordbiomed.com/sites/default/files/spec_sheet/NB78.141410.pdf.
- (128) Bredt, D. S.; Snyder, S. H. *Proc. Natl. Acad. Sci. U. S. A.* **1989**, *86*, 9030–9033.
- (129) Kelm, M.; Wink, D.; Feelisch, M. *J Biol Chem* **1997**, *272*, 9922–9932.
- (130) GraphPad Software, San Diego California USA, www.graphpad.com.
- (131) Shevchenko, A.; Tomas, H.; Havlis, J.; Olsen, J. V; Mann, M. *Nat. Protoc.* **2007**, *1*, 2856–2860.
- (132) Vanommeslaeghe, K.; Guvench, O.; MacKerell, J. A. D. *Curr. Pharm. Des.* **2014**, *20*, 3281–3292.
- (133) Leach, A. R. *Molecular Modelling Principles and Applications*; 2nd ed.; Pearson Education, 2001.
- (134) Brooks, B. R.; Bruccoleri, R. E.; Olafson, B. D.; States, D. J.; Swaminathan, S.; Karplus,

- M. J. *Comput. Chem.* **1983**, *4*, 187–217.
- (135) Schlick, T. *Molecular Modelling and Simulation, An Interdisciplinary Guide*; Springer, 2002.
- (136) Jones, J. E. *Proc. R. Soc. Lon* **1924**, *106*, 463–477.
- (137) Sippl, W. *J. Comput. Aided. Mol. Des.* **2002**, *16*, 825–830.
- (138) Kroemer, R. T. *Curr. Protein Pept. Sci.* **2007**, *8*, 312–328.
- (139) Hawkins, P. C. D.; Skillman, a G.; Warren, G. L.; Ellingson, B. a; Stahl, M. T. *J. Chem. Inf. Model.* **2010**, *50*, 572–84.
- (140) Halgren, T. A. *J. Comput. Chem.* **1996**, *17*, 490–519.
- (141) Irwin, J. J.; Shoichet, B. K. *J. Chem. Inf. Model.* **2005**, *45*, 177–182.
- (142) Sitzmann, M.; Ihlenfeldt, W.-D.; Nicklaus, M. C. *J. Comput. Aided. Mol. Des.* **2010**, *24*, 521–551.
- (143) Ho, B. K.; Thomas, A.; Brasseur, R. *Protein Sci.* **2003**, *12*, 2508–2522.
- (144) Fawcett, T. *Pattern Recognit. Lett.* **2006**, *27*, 861–874.
- (145) Metz, C. E.; Herman, B. A.; Shen, J. *Stat. Med.* **1998**, *1053*, 1033–1053.
- (146) Cook, N. R. *Circulation* **2007**, *115*, 928–935.
- (147) Krieger, E.; Nabuurs, S. B.; Vriend, G. *Structural Bioinformatics*; Wiley-Liss, 2003.
- (148) Xiang, Z. *Curr. Protein Pept. Sci.* **2006**, *7*, 217–227.
- (149) Sali, A.; Blundell, L. T. *J. Mol. Biol.* **1993**, *234*, 779–815.
- (150) Shen, M.-Y.; Sali, A. *Protein Sci.* **2006**, *15*, 2507–2524.
- (151) McGann, M. R.; Almond, H. R.; Nicholls, A.; Grant, J. A.; Brown, F. K. *Biopolymers*

- 2003**, 68, 76–90.
- (152) Software, O. S. **2012**.
- (153) Pencheva, T.; Soumana, O. S.; Pajeva, I.; Miteva, M. a *Eur. J. Med. Chem.* **2010**, 45, 2622–8.
- (154) Software, O. E. *FRED, Fast Rigid Exhaustive Docking*; 2009.
- (155) Bohm, H.-J. *J. Comput. Aided. Mol. Des.* **1994**, 8, 243–256.
- (156) Eldridge, M. D.; Murray, C. W.; Auton, T. R.; Paolini, G. V; Mee, R. P. *J. Comput. Aided. Mol. Des.* **1997**, 11, 425–445.
- (157) Leach, A. R.; Shoichet, B. K.; Peishoff, C. E. *J. Med. Chem.* **2006**, 49, 5851–5855.
- (158) Openeye 3.0.0 release notes
<https://docs.eyesopen.com/oedocking/algorithm.html#chemgauss4>.
- (159) Kitchen, D. B.; Decornez, H.; Furr, J. R.; Bajorath, J. *Nat. Rev. Drug Discov.* **2004**, 3, 935–949.
- (160) Koska, J.; Spassov, V. Z.; Maynard, A. J.; Yan, L.; Austin, N.; Flook, P. K.; Venkatachalam, C. M. *J. Chem. Inf. Model.* **2008**, 48, 1965–1973.
- (161) Spassov, V. Z.; Yan, L.; Flook, P. K. *Protein Sci.* **2007**, 16, 494–506.
- (162) Acharya, C.; Coop, A.; Polli, J. E.; MacKerell, A. D. *J. Curr Comput Aided Drug Des* **2011**, 7, 10–22.
- (163) Barnum, D.; Greene, J.; Smellie, a; Sprague, P. *J. Chem. Inf. Comput. Sci.* **1996**, 36, 563–571.
- (164) Norinder, U. *J. Comput. Aided. Mol. Des.* **2000**, 14, 545–557.
- (165) Greenidge, P. a.; Carlsson, B.; Bladh, L. G.; Gillner, M. *J. Med. Chem.* **1998**, 41, 2503–2512.
- (166) Kranthi, R. K.; Rekha, R.; Lokesh.P; Muttineni, Ravikumar Ramachandran, D. *Int. J. Environ. Sci. Dev.* **2010**, 1, 40–46.

- (167) Chen, X.; Reynolds, C. H. *J. Chem. Inf. Comput. Sci.* **2002**, *42*, 1407–1414.
- (168) Kaufman, L.; Rousseeuw, P. J. *Finding groups in Data: An Introduction to Cluster Analysis*; John Wiley & Sons, Ltd, 2009.
- (169) Accelrys Discovery Studio ADMET Collection User Guide **2012**, 1–19.
- (170) Egan, W. J.; Merz, K. M.; Baldwin, J. J. *J. Med. Chem.* **2000**, *43*, 3867–3877.
- (171) Ponder, J. W.; Richards, F. M. *J. Mol. Biol.* **1987**, *193*, 775–791.
- (172) Li, Y.; Hu, Y.; Jiang, H.; Hou, X.; Li, C. *Chem. Commun.* **2008**, 4126–4128.
- (173) Eisenführ, A.; Arora, P. S.; Sengle, G.; Takaoka, L. R.; Nowick, J. S.; Famulok, M. *Bioorganic Med. Chem.* **2003**, *11*, 235–249.
- (174) Wiget, P. a.; Manzano, L. a.; Pruet, J. M.; Gao, G.; Saito, R.; Monzingo, A. F.; Jasheway, K. R.; Robertus, J. D.; Anslyn, E. V. *Bioorganic Med. Chem. Lett.* **2013**, *23*, 6799–6804.
- (175) Zheng, C. H.; Yang, H.; Zhang, M.; Lu, S. H.; Shi, D.; Wang, J.; Chen, X. H.; Ren, X. H.; Liu, J.; Lv, J. G.; Zhu, J.; Zhou, Y. J. *Bioorganic Med. Chem. Lett.* **2012**, *22*, 39–44.

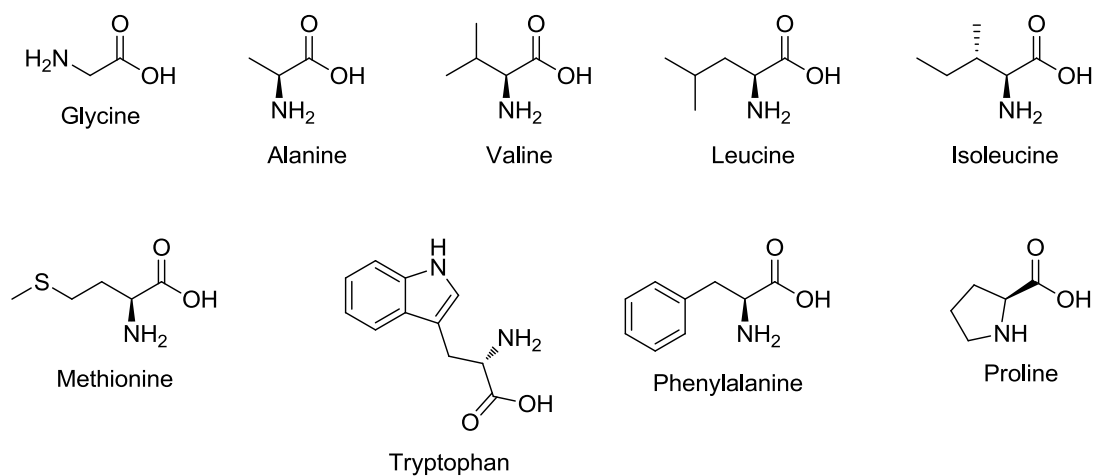
8 Appendix

8.1 Amino acids

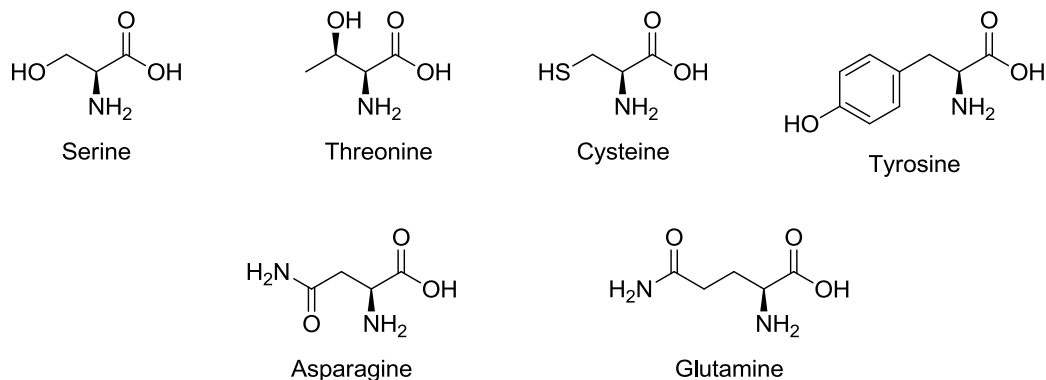
Table 8.1. Amino acid three letter and one letter codes.

Amino Acid	Three letter code	One letter code
Alanine	Ala	A
Arginine	Arg	R
Asparagine	Asn	N
Aspartic acid	Asp	D
Cysteine	Cys	C
Glutamine	Gln	Q
Glutamic acid	Glu	E
Glycine	Gly	G
Histidine	His	H
Isoleucine	Ile	I
Leucine	Leu	L
Lysine	Lys	K
Methionine	Met	M
Phenylalanine	Phe	F
Proline	Pro	P
Serine	Ser	S
Threonine	Thr	T
Tryptophan	Trp	W
Tyrosine	Tyr	Y
Valine	Val	V

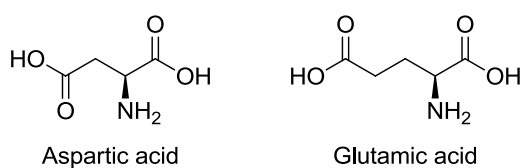
Non polar amino acids



Polar amino acids



Negatively charged amino acids



Positively charged amino acids

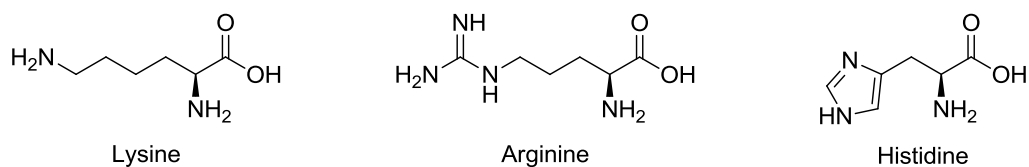


Figure 8.1. Amino acid side chains.

8.2 Rat nNOS aligned with human nNOS

```

Rat   MEENTFGVQQIQPNVISVRLFKRKVGGGLGFLVKERVSKPPVVISDLIRGGAAEQSGLIQA
Human MEDHMFVGVQQIQPNVISVRLFKRKVGGGLGFLVKERVSKPPVVISDLIRGGAAEQSGLIQA
      **: . *****

Rat   GDIILAVNDRPLVDLSYDSALEVLRGIASETHVVLILRGPEGFTTHLETTFTGDGTPKTI
Human GDIILAVNGRPLVDLSYDSALEVLRGIASETHVVLILRGPEGFTTHLETTFTGDGTPKTI
      *****

Rat   RVTQPLGPPTKAVDLSHQPSASKDQSLAVDRVTGLGNGPQHAQGHGQGAGSVSQANGVAI
Human RVTQPLGPPTKAVDLSHQPPAGKEQPLAVDVGASGPGNGPQHAYDDGQEQAGSLPHANGLAP
      ***** *.:* **** .:* ***** .* ***: :***:*

Rat   D-----PTMKSTKANLQDIGEHDELLKEIEPVLSILNSGSKATNRGGPAKAEMKDTGIQV
Human RPPGQDPAKKATRVSLQGRGENNELLKEIEPVLSLLTSGSRGVKGGAPAKAEMKDMGIQV
      *: *.:*. ** **.:*****:*.***:..: *.***** ****

Rat   DRDLDGKSHKAPPLGGDNDRVFNDLWGKDNVPVILNNPYSEKEQSPTSGKQSPTKNGSPS
Human DRDLDGKSHKPLPLGVENDRVFNDLWGKGNVPVVLNNPYSEKEQPPTSGKQSPTKNGSPS
      ***** *** :***** *****:***** *****

Rat   RCPNFLKVKNWETDVVLTDTLHLKSTLETGCTEHCIMGSIMLPSQHTRKPEDVVRTKDQLF
Human KCPNFLKVKNWETEVLVLTDTLHLKSTLETGCTEYICMGSIMHPSQHARRPEDVVRTKQQLF
      :*****:*****:***** ****.*:***** **

Rat   PLAKEFLDQYYSSIKRFGSKAHMDRLEEVENKEIESTSTYQLKDTELIYGAKHAWRNASRC
Human PLAKEFIDQYYSSIKRFGSKAHMERLEEVENKEIDTTSTYQLKDTELIYGAKHAWRNASRC
      *****:*****:*****:*****

Rat   VGRIQWSKLVQVFDARDCTTAHGFMFNYICNHVKYATNKGNLRSAITIFPQRTDGHDFRVW
Human VGRIQWSKLVQVFDARDCTTAHGFMFNYICNHVKYATNKGNLRSAITIFPQRTDGHDFRVW
      *****

Rat   NSQLIRYAGYKQPDGSLTGD PANVQFTEICIQGWKAPRGRFDVLP LLLQANGNDPEL FQ
Human NSQLIRYAGYKQPDGSLTGD PANVQFTEICIQGWKAPRGRFDVLP LLLQANGNDPEL FQ
      ***** *****

Rat   IPPELVLEVPPIRHPKFDWFKDLGLKWKYGLPAVSNMLLEIGGLEFSACPFSGWYMGTEIGV
Human IPPELVLEVPPIRHPKFEWFKDLGLKWKYGLPAVSNMLLEIGGLEFSACPFSGWYMGTEIGV
      *****:*****

Rat   RDYCDNSRYNILEEVAKKMDLDMRKTSSLWKDQALVEINIAVLYSFQSDKVTIVDHHSAT
Human RDYCDNSRYNILEEVAKKMNLDLDMRKTSSLWKDQALVEINIAVLYSFQSDKVTIVDHHSAT
      *****:*****

Rat   ESFIKHMENEYRCRGGCPADWVWIVPPMSGSITPVFHQEMLNYRLTPSF EYQPD PWNTHV
Human ESFIKHMENEYRCRGGCPADWVWIVPPMSGSITPVFHQEMLNYRLTPSF EYQPD PWNTHV
      *****

Rat   WKGTNGTPTKRRRAIGFKKLAEAVKFS AKLMGQAMAKRVKATILYATETGKSQAYAKTLCE
Human WKGTNGTPTKRRRAIGFKKLAEAVKFS AKLMGQAMAKRVKATILYATETGKSQAYAKTLCE
      *****

Rat   IFKHAFDAKAMSME EYDIVHLEHEALV LVVTSTFGNGDPPENGEKFGCALMEMRHPNSVQ
Human IFKHAFDAKAMSME EYDIVHLEHETLVLVVTSTFGNGDPPENGEKFGCALMEMRHPNSVQ

```

```

*****.*****:*****
Rat   EERKSYKVRFNFSVSSYSDSRKSSGDPDLRDNFESTGPLANVRFVSVFGLGSRAYPHFCAF
Human EERKSYKVRFNFSVSSYSDSQKSSGDPDLRDNFESAGPLANVRFVSVFGLGSRAYPHFCAF
*****:*****:*****
Rat   GHAVDTLLEELGGERILKMREGDELCEGQEEAFRTWAKKVFKAACDVFCVGDVNIIEKPNN
Human GHAVDTLLEELGGERILKMREGDELCEGQEEAFRTWAKKVFKAACDVFCVGDVNIIEKANN
***** **
Rat   SLISNDRSWKRNKFRLLTYVAEAPDLTQGLSNVHKKRVSAARLLSRQNLQSPKFSRSTIFV
Human SLISNDRSWKRNKFRLLTFVAEAPDLTQGLSNVHKKRVSAARLLSRQNLQSPKSSRSTIFV
*****:*****:***** **
Rat   RLHTNGNQELQYQPGDHLGVFPGNHEDLVNALIERLEDAPPANHVVKVEMLEERNTALGV
Human RLHTNGSQELQYQPGDHLGVFPGNHEDLVNALIERLEDAPPVNMVKVELLEERNTALGV
*****.*****.*:***:*****
Rat   ISNWKDESRLPPCTIFQAFKYYLDITTPPTPLQLQQFASLATNEKEKQRLLVLSKGLQEY
Human ISNWTDELRLPPCTIFQAFKYYLDITTPPTPLQLQQFASLATSEKEKQRLLVLSKGLQEY
****.*** *****.*****
Rat   EEWKWGNPTMVEVLEEFPSIQMPATLLLLTQLSLLQPRYYSISSSPDMYPDEVHLTVAIV
Human EEWKWGNPTIVEVLEEFPSIQMPATLLLLTQLSLLQPRYYSISSSPDMYPDEVHLTVAIV
*****:*****
Rat   SYHTRDGEQVHGVCSWLNRIQADDVVPFCFVRGAPSFHLPRNPQVPCILVGPGTGIAP
Human SYRTRDGEQPIHHGVCSWLNRIQADELVPCFVRGAPSFHLPRNPQVPCILVGPGTGIAP
*:*****:*****:*****
Rat   FRSFWQQRQFDIQHKGMNPCPMVLVFGCRQSKIDHIYREETLQAKNKGVFRELYTAYSRE
Human FRSFWQQRQFDIQHKGMNPCPMVLVFGCRQSKIDHIYREETLQAKNKGVFRELYTAYSRE
*****
Rat   PDRPKKYVDVLEQQLAESVYRALKEQGGHIYVCGDVTMAADV LKAIQRIMTQQGKLSEE
Human PDKPKKYVDILQEQQLAESVYRALKEQGGHIYVCGDVTMAADV LKAIQRIMTQQGKLSAE
*:*****:***** *
Rat   DAGVFISRLRDDNRYHEDIFGVTLRITYEVTNRLRSESI AFIEESK KDADEVFSS
Human DAGVFISRMRDDNRYHEDIFGVTLRITYEVTNRLRSESI AFIEESK KDTDEVFSS
*****:*****:*****

```

8.3 Human nNOS construct aligned with published human nNOS sequence

pQE30 forward primer;

```

nNOS FHTEFIKEEKLTMRGSHHHHHGSACELGTMEDHMFVQVQIQPNVISVRLFKRKVGGLGF 60
Pub  -----MEDHMFVQVQIQPNVISVRLFKRKVGGLGF 30
      *****
nNOS LVKERVSKPPVVISDLIRGGAAEQSGLIQAGDIILAVNGRPLVDLSYDSALEVLRGIASE 120

```

Pub LVKERVSKPPVVIISDLIRGGAAEQSGLIQAGDIILAVNGRPLVDLSYDSALEVLRGIASE 90

nNOS THVVLILRGPEGFTTHLETTFTGDGTPKTI RVTQPLGPPTKAVDLSHQPPAGKEQPLAVD 180
 Pub THVVLILRGPEGFTTHLETTFTGDGTPKTI RVTQPLGPPTKAVDLSHQPPAGKEQPLAVD 150

nNOS GASGPGNGPQHAYDDGQEAGSLPHANGLAPRPPGQDPAKKATRVSLQGRGENNELLKEIE 240
 Pub GASGPGNGPQHAYDDGQEAGSLPHANGLAPRPPGQDPAKKATRVSLQGRGENNELLKEIE 210

nNOS FVLSLLTSGSRGVKGGAPAKAEMKDMGIQVDRDLDGKSHKPLPLGVENDRVFNDLWGKGN 300
 Pub FVLSLLTSGSRGVKGGAPAKAEMKDMGIQVDRDLDGKSHKPLPLGVENDRVFNDLWGKGN 270

nNOS VPVVLNNPYSEK----- 312
 Pub VPVVLNNPYSEKQPPTSGKQSPTKNGSPSKCPRFLKVKNWETEVLDTLHLKSTLETG 330

Internal primer 1;

nNOS CPRFLKVKNWETEVLDTLHLKSTLETGCTEYICMGSIMHPSQHARRPEDVRTKGQLF 59
 Pub KCPRFLKVKNWETEVLDTLHLKSTLETGCTEYICMGSIMHPSQHARRPEDVRTKGQLF 360

nNOS PLAKEFIDQYSSIKRFGSKAHMERLEEVNKEIDTTSTYQLKDELIYGAKHAWRNASRC 119
 Pub PLAKEFIDQYSSIKRFGSKAHMERLEEVNKEIDTTSTYQLKDELIYGAKHAWRNASRC 420

nNOS VGRIQWSKLQVFDARDCTTAHGMFNICYCNHVKYATNKGNLRSAITIFPQRTDGKHD FRVW 179
 Pub VGRIQWSKLQVFDARDCTTAHGMFNICYCNHVKYATNKGNLRSAITIFPQRTDGKHD FRVW 480

nNOS NSQLIRYAGYKQPDGSTLGD PANVQFTEICIQGWKPPRGRFDVLP LLLQANGNDPELFQ 239
 Pub NSQLIRYAGYKQPDGSTLGD PANVQFTEICIQGWKPPRGRFDVLP LLLQANGNDPELFQ 540

nNOS IPPELVLEVP IRHPKFEWFKDLGLK WYGLPAVSNM LLEIGGLSSAP----- 285
 Pub IPPELVLEVP IRHPKFEWFKDLGLK WYGLPAVSNM LLEIGGLEFSACPFSGWYMGTEIGV 600

Internal primer 2;

nNOS -----SITPVFHQEMLN YRLTPSF EYQPD PWNTHV 30
 Pub ESFIKHMENEYRCRGGCPADWWIVPPMSGISITPVFHQEMLN YRLTPSF EYQPD PWNTHV 720

nNOS WKGTNGTPTKRRAIGFKKLA EAVKFSAKLMGQAMAKRVKATILYATETGKSQAYAKTLCE 90
 Pub WKGTNGTPTKRRAIGFKKLA EAVKFSAKLMGQAMAKRVKATILYATETGKSQAYAKTLCE 780

nNOS IFKHAFDAKVM S MEYDIVHLEHETLVLVVTSTFGNGDPPENGEKFGCALMEMRHPNSVQ 150
 Pub IFKHAFDAKVM S MEYDIVHLEHETLVLVVTSTFGNGDPPENGEKFGCALMEMRHPNSVQ 840

nNOS EERKSYKVRFN SVSSYSDSQSSGDGPD LRDNFESAGPLANVRF SVFGLGSRAYPHFCF 210
 Pub EERKSYKVRFN SVSSYSDSQSSGDGPD LRDNFESAGPLANVRF SVFGLGSRAYPHFCF 900

nNOS GHAVDTLLEELGGERILKMREGDEL CGQEEAFRTWAKKVFKAACDVFCVGD DVNIEKANN 270
 Pub GHAVDTLLEELGGERILKMREGDEL CGQEEAFRTWAKKVFKAACDVFCVGD DVNIEKANN 960

nNOS SLISNDRSWKR NKFRLTFVAEAPELTQGLSNVHKKRVSAARLL----- 313

Pub SLISNDRSWKRNKFRLTFVAEAPELTQGLSNVHKKRVSAARLLSRQNLQSPKSSRSTIFV 1020

Internal primer 3;

nNOS -----G EAFRTWAKKVFKAACDVFCVGDDVNI EKANN 32
Pub GHAVDTLLEELGGERILKMREGDEL CGQEEAFRTWAKKVFKAACDVFCVGDDVNI EKANN 960

nNOS SLISNDRSWKRNKFRLTFVAEAPELTQGLSNVHKKRVSAARLLSRQNLQSPKSSRSTIFV 92
Pub SLISNDRSWKRNKFRLTFVAEAPELTQGLSNVHKKRVSAARLLSRQNLQSPKSSRSTIFV 1020

nNOS RLHTNGSQELQYQPGDHLGVFPGNHEDLVNALIERLEDAPPVNQMVKVELLEERNTALGV 152
Pub RLHTNGSQELQYQPGDHLGVFPGNHEDLVNALIERLEDAPPVNQMVKVELLEERNTALGV 1080

nNOS ISNWTDELRLPPCTIFQAFKYLDITTPPTPLQLQQFASLATSEKEKQRLLVLSKGLQEY 212
Pub ISNWTDELRLPPCTIFQAFKYLDITTPPTPLQLQQFASLATSEKEKQRLLVLSKGLQEY 1140

nNOS EEWKWGNPTIVEVLEEFPSIQMPATLLLLQLSLLQPRYYSISSSPDMPDEVHLTVAIV 272
Pub EEWKWGNPTIVEVLEEFPSIQMPATLLLLQLSLLQPRYYSISSSPDMPDEVHLTVAIV 1200

nNOS SYRTRDGE GPIHHGVCSSWLNRIQADELVPCFVRGAPSFHLP RNPQVPCILVGP----- 326
Pub SYRTRDGE GPIHHGVCSSWLNRIQADELVPCFVRGAPSFHLP RNPQVPCILVGP GTGIAP 1260

pQE30 reverse primer;

nNOS -----KEKQRLLVLSKGLQEY 16
Pub ISNWTDELRLPPCTIFQAFKYLDITTPPTPLQLQQFASLATSEKEKQRLLVLSKGLQEY 1140

nNOS EEWKWGNPTIVEVLEEFPSIQMPATLLLLQLSLLQPRYYSISSSPDMPDEVHLTVAIV 76
Pub EEWKWGNPTIVEVLEEFPSIQMPATLLLLQLSLLQPRYYSISSSPDMPDEVHLTVAIV 1200

nNOS SYRTRDGE GPIHHGVCSSWLNRIQADELVPCFVRGAPSFHLP RNPQVPCILVGP GTGIAP 136
Pub SYRTRDGE GPIHHGVCSSWLNRIQADELVPCFVRGAPSFHLP RNPQVPCILVGP GTGIAP 1260

nNOS FR SFWQQRQFDIQHKG MNPCPMVLVFGCRQSKIDHIYSEETLQAKNKGVFRELYTAYSRE 196
Pub FR SFWQQRQFDIQHKG MNPCPMVLVFGCRQSKIDHIYREETLQAKNKGVFRELYTAYSRE 1320

nNOS PDKPKKYVQDILQEQLAESVYRALKEQGGHIYVCGDVTMAADVLKAIQRIMTQQGKLSAE 256
Pub PDKPKKYVQDILQEQLAESVYRALKEQGGHIYVCGDVTMAADVLKAIQRIMTQQGKLSAE 1380

nNOS DAGVFISMRDDNRYHEDIFGVTLR TYEVTNRLRSESIAFIEESK KDTDEVFSS 310
Pub DAGVFISMRDDNRYHEDIFGVTLR TYEVTNRLRSESIAFIEESK KDTDEVFSS 1434

8.4 Human eNOS construct aligned with published human eNOS sequence

pQE30 forward primer;

```
eNOS -----MFTYICNHIKYATNRGNLRSAITVFPQRCPGRGD 34
Pub  APRCVGRIQWGLQVFDARDCRSAQEMFTYICNHIKYATNRGNLRSAITVFPQRCPGRGD 240
      *****

eNOS  FRIWNSQLVRYAGYRQQDGSVRGDPANVEITELCIQHGWTPGNRFDVLPDLLQAPDEPP 94
Pub  FRIWNSQLVRYAGYRQQDGSVRGDPANVEITELCIQHGWTPGNRFDVLPDLLQAPDEPP 300
      *****

eNOS  ELFLLPPELVLEVPLEHPTLEWF AALGLRWYALPAVSNMLEIGGLEFPAAPFSGWYMST 154
Pub  ELFLLPPELVLEVPLEHPTLEWF AALGLRWYALPAVSNMLEIGGLEFPAAPFSGWYMST 360
      *****

eNOS  EIGTRNLCDPHRYNILEDVAVCMDLDRTRTSSLWKDKAAVEINAVLHSYQLAKVTIVDH 214
Pub  EIGTRNLCDPHRYNILEDVAVCMDLDRTRTSSLWKDKAAVEINAVLHSYQLAKVTIVDH 420
      *****

eNOS  HAATASFMKHLENEQKARGGCPADWAWIVPPIISGSLTPVVFHQEMVNYFLSPA FRYQPDPW 274
Pub  HAATASFMKHLENEQKARGGCPADWAWIVPPIISGSLTPVVFHQEMVNYFLSPA FRYQPDPW 480
      *****

eNOS  KGSAAKGTGITRKKTFKEVANAVKISASLMGTVM AKRVK----- 313
Pub  KGSAAKGTGITRKKTFKEVANAVKISASLMGTVM AKRVKATILYGSETGRAQSYAQQ LGR 540
      *****
```

Internal primer 1;

```
eNOS -----TPVVFHQEMVNYFLSPA FRYQPDPW 24
Pub  HAATASFMKHLENEQKARGGCPADWAWIVPPIISGSLTPVVFHQEMVNYFLSPA FRYQPDPW 480
      *****

eNOS  KGSAAKGTGITRKKTFKEVANAVKISASLMGTVM AKRVKATILYGSETGRAQSYAQQ LGR 84
Pub  KGSAAKGTGITRKKTFKEVANAVKISASLMGTVM AKRVKATILYGSETGRAQSYAQQ LGR 540
      *****

eNOS  LFRKAFDPRVLCMDEYDVVSLEHETLVLVVTSTFGNGDP PENGESFAAALMEMSGPYNSS 144
Pub  LFRKAFDPRVLCMDEYDVVSLEHETLVLVVTSTFGNGDP PENGESFAAALMEMSGPYNSS 600
      *****

eNOS  PRPEQHKS YKIRFNSISCS DPLVSSWRRKRKESNTDSAGALGTLR FCFVGLGS RAYPHF 204
Pub  PRPEQHKS YKIRFNSISCS DPLVSSWRRKRKESNTDSAGALGTLR FCFVGLGS RAYPHF 660
      *****

eNOS  CAFARAVDTRLEELGGERLLQLGQGDEL CGQEEAFRGWAQAAFQAACETFCVGEDAKAAA 264
Pub  CAFARAVDTRLEELGGERLLQLGQGDEL CGQEEAFRGWAQAAFQAACETFCVGEDAKAAA 720
      *****

eNOS  RDIFSPKRSWK RQRYRLSAQAEGLQLLPGLIHVHRRKMF----- 303
Pub  RDIFSPKRSWK RQRYRLSAQAEGLQLLPGLIHVHRRKMFQATIRSVENLQSSKSTRATIL 780
      *****
```

Internal primer 2;

```

eNOS      -----GGLGGERLLQLGQGDELQEEAFRGWAQAAFQAACETFCVGEDAKAAA 49
Pub       CAFARAVDTRLEELGGERLLQLGQGDELQEEAFRGWAQAAFQAACETFCVGEDAKAAA 720
          *****

eNOS      RDIFSPKRSWKRQRYRLSAQAEGQLLPLGLIHVHRRKMFQATIRSVENLQSSKSTRATIL 109
Pub       RDIFSPKRSWKRQRYRLSAQAEGQLLPLGLIHVHRRKMFQATIRSVENLQSSKSTRATIL 780
          *****

eNOS      VRLDTGGQEGLYQPGDHIGVCPNRPGLVEALLSRVEDPPAPTEPVAVEQLEKGSPPGGP 169
Pub       VRLDTGGQEGLYQPGDHIGVCPNRPGLVEALLSRVEDPPAPTEPVAVEQLEKGSPPGGP 840
          *****

eNOS      PPGWVRPRLPPCTLRQALTFFLDITSPSPQLLRLSTLAEFPREQQEALQSODPRRY 229
Pub       PPGWVRPRLPPCTLRQALTFFLDITSPSPQLLRLSTLAEFPREQQEALQSODPRRY 900
          *****

eNOS      EEWKWFRCP TLLEVLEQFPSVALPAPLLLTQLPLLQPRYYSVSSAPSTHPGEIHLTVAVL 289
Pub       EEWKWFRCP TLLEVLEQFPSVALPAPLLLTQLPLLQPRYYSVSSAPSTHPGEIHLTVAVL 960
          *****

eNOS      AYRTHDGLGPLHYGVCSTWLSQLKPGRP----- 317
Pub       AYRTQDGLGPLHYGVCSTWLSQLKPGDPVPCFIRGAPSFRLPPDPSLPCILVGPGTGIAP 1020
          **** *****

```

Internal primer 3;

```

eNOS      -----TLLEVLEQFPSVALPAPLLLTQLPLLQPRYYSVSSAPSTHPGEIHLTVAVL 51
Pub       EEWKWFRCP TLLEVLEQFPSVALPAPLLLTQLPLLQPRYYSVSSAPSTHPGEIHLTVAVL 960
          *****

eNOS      AYRTQDGLGPLHYGVCSTWLSQLKPGDPVPCFIRGAPSFRLPPDPSLPCILVGPGTGIAP 111
Pub       AYRTQDGLGPLHYGVCSTWLSQLKPGDPVPCFIRGAPSFRLPPDPSLPCILVGPGTGIAP 1020
          *****

eNOS      FRGFQWERLHDIESKGLQPTPMTLVFGCRCSQLDHLRDEVQNAQQRGVFRVLTAFSRE 171
Pub       FRGFQWERLHDIESKGLQPTPMTLVFGCRCSQLDHLRDEVQNAQQRGVFRVLTAFSRE 1080
          *****

eNOS      PDNPKTYVDILRTELAAEVHRVLCLEGRHMFVCGDVTMATNVLQTVQRILATEGDMELD 231
Pub       PDNPKTYVDILRTELAAEVHRVLCLEGRHMFVCGDVTMATNVLQTVQRILATEGDMELD 1140
          *****

eNOS      EAGDVIGVLRDQQRYHEDI FGLTLRTQEVTSRIRTQSFSLQERQLRGAVPWAFDPPGSDT 291
Pub       EAGDVIGVLRDQQRYHEDI FGLTLRTQEVTSRIRTQSFSLQERQLRGAVPWAFDPPGSDT 1200
          *****

eNOS      NSPHHHHHH 300
Pub       NSP----- 1203
          ***

```

8.5 Human iNOS construct aligned with published human iNOS sequence

pQE30 forward primer;

```

iNOS  ADNNYNRFNCERITISHRIDLEMACPWKFLFKTKFHQYAMNGEKDINNNVEKAPCATSSP 60
Pub    -----MACPWKFLFKTKFHQYAMNGEKDINNNVEKAPCATSSP 38
          *****

iNOS  VTQDDLQYHNLSKQQNESQPPLVETGKKSPESLVKLDATPLSSPRHVRIKNWGSGMTFQD 120
Pub    VTQDDLQYHNLSKQQNESQPPLVETGKKSPESLVKLDATPLSSPRHVRIKNWGSGMTFQD 98
          *****

iNOS  TLHHKAKGILTCRSKSLGSIIMTPKSLTRGPRDKPTPPDELLPQAIEFVNQYYGSFKEAK 180
Pub    TLHHKAKGILTCRSKSLGSIIMTPKSLTRGPRDKPTPPDELLPQAIEFVNQYYGSFKEAK 158
          *****

iNOS  IEEHLARVEAVTKEIETTGTQYLTGDELI FATKQAWRNAPRCIGRIQWSNLQVFDARSCS 240
Pub    IEEHLARVEAVTKEIETTGTQYLTGDELI FATKQAWRNAPRCIGRIQWSNLQVFDARSCS 218
          *****

iNOS  TAREMFEHICRHVRYSTNNGNIRSII----- 267
Pub    TAREMFEHICRHVRYSTNNGNIRSAITVFPQRSDBGKHDFRVWNAQLIRYAGYQMPDGSIR 278
          *****

```

Internal primer 1;

```

iNOS  -----WQHDFRVWNAQLIRYAGYQMPDGSIRGDPANVEFTQLCIDLGWPKPKYG 48
Pub    RSAITVFPQRSDBGKHDFRVWNAQLIRYAGYQMPDGSIRGDPANVEFTQLCIDLGWPKPKYG 300
          *****

iNOS  RFDVVPLVLQANGRDPELFEIPDLVLEVAMEHPKYEFWFRELELKWYALPAVANMLLEV 108
Pub    RFDVVPLVLQANGRDPELFEIPDLVLEVAMEHPKYEFWFRELELKWYALPAVANMLLEV 360
          *****

iNOS  GLEFPGCPFNWYMGTEIGVRDFCDVQRYNILEEVGRRMGLETHKLASLWKDQAVVEINI 168
Pub    GLEFPGCPFNWYMGTEIGVRDFCDVQRYNILEEVGRRMGLETHKLASLWKDQAVVEINI 420
          *****

iNOS  AVLHSFQKQNVTIMDHSAAESFMKYMONEYRSRGGCPADWIWLVPMSGSITPVFHQEM 228
Pub    AVLHSFQKQNVTIMDHSAAESFMKYMONEYRSRGGCPADWIWLVPMSGSITPVFHQEM 480
          *****

iNOS  LNYVLSPFYYQVEAWKTHVWQDEKRRPKRREIPLKVLVKAVLFACMLMRKTMASRVRVT 288
Pub    LNYVLSPFYYQVEAWKTHVWQDEKRRPKRREIPLKVLVKAVLFACMLMRKTMASRVRVT 540
          *****

iNOS  ILFATETGKSEALAWGPGGLIQLCLQPQ-----GCLHG----- 321
Pub    ILFATETGKSEALAWDLGALFSCAFNPKVVCMDKYRLSCLEEEERLLLVVTSTFGNGDCPG 600
          *****

```

Internal primer 2;

```

iNOS  -----SLGQAVLFACMLMRKTMASRVRVT 24
Pub    LNYVLSPFYYQVEAWKTHVWQDEKRRPKRREIPLKVLVKAVLFACMLMRKTMASRVRVT 540
          *****

iNOS  ILFATETGKSEALAWDLGALFSCAFNPKVVCMDKYRLSCLEEEERLLLVVTSTFGNGDCPG 84
Pub    ILFATETGKSEALAWDLGALFSCAFNPKVVCMDKYRLSCLEEEERLLLVVTSTFGNGDCPG 600
          *****

```

```

iNOS  NGEKLLKSLFMLKELNNKFRYAVFGLGSSMYPRFCAFAHDIDQKLSHLGASQLTPMGEGD 144
Pub    NGEKLLKSLFMLKELNNKFRYAVFGLGSSMYPRFCAFAHDIDQKLSHLGASQLTPMGEGD 660
      *****

iNOS  ELSGQEDAFRSWAVQTFKAACETFDVRGKQHIQIPKLYTSNVTWDPHHYRLVQDSQPLDL 204
Pub    ELSGQEDAFRSWAVQTFKAACETFDVRGKQHIQIPKLYTSNVTWDPHHYRLVQDSQPLDL 720
      *****

iNOS  SKALSSMHAKNVFTMRLKSRQNLQSPTSSRATILVELSCEDGQGLNYLPGEHLGVCPCGNQ 264
Pub    SKALSSMHAKNVFTMRLKSRQNLQSPTSSRATILVELSCEDGQGLNYLPGEHLGVCPCGNQ 780
      *****

iNOS  PALVQGILS----- 279
Pub    PALVQGILERVVDGPTPHQTVRLEALDESGSYWVSDKRLPPCSLSQALTYFLDITTPPTQ 840
      *****

```

pQE30 reverse primer;

```

iNOS  -----LEALCQPSEYSKWKFTNSPTFLEVLEEFPSLRVSAGFLLSQL 42
Pub    LLLQKLAQVATEEPERQRLLEALCQPSEYSKWKFTNSPTFLEVLEEFPSLRVSAGFLLSQL 900
      *****

iNOS  PILKPRFYSISSRDHTPTEIHLTVAVVTYHTRDGGQPLHHGVCSTWLNLSLKPQDPVPCF 102
Pub    PILKPRFYSISSRDHTPTEIHLTVAVVTYHTRDGGQPLHHGVCSTWLNLSLKPQDPVPCF 960
      *****

iNOS  VRNASGFHLPEDPSHPCILIGPGTGIAPFRSFWQORLHDSQHKGVRRGGRMTLVFGCRRPD 162
Pub    VRNASGFHLPEDPSHPCILIGPGTGIAPFRSFWQORLHDSQHKGVRRGGRMTLVFGCRRPD 1020
      *****

iNOS  EDHIYQEEMLEMAQKGV LHAVHTAYSRLPGKPKVYVQDILRQQLASEVLRV LHKEPGHLY 222
Pub    EDHIYQEEMLEMAQKGV LHAVHTAYSRLPGKPKVYVQDILRQQLASEVLRV LHKEPGHLY 1080
      *****

iNOS  VCGDVRMARDVAHTLKQLVAAKLLKLNEEQVEDYFFQLKSQKRYHEDIFGAVFPYEAKKDR 282
Pub    VCGDVRMARDVAHTLKQLVAAKLLKLNEEQVEDYFFQLKSQKRYHEDIFGAVFPYEAKKDR 1140
      *****

iNOS  VAVQPSSEMSALHHHHHH 301
Pub    VAVQPSSEMSAL----- 1153
      *****

```

8.6 Human calmodulin construct aligned with published human calmodulin sequence

T7 promotor primer;

```

CaM  MADQLTEEQIAEFKEAFSLFDKDG DGTITTKELGTVMRSLGQNPTAEELQDMINEVDADG
Pub  MADQLTEEQIAEFKEAFSLFDKDG DGTITTKELGTVMRSLGQNPTAEELQDMINEVDADG
      *****

CaM  NGTIDFPEFLTMMARKMKD TDSEEEIREAFRVFDKDGNGYISAAELRHVMTNLGEKLTDE
Pub  NGTIDFPEFLTMMARKMKD TDSEEEIREAFRVFDKDGNGYISAAELRHVMTNLGEKLTDE
      *****

```

```
CaM  EVDEMIREADIDGGDGVNYEEFVQMMTAK
Pub  EVDEMIREADIDGGDGVNYEEFVQMMTAK
*****
```

8.7 Oral presentations

2014

- Computer aided drug design techniques in the search for human nNOS inhibitors, CADD training workshop, NUI Maynooth, June 2014
- Expression, inhibition and in silico studies of human nNOS. ITT research day, IT Tallaght, May 2014
- Expression, inhibition and in silico studies of human nNOS. BioAT research day, DCU.

2013

- Expression, inhibition and in silico studies of human nNOS. ITT research day, IT Tallaght, May 2013

2012

- *In silico* design of human nNOS inhibitors. BioAT research day, NUIM, June 2012
- Expression and in silico studies of human nNOS. ITT research day, IT Tallaght, May 2012

8.8 Poster presentations

2014

- Expression, inhibition and in silico studies of human nNOS. Irish Universities Chemistry Research Colloquium, NUIG, July 2014

2013

- Selective inhibition of human neuronal nitric oxide synthase, ISACCS 11 conference, MIT, Boston, July 2013

- Selective inhibition of human neuronal nitric oxide synthase, BioAT research day, RCSI, Dublin, June 2013
- Design of selective human nNOS inhibitors, Irish Universities Chemistry Research Colloquium, TCD, June 2013
- In silico design of human nNOS inhibitors, Wellcome Trust CADD workshop, Hinxton, Cambridge, November 2013

2012

- Expression, inhibition and in silico modelling of human nNOS. CSCB conference, RCSI, Dublin, November 2012

8.9 Publications

Computational Development of Selective nNOS Inhibitors: Binding Modes and Pharmacokinetic Considerations. Curtin, A. M.; Kinsella, G. K.; Stephens, J. C. *Curr. Med. Chem.* **2015**, *22*, 2558–2579.